



HAL
open science

Fabrication, integration and study of micropillars for cell culture

Jin Wei

► **To cite this version:**

Jin Wei. Fabrication, integration and study of micropillars for cell culture. Analytical chemistry. Université Paris sciences et lettres, 2017. English. NNT : 2017PSLEE042 . tel-01813403

HAL Id: tel-01813403

<https://theses.hal.science/tel-01813403>

Submitted on 12 Jun 2018

HAL is a multi-disciplinary open access archive for the deposit and dissemination of scientific research documents, whether they are published or not. The documents may come from teaching and research institutions in France or abroad, or from public or private research centers.

L'archive ouverte pluridisciplinaire **HAL**, est destinée au dépôt et à la diffusion de documents scientifiques de niveau recherche, publiés ou non, émanant des établissements d'enseignement et de recherche français ou étrangers, des laboratoires publics ou privés.

THÈSE DE DOCTORAT

de l'Université de recherche Paris Sciences et Lettres
PSL Research University

Préparée à l'École normale supérieure

Fabrication, integration and study of micropillars for cell culture

Fabrication, intégration et étude de micropiliers pour la culture cellulaire

Ecole doctorale n°388

Chimie physique et chimie analytique de Paris Centre

Spécialité Chimie Analytique

Soutenue par Jin WEI
le 15. 09. 2017

Dirigée par **Yong CHEN**

COMPOSITION DU JURY :

M. CHEN Yong
Ecole normale supérieure
Directeur de thèse

M. BOUROUINA Tarik
ESIEE Paris
Rapporteur

M. THEODOLY Olivier
INSERM
Rapporteur

Mme. MARIE-BEGUE Emmanuelle
Ecole normale supérieure
Membre du jury

M. MADOURI Aii
CNRS/C2N
Membre du jury



Acknowledgement

“What's past is prologue...” (The Tempest, Act 2, Scene I, William Shakespeare). All happened before that time, namely the "past", direct me to the opportunity to do what I am about to do. The conclusion of my work is much more than the summary of research in the last three years, rather a new beginning for further research. All the achievements in this period are due to our joint efforts with the people who provided helpful assistance and suggestion. Here is my sincere acknowledgement.

Before all, I would like to present my acknowledgment to sponsors and organizations: Chinese Scholar Council (CSC) for funding me to study in the past three years, Ecole Normale Supérieure (ENS) for offering me the position and excellent environment for my research, Institut Pierre-Gilles de Gennes (IPGG) for establishing remarkable platform of microfluidic community, Scuola Internazionale Superiore di Studi Avanzati (SISSA) and Suzhou Institute of Nano-Tech and Nano-Bionics (SINANO) for hosting me as a visiting scholar. It was my great honor to join the advanced research groups based on the efforts of all the shared sponsors and or above.

First of all, I would like to express my gratitude to my supervisor, Prof. Yong CHEN. Throughout the study period, he guides me with great patience, wisdom, humor and enthusiasm in research and life, achieving strict and precise scientific standards. Prof. CHEN offers pure academic atmosphere in which I was immersed with less pressure. The foundation for my thesis is his broad knowledge, cautious attitude and working enthusiasm. I am deeply influenced with his noble personality, not only in the scientific research but also in abstract thought.

Next, I would like to thank to the professors, colleagues and friends in ENS for their kindly help, support and encouragement. They are: Prof. Ludovic JULLIEN, Dr. Jian SHI, Dr. Li WANG, Dr. Xiaoqing LIU, Dr. Yadong TANG, Bin WANG, Chenge LI, Lihui HU, Xiaolong TU.

Additionally, I am grateful to all my collaborator: Prof. Matthieu PIEL, Dr

Guilherme NADER, Dr. Jacques FATTACCIOLI, Dr. Sandrine QUIGNARD, Dr. Yanjun LIU, Alexandra LANIECE, Juan Manuel GARCÍA ARCOS, Olivier MESDJIAN in IPGG; Prof. Vincent TORRE, Diletta POZZI, Francesco Paolo ULLOA SEVERINO in SISSA; Prof. Guosheng CHENG, Lingyan YANG, Ziyun JIANG in SINANO.

Last but not least, I am deeply grateful to my family. To my mama, thanks for her warmness, kindness and unconditional tolerance to me. To my papa, thanks for his grit, supporting me behind my back. To my wife, thanks for her accompany, accouraging me to grasp every opportunity for promising future.

Sincere acknowledgement to all the people. "Tous pour un, un pour tous".

WEI Jin

Outline

In-vitro cell assays are of great importance for fundamental research, drug screening, disease modeling and tissue engineering. While most of the conventional studies are based on the routine use of plastic culture dish, flask and multi-wells, the more recent approaches rely on micro-engineered substrates and devices. Indeed, cells interact with the extracellular matrix (ECM) which in turn determines the cell behaviors including adhesion, migration, differentiation, proliferation, and apoptosis. In a conventional culture, cells often adhere on a flat surface with substrate stiffness significantly different from that of the cells. In contrast, micro-engineered substrates can provide topographic cues for a better regulation of the cellular functions. In addition, a textured surface facilitates the diffusion of nutrients and metabolites underneath the cell contact area.

A large variety of patterned substrates are used to study surface-morphology and material-stiffness dependent cell adhesion and cell migration. The micro-engineering techniques can also be used to modulate the stiffness of the substrate. Typically, the size of a cell is in the order of 10-20 μm so that when the cell is attached on the top of a dense pillar array, its behavior will be sensitive to the effective stiffness of the substrate which is determined by the Young's modulus of the material as well as the height to width aspect ratio of the pillars. Therefore, micropillar arrays are powerful artificial ECM with adaptable stiffness for the studies of cell adhesion, migration, proliferation and differentiation. Comparing to the gel layers which are also used for the substrate stiffness regulation, the micropillar arrays perform advantages of accurate design and patterning, easy handling and easy manipulation.

In addition to the fine tuning of the effective stiffness, biochemical decoration of the pillar surfaces can also be used to modulate the cell-ECM affinity, which is important for biomedical research as well as advanced applications such as tissue

engineering, disease modeling and cancer treatment. Moreover, nanofibers can be deposited on the top of the pillar arrays, resulting in in-vivo ECM like surface morphology. In both cases, the cell-medium exchange will be efficient comparing to the flat surface culture due to large free spaces underneath the cell-contact area. The exchange of substances and signals affects cellular functions via complex intracellular pathways within surrounding media.

Additionally, micropillar substrates can be easily integrated into a microfluidic chip or even in a body. To understand more clearly how cells are dictated by both chemical (chemokines) and physical (ECM) cues, many studies have been developed to observe the cell migration in a microfluidic device enabling delivery of reagents, nutrients, and other cell factors at high temporal resolution. Typically, chemical gradients can be created in a microfluidic channel allowing systematical investigations of cell migration responding the change of growth factor, hormones and chemokines.

The purpose of this work is to explore elastomer pillars to control the effective stiffness of the culture substrate. We fabricated micropillar arrays of different parameters of diameter, space and height to explore several types of substrates, with or without microfluidic device integration.

The thesis is organized in the following way:

In Chapter 1, we will firstly introduce the concepts of cell and describe the basic structure and the principal components of the cell. Then, we discuss the ECM and the ECM dependent cell behaviors, including cell adhesion, spreading, migration, proliferation, etc. Afterward, we introduce the concept of microfluidics and lab on-a-chip systems. We also provide an overview of recent development of so-called organs on-a-chip approaches, before presenting the objectives and the organization of this thesis.

In Chapter 2, we present the fabrication methods used in this thesis work. Attention has also been paid to the conventional and non-conventional lithography methods as well as non-lithography techniques. More specifically, two pattern

replication techniques i.e., elastomer casting and thermoplastic hot embossing, were chose to produce micropillar arrays of different materials at high fabrication throughput. Electrospinning was used to produce nanofibers of biocompatible materials. The methods to fabricate microfluidic devices and surface activation or deactivation are also described.

In Chapter 3, we describe the fabrication of adjacent micropillar arrays of different heights using both elastomer PDMS and thermoplastic PCL, which have different Young's modules. Such substrates were used to evaluate the surface stiffness dependent cell culture of NIH 3T3 cells. Our results showed that the cells were sensitive to the height of PDMS pillars, due to their comparable Young's module, and that the cells were preferentially localized on the stiffer surfaces. However, no such effect was observed when the cells were placed on the PCL substrate because of the excessive rigidity of the PLGA pillars.

In Chapter 4, we present a study of cell culture on a nano-composite substrate made of PLGA nanofibers on PDMS micropillar arrays. This nano-composite substrate combines the advantage of the ECM-like surface morphology and high porosity and low stiffness of underneath supporting material. Our results showed that primary hippocampal neurons on such a nano-composite substrate have different cell morphology from those on flat surfaces and they showed more electric activities. Thus, the nanofibers-micropillar composite substrates were shown to be useful for neuron culture studies.

In Chapter 5, we describe a study of the confinement and deformation of cell nuclei in the inter-pillar spaces. Micropillars made of two types of materials, i.e., elastomer PDMS and thermoplastic PCL, are used to illustrate the stiffness dependency of the confinement. Different cell lines, including cancer cells and induced pluripotent stem cells, are used to demonstrate the relevance of this study. Our results show that the nuclei of iPSCs can be more easily confined and deformed in the inter-pillar areas than that of cancer cells, due to their relative small value of Young's modules.

In Chapter 6, we focus on the fabrication of a microfluidic platform with integrated micropillar arrays for spatiotemporal control of the cellular microenvironment. This platform allowed us to culture cells on a stiffness well-defined substrate and monitoring the cell migration in a chemical gradient. PDMS pillars were firstly produced on a glass slide by molding. A thick PDMS layer with channels were obtained and bonded to the patterned glass slide. Afterward, NIH 3T3 cells were seeded into the channel and a concentration gradient of Fetal Bovine Serum (FBS) was generated in the channel. As results, cells migrated to the higher FBS concentration part but the migration speed of the cells on pillars was almost twice slower than on the flat PDMS, due to different migration mechanisms. By measuring the deformation of the pillars during cell migration, migration related cellular forces could be determined, which is significantly different from static or cell adhesion forces

Table of Contents

Acknowledgement.....	I
Outline	III
Chapter 1 Introduction.....	1
1.1.1 Cell and cellular constitution	3
1.1.2 Cell.....	3
1.1.3 Cytoskeleton.....	6
1.1.4 Cell nuclei	8
1.2 Extracellular matrix and cell behaviors	11
1.2.1 Cell adhesion	13
1.2.2 Cell migration	16
1.2.3 Cell proliferation and differentiation	19
1.3 Cells in a chip.....	23
1.3.1 Microfluidics and lab on a chip	23
1.3.2 Organs on a chip	27
1.4 Research objectives	30
References.....	32
Chapter 2 Micro/Nano Fabrication	41
2.1 Introduction	43
2.2 Mold fabrication.....	44
2.2.1 Mask.....	45
2.2.2 Photoresist	47
2.2.3 Exposure.....	49
2.3 Pattern transfer replication	51
2.3.1 Soft lithography.....	51
2.3.2 Hot embossing	54

2.4	Surface modification	57
2.4.1	Plasma	57
2.4.2	Vacuum deposition	61
2.5	Electrospinning	63
2.6	Summary	69
	References.....	69
Chapter 3 Cell culture on micropillar arrays of different heights.....		77
3.1	Introduction	79
3.2	Micropillar arrays with different height.....	80
3.2.1	Fabrication of mold by one-step backside exposure	80
3.2.2	PDMS replica of micropillar array	83
3.2.3	Cell culture on PDMS substrates.....	86
3.2.4	PCL replica of micropillar array	90
3.2.5	Cell culture on PCL substrates.....	92
3.3	Adjacent micropillar arrays with different height.....	96
3.3.1	Fabrication of mold with tow-step double-side exposure.....	96
3.3.2	PDMS replica vs PCL replica	98
3.4	Summary	102
	References.....	102
Chapter 4 Cell culture on nanofibers deposited on micropillar arrays.....		105
4.1	Introduction	107
4.2	Fabrication of micro/nano hybrid substrates	108
4.2.1	Fabrication of micropillars	108
4.2.2	Fabrication of nanofibers	110
4.3	Cell culture on hybride substrates	111
4.3.1	NIH 3T3 cell culture on hybride substrates.....	111
4.3.2	Neuronal cell culture on hybride substrates.....	114
4.4	Summary	120
	References.....	121

Chapter 5	Confinement and deformation of cell nuclei in the interpillar area.	125
5.1	Introduction	127
5.2	Cell confinement	128
5.2.1	The behaviors of cancer cells	129
5.2.2	The behaviors of iPS cells	132
5.3	Deformability of iPS cells	136
5.4	Summary	139
	References.....	139
Chapter 6	Integration of micropillars into microfluidic devices for cell culture studies	141
6.1	Introduction	143
6.2	Fabrication of Microfluidic Chip.....	144
6.2.1	Fabrication of micropillar array.....	144
6.2.2	Fabrication of microchannel	145
6.3	Microfluidic control and gradient generation.....	146
6.3.1	Basic theory of microfluidic flow	146
6.3.2	Gradient generation	147
6.4	Cell culture in microfluidic chip.....	149
6.5	Summary	151
	References.....	152
Chapter 7	Conclusion and perspective	155
Appendix A	Summary in French	161
A.1	Introduction et méthodes.....	163
A.2	Culture cellulaire sur un substrat de micropiliers	165
A.2.1	Réseaux de micropiliers à différentes hauteurs.....	165
A.2.2	Micropiliers adjacents à hauteurs différentes	170
A.3	Micro/Nano substrat hybride pour études de culture cellulaire...	172
A.4	Cellules confinées sur des substrats micropiliers	177

A.5	Intégration des micropiliers dans les dispositifs microfluidiques pour les études sur la culture cellulaire	182
	Appendix B Quantification and simulation of microfluidic flow	185
B.1	Introduction	187
B.2	Simulation of diffusion based gradient generators.....	187
B.3	Simulation of flow based gradient generators.....	192
B.4	Summary and perspective	195
	Abbreviation list	197
	Publication list.....	201

Chapter 1 Introduction

In this chapter, we will firstly introduce the concepts of cell and describe the basic structure and the principal components of the cell. Then, we discuss the extracellular matrix (ECM) and the ECM dependent cell behaviors, including cell adhesion, spreading, migration, proliferation, etc. Afterward, we introduce the concept of microfluidics and lab on-a-chip systems. We also provide an overview of recent development of so-called organs on-a-chip approaches, before presenting the objectives and the organization of this thesis.

1.1.1 Cell and cellular constitution

1.1.2 Cell

Cell is the basic unit of human body, which is itself functional and highly sophisticated for energy and information handling and transforming. Therefore, “The key to every biological problem must finally be sought in the cell” [1], as pointed out by Wilson in 1925.

The structure, function and behavior of cells are various in different parts of our body, as shown in Figure 1.1. For example, typical neurons have cell body, dendrites and axon. The outgrowth of dendrites and fibrous axons of the neurons can form a network of neurons, which ensures the information exchange [2]. In comparison, the muscle cell (myocytes), including cardiac muscle cell (cardiomyocyte) and skeletal muscle cell, is in the shape of columnar. Cardiomyocytes usually have only one central nucleus, while skeletal muscle fibers are multinucleated cells. Different from fibrous neurons, muscle cells with columnar morphology are more conducive to the arrangement and connection of cells to accomplish the function of complete synchronous contraction or relaxation [3]. Ordinary cardiomyocytes, including atrial and ventricular muscles, are rich in myofibrils, mainly in systolic function [4]. Specially differentiated cardiomyocytes, self-regulatory cardiomyocytes, have special conduction system, which mainly control the excitability, conductivity and spontaneous rhythm [4].

In the development of complex multicellular organisms such as plants and animals, progenitor cells differentiate into distinct "types" that have characteristic compositions, structures and functions. Cells of a given type often aggregate into a tissue to cooperatively perform a common function. Different tissues can be organized into organ to perform one or more specific functions. The coordinated functioning of many types of cells and tissues permits the organ to move, metabolize, reproduce, and carry out essential activities [5].

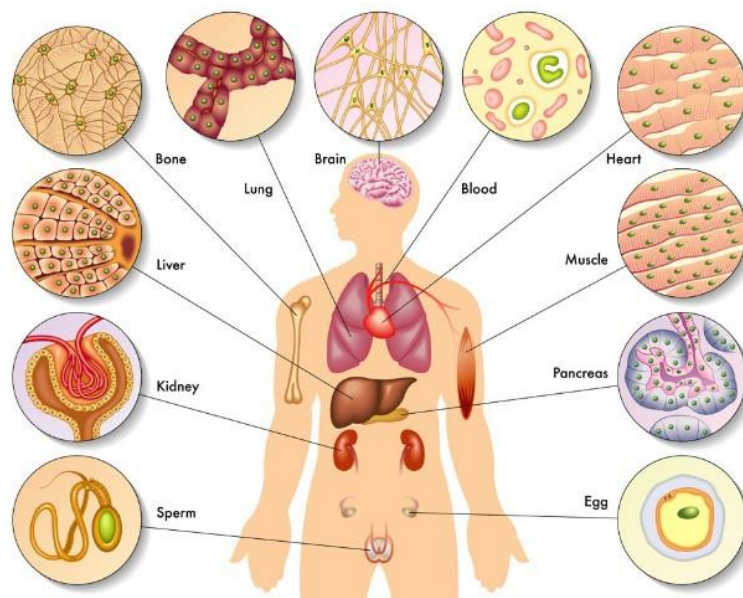


Figure 1.1 Illustration of different cell morphology in different organ tissues of human body [6].

Three main systems can be identified in a cell: (1) plasma membrane system, (2) cytoplasm system, and (3) genetic expression system, as demonstrated in Figure 1.2.

(1) Plasma membrane system

The membrane of cell is made of phospholipid bilayer and membrane proteins where water, oxygen and other small molecules can pass easily whereas some ions and macromolecules cannot pass freely. Therefore, the role of membrane is not only a boundary of cellular substances but also a gate for ions and macromolecules [7]. In addition, information exchange between cells often occurs on the surface of membrane by biochemical signal [7].

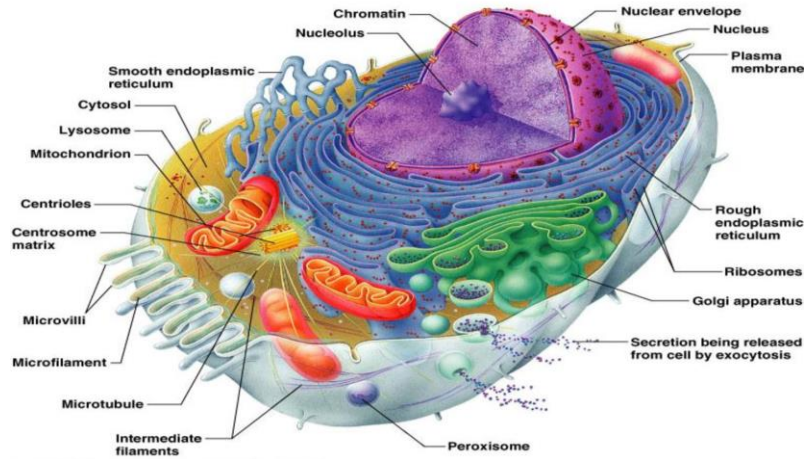


Figure 1.2 Schematic diagram of the structure of a typical animal cell [8]

(2) Cytoplasm system

Cytoplasm system includes cytosol as well as cytoskeleton and organelles (mitochondria, endoplasmic reticulum, Golgi apparatus and lysosomes, etc.) surrounded by the cytosol. Inside the cell membrane, outside the nuclear membrane, the cytoplasm system is the significant place for external behavior and characteristic performance of cell activities [9].

(3) Genetic expression system

Genetic expression system can be divided into four parts: nuclear membrane, chromatin, chromosomes and nucleolus. The function of the system is to preserve genetic material, control biochemical synthesis and cell metabolism, determine the performance of cells or body performance [10]. The genetic material from cell (in micro) or individual (in macro) is transferred from generation to generation in the mechanism of genetic expression system [10].

Overall, the systems are not isolated from the others. Genetic expression system controls the characteristics of cytoplasm, and the cytoplasm system plays an important role in supply to cell differentiation, development and inheritance. The internal constitution of cells interacts with external environment through plasma membrane system, in isolation or exchange.

1.1.3 Cytoskeleton

The concept of cytoskeleton in the narrow sense refers to the protein network in eukaryotic cells. Similar to the skeleton in human body, cytoskeleton is essential in providing a framework for cellular organization. The cytoskeleton is composed of three well-defined filamentous structures: microtubules, microfilaments and intermediate filaments [11], as show in Figure 1.3.

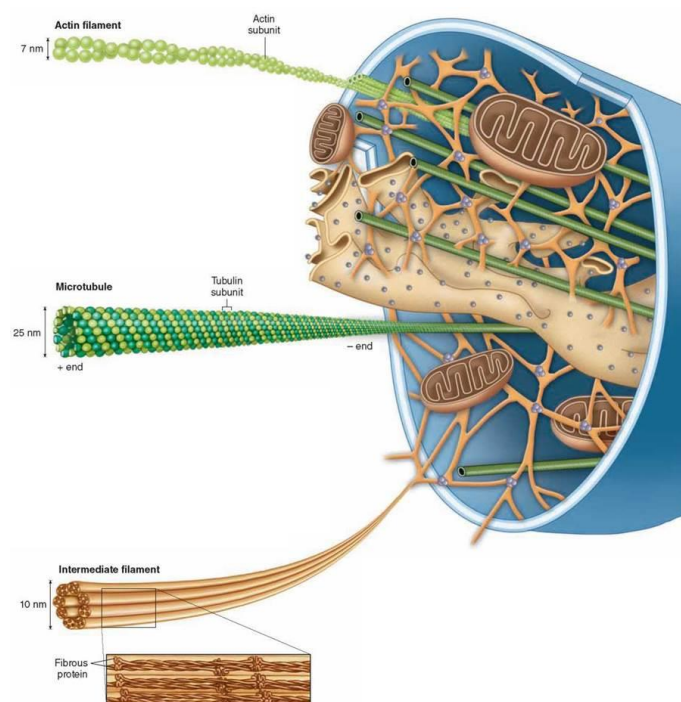


Figure 1.3 Three different kinds of protein fibers that make up the cytoskeleton, actin filament, microtubule and intermediated filament [12].

(1) Microtubule

Microtubules is composed by about α and β tubulin. Normally, tubulin fibrils (protofilaments) are in the form of ($\alpha\beta$) dimer with head and tail polymerization. Several (11-15) protofilaments constitute to a hollow microtubule with the diameter of 22-25nm [11,13].

(2) Microfilament

Microfilament, mainly composed of actin and myosin (a molecular motor

protein), is also commonly found in eukaryotic cells. Microfilament occupies approximately 1% to 2% in average content of total intracellular protein, but account for 20% to 30% in the case of strong activity. Microfilament is a solid fiber with a diameter of 4-7 nm [11,13].

(3) Intermediate filament

Intermediate filament, diameter between microtubules and microfilaments (8-10 nm), is with chemically complex composition, with protein of vimentin, keratin, desmin, etc. [11]. In different cells, the composition changes greatly. The intermediate filaments make the cells have tension and shear resistance [11,13].

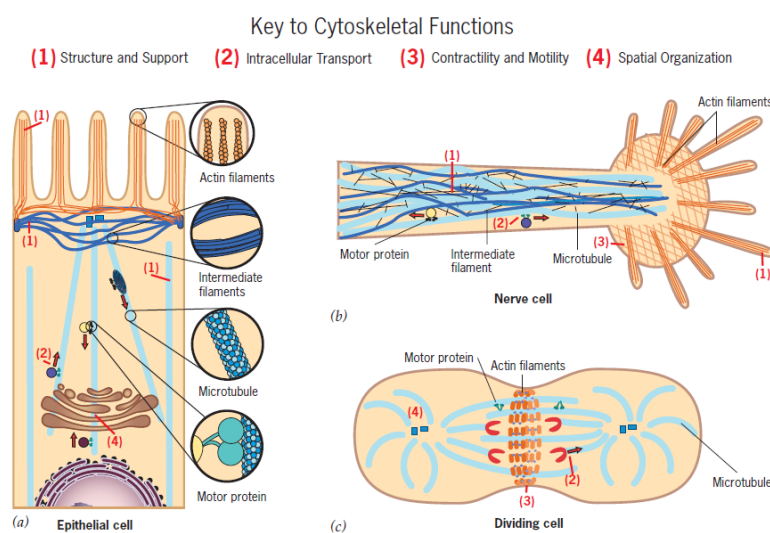


Figure 1.4 Schematic drawings of (a) an epithelial cell, (b) a nerve cell and (c) a dividing cell. The microtubules of the epithelial and nerve cells function primarily in support and organelle transport, whereas the microtubules of the dividing cell form the mitotic spindle required for chromosome segregation. Intermediate filaments provide structural support for both the epithelial cell and nerve cell. Microfilaments support the microvilli of the epithelial cell and are an integral part of the motile machinery involved in nerve cell elongation and cell division [14].

As shown in Figure 1.4, the cytoskeleton plays an important role not only in maintaining internal structure and subjecting to external forces, but also in many cell activities, for example, traction of chromosome separation during cell division [14]. White blood cell migration, spermatozoa swimming, axons extension and other

aspects are related to the cytoskeleton [11,14].

1.1.4 Cell nuclei

Nucleus is one of the most important constitution in eukaryotic cells. It is a regulatory center for cell inheritance and metabolism and is one of the most significant difference between eukaryotic cells and prokaryotic cells. The nucleus are mainly composed of nucleolus, nuclear matrix and chromosome/chromatin, as shown in Figure 1.5.

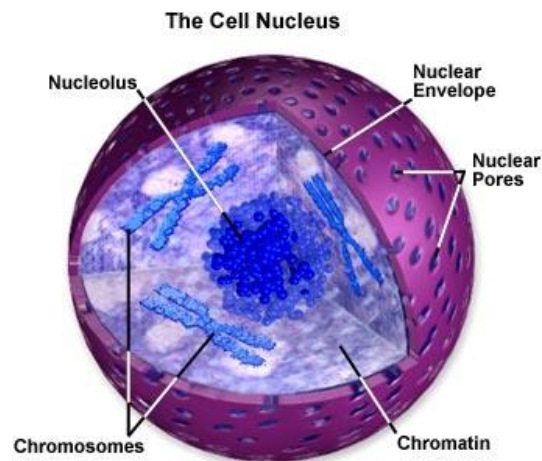


Figure 1.5 Schematic diagram of the nucleus structure of a typical animal cell [15].

(1) Nucleolus

Nucleolus is often found in the interphase nuclei and is a homogeneous sphere. The shape, size, and number of nucleolus vary with the species, formation, and physiological state of cell line [16]. The main function of nucleolus is to carry out ribosomal RNA synthesis and ribosome formation [17].

(2) Nuclear matrix

Nuclear matrix is the surroundings around nucleolus and chromosomes, including nuclear liquid and skeleton. Nuclear liquid is composed with water, ions, HE enzymes and other inorganic components, and nuclear skeleton is a 3D fiber mesh formed by a variety of proteins. The matrix plays important roles in connection of

nucleolus to nuclear membrane and support to the nuclei sphere [16,18].

(3) Chromosome/chromatin

Chromosome and chromatin are different forms of the same substance during cell division interval and division. Chromosomes appear in the division and filamentous chromatin appears in the division interval [16,19]. As the main carriers of genetic information, chromosome and chromatin are mainly the composition of nuclear protein, unevenly distributed in the nucleus [19].

Cell type	Young's modulus E (kPa)
HUVEC endothelial cells	10 – 11
BPAEC endothelial cells	0.2 – 2
HL60 - leukemia myeloid cells	0.2 – 1.4
Jurkat cells - leukemia lymphoid	0.02 – 0.08
Outer hair cells of Corti organ	300 – 400
Mouse outer hair cells of Corti organ	2 – 4
Osteoblasts	0.3 – 20
Migrating 3T3 fibroblast cells	3 – 12
L 929 fibroblast cells	4 – 5
Epidermal keratocytes	10 – 55
Platelets	1 - 50
Murine C2C12 myoblasts	11 - 45
Rat cardiocytes	32 – 42
Chicken cardiocytes	5 – 200
Erythrocytes	19 - 33

Table 1.1 Young's modulus of mammalian cells [20].

Due to the non-uniform components distributed in cells, generally, nuclei and the region around is the hardest area. The stiffness of nucleus indicates the characteristic mechanics of the cell and can be measured by atomic force microscopy (AFM) [21], as indicated in Table 1.1. Metastatic cells (cancer cells) and stem cells are extremely softer than the ordinary cells [22]. Furthermore, the mechanical properties of nucleus could directly or indirectly modulate gene transcription, dependent on its physical connection to the surrounding cytoskeleton [23].

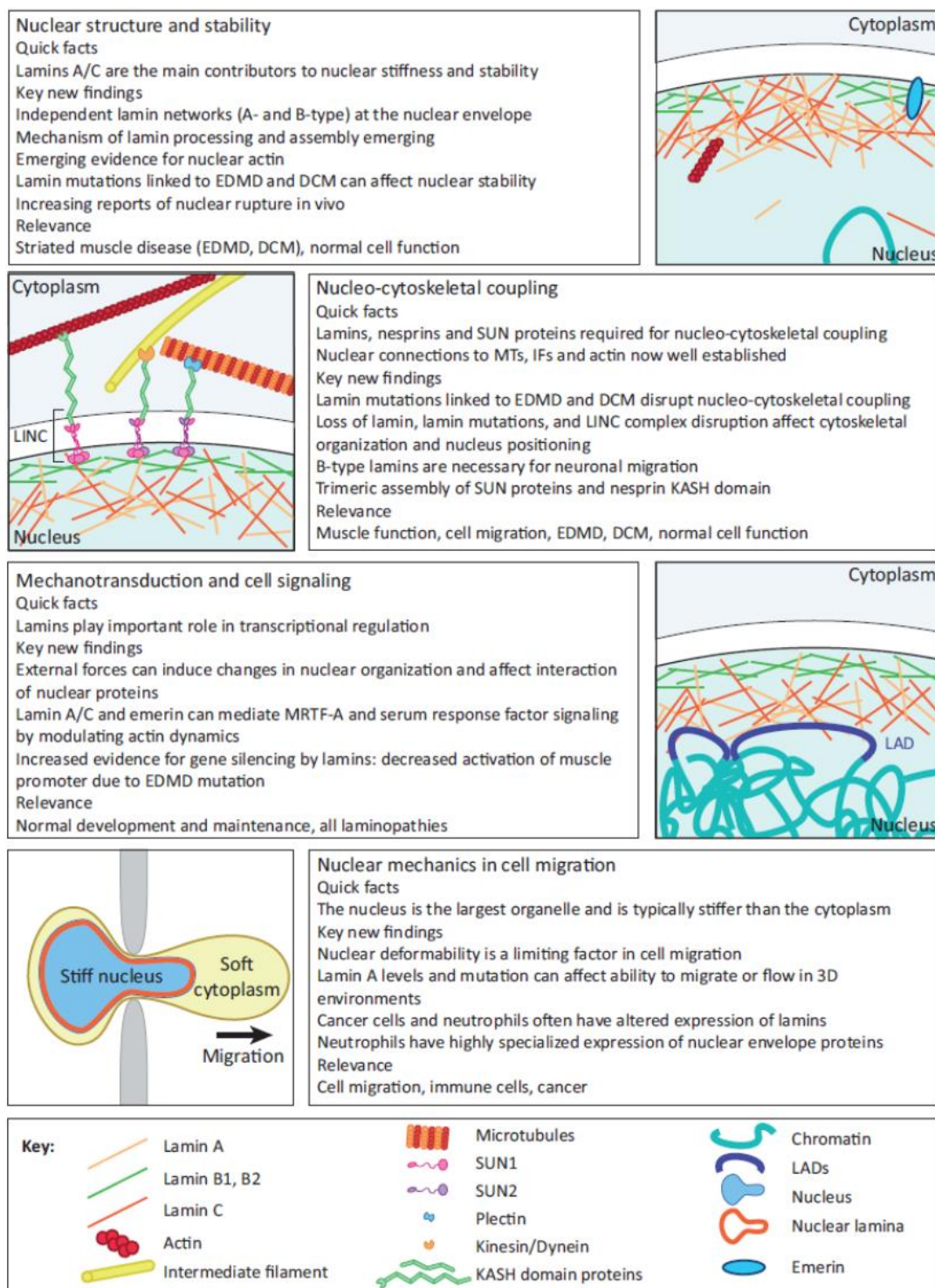


Figure 1.6 Overview of the diverse functions of lamins in nuclear and cellular mechanics and mechanotransduction. Abbreviations: EDMD, Emery–Dreifuss muscular dystrophy; DCM, dilated cardiomyopathy; IF, intermediate filament; LAD, lamina-associated domain; LINC, linker of nucleoskeleton to cytoskeleton complex; MRTF-A, myocardin-related transcription factor A [24].

Figure 1.6 illustrates that protein in nucleus like (lamin A/C) domain the stiffness modulation [24], including nuclear structure and stability, necleo-cytoskeletal coupling, mechanotransduction and cell signaling, and nuclear mechanics in cell migration. The decisive factor to the stiffness of nucleus, cells, tissue fundamentally lies in the expression of specific genes, particularly LMNA [23,25]. When cells sense the stiff culture matrix, LMNA expression increases with synthesizing more lamin A/C in nuclear matrix to enhance stiffness. On the contrary, on soft matrix, LMNA inhibits expression and nucleus is more deformable [23,26]. Expression of LMNA in cancer cell is critical during morphological damage, such as extensive deformation, flow shear force [27]. For stem cells with ultra-low expression of LMNA, the nucleus is ultra-soft, nevertheless, the lamins increase undergoing normal differentiation [28].

1.2 Extracellular matrix and cell behaviors

Extracellular matrix (ECM), as macromolecules compounded and secreted by cells, distributes on cellular outer surface and between cells. ECM is mainly divided into three categories: glycosaminoglycan/proteoglycan, structural protein and adhesive protein [29]. These substances constitute to a complex network, supporting and connecting the organizational structures, regulating the occurrence of tissue and cell physiological activities. ECM in vivo is a part of tissue and not included into any cell. It determines the characteristics of connective tissues [30]. As illustrated in Figure 1.7, different types of components play different roles in the process of interaction.

(1) Glycosaminoglycan/proteoglycan

Glycosaminoglycan is a non-branched long chain polysaccharide, consisting of repeating disaccharide units. The disaccharide units are usually composed of aminoglucose (glucosamine or aminogalactose) and uronic acid [31]. Glycosaminoglycan, according to the composition of sugar base, connection, sulfation degree and location, can be divided into six categories: hyaluronic acid, chondroitin sulfate, dermatan sulfate, heparan sulfate, heparin, keratan sulfate.

Proteoglycans are covalent conjugates of glycosaminoglycans (except for hyaluronic acid) and coreprotein. The serine residues of the core protein (in Ser-Gly-X-Gly sequences) can be fitted with glycosaminoglycan chain in the Golgi complex [32]. Both glycosaminoglycan and proteoglycan are the important media for cell interaction with ECM aqueous colloid, in which many other matrix components are embedded [30].

(2) Structural protein

Structural protein (typically collagen) is the most abundant protein in animals, accounting for more than 30% of the total body proteins. It is distributed in the various organs and tissues of body, as the framework of ECM structure, synthesized and secreted by fibroblasts, chondrocytes, osteoblasts and some epithelial cells [33]. At present, there are at least 19 kinds of collagen, encoded by different structural genes, with different chemical structures and immunological properties [33]. For example, I, II, III V and XI collagens are a striped fibrous collagen [34,35]. Collagen is composed of three identical or different peptide chain formations of three strands, containing three structures: spiral, non-spiral and spherical domain [33,35].

(3) Adhesive protein

Adhesive protein, like fibronectin and laminin, promotes cell binding to the matrix. On the frame formed by proteoglycans and collagen, adhesive protein locates on anchor points, integrated into the network on the surface of cells. Such network directly adheres and links to the receptor at cell junction domain via fibronectin, laminin and other linking molecules [33,36]. Since most of receptors are membrane-integrin which connects to the cytoskeletal protein in cells, ECM binds to cells as an entirety via the membrane-integrin network [13,37].

ECM has been found in making great contributions to the physiological and pathological processes. ECM is not only the wrap in extracellular environment, but also supply of necessary armamentarium for physiological functions of cells [38]. Moreover, the morphology, movement and differentiation of cells are highly related to ECM [29,39]. ECM, containing with growth factors and hormones, provides cells

physical and chemical regulations in the specific functions.

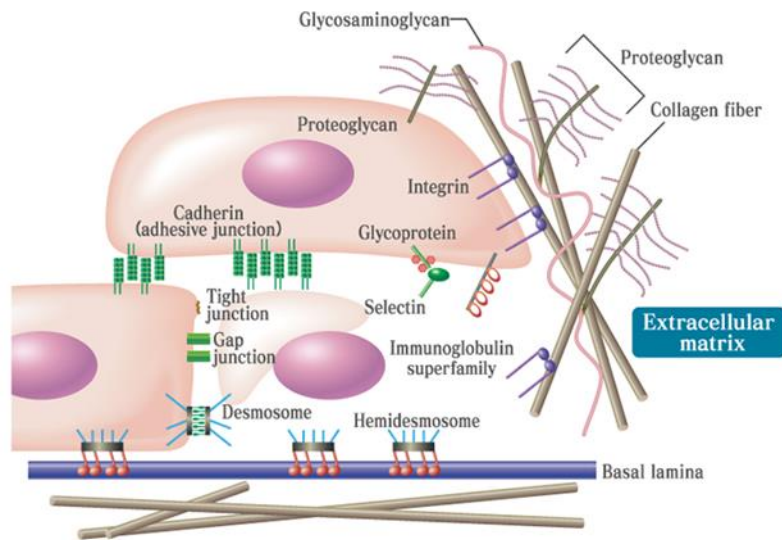


Figure 1.7 Typical model of interaction between cell and ECM [40].

1.2.1 Cell adhesion

Cell adhesion refers to the adhesively cellular behaviors of binding and spreading on the culture surface. The adhesion to the culture substrates of cells depends on contact-surface chemical/physical characteristics as (1) the adhesive ability of the cell line, (2) the contact rate between cell and the culture surface, (3) the surface compatibility of cells and substrate [41]. The cell adherence rate is also related to the chemical and physical properties of the culture surface, especially the density of electrons on the culture surface [42,43]. One of the efficient methods to increase the adhesion rate and quality is to introduce matrix of adhesive protein. For example, cold protein and fibronectin in serum can bridge between cells and culture surface, conducive to speed up the cell attachment rate [42]. The whole cell adhesion process is complex, nonuniform and environment- and time dependent [41].

Cell binding

Adhesive binding and coupling between cells and culture substrates is the initial and fundamental aspect, which influences subsequent behaviors and processes like

chemotaxis distribution [44], apoptosis [45], wound healing [46], metastasis [47], etc. As demonstrated in Figure 1.8, the binding mechanism [48] shows that cells attach to the culture substrates through adhesion domains. A binding and coupling domain forms between cell surface proteins and a cluster of receptors (such as integrins linked to the tissue). The domains also serve as anchors for the arrangement and fixation of stress fibers. Polymeric microtubules connect the adhesion domains and the cell-organizing centrosome [49] through stress fibers. The coupling of these semi-stiff microtubules to the adhesion domains controls the global mechanical stability of the cell and could also contribute to the force-sensing ability of the cell.

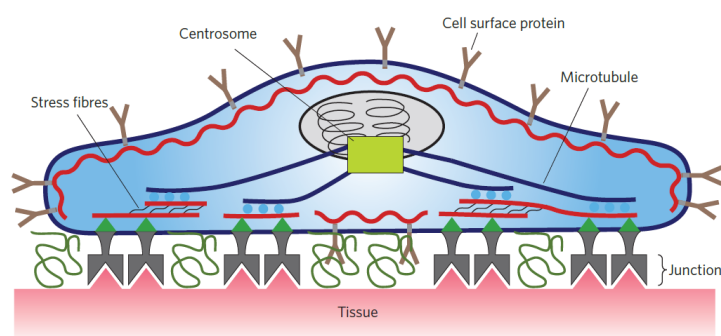


Figure 1.8 Cell binding. A cell adheres to a soft surface, such as tissue, through adhesion domains. An adhesion domain forms between cell surface proteins and a cluster of receptors (such as integrins) linked to the tissue [48].

Cell spreading

Cell spreading is an active and rate process [50], which involves complex biochemical and biophysical events, like actin-based membrane extensions and integrin-mediated adhesions (Figure 1.9). First, chemical and physical cues of the ECM influence the internal proteins of cells. By constant remodeling of cell shape, continuous extensions are sustained by continued integrins bindings [51]. The binding force between integrins and ECM influences the actin assembly and the variation of cell membrane resistance affects actin polymerization at the membrane periphery. Without considering the network of filapodia or lamellipodia, isotropic spreading is studied here as the simplest form of this model [52]. In addition to the

above factors, cell spreading on the culture surface is influenced by the surface conditions, especially the roughness [53].

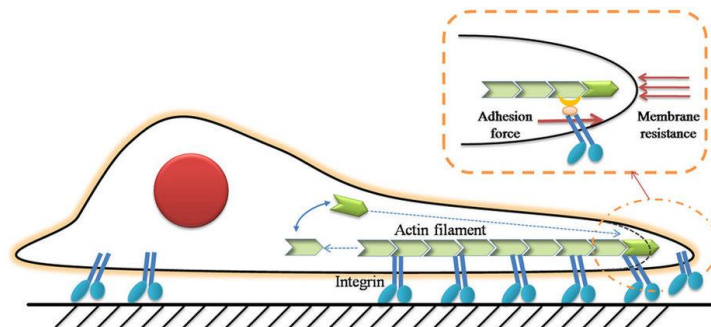


Figure 1.9 Schematic of cell spreading over a substrate [54].

Cell patterning and alignment

Based on cell binding and spreading, it is proved that cell morphology is controllable. Since the cells are complicated biochemical automata, most studies on controlling of cell morphology take advantage of cell patterning and alignment. Control strategies of guidance cue can be divided into two categories: biochemical and biophysical.

(1) Biochemical cue guidance

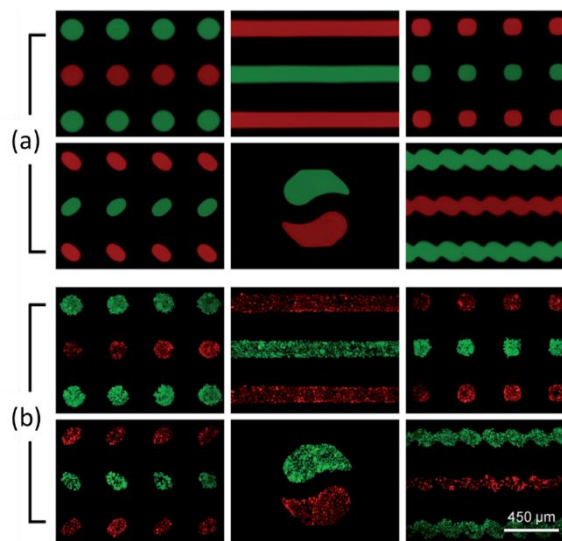


Figure 1.10 Co-micropatterning of different proteins/cells using P μ Ss. (a) Immobilization of both FITC-labelled BSA and Alexa Fluoro594-labelled CEA with various shapes. (b) Localization of both HUVEC-C cells (red) and HepG2 cells (green) with various shapes [55].

Biochemical cue guidance refers to the achievement of selective adhesion of cells by the patterning of adhesive protein, especially fibronectin and laminin [56,57]. As shown in Figure 1.10, cells are sensitive to albumin coating pattern [55]. HUVEC-C cells prefer CEA while HepG2 cells prefer BSA.

(2) Biophysical cue guidance

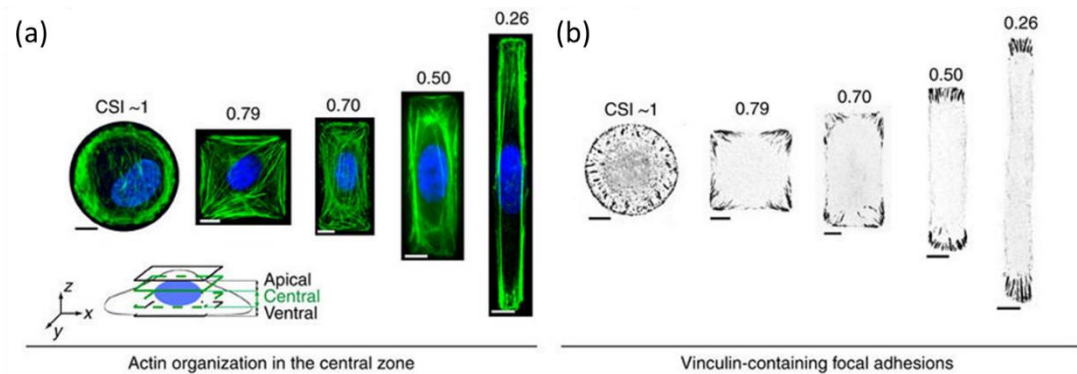


Figure 1.11 (a) The spatial distribution of actin filaments in the central zone (see cartoon) of endothelial cells plated on $1600 \mu\text{m}^2$ FN-coated micropatterns. The scale bars correspond to $10 \mu\text{m}$. (b) Immunofluorescence staining for vinculin in $1600 \mu\text{m}^2$ shaped cells showing the coordinated reorganization of FAs with cell shape changes. The color was inverted. The scale bars correspond to $10 \mu\text{m}$ [58].

For biophysical cue guidance, in the condition of certain degree of affinity and isotropic between cells and substrates, cell morphology can be controlled by changing physical characteristics of culture substrate, such as shape [58], stiffness [59], etc. As shown in Figure 1.11, the distribution of cell cytoskeleton varies significantly with the substrates of different shapes. With the increasing of aspect ratio, F-actin is polarized to the end corner.

1.2.2 Cell migration

Cell migration results from the coordination of motions generated in different parts of a cell which is induced by receipt of a migration signal or a gradient of physical/chemical cues. Cell migration mechanism in 2D planar [60], as shown in

Figure 1.12, is the cycle of isosmotic volume: (1) extension of front-end pseudopodia, (2) anchor of new adhesions, (3) tail contraction cell body. Cell migration, in space and time on the alternating process, is the basic functions of normal cells, essentially in tissue organization. Physiological processes, such as embryonic development, angiogenesis, wound healing, immune response, inflammatory response, atherosclerosis, cancer metastasis, etc., are involved in cell migration [61].

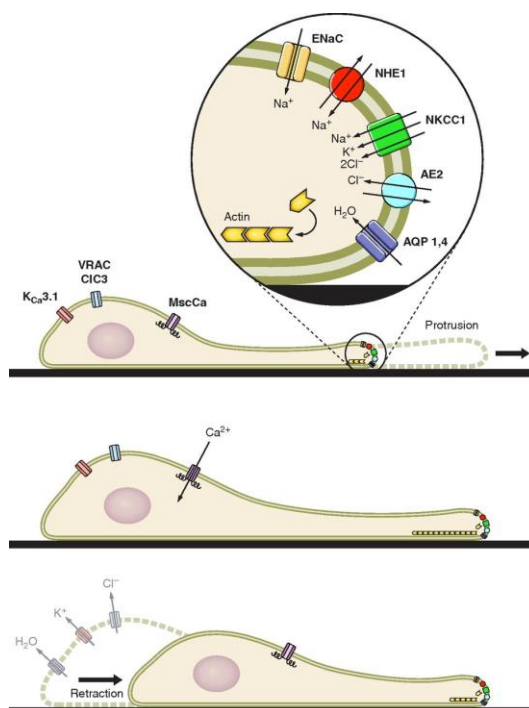


Figure 1.12 Cell volume changes during cell migration. Cell migration is a continuous cycle of protrusion of the cell front and retraction of the trailing end. This can be modeled as a cycle of isosmotic volume increase at the cell front and isosmotic volume decrease at the rear end [60].

For in vivo environment, the matrix around the cell is three-dimensional, and the migration is three-dimensional rather than the two-dimensional planar. Conventional model of migration cannot completely explain the movement of cells in the human body. Therefore, the migration model of cells in the three-dimensional matrix makes more sense, especially in complex environments, such as the case of confinement [62], as shown in Figure 1.13. In confined environment, the adjustment and reconstruction of nucleus and cytoskeleton are more complex and interesting

than the two-dimensional plane.

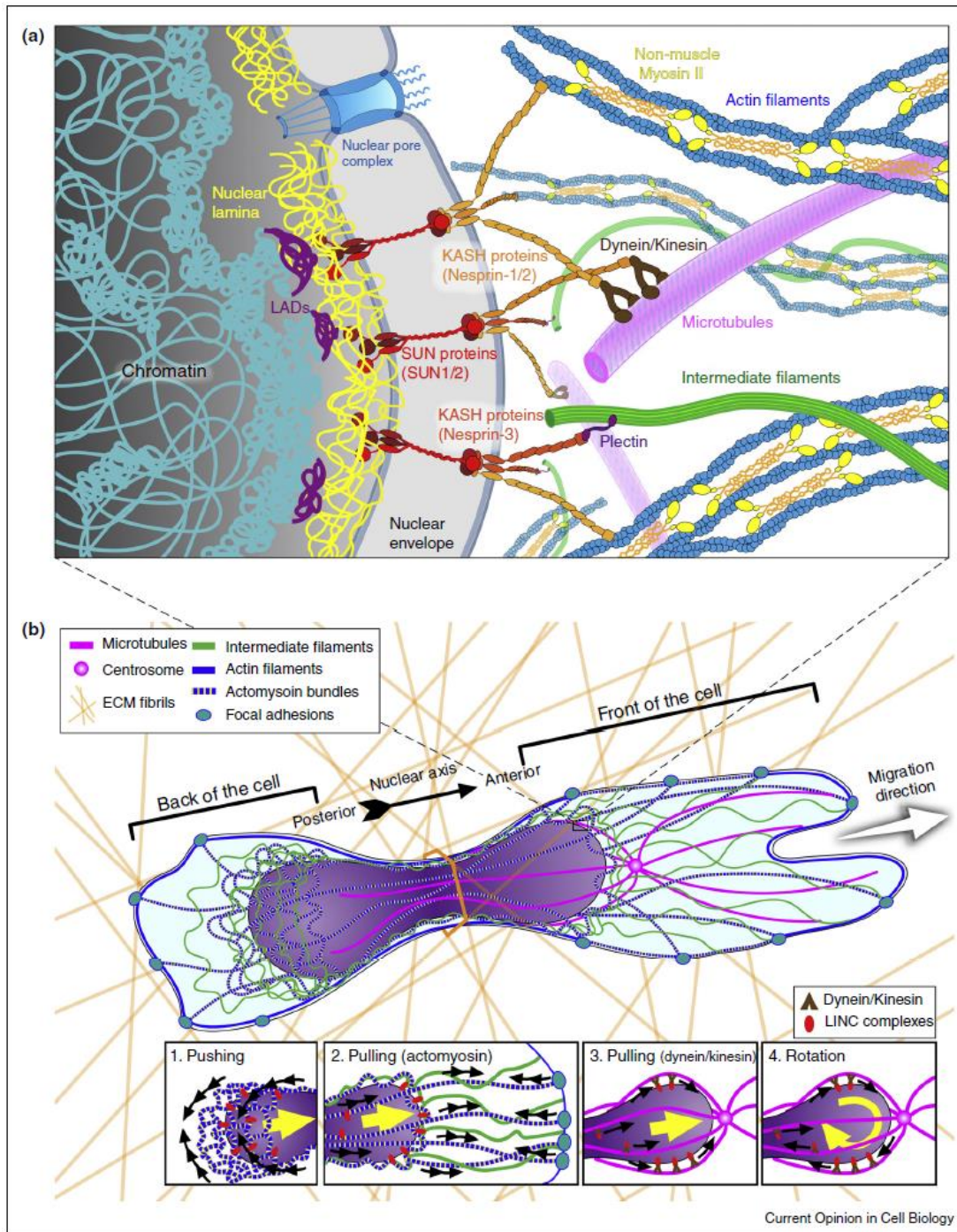


Figure 1.13 Schematic overview of the physical connections between the nucleus and cytoskeleton, and their roles in moving the nucleus through confined spaces. (a) At the nuclear periphery, chromatin interacts with lamins at lamina-associated domains (LADs). (b) Cytoskeletal organization and dynamics during migration in confined 3D environments [62].

Based on the model, the importance of microtubules and intermediate filaments in cytoskeleton appears in the process of reorganization and deconstruction forcing on nucleus during confined cell migration [22,62]. Compared 3D matrix to 2D planar and 1D fiber, as illustrated in Figure 1.14, ECM-dependent regulators are more complex in affecting on intracellular regulators [63,64]. During migration, cells adjust through adjusting the gene expression pathway and specific protein content to adapt to external environment and to complete movement. In the experimental three-dimensional environment (more complex ECM-dependent regulators), cell migration model based on intracellular regulators is more challenging for cells and more resemble to in-vivo situation of human body.

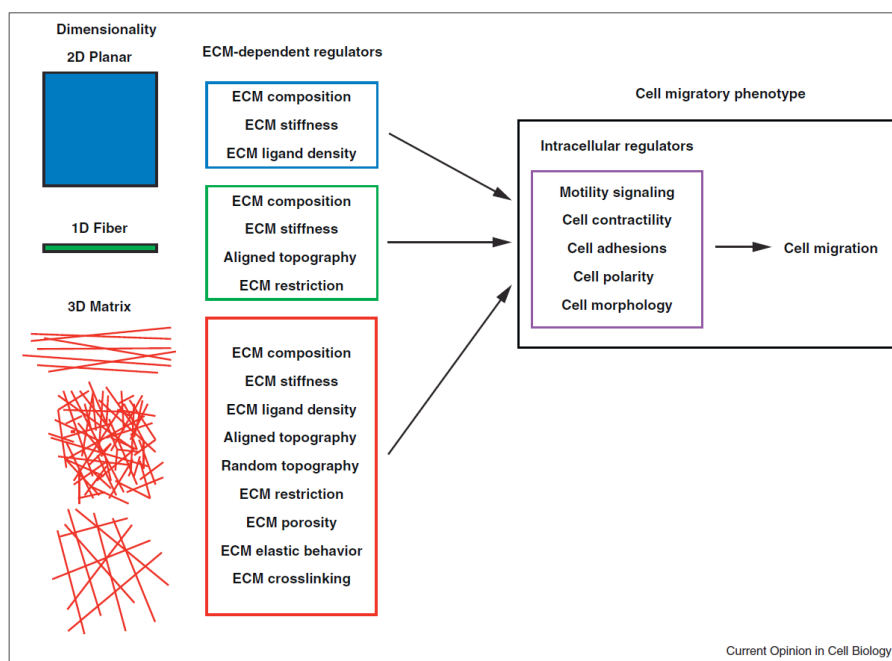


Figure 1.14 Dimensional regulation of cell migration. Illustration of the numerous unique ECM-dependent regulators (center column) associated with 2D, 1D, and 3D migration. These microenvironmental regulators in turn influence intracellular regulatory pathways that govern the migratory phenotype (right panel) and determine how cell migration proceeds [63].

1.2.3 Cell proliferation and differentiation

After cells adapting to the suitable environment through adhesion and

migration, they proliferate and differentiate in the ECM microenvironment. Multicellular organisms produce new cells in cell division to replenish cells that grow and die in the body. Simultaneously, multicellular organisms can be reproduced from one fertilized egg, through cell proliferation and differentiation, eventually develop to a new multicellular individual.

Cell proliferation

Mitosis is the main way of eukaryotic cell division. Multicellular organisms increase the number of somatic cells in a mitotic manner which is cyclical (cell cycle). As demonstrated in Figure 1.15, cell cycle refers to the highly regulated and precise process through which accurately duplicate and faithfully segregate their chromosomes at each cell division [14].

Cell cycle consists of two phases: M phase (mitosis phase and cytokinesis) and interphase. The interphase is between two continuous M phases. In interphase, the duration is divided into G1, S, and G2 phases: in G1, cell grows, carries out normal metabolism and duplicates organelles; in S, the major behaviors are DNA replication and chromosome duplication; in G2, cell grows continuously in preparation for mitosis. In mitosis phase, the process is composed of prophase (chromosome appears in nucleus), prometaphase, metaphase (apparent spindle), anaphase (separation of sister chromatid), and telophase (formation of daughter cells). Cytokinesis appears accompany with nucleus division, after anaphase.

In a cell cycle, there is a large difference of the duration of M phase and interphase. Generally, interphase occupies about 90% to 95% of the whole cell cycle, M phase about 5% to 10% [65]. Naturally, different cell types are with different durations of cell cycle.

In common, interphase is the beginning of a new cell cycle, in which cells carry out extremely complex change and preparation for cell mitosis in interior. In recent years, the application of radioisotope labeling self-development technology [66] indicates that the important feature of interphase cells is to complete the replication of DNA molecules and related protein synthesis [66,67]. Therefore, interphase is

critical preparation phase throughout the cell cycle.

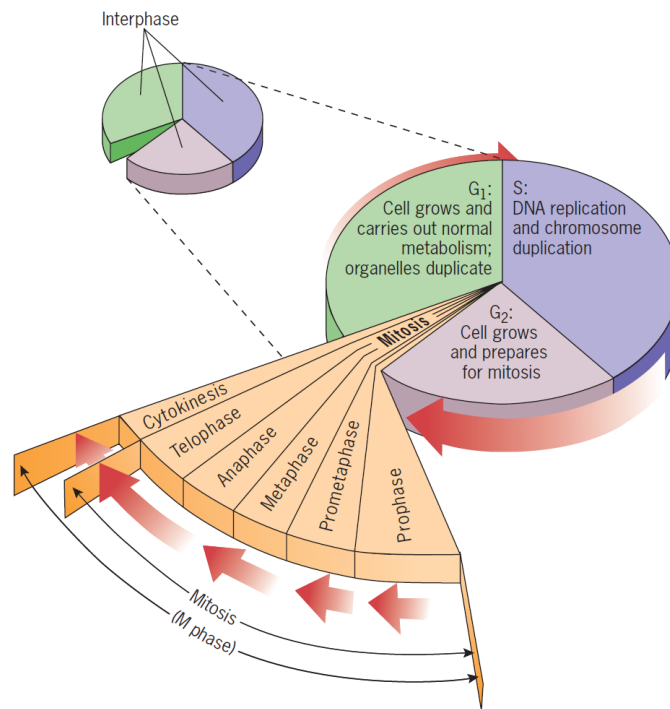


Figure 1.15 An overview of the eukaryotic cell cycle [14].

Cell proliferation is an important vital feature of the organism. Cells proliferate in a division manner. It must be emphasized that, by cell proliferation, the genetic material can be transferred and distributed equally to two daughter cells. Cell proliferation is the basis for the growth, development, reproduction and inheritance of organisms.

Cell differentiation

Cell differentiation refers to the process by which a stem cell is derived to an adult cell, which is both morphologically and functionally different from the original stem cell. The essence of cell differentiation is the selective expression of the genome [68]. Through the opening or closing of different gene expression, ultimately iconic proteins are synthesized [69]. In general, the cell differentiation process is irreversible. However, under specific conditions the gene expression of a differentiated cell can be changed. In particular, an adult cell can be reprogrammed to reach an undifferentiated state. Such a dedifferentiation process allows producing

stem cells, e.g. induced pluripotent stem cells (iPSCs) which have the same pluripotency as embryonic stem cells [70-72].

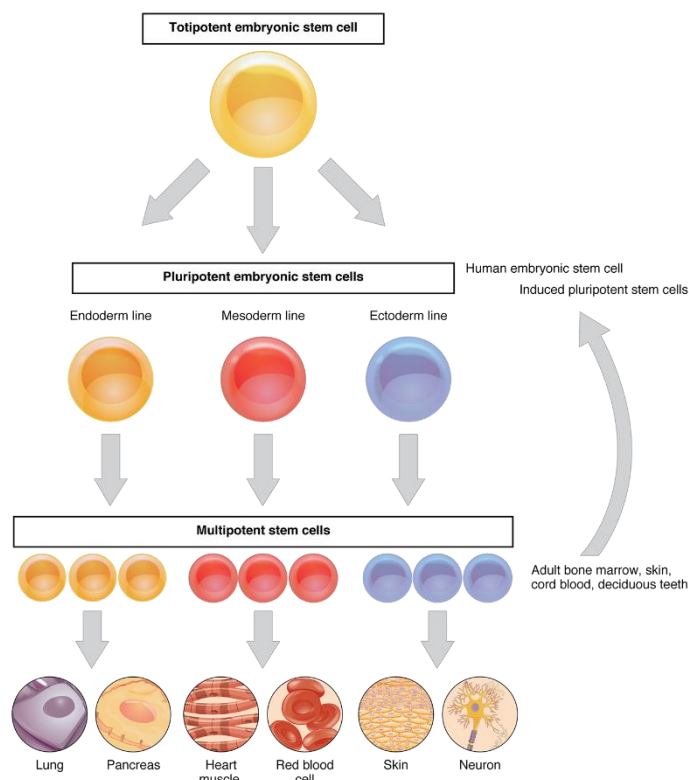


Figure 1.16 The capacity of stem cells to differentiate into specialized cells make them potentially valuable in therapeutic applications designed to replace damaged cells of different body tissues [73].

Figure 1.16 illustrates differentiation and dedifferentiation processes and passage of a totipotent embryonic stem cell to cells of multicellular organisms. Pluripotent embryonic stem cells including endoderm, mesoderm and ectoderm are produced from the totipotent cell for subsequent differentiations to organ tissue. All the studies of embryonic stem cells face the ethic problem and the lack of cell supplement. iPS cells without the use of germ cells can avoid the ethics. In addition, cells induced from individual are advantageous on immune response and accurate medical care [74,75].

The application of iPSCs needs to overcome many obstacles, for example, carcinogenic and genetic defect as well as low efficiency of culture and

differentiation [76,77]. The key factor that causes the problem may be due to the culture method, petri dish and flask. The conventional culture methods which was used for more than hundreds of years are different for in vivo environment. Recent studies focus on the solution in novel devices for cell culture, such as microfluidic chip [78], micro/nano patterned substrates [79], artificial scaffolds [80] etc. Figure 1.17 presents a novel method for iPSC culture and differentiation, mimic patch [81,82]. The patch combines the PEG frame and monolayer gelation nanofiber, in the mimic composition of organ tissue avoiding external substances [81,82].

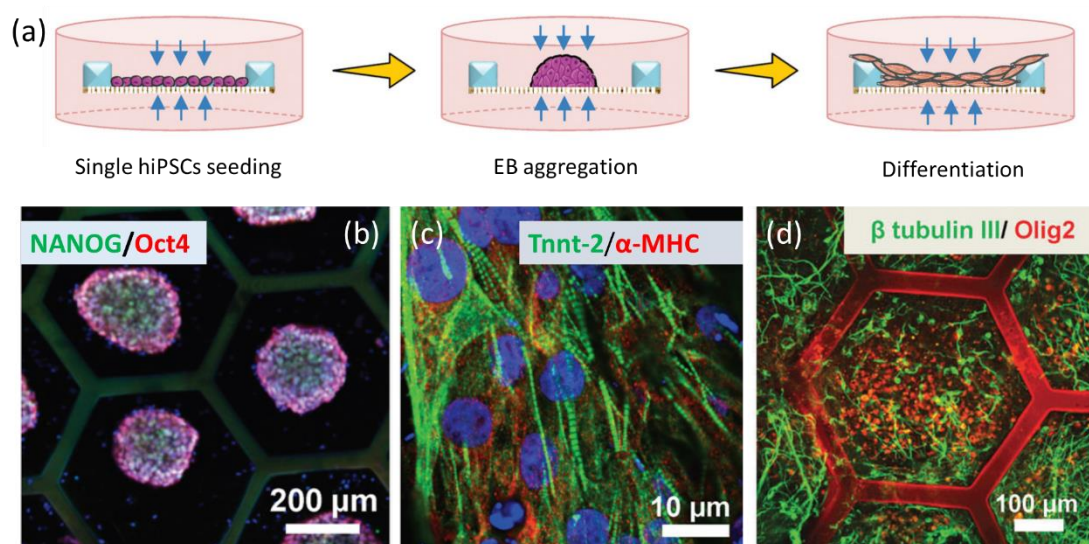


Figure 1.17 (a) Schematic of novel patch method for cell culture and differentiation under off-ground conditions. (b) Immunofluorescence image of the cells in embryoid bodies aggregation. (c) Immunofluorescence image of cardiomyocytes differentiated on a patch. (d) Immunofluorescence images of hiPSC-derived motor neuron progenitors on a patch. [81,82]

1.3 Cells in a chip

1.3.1 Microfluidics and lab on a chip

Lab on a chip or micro total analysis system (μ TAS) refers to the integration of biological and chemical operating units, such as preparation [83], reaction [84], and

separation [85], into a region of tens of square centimeters (or even smaller). The technique in high integration, as show in Figure 1.18, is to complete and analyze different biological or chemical process [86]. Through micro-electromechanical processing [87], electronics [88], and materials science [89] inter-discipline with analytical chemistry [90], biological detection [91] and medicine engineering [92], lab on a chip aims the goal of overall miniaturization, integration and portability for complex sample processing.

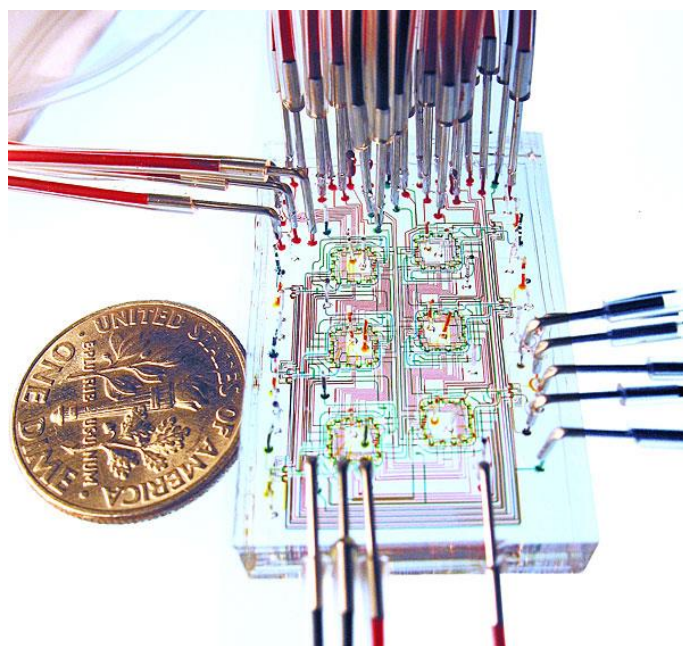


Figure 1.18 Optical micrograph showing six microchemostats that operate in parallel on a single chip. Various inputs have been loaded with food dyes to visualize channels and sub-elements of the microchemostats [86].

Based on recent studies, researchers expect a revolution in the field of chemical and biological processing as the microelectronics and integrated circuit in the field of information science [93]. Lab on a chip and related industries is blooming for the application of micro- and nanofabrication [94] and analytical technique in microscopic scale [95]. Central processing unit makes the miniaturization of computer, while the microfluidic chip makes the miniaturization of lab. Therefore, in biomedical processing, microfluidic chip can increase the speed of analysis in times

and reduce the consumption of a precious biological samples and reagent to milliliter even nanoliter [96]. In the field of analytical chemistry, the experiments cost greatly less samples and reagents to achieve same analysis and synthesis as in conventional large laboratory. Because of the transformation of expensive analytical instruments into the chip in square centimeters, as well as highly saving of resources and energy, lab on a chip is a renewable technology.

According to the current studies, lab on a chip is the composition of three key functional parts: (1) chip, (2) analyzer including drive source and signal detection device and (3) modular kits including functionality accessories.

(1) Chip

Chip involves two key aspects: dimension and material. Typically, the width of micro feature is 10-100 μm , depth 5-30 μm , length 3-10 cm. The total volume of feature is in the scale of nanoliter, much smaller than average electrophoretic capillary [97]. The most widely used materials for microfluidic chip are glass, quartz and various plastics. Glass and quartz have good electroosmotic properties and excellent optical properties, and they are suitable for manufacturing via standard etching process. The surface of glass and quartz chip can be modified by commonly chemical methods which indeed are high-cost and difficult for bonding and sealing [98]. In contrast, polymer chips, such as rigid polymethylmethacrylate (PMMA), elastomeric polydimethylsiloxane (PDMS), are low-cost and can be modified physically or chemically [95,99], with different fabrication glass and quartz chips.

(2) Analyzer

The sufficient contact, reaction or separation of sample and reagent need external driving force that is generally electric field force, positive pressure and negative pressure. Correspondingly, devices of electric power source and pressure pump are widely used in experiments via numerical control.

Detection, mostly in the method of laser induced fluorescence [100], is the core point of signals generated by chips. In addition, electrochemical [101], mass spectrometry [102], ultraviolet [103], chemiluminescence [104] and microsensors

[105] are also applied in the data input/output.

The driving source and the detection device are the main components of lab on a chip setup. The size of the two components directly determines the size of the chip analyzer. Therefore, research groups cooperate with commercial company to minimize the two parts and make them more accurate.

(3) Modular kits

Functionalized kits are auxiliary accessories in microfluidic setup, for example, chip fixture, connector, tube, etc. Although these accessories are inconspicuous, they are the key factors to complete experiments and achieve intelligent industrialization.

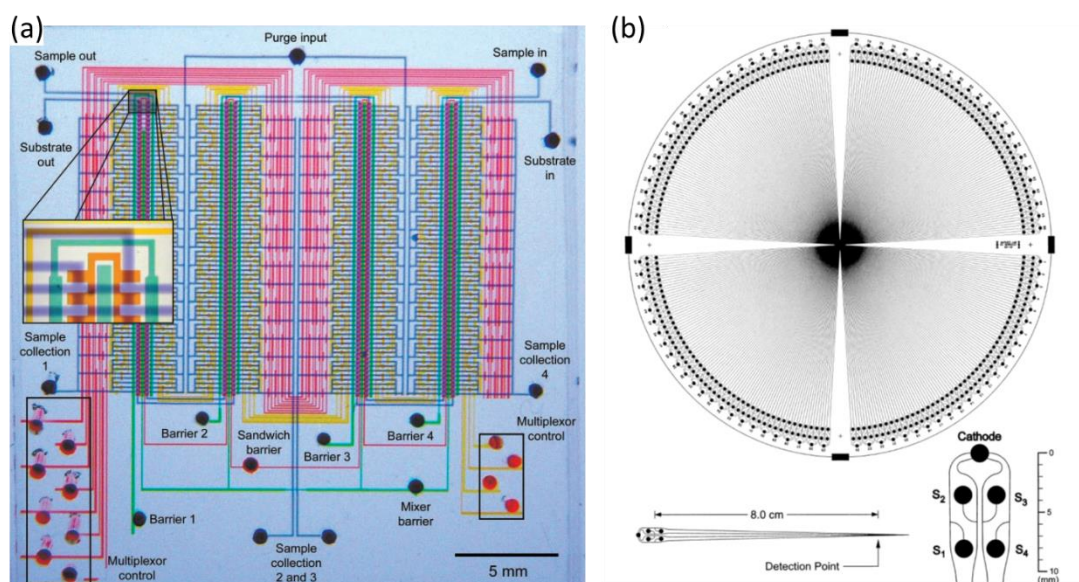


Figure 1.19 (a) Optical micrograph of the microfluidic comparator chip. The various inputs have been loaded with food dyes to visualize the channels and subelements of the fluidic logic [106]. (b) Layout of the 384-lane μ CAE device on a 200-mm-diameter wafer. Lanes are $\sim 60 \mu\text{m}$ wide and $30 \mu\text{m}$ deep, and the effective separation length is 8.0 cm [107].

In the consideration of five main advantages of lab on chip as following: (1) integration, Quake et al [106] who integrated 3574 microvalves, 1000 microreactors and 1024 microchannels in the chip with only $3.3 \text{ mm} \times 6 \text{ mm}$ area, accomplishing flow internal directional move and distribution (Figure 1.19a); (2) rapid analysis, Mathies team [107] who integrated 384 microchannels electrophoresis chips on a

200-mm-diameter disk and tested 384 H63D mutants (on the human HFE gene) linked to the hematopoietic disease in 325 seconds, each of which was less than one second (Figure 1.19b); (3) high throughput, referred to the work of Quake and Mathis; (4) Low energy and material consumption as well as little pollution, Ramsey [108] reported the channel with depth of 80 nm and volume of picoliter even less; (5) low cost and safety, the unit price of microfluidic chip will be more and more chip along with the development of technique.

Particularly, the biological and medical applications of lab on a chip are carried out as following: (1) clinical blood cell analysis, Gaward et al [109] developed a cell analysis chip with 2 cm × 3 cm to achieve cell analysis and particle size determination via impedance and optical analysis techniques; (2) nucleic acid analysis, Tezuka et al. [110] constructed a monolithically integrated nanopillars with diameter of 200-500 nm and height of 5 μm for the study of DNA electrophoresis characteristics and separation; (3) protein analysis, Duffy et al. [111] used plastic disk chip with centrifugal methods for alkaline phosphatase analysis, each sample was tested with only 3 mL of reagent in seconds; (4) drug analysis, Sathuluri et al. [112] used microchip for high-throughput screening of antitumor drugs; (5) molecule analysis, Argaint et al. [113] developed a chip containing PO₂, PCO₂ and pH sensors for blood gas analysis in the size of only 6 mm × 22 mm.

1.3.2 Organs on a chip

For biological and medical applications, the establishment of in vitro physiological model is important. To this regard, the regulation of cellular microenvironment is necessary to ensure the authenticity of the model.

The concept of organs on a chip puts forward the capacity of microenvironment regulation to the cellular function, such as fluid shear [114], mechanical stress [115], biochemical concentration gradient [116] and physical and chemical stimulation [117,118], which is more accessible compared to conventional technologies. Cells can respond to these stimuli and self-assemble, presenting a more realistic physiological

function, and thus the technique of organ on a chip has a special advantage in the establishment of in vitro physiological model [119], as concluded in Table 1.2.

Organ	Incorporated cell types	Demonstrated organ-specific features
Liver	Hepatocytes Vascular endothelial cells Fibroblasts	Serum protein synthesis Bile canaliculi Liver sinusoid Liver zonation
Lung	Airway epithelial cells Alveolar epithelial cells Pulmonary microvascular endothelial cells	Airway closure and reopening Small airway protein (CC10) synthesis Alveolar–capillary interface Surfactant production Lung inflammation Extrapulmonary absorption
Kidney	Renal tubular epithelial cells	Molecular transport
Gut	Intestinal epithelial cells	Intestinal absorption
Bone	Osteoblasts Osteocytes	Lacuna–canalicular network
Breast	Mammary epithelial cells Mammary fibroblasts Vascular endothelial cells	Malignant tumor invasion Cancer metastasis
Eye	Corneal epithelial cells Vascular endothelial cells	Epithelial barrier function
Brain	Neurons Astrocytes Oligodendrocytes	Axon–glia interaction Tumor angiogenesis

Table 1.2 Summary of microengineered organ models [119].

To achieve a reliable model of organ on a chip, the following factors have to be considered:

(1) Fluid shear

Fluidic flow produces shear force, as in human body fluid shear is everywhere in every moment. However, traditional static culture cannot functionalize system shear force. Microfluidic technology can achieve dynamic culture of cells by micropump [120], which is conducive to the stable supply of cell nutrients and discharge of waste timely. Compared to static culture, dynamic environment is more similar the cell in vivo.

(2) Mechanical stress

Mechanical stress is associated with life activity in human body, such as blood pressure, lung pressure, bone stress, etc. [121] The steady pressure plays an important role in maintaining the physiological functions, such as tissue formation, cell differentiation, and even tumor formation [121]. Microfluidic technique with elastic porous membranes produces periodic mechanical stresses, for example

culturing cells on a porous membrane is convenient for applying external forces to deform the membrane to simulate the partial physiological functions, such as lung respiration [122], intestinal peristalsis [123], and myocardial beating [124], etc.

(3) Gradient

Since laminar flow is the main formation microscale, it is advantageous to produce various types of concentration gradients in microchannels. Various biochemical signals driven by concentration gradients are significant in many physiological processes, such as cell migration [125], differentiation [126], and metastasis of cancer [127]. Lab on a chip is composed with of microvalves, micropumps and microchannels for the simulation of complex physiological processes by changing flow rate and feature size as well as generating a stable, 2D or 3D biochemical concentration gradient [128]. In addition, the achievement of concentration gradients in multi-channel chips provides the possibility for high-throughput screening of drugs test [96,129].

(4) Stimulation

The organization of human body is not made up of a cell stack, additionally requires a variety of signal transmission in an orderly arrangement, through the formation of complex interactions functionally. Organ on a chip offers the platform with superior handling ability in physical and chemical stimulation, such as electrical [130], optical [131], magnetic [132], etc.

Organ on a chip is useful for building in vitro physiologic models with complex geometries and providing an ideal platform for studying cell-cell and cell-ECM interactions even organ-organ and organ-ECM interactions [119,133], as illustrated in Figure 1.20. The appearance of organ on a chip or human on a chip is extremely helpful to drug research and development, because it not only simulates partial functions of human organs, but also saves costs dramatically, with short testing duration and rapid mechanism characterization without ethical controversy. Even in the screening of new drugs [134], microfluidic chip is more specific and effective than animal test, more, because chip test is directly to human cell lines.

Avoiding influence on cell characteristics, the potential of organ on a chip even human on a chip can be fully exerted to achieve accurate real-time operation. Therefore, standardized chips, including electrochemical, optical and immunological detection methods or sensors suitable for the chip, are inevitable become the focus of studies and commercial development.

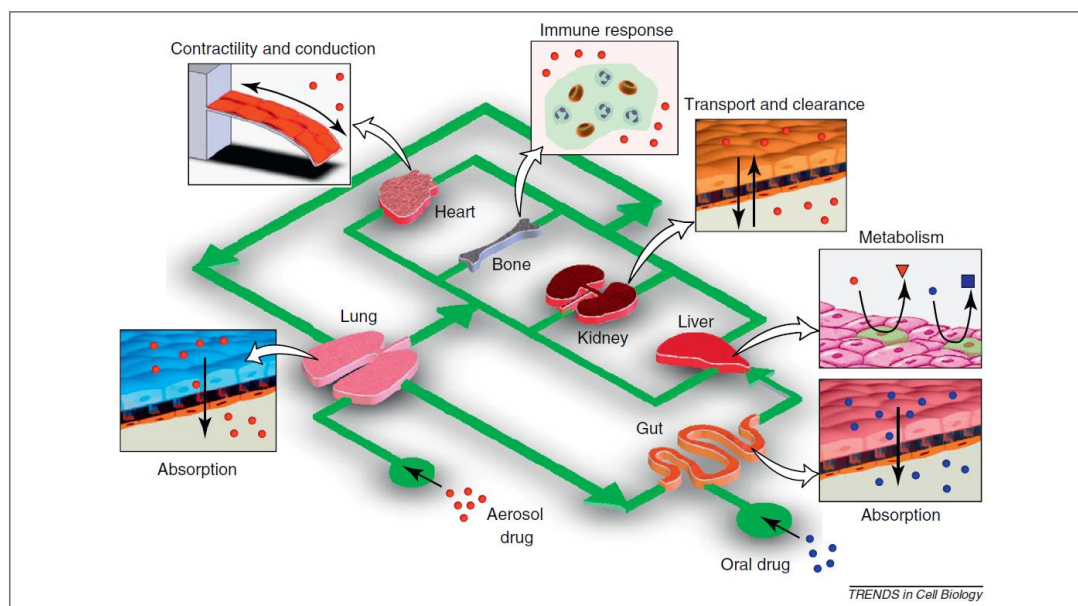


Figure 1.20 The human-on-a-chip concept. Biomimetic microsystems representing different organs can be integrated into a single microdevice and linked by a microfluidic circulatory system in a physiologically relevant manner to model a complex, dynamic process of drug absorption, distribution, metabolism and excretion, and to more reliably evaluate drug efficacy and toxicity [119].

1.4 Research objectives

The main purpose of this thesis work is to develop cell culture substrates of different properties for improved control of *in vitro* cellular functions. More specifically, we fabricate micropillar arrays of different diameter, height and spacing using different materials. We expect different adhesion and migration behaviors of cells from that of the flat culture surface. We also expect a nucleus deformation in the narrowly spaced inter-pillar spaces. In addition, we deposit electrospun

nanofibers to the top micropillar arrays to improve the culture performances. Once optimized, the pillar arrays are integrated into microfluidic devices to control the cell migration on pillar arrays under conditions of biochemical concentration gradients.

In chapter 2, we will describe the fabrication methods used or developed in this work, including both conventional and non-conventional lithography methods as well as non-lithography techniques.

In chapter 3, we will focus on the fabrication of micropillar arrays of different heights using materials of different stiffness such as elastomer PDMS and thermoplastic PCL/PLGA. In such a way, we will be able to tune the effective stiffness of the substrate, which is necessary to study the cell adhesion and migration over a broad range of substrate stiffness.

In chapter 4, we will present the deposition of electrospun nanofibers on the top of elastomer pillars. We will observe the formation of filamentous pseudopodia of cells, which is prominent for the formation of neuronal network. Thus, we will show the importance of engineered morphology and stiffness of the substrate on the cell culture behaviors.

In chapter 5, we will discuss a particular case where the inter-pillar space is regulated for single cell confinement. The deformation of the cell nuclei will be studied for two types of cells, i.e., cancer cells and stem cells. Through the control of nucleus morphology, we expect to grasp another key to modulate the cell behavior.

Finally, we will show in chapter 6 the feasibility of integrating micropillars in a microfluidic device for cell culture studies. Such integration will allow generation of a biochemical gradient for monitoring cell migration on micropillar arrays. Thus, we will be able investigate the influence of the substrate stiffness on cell migration under biochemical concentration gradients which should be relevant for drug-screening and analyses.

The substrates made of micropillars of different stiffness can be used for cell culture and cell assays. Comparing to the flat substrate, the substrate also provides a quasi 3D culture microenvironment, which might be necessary for advanced studies

in drug screening, stem cell differentiation or metastasis characterization. Micropillar arrays can also be easily manufactured and easily integrated into functional micro-devices, thereby holding a high potential of for large scale applications.

References

1. E. B. Wilson, *Cell In Development And Heredity*, 3rd. Rev. (Macmillan Company.; New York, 1925).
2. C. R. Noback, N. L. Strominger, R. J. Demarest, D. A. Ruggiero, *The human nervous system: structure and function*. (Springer Science & Business Media, 2005).
3. D. G. Moerman, A. Fire, 16 Muscle: Structure, Function, and Development. *Cold Spring Harbor Monograph Archive* **33**, 417-470 (1997).
4. G. R. Skuse, M. C. Ferran, *Cardiomyocytes*. (Springer, 2015).
5. S. I. Fox, *Human Physiology 9th Editon*. (McGraw-Hill press, New York, USA, 2006).
6. <https://www.dreamstime.com/royalty-free-stock-photos-human-body-cells-image25962548>.
7. R. T. Leonard, T. K. Hodges, The plasma membrane. *The Biochemistry of Plants. A Comprehensive Treatise* **1**, 163-182 (2013).
8. <https://www.thinglink.com/scene/695520754959122433>.
9. S. Standring, *Gray's anatomy: the anatomical basis of clinical practice*. (Elsevier Health Sciences, 2015).
10. J. M. Fernandez, J. P. Hoeffler, *Gene expression systems: using nature for the art of expression*. (Academic Press, 1998).
11. R. Dermietzel, *The cytoskeleton: imaging, isolation, and interaction*. (Humana Press, 2013).
12. <http://schoolbag.info/biology/living/31.html>.
13. B. Alberts, A. Johnson, J. Lewis, M. Raff, K. Roberts, P. Walter, *Molecular biology of the cell*. new york: Garland science; 2002. *Classic textbook now in its 5th Edition*, (2002).
14. G. Karp, N. L. Pruitt, *Cell and molecular biology: concepts and experiments*. (Wiley, 1999).
15. <http://micro.magnet.fsu.edu/cells/animals/nucleus.html>.
16. H. Busch, *The cell nucleus*. (Elsevier, 2012), vol. 3.
17. T. Fair, P. Hyttel, J. Motlik, M. Boland, P. Lonergan, Maintenance of meiotic arrest in bovine oocytes in vitro using butyrolactone I: effects on oocyte ultrastructure and nucleolus function. *Molecular reproduction and development* **62**, 375-386 (2002).
18. R. Berezney, M. J. Mortillaro, H. Ma, X. Wei, J. Samarabandu, The nuclear matrix: a structural milieu for genomic function. *International review*

of cytology **162**, 1-65 (1996).

19. E. Therman, M. Susman, *Human chromosomes: structure, behavior, and effects*. (Springer Science & Business Media, 2012).

20. T. G. Kuznetsova, M. N. Starodubtseva, N. I. Yegorenkov, S. A. Chizhik, R. I. Zhdanov, Atomic force microscopy probing of cell elasticity. *Micron* **38**, 824-833 (2007).

21. K. Tomankova, P. Kolar, J. Malohlava, H. Kolarova, Mechanical characterisation of HeLa cells using atomic force microscopy. *Current microscopy contributions to advances in science and technology* **1**, 549-554 (2012).

22. G. R. Fedorchak, A. Kaminski, J. Lammerding, Cellular mechanosensing: getting to the nucleus of it all. *Progress in biophysics and molecular biology* **115**, 76-92 (2014).

23. J. Swift, I. L. Ivanovska, A. Buxboim, T. Harada, P. D. P. Dingal, J. Pinter, J. D. Pajerowski, K. R. Spinler, J.-W. Shin, M. Tewari, Nuclear lamin-A scales with tissue stiffness and enhances matrix-directed differentiation. *Science* **341**, 1240104 (2013).

24. P. M. Davidson, J. Lammerding, Broken nuclei–lamins, nuclear mechanics, and disease. *Trends in cell biology* **24**, 247-256 (2014).

25. C. Y. Ho, D. E. Jaalouk, M. K. Vartiainen, J. Lammerding, Lamin A/C and emerin regulate MKL1-SRF activity by modulating actin dynamics. *Nature* **497**, 507-511 (2013).

26. P. D. P. Dingal, A. M. Bradshaw, S. Cho, M. Raab, A. Buxboim, J. Swift, D. E. Discher, Fractal heterogeneity in minimal matrix models of scars modulates stiff-niche stem-cell responses via nuclear exit of a mechanorepressor. *Nature materials* **14**, 951-960 (2015).

27. C. M. Denais, R. M. Gilbert, P. Isermann, A. L. McGregor, M. te Lindert, B. Weigel, P. M. Davidson, P. Friedl, K. Wolf, J. Lammerding, Nuclear envelope rupture and repair during cancer cell migration. *Science* **352**, 353-358 (2016).

28. J. D. Pajerowski, K. N. Dahl, F. L. Zhong, P. J. Sammak, D. E. Discher, Physical plasticity of the nucleus in stem cell differentiation. *Proceedings of the National Academy of Sciences* **104**, 15619-15624 (2007).

29. E. D. Hay, *Cell biology of extracellular matrix*. (Springer Science & Business Media, 2013).

30. F. Travascio, *Composition and Function of the Extracellular Matrix in the Human Body*. (InTech, 2016).

31. A. D. Cardin, H. Weintraub, Molecular modeling of protein-glycosaminoglycan interactions. *Arteriosclerosis, Thrombosis, and Vascular Biology* **9**, 21-32 (1989).

32. E. Ruoslahti, Y. Yamaguchi, Proteoglycans as modulators of growth factor activities. *Cell* **64**, 867-869 (1991).

33. R. P. Mecham, D. E. Birk, P. D. Yurchenco, *Extracellular matrix assembly and structure*. (Academic Press, 2013).

34. H. Lodish, S. L. Zipursky, Molecular cell biology. *Biochemistry and Molecular Biology Education* **29**, 126-133 (2001).
35. P. Fratzl, *Collagen: structure and mechanics*. (Springer Science & Business Media, 2008).
36. H. Lee, J. Rho, P. B. Messersmith, Facile conjugation of biomolecules onto surfaces via mussel adhesive protein inspired coatings. *Advanced materials* **21**, 431-434 (2009).
37. R. O. Hynes, Integrins: versatility, modulation, and signaling in cell adhesion. *Cell* **69**, 11-25 (1992).
38. A. Didangelos, X. Yin, K. Mandal, A. Saje, A. Smith, Q. Xu, M. Jahangiri, M. Mayr, Extracellular matrix composition and remodeling in human abdominal aortic aneurysms: a proteomics approach. *Molecular & Cellular Proteomics* **10**, M111. 008128 (2011).
39. N. Hansen, F. Genovese, D. Leeming, M. Karsdal, The importance of extracellular matrix for cell function and in vivo likeness. *Experimental and molecular pathology* **98**, 286-294 (2015).
40. http://csls-text.c.u-tokyo.ac.jp/active/11_01.html.
41. J. Behrens, W. J. Nelson, *Cell adhesion*. (Springer Science & Business Media, 2010), vol. 165.
42. N. Demling, C. Ehrhardt, M. Kasper, M. Laue, L. Knels, E. P. Rieber, Promotion of cell adherence and spreading: a novel function of RAGE, the highly selective differentiation marker of human alveolar epithelial type I cells. *Cell and tissue research* **323**, 475-488 (2006).
43. C. E. Orsello, D. A. Lauffenburger, D. A. Hammer, Molecular properties in cell adhesion: a physical and engineering perspective. *Trends in biotechnology* **19**, 310-316 (2001).
44. L. Liaw, M. Almeida, C. E. Hart, S. M. Schwartz, C. M. Giachelli, Osteopontin promotes vascular cell adhesion and spreading and is chemotactic for smooth muscle cells in vitro. *Circulation Research* **74**, 214-224 (1994).
45. J. S. Damiano, A. E. Cress, L. A. Hazlehurst, A. A. Shtil, W. S. Dalton, Cell adhesion mediated drug resistance (CAM-DR): role of integrins and resistance to apoptosis in human myeloma cell lines. *Blood* **93**, 1658-1667 (1999).
46. G. S. Ashcroft, M. A. Horan, M. Ferguson, Aging alters the inflammatory and endothelial cell adhesion molecule profiles during human cutaneous wound healing. *Laboratory investigation; a journal of technical methods and pathology* **78**, 47-58 (1998).
47. S. Albelda, Role of integrins and other cell adhesion molecules in tumor progression and metastasis. *Laboratory investigation; a journal of technical methods and pathology* **68**, 4-17 (1993).
48. E. Sackmann, Biophysics: How cells feel the force. *Nature Physics* **6**, 407-408 (2010).
49. I. B. Bischofs, U. S. Schwarz, Cell organization in soft media due to

active mechanosensing. *Proceedings of the National Academy of Sciences* **100**, 9274-9279 (2003).

50. S. Glasstone, H. Eyring, K. J. Laidler, *The theory of rate processes*. (McGraw-Hill, 1941).

51. B. J. Dubin-Thaler, G. Giannone, H.-G. Döbereiner, M. P. Sheetz, Nanometer analysis of cell spreading on matrix-coated surfaces reveals two distinct cell states and STEPs. *Biophysical journal* **86**, 1794-1806 (2004).

52. S. P. Carey, J. M. Charest, C. A. Reinhart-King, in *Cellular and biomolecular mechanics and mechanobiology*. (Springer, 2010), pp. 29-69.

53. I. Degasne, M. Basle, V. Demais, G. Hure, M. Lesourd, B. Grolleau, L. Mercier, D. Chappard, Effects of roughness, fibronectin and vitronectin on attachment, spreading, and proliferation of human osteoblast-like cells (Saos-2) on titanium surfaces. *Calcified tissue international* **64**, 499-507 (1999).

54. J. Li, D. Han, Y.-P. Zhao, Kinetic behaviour of the cells touching substrate: the interfacial stiffness guides cell spreading. *Scientific reports* **4**, 3910 (2014).

55. J.-C. Wang, W. Liu, Q. Tu, C. Ma, L. Zhao, Y. Wang, J. Ouyang, L. Pang, J. Wang, High throughput and multiplex localization of proteins and cells for in situ micropatterning using pneumatic microfluidics. *The Analyst* **140**, 827-836 (2015).

56. S. M. Albelda, C. A. Buck, Integrins and other cell adhesion molecules. *The FASEB Journal* **4**, 2868-2880 (1990).

57. R. J. Linnola, L. Werner, S. K. Pandey, M. Escobar-Gomez, S. L. Znoiko, D. J. Apple, Adhesion of fibronectin, vitronectin, laminin, and collagen type IV to intraocular lens materials in pseudophakic human autopsy eyes: Part 2: explanted intraocular lenses. *Journal of Cataract & Refractive Surgery* **26**, 1807-1818 (2000).

58. M. Versaevel, T. Grevesse, S. Gabriele, Spatial coordination between cell and nuclear shape within micropatterned endothelial cells. *Nature communications* **3**, 671 (2012).

59. J. Fu, Y. K. Wang, M. T. Yang, R. A. Desai, X. Yu, Z. Liu, C. S. Chen, Mechanical regulation of cell function with geometrically modulated elastomeric substrates. *Nature methods* **7**, 733-736 (2010); published online EpubSep (10.1038/nmeth.1487).

60. A. Schwab, A. Fabian, P. J. Hanley, C. Stock, Role of ion channels and transporters in cell migration. *Physiological reviews* **92**, 1865-1913 (2012).

61. G. Sieck. (Am Physiological Soc, 2013).

62. A. L. McGregor, C.-R. Hsia, J. Lammerding, Squish and squeeze—the nucleus as a physical barrier during migration in confined environments. *Current opinion in cell biology* **40**, 32-40 (2016).

63. A. D. Doyle, R. J. Petrie, M. L. Kutys, K. M. Yamada, Dimensions in cell migration. *Current opinion in cell biology* **25**, 642-649 (2013).

64. R. J. Petrie, K. M. Yamada, Multiple mechanisms of 3D migration:

- the origins of plasticity. *Current opinion in cell biology* **42**, 7-12 (2016).
65. G. M. Cooper, D. Ganem, The Cell: A Molecular Approach. *Nature medicine* **3**, 1042-1042 (1997).
66. D. C. Macallan, C. A. Fullerton, R. A. Neese, K. Haddock, S. S. Park, M. K. Hellerstein, Measurement of cell proliferation by labeling of DNA with stable isotope-labeled glucose: studies in vitro, in animals, and in humans. *Proceedings of the National Academy of Sciences* **95**, 708-713 (1998).
67. M. Bachman, S. Uribe-Lewis, X. Yang, H. E. Burgess, M. Iurlaro, W. Reik, A. Murrell, S. Balasubramanian, 5-Formylcytosine can be a stable DNA modification in mammals. *Nature chemical biology* **11**, 555-557 (2015).
68. J. Reinert, H. Holtzer, *Cell cycle and cell differentiation*. (Springer Science & Business Media, 2013), vol. 7.
69. M. S. Kallos, *Embryonic Stem Cells - Differentiation and Pluripotent Alternatives*. (InTech, 2011).
70. K. Takahashi, S. Yamanaka, Induction of pluripotent stem cells from mouse embryonic and adult fibroblast cultures by defined factors. *Cell* **126**, 663-676 (2006).
71. K. Okita, T. Ichisaka, S. Yamanaka, Generation of germline-competent induced pluripotent stem cells. *Nature* **448**, 313-317 (2007).
72. K. Takahashi, K. Tanabe, M. Ohnuki, M. Narita, T. Ichisaka, K. Tomoda, S. Yamanaka, Induction of pluripotent stem cells from adult human fibroblasts by defined factors. *Cell* **131**, 861-872 (2007).
73. [http:// philschatz.com/anatomy-book/contents/m46036.html](http://philschatz.com/anatomy-book/contents/m46036.html).
74. V. K. Singh, M. Kalsan, N. Kumar, A. Saini, R. Chandra, Induced pluripotent stem cells: applications in regenerative medicine, disease modeling, and drug discovery. *Frontiers in cell and developmental biology* **3**, 2 (2015).
75. X. Duan, Q. Tu, J. Zhang, J. Ye, C. Sommer, G. Mostoslavsky, D. Kaplan, P. Yang, J. Chen, Application of induced pluripotent stem (iPS) cells in periodontal tissue regeneration. *Journal of cellular physiology* **226**, 150-157 (2011).
76. S. Yamanaka, A fresh look at iPS cells. *Cell* **137**, 13-17 (2009).
77. G. Romano, F. Morales, I. R. Marino, A. Giordano, A commentary on iPS cells: potential applications in autologous transplantation, study of illnesses and drug screening. *Journal of cellular physiology* **229**, 148-152 (2014).
78. S. C. Lesher - Perez, J. P. Frampton, S. Takayama, Microfluidic systems: A new toolbox for pluripotent stem cells. *Biotechnology journal* **8**, 180-191 (2013).
79. Y. Shao, K. Taniguchi, K. Gurdziel, R. F. Townshend, X. Xue, K. M. A. Yong, J. Sang, J. R. Spence, D. L. Gumucio, J. Fu, Self-organized amniogenesis by human pluripotent stem cells in a biomimetic implantation-like niche. *Nature materials* **16**, 419-425 (2017).

80. Y. Wang, J. Hu, J. Jiao, Z. Liu, Z. Zhou, C. Zhao, L.-J. Chang, Y. E. Chen, P. X. Ma, B. Yang, Engineering vascular tissue with functional smooth muscle cells derived from human iPSCs and nanofibrous scaffolds. *Biomaterials* **35**, 8960-8969 (2014).
81. Y. Tang, L. Liu, J. Li, L. Yu, L. Wang, J. Shi, Y. Chen, Induction and differentiation of human induced pluripotent stem cells into functional cardiomyocytes on a compartmented monolayer of gelatin nanofibers. *Nanoscale* **8**, 14530-14540 (2016).
82. Y. Tang, L. Liu, J. Li, L. Yu, F. P. U. Severino, L. Wang, J. Shi, X. Tu, V. Torre, Y. Chen, Effective motor neuron differentiation of hiPSCs on a patch made of crosslinked monolayer gelatin nanofibers. *Journal of Materials Chemistry B* **4**, 3305-3312 (2016).
83. J. Kim, M. Johnson, P. Hill, B. K. Gale, Microfluidic sample preparation: cell lysis and nucleic acid purification. *Integrative Biology* **1**, 574-586 (2009).
84. H. Song, D. L. Chen, R. F. Ismagilov, Reactions in droplets in microfluidic channels. *Angewandte chemie internationale edition* **45**, 7336-7356 (2006).
85. S. Shen, C. Ma, L. Zhao, Y. Wang, J.-C. Wang, J. Xu, T. Li, L. Pang, J. Wang, High-throughput rare cell separation from blood samples using steric hindrance and inertial microfluidics. *Lab on a chip* **14**, 2525-2538 (2014).
86. F. K. Balagaddé, L. You, C. L. Hansen, F. H. Arnold, S. R. Quake, Long-term monitoring of bacteria undergoing programmed population control in a microchemostat. *Science* **309**, 137-140 (2005).
87. M. W. Ashraf, S. Tayyaba, N. Afzulpurkar, Micro electromechanical systems (MEMS) based microfluidic devices for biomedical applications. *International journal of molecular sciences* **12**, 3648-3704 (2011).
88. T. Someya, A. Dodabalapur, A. Gelperin, H. E. Katz, Z. Bao, Integration and response of organic electronics with aqueous microfluidics. *Langmuir : the ACS journal of surfaces and colloids* **18**, 5299-5302 (2002).
89. S. Marre, Y. Roig, C. Aymonier, Supercritical microfluidics: Opportunities in flow-through chemistry and materials science. *The Journal of Supercritical Fluids* **66**, 251-264 (2012).
90. K. i. Ohno, K. Tachikawa, A. Manz, Microfluidics: applications for analytical purposes in chemistry and biochemistry. *Electrophoresis* **29**, 4443-4453 (2008).
91. P. S. Waggoner, H. G. Craighead, Micro-and nanomechanical sensors for environmental, chemical, and biological detection. *Lab on a chip* **7**, 1238-1255 (2007).
92. B. D. Plouffe, T. Kniazeva, J. E. Mayer, S. K. Murthy, V. L. Sales, Development of microfluidics as endothelial progenitor cell capture technology for cardiovascular tissue engineering and diagnostic medicine. *The FASEB Journal* **23**, 3309-3314 (2009).
93. I. A. Grout, *Integrated circuit test engineering: modern techniques*.

- (Springer Science & Business Media, 2005).
94. S. Thomas, R. Shanks, J. Joy, *Micro-and Nanostructured Polymer Systems: From Synthesis to Applications*. (Apple Academic Press, 2015).
 95. E. Oosterbroek, A. Van den Berg, *Lab-on-a-chip: miniaturized systems for (bio) chemical analysis and synthesis*. (Elsevier, 2003).
 96. P. S. Dittrich, A. Manz, Lab-on-a-chip: microfluidics in drug discovery. *Nature Reviews Drug Discovery* **5**, 210-218 (2006).
 97. D. Mark, S. Haeberle, G. Roth, F. von Stetten, R. Zengerle, Microfluidic lab-on-a-chip platforms: requirements, characteristics and applications. *Chemical Society reviews* **39**, 1153-1182 (2010).
 98. O. Geschke, H. Klank, P. Telleman, *Microsystem Engineering of Lab-on-a-chip Devices*. (John Wiley & Sons, 2004).
 99. F. E. Tay, *Microfluidics and BioMEMS applications*. (Springer, 2002).
 100. J.-L. Fu, Q. Fang, T. Zhang, X.-H. Jin, Z.-L. Fang, Laser-induced fluorescence detection system for microfluidic chips based on an orthogonal optical arrangement. *Analytical chemistry* **78**, 3827-3834 (2006).
 101. K. Hsieh, A. S. Patterson, B. S. Ferguson, K. W. Plaxco, H. T. Soh, Rapid, Sensitive, and Quantitative Detection of Pathogenic DNA at the Point of Care through Microfluidic Electrochemical Quantitative Loop - Mediated Isothermal Amplification. *Angewandte Chemie* **124**, 4980-4984 (2012).
 102. C. Wang, R. Oleschuk, F. Ouchen, J. Li, P. Thibault, D. J. Harrison, Integration of immobilized trypsin bead beds for protein digestion within a microfluidic chip incorporating capillary electrophoresis separations and an electrospray mass spectrometry interface. *Rapid Communications in Mass Spectrometry* **14**, 1377-1383 (2000).
 103. R. J. Jackman, T. M. Floyd, R. Ghodssi, M. A. Schmidt, K. F. Jensen, Microfluidic systems with on-line UV detection fabricated in photodefinable epoxy. *Journal of Micromechanics and Microengineering* **11**, 263 (2001).
 104. X. Wang, O. Hofmann, R. Das, E. M. Barrett, D. D. Bradley, Integrated thin-film polymer/fullerene photodetectors for on-chip microfluidic chemiluminescence detection. *Lab on a chip* **7**, 58-63 (2007).
 105. G. M. Birnbaumer, P. A. Lieberzeit, L. Richter, R. Schirhagl, M. Milnera, F. L. Dickert, A. Bailey, P. Ertl, Detection of viruses with molecularly imprinted polymers integrated on a microfluidic biochip using contact-less dielectric microsensors. *Lab on a chip* **9**, 3549-3556 (2009).
 106. T. Thorsen, S. J. Maerkl, S. R. Quake, Microfluidic large-scale integration. *Science* **298**, 580-584 (2002).
 107. C. A. Emrich, H. Tian, I. L. Medintz, R. A. Mathies, Microfabricated 384-lane capillary array electrophoresis bioanalyzer for ultrahigh-throughput genetic analysis. *Analytical Chemistry* **74**, 5076-5083 (2002).
 108. J. M. Ramsey, J. P. Alarie, S. C. Jacobson, N. Peterson, in *Micro Total Analysis Systems 2002*. (Springer, 2002), pp. 314-316.
 109. S. Gawad, L. Schild, P. Renaud, Micromachined impedance

spectroscopy flow cytometer for cell analysis and particle sizing. *Lab on a chip* **1**, 76-82 (2001).

110. Y. Tezuka, M. Ueda, Y. Baba, H. Nakanishi, T. Nishimoto, Y. Takamura, Y. Horiike, in *Micro Total Analysis Systems 2002*. (Springer, 2002), pp. 212-214.

111. D. C. Duffy, H. L. Gillis, J. Lin, N. F. Sheppard, G. J. Kellogg, Microfabricated centrifugal microfluidic systems: characterization and multiple enzymatic assays. *Analytical Chemistry* **71**, 4669-4678 (1999).

112. S. R. Rao, Y. Akagi, Y. Morita, E. Tamiya, in *Micro Total Analysis Systems 2002*. (Springer, 2002), pp. 862-864.

113. P. Arquint, M. Koudelka-Hep, B. H. van der Schoot, P. van der Wal, N. de Rooij, Micromachined analyzers on a silicon chip. *Clinical chemistry* **40**, 1805-1809 (1994).

114. R. H. Lam, Y. Sun, W. Chen, J. Fu, Elastomeric microposts integrated into microfluidics for flow-mediated endothelial mechanotransduction analysis. *Lab on a chip* **12**, 1865-1873 (2012).

115. D. Huh, H. J. Kim, J. P. Fraser, D. E. Shea, M. Khan, A. Bahinski, G. A. Hamilton, D. E. Ingber, Microfabrication of human organs-on-chips. *Nature protocols* **8**, 2135-2157 (2013); published online EpubNov (10.1038/nprot.2013.137).

116. X. Lou, G. Kim, H. K. Yoon, Y. E. Lee, R. Kopelman, E. Yoon, A high-throughput photodynamic therapy screening platform with on-chip control of multiple microenvironmental factors. *Lab on a chip* **14**, 892-901 (2014); published online EpubMar 7 (10.1039/c3lc51077h).

117. G. Robertson, T. J. Bushell, M. Zagnoni, Chemically induced synaptic activity between mixed primary hippocampal co-cultures in a microfluidic system. *Integrative biology : quantitative biosciences from nano to macro* **6**, 636-644 (2014); published online EpubJun (10.1039/c3ib40221e).

118. E. E. Hui, S. N. Bhatia, Micromechanical control of cell-cell interactions. *Proceedings of the National Academy of Sciences of the United States of America* **104**, 5722-5726 (2007); published online EpubApr 3 (10.1073/pnas.0608660104).

119. D. Huh, G. A. Hamilton, D. E. Ingber, From 3D cell culture to organs-on-chips. *Trends in cell biology* **21**, 745-754 (2011).

120. M.-H. Wu, S.-B. Huang, Z. Cui, Z. Cui, G.-B. Lee, A high throughput perfusion-based microreactor platform integrated with pneumatic micropumps for three-dimensional cell culture. *Biomedical microdevices* **10**, 309-319 (2008).

121. A. G. Kamkin, I. S. Kiseleva, *Mechanosensitivity in cells and tissues*. (Springer, 2005).

122. K. H. Benam, R. Novak, J. Nawroth, M. Hirano-Kobayashi, T. C. Ferrante, Y. Choe, R. Prantil-Baun, J. C. Weaver, A. Bahinski, K. K. Parker, Matched-Comparative Modeling of Normal and Diseased Human Airway Responses Using a Microengineered Breathing Lung Chip. *Cell Systems* **3**, 456-466. e454 (2016).

123. H. J. Kim, D. Huh, G. Hamilton, D. E. Ingber, Human gut-on-a-chip inhabited by microbial flora that experiences intestinal peristalsis-like motions and flow. *Lab on a chip* **12**, 2165-2174 (2012); published online EpubJun 21 (10.1039/c2lc40074j).

124. J. U. Lind, T. A. Busbee, A. D. Valentine, F. S. Pasqualini, H. Yuan, M. Yadid, S.-J. Park, A. Kotikian, A. P. Nesmith, P. H. Campbell, Instrumented cardiac microphysiological devices via multimaterial three-dimensional printing. *Nature materials*, (2016).

125. S. Y. Cheng, S. Heilman, M. Wasserman, S. Archer, M. L. Shuler, M. Wu, A hydrogel-based microfluidic device for the studies of directed cell migration. *Lab on a chip* **7**, 763-769 (2007); published online EpubJun (10.1039/b618463d).

126. B. G. Chung, L. A. Flanagan, S. W. Rhee, P. H. Schwartz, A. P. Lee, E. S. Monuki, N. L. Jeon, Human neural stem cell growth and differentiation in a gradient-generating microfluidic device. *Lab on a chip* **5**, 401-406 (2005).

127. S. Bersini, J. S. Jeon, G. Dubini, C. Arrigoni, S. Chung, J. L. Charest, M. Moretti, R. D. Kamm, A microfluidic 3D in vitro model for specificity of breast cancer metastasis to bone. *Biomaterials* **35**, 2454-2461 (2014).

128. S. G. Uzel, O. C. Amadi, T. M. Pearl, R. T. Lee, P. T. So, R. D. Kamm, Simultaneous or sequential orthogonal gradient formation in a 3D cell culture microfluidic platform. *Small* **12**, 612-622 (2016).

129. B. Hong, P. Xue, Y. Wu, J. Bao, Y. J. Chuah, Y. Kang, A concentration gradient generator on a paper-based microfluidic chip coupled with cell culture microarray for high-throughput drug screening. *Biomedical microdevices* **18**, 1-8 (2016).

130. W. Cheng, N. Klauke, H. Sedgwick, G. L. Smith, J. M. Cooper, Metabolic monitoring of the electrically stimulated single heart cell within a microfluidic platform. *Lab on a chip* **6**, 1424-1431 (2006).

131. J. M. Jang, J. Lee, H. Kim, N. L. Jeon, W. Jung, One-photon and two-photon stimulation of neurons in a microfluidic culture system. *Lab on a chip* **16**, 1684-1690 (2016).

132. S. Rossi, M. Hallett, P. M. Rossini, A. Pascual-Leone, S. o. T. C. Group, Safety, ethical considerations, and application guidelines for the use of transcranial magnetic stimulation in clinical practice and research. *Clinical neurophysiology* **120**, 2008-2039 (2009).

133. S. N. Bhatia, D. E. Ingber, Microfluidic organs-on-chips. *Nature biotechnology* **32**, 760-772 (2014).

134. E. W. Esch, A. Bahinski, D. Huh, Organs-on-chips at the frontiers of drug discovery. *Nature reviews Drug discovery* **14**, 248-260 (2015).

Chapter 2 Micro/Nano Fabrication

In this chapter, we present the micro/nano fabrication methods used in this thesis work. Firstly, we describe the conventional lithographic methods for pattern generation and pattern replication. Then, we discuss the method of electrospinning to fabricate nano-fibers. For both conventional and electrospinning approaches, surface treatment is necessary for cell culture studies. In addition, 3D printing and cutting plotter are presented to rapid prototyping of scaffolds and microfluidic devices.

2.1 Introduction

Since more than two decades, intensive studies have been developed on micro and nano-structures due to their outstanding properties [1,2] as well as their commercial values in many fields such as machinery, electronics, materials, chemistry, physics and biology [3]. For example, micro and nanostructures are now used in artificial muscle [4], solar cell [5], chemical sensor [6], optical fiber [7], etc. To meet the industrial requirements, low-cost and high throughput manufacturing technologies have also to be developed [8,9], including both conventional and nonconventional nanofabrication techniques. For example, low cost chemical syntheses can be used to produce a variety of micro/nano structures, including fiber, yarn, rod, ribbon, tube, helix, ring, etc. as shown in Figure 2.1 [10]. In addition, micro and nanostructures can now be made of a variety of materials, including polymers [11], metals [12], composites [13], and ceramic [14]. To this regards, non-lithographic methods such as phase separation [15], self-assembly [16], gas-phase polymerization [17], chemical oxidation [18], etc., are widely used.

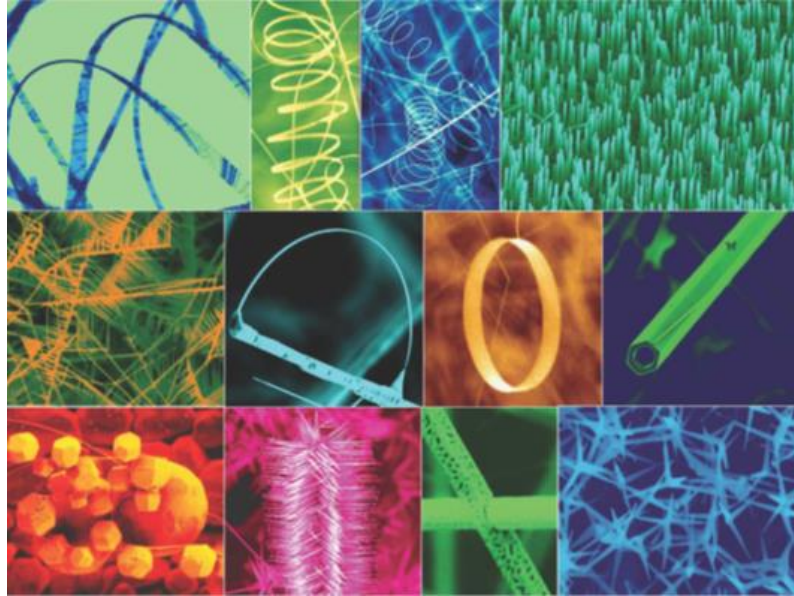


Figure 2.1 A collection of micro/nano-structures of ZnO synthesized under controlled conditions by thermal evaporation of solid powders [10].

The application field of micro and nanostructures is extremely broad. Reversely, the progresses in biology, medicine, mechanics, electronics, chemistry, materials, physics and mathematics created new needs for further development of nanofabrication technologies. Together with the high potential for industrial applications, a huge number of micro and nanostructures can now be manufactured with break-through accuracy, stability and controllability.

In the following, we first describe lithography and pattern replication techniques. Then, we focus on electrospinning for the fabrication of nanofibers.

2.2 Mold fabrication

Photolithography (or optical lithography) is a basic fabrication process of electronic circuits in semiconductor industry which transfers a pattern from a photo mask onto a thin layer of photoresist spin coated on the surface of a semiconductor and metal layer [19].

Invented in the 60's, photolithography has been improved continuously in term of resolution, throughput, and structure complexity [20]. Typically, up-to-20

lithography processes are used in the manufacturing of large-scale and ultra-large-scale integrated circuits [19,21].

In addition to the photolithography, electron beam lithography, ion beam lithography and X-ray lithography have also been developed for decades [22-24]. In principle, these techniques can have higher resolutions than photolithography but they are not used only for mask making or other purposes so that photolithography is always dominant in manufacturing [19,25].

Depending on the wavelength of exposure, photolithography generally refers ultraviolet (UV), deep UV and extreme UV (EUV) lithography [26,27]. Depending on the exposure technique, photolithography also refers to contact/proximity photolithography and projection photolithography [25].

In general, UV lithography is performed by (1) pattern generation of photo mask, (2) substrate preparation, (3) photoresist spin coating, (4) pre-exposure bake (Soft bake), (5) UV-exposure with an aligner, (6) post-exposure bake, (7) development. Among these, mask, photoresist and aligner are the key elements in UV lithography.

2.2.1 Mask

For UV lithography, the mask is made of a quartz plate and an UV absorber layer on which a pattern is generated [25]. Typically, a blank mask is consisted of a glass plate (3-5 mm), a chrome layer (~75 nm) with a chromium oxide layer (~75 nm), and a photoresist layer (0.6-1 μm) [25].

In this work, the photomask patterns were generated using commercial blank mask plates and a micro-pattern generator (μPG101 , Heidelberg), as shown in Figure 2.2a. When a UV beam irradiates on the photoresist layer through a mask, the exposed part of the photoresist layer can be developed later on to form a resist pattern. After development, chromium layer under the photoresist is etched in a chromium etchant solution. The etched part becomes then transparent and the resist protected part remains opaque, as shown in Figure 2.2b.

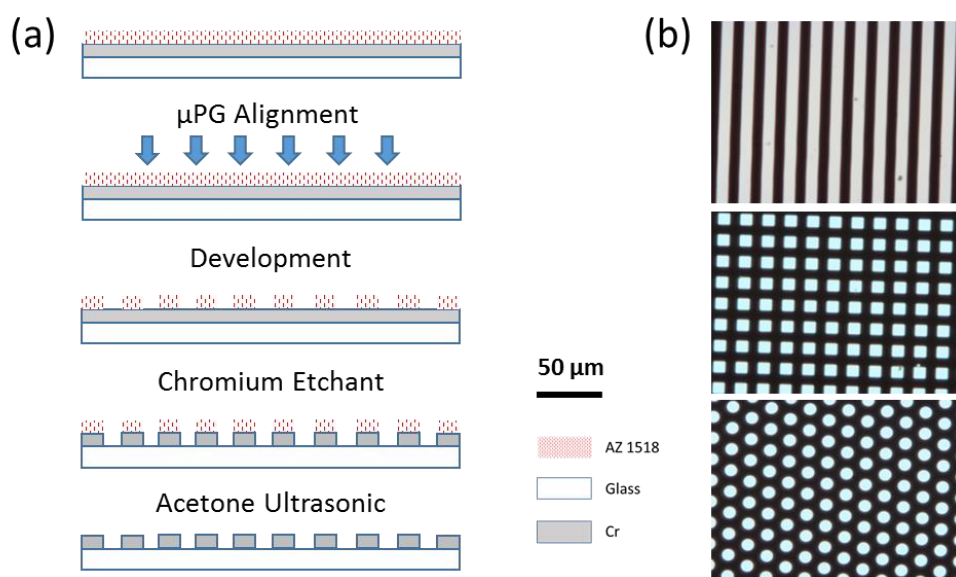


Figure 2.2 (a) Schematic diagrams of the fabrication process of optical mask. (b) Photos of optical mask in strip, square and circle array under microscope bright filed.

The micro-pattern generator we used has a focused laser beam and a high precision two-dimensional (2D) motion platform, as shown in Figure 2.3a. Commercial blank masks (Nanofilm, CIPEC Company) were with 1000-Å-thick chromium and 1- μ m-thick AZ 1518 positive photoresist. With computer aided design (CAD) process, we could input CAD drawing from software (AutoCAD, L-edit, Layout) to the system program. After micro-pattern generating, the optical mask was immersed AZ-726 MIF developer solvent (Microchemicals Company) for 30 s with gentle agitation and rinsed with deionized water (DIW), dried with Nitrogen. Subsequently, the developed mask was immersed in chromium etchant (Honeywell, Chrome-Etch 3144) for 1 min with gentle agitation and rinsed with DIW, dried with Nitrogen. Finally, the patterned mask was cleaned excess photoresist protect layer in Acetone with Ultrasonic for 3 min, rinsed with Isopropanol and dried with Nitrogen. The final functional optical mask is shown in Figure 2.3b.

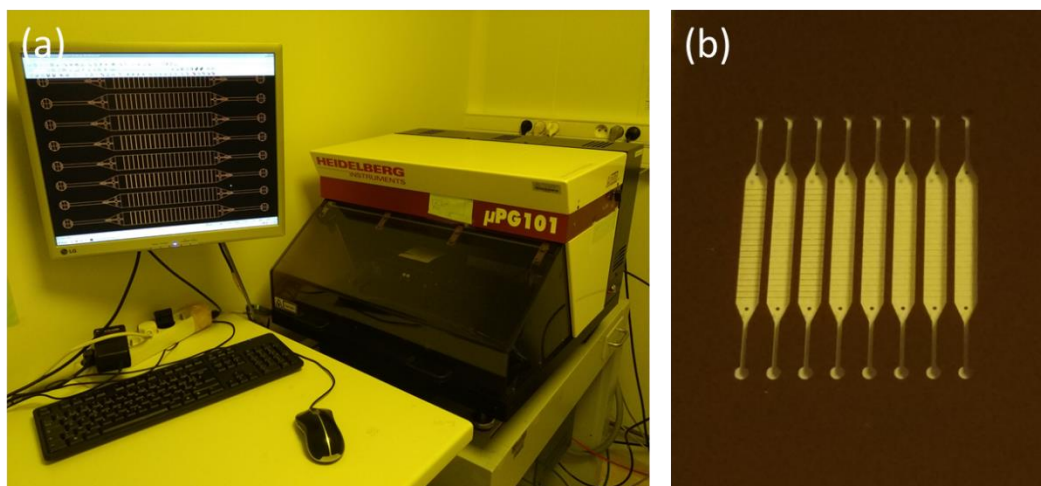


Figure 2.3 (a) Photo of μ PG 101 (Heidelberg Instruments) installed in ENS laboratory. (b) Photo of optical mask with microfluidic channel.

2.2.2 Photoresist

Photoresist is composed of three main components (1) resin, the inert polymer matrix, a binder, providing photoresist adhesion and thickness, (2) sensitizer, the core component, sensitive to the radiant energy in the form of light, specifically in the ultraviolet region, determining the exposure time and base material, (3) solvent, the most content of the composition, with good mobility and solubility, suitable for coating [25,28]. After exposure in sensitive light, photoresist generates light-curing reaction in the exposed area, resin making the physical properties of photoresist, especially the solubility and affinity significantly change. Development with appropriate solvent, dissolving the soluble part, designed pattern is achieved. Photoresist are classified into two groups: positive and negative.

Positive photoresist

Before exposure, positive photoresist is insoluble in developer but soluble after exposure, achieving the same pattern as the opaque area of mask where the energetic photons of the light break certain bonds in the long-chain polymers of the resist [25,28]. Positive resist is with the advantages of high resolution and fine contrast while with the disadvantages of poor adhesion and corrosion resistance [25,28]. The schematic diagram is illustrated in Figure 2.4.

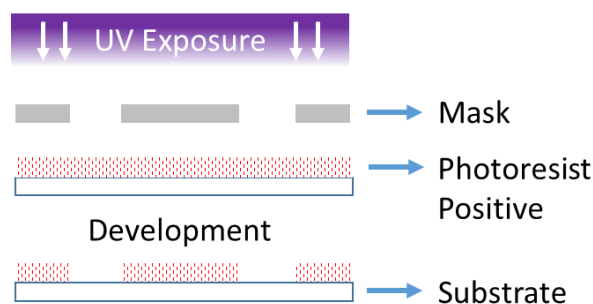


Figure 2.4 Schematic diagrams of conventional photolithography with positive photoresist.

AZ 40XT and AZ 9260 are the typical positive photoresist used in our experiments. AZ 40XT is a chemically amplified ultrathick positive resist, which application thickness at 15-30 μm . Compared to conventional positive resists, AZ 40XT is significantly time-saving due to not requirement of delays for rehydration of N^2 -outgassing. Even for ultra-high resist film thicknesses, AZ 40XT advantages short softbake times, small exposure doses and high development rate resulting from its chemical amplification [29]. AZ 9260 thick film photoresist is designed for the thick resist requirements with demanding higher resolution, superior aspect ratios, wide focus and exposure latitude and good sidewall profiles. AZ 9260 photoresist is available in two viscosity grades for film thicknesses of 4 to 24 μm . Aspect ratios of 5-7 can be achieved by using standard exposure tools in our laboratory. AZ 9260 photoresist is sensitivity to both h/i-line exposure devices and steppers [30].

Negative photoresist

On the contrary, before exposure, negative photoresist is soluble in developer but insoluble after exposure, achieving the same pattern as the translucent area of mask where the energetic photons cause the cross-linking between the resist polymers [25,28]. Negative resist is with the merits of fine adhesion and corrosion resistance while with the defects of deformation, expansion and low resolution [25,28]. The schematic diagram is illustrated in Figure 2.5.

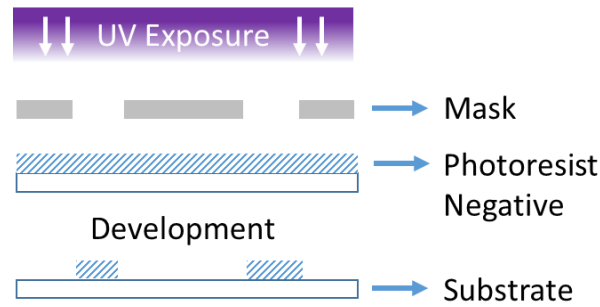


Figure 2.5 Schematic diagram of conventional photolithography with negative photoresist.

SU8 series is typical negative photoresist used in our experiments including SU8-2000 and SU8-3000. SU8-2000 is an improved formulation of SU8 series with high contrast for high aspect ratio structure, fast drying for increased throughput and film thicknesses of 0.5 to $>200\ \mu\text{m}$ in a single coat. Due to the improved coating properties as well as thick, chemically and thermally stable image, SU8-2000 is been widely used in micromachine and microelectronic application [31]. SU8-3000 is an improved formulation of SU8 and SU8-2000 series with higher contrast for over 5:1 aspect ratio structure, improved adhesion, reduced coating stress and appropriate viscosity for film thicknesses of 4 to $120\ \mu\text{m}$ in a single coat. SU8-3000 is suited for permanent applications in microelectromechanical systems (MEMS) and micro total analysis systems (μTAS) [32].

2.2.3 Exposure

Figure 2.6 demonstrates the principle of contact/proximity photolithography and projection photolithography. Contact/proximity photolithography usually uses the mercury lamp generated 365-436 nm UV band, and projection lithography usually excimer laser generated deep ultraviolet (248 nm) and extreme ultraviolet light (193 nm and 157 nm) [26,27]. The device of contact/proximity photolithography is much simpler than projection. Due to the full contact, the resolution is high but short usage time of mask and much pattern defect in contact photolithography. In comparison, proximity photolithography is long usage time of mask and little pattern

defect but low resolution caused by diffraction effect of gap. The most ideal exposure method is projection photolithography but the equipment is expensive and complicatedly time-consuming.

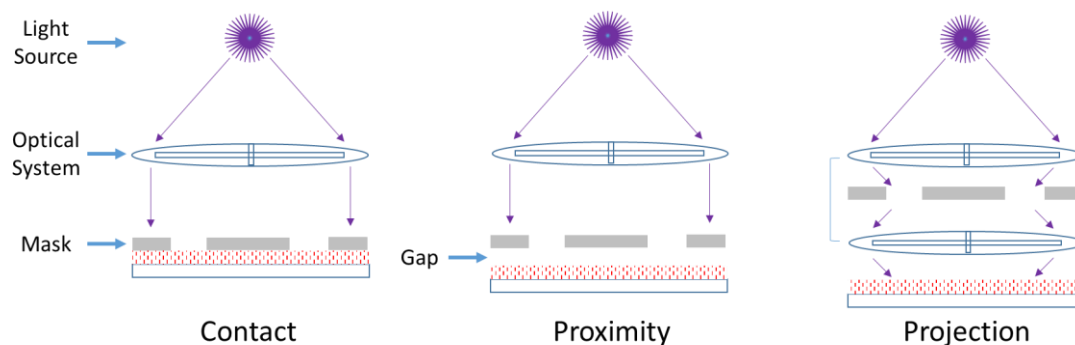


Figure 2.6 Schematic diagrams of contact/proximity photolithography and projection photolithography.

To fabrication simple structure, we use contact exposure via UV lamp shown in Figure 2.7a. Hamamatsu spot light sources employ long life, high intensity, minimize light loss and less heat [33]. Simply setting mask and substrate under the UV lamp, timing for seconds, the process is accomplished. Changing the place position, angle and motion of substrate, different complex structures are obtained from a single simple template.

In order to make multilevel structure, the patterned mask should be aligned by the designed order steps by steps with aligner. SUSS Mask Aligner (shown in Figure 2.7b) are using well established diffraction reducing illumination optics with an annular spectrum of planar waves, designed to compensate diffraction effects in contact and proximity lithography [34]. The key point of multilevel structure via aligner is the alignment of the marks on multi masks.

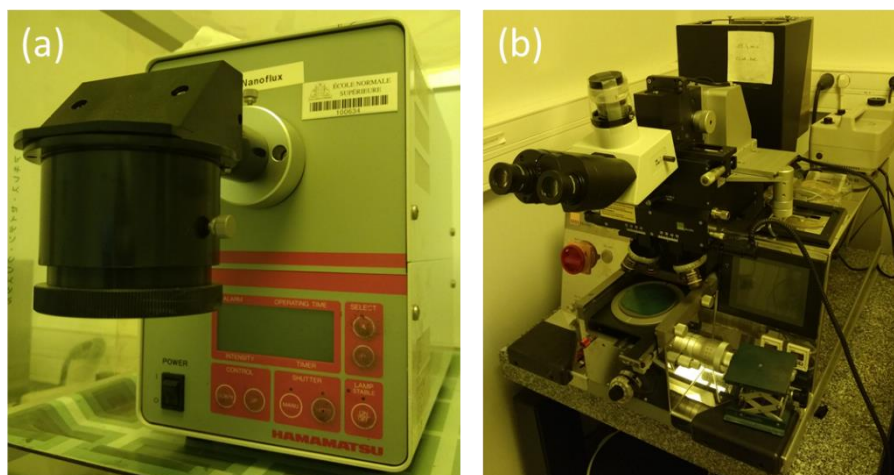


Figure 2.7 Photos of exposure devices installed in ENS laboratory. (a) UV spot light source illuminator (Lightningcure LC5, Hamamatsu). (b) Mask aligner (MJB4, MicroTec).

2.3 Pattern transfer replication

Pattern transfer replication is a fabrication method based on mold and its pattern and geometric dimensions [35]. The advantage of this method is being capable to reproduce the same structure and size and maintain the uniformed graphics with one mold. Due to the productivity, replication is able not only to reduce costs of mold manufacturing, but also improve the efficiency of complicated fabrication process. In research topics, we use mainly polymer material on photolithography mold to accomplish replication. In this way, the replica with microstructure can be transferred from photoresist into a biocompatible material, which can be characteristically modified in purpose. Therefore, the flexibility of substrates and its fabrication are enhanced.

2.3.1 Soft lithography

Soft lithography is generally a series of techniques for fabricating or replicating structures using "elastomeric stamps, molds, and conformable photomasks" [36]. The most notable feature of soft lithography is the use of soft materials, such as polydimethylsiloxane (PDMS). PDMS is one typical polymer of polysiloxanes, which

can be characterized by silicon backbone and oxygen atoms [37]. PDMS has outstanding physical properties and chemical stability, for example, optical transparency (~ 300 nm), thermal stability to 150 °C and especially low surface energy (21.6×10^{-3} J/m²) [38]. In experiments, we use PDMS of RTV 615 (T GE Toshiba Silicones Co., Ltd.) including solution A (prepolymer) and solution B (crosslinking agent). Usually, the mixture ratio of A:B is 10:1 (w/w), crosslinking for 2 h @ 80 °C. The schematic of PDMS crosslinking is shown in Figure 2.8

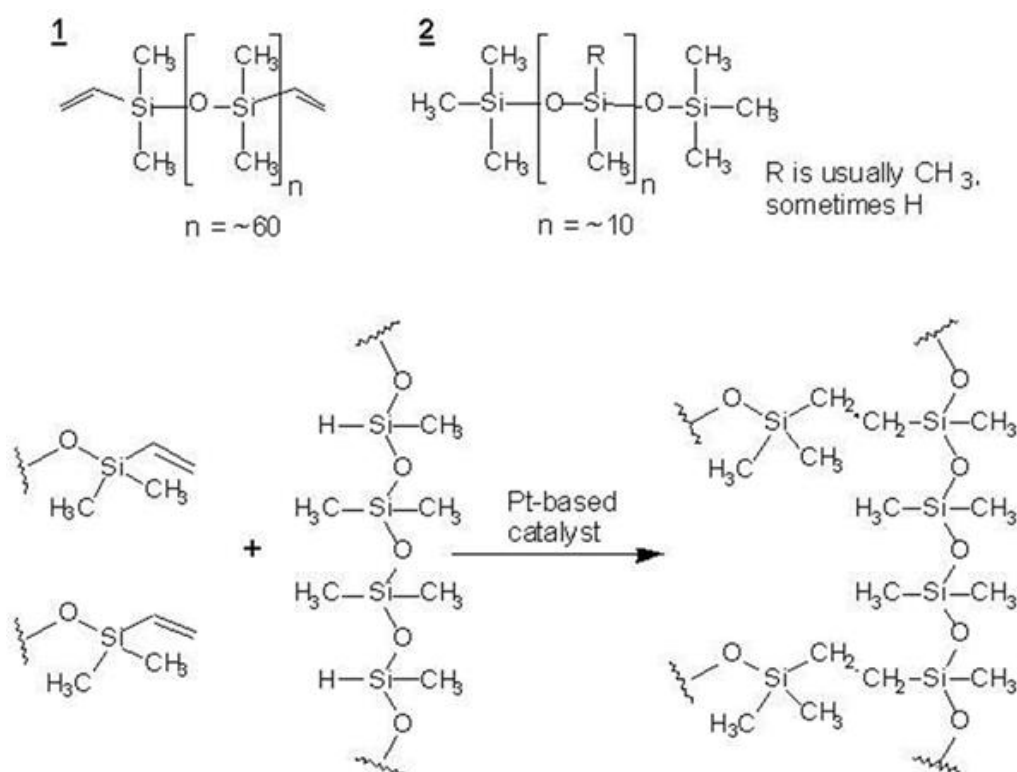


Figure 2.8 Schematic of PDMS crosslinking [39].

PDMS stamp allows easy release from templates and surfaces with a micro/nano-structure. Replication based on PDMS stamp is easier and less costly than traditional photolithography because soft lithography can replicate complex three-dimensional (3D) structures and can be applied on irregular surfaces with different materials with different chemical properties as needed, such as biological materials, polymers, colloidal materials, glass, ceramics, etc. Without the accuracy limit caused by light scattering, PDMS lithography is able to achieve feature size of 30

nm to 1 μm [40]. The equipment of soft lithography is relatively simple compared to photolithography and can be installed in wide-range laboratory. The typical fabrication process includes: replica molding, microcontact printing, micromolding in capillaries and microtransfer printing, as illustrated in Figure 2.9.

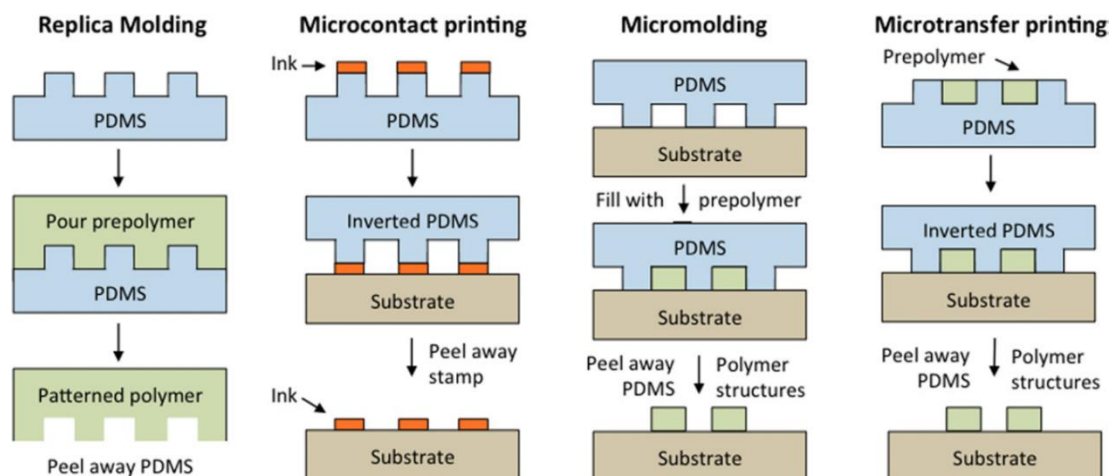


Figure 2.9 Various soft lithography techniques: replica molding, microcontact printing, micromolding in capillaries and microtransfer printing [41].

Replica molding: Using high-precision soft lithography technology to produce the original PDMS stamp, the stamp with microstructure is covered with prepolymer. The prepolymer is impregnated with the stamp and cured by UV irradiation or heating. Peeling off, complex 3D structure can be achieved by one step [42].

Microcontact printing: Microcontract printing technology is a flexible and effective method for constructing patterned self-assembled monolayers. PDMS stamp is attached to a self-assembled monolayer film for minutes. The elastomer template is covered with a thin layer of ink. Then, the ink-coated PDMS stamp is contacted to the target surface, and the contact section is transferred with thin layer of assembled ink film. Integrated into the automation device, such as drums, the technology can be printed on a massive area [43].

Micromolding in capillaries: PDMS stamp with capillary structure is placed on flat substrate (such as glass slide), and prepolymer is placed at one end of capillary structure. Due to capillary effect, the prepolymer will spontaneously fill the capillary

mold. The prepolymer must have low viscosity and be in sufficient contact with PDMS stamp. After the liquid prepolymer filling the mold completely, it is the time for curing. Based on this method, microchannel molding can be derived [44].

Microtransfer printing: Right amount of prepolymer is placed on a patterned PDMS template, then remove excess prepolymer from the surface. The PDMS template with the prepolymer is brought into close contact with flat substrate, and the prepolymer is cured by heating or UV irradiation. Peeling off the PDMS template, the patterned prepolymer structure will remain on the substrate [45].

2.3.2 Hot embossing

Hot embossing is a simple and universal processing method in the plastic manufacturing industry [46]. The main process of hot embossing is divided into three steps, as illustrated in Figure 2.10.

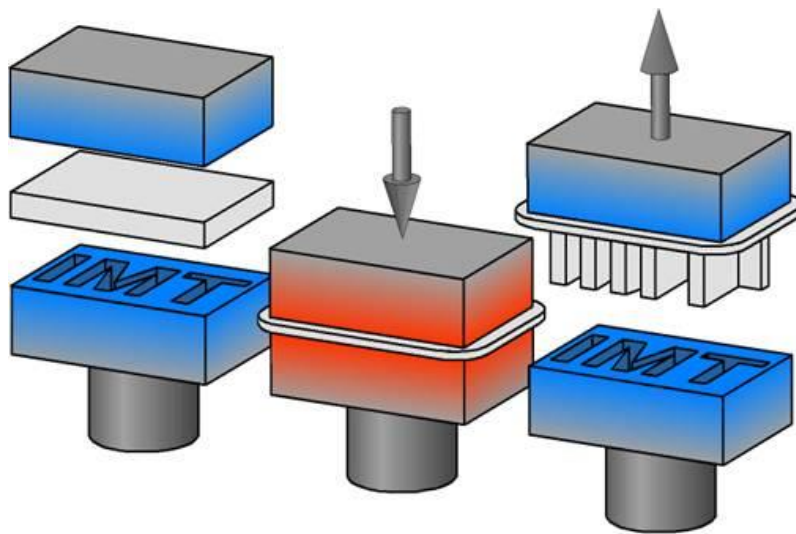


Figure 2.10 Schematic diagrams of hot embossing process [47].

The process starts with (1) placing thin polymer foil between a pair of mold with designed structure, followed by (2) fixing the molds with pressure on the heating hot plate and waiting isothermal temperature higher than the melting point of the polymer, finally (3) demolding of the component after cooling of the molds to

appropriate temperature with the pressure being maintained.

In our laboratory, hot embossing device (Film Maker, Specac eurolabo) is installed as shown in Figure 2.11. The Constant Thickness Film Maker Kit II provides temperatures of up to 300 °C to produce thin films and microstructure. The Manual Hydraulic Press GS15011 provides acceptable pressure of up to 15 KN [48].

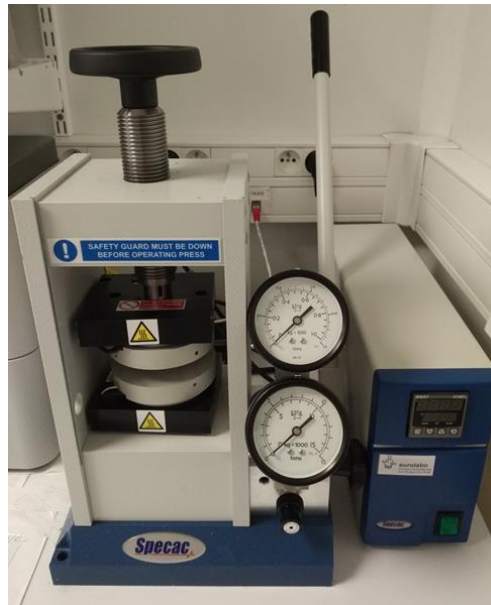


Figure 2.11 Photo of hot embossing device (Film Maker, Specac eurolabo) installed in ENS laboratory.

Thermoplastic materials for hot embossing are with two important features as following:

(1) Plastic memory

Plastic memory is the property that heated plastic turns into sticky closely to the mold. Due to this characteristic, the poorly molded product can be heated to restore the original planar shape.

(2) Thermal strength and thermal elongation

Thermal strength and thermal extension are two properties associated with plastic memory. Thermal strength is the residual intensity after the plastic is heated. Some plastic loses all the strength and become soft and sticky in heating process, but some plastic still has strong rebound. With high thermal strength, plastic can be

extended on the mold, but with low thermal strength, the plastic extension results in stress tear.

Based on the requirement of materials feature and biocompatibility, we choose two thermoplastic materials in experiments, poly lactic-co-glycolic acid (PLGA) and polycaprolactone (PCL).

PLGA is a kind of biodegradable functional macromolecule organic compound, which has good biocompatibility, non-toxic, good encapsulation and film-forming properties. It is widely used in pharmaceutical, medical materials engineering. In the United States (US), PLGA is officially included as pharmaceutical excipients into the US Pharmacopoeia (USP) through food and drug administration (FDA) certification [49]. Depending on the ratio of lactide to glycolide used for the polymerization (Figure 2.12), different forms of PLGA can be obtained, for example: PLGA 75:25 identifies a polymer consists of 75% lactic acid and 25% glycolic acid. The glass transition temperature of PLGA is between 40-60 °C [50]. Failure of the ester bond leads to the degradation of PLGA. The degree of degradation varies with the monomer ratio, the higher the proportion of glycolide, the more easily degrades [51].

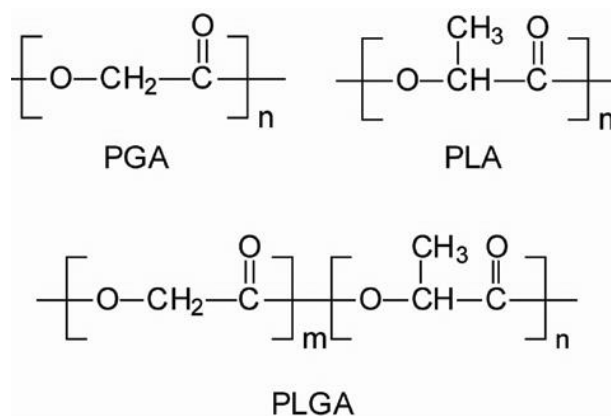


Figure 2.12 Structure schematic of PLGA [52].

PCL is polymerized polyester made from ϵ -caprolactone in the presence of catalyst (such as tetraphenyltin) as shown in Figure 2.13. The molecular weight and disproportionate degree vary with the type and amount of starting materials and the

melting point is around 60 °C. Like PLGA, PCL is officially certificated by FDA because of its (1) biocompatibility, *in-vivo* and *in-vitro*, cells can grow normally and compatibly on the PCL substrates that can be biologically degraded into CO₂ and H₂O, and (2) biodegradability, in soil and water environment, PCL substrates can be fully decomposed into CO₂ and H₂O after 6-12 months [53]. Compared to PLGA, the degradation rate of PCL is slower resulting in particularly the preparation of long term implantable devices [54].

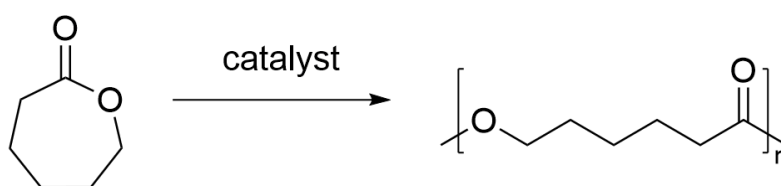


Figure 2.13 Structure schematic of PCL [53].

2.4 Surface modification

Surface treatment refers to modifying surface properties under the preservation of the original properties of materials or products, such as biocompatibility, antistatic properties, hydrophilicity/hydrophobicity, dyeing performance [55]. The methods of surface modification generally can be attributed to surface chemical reaction, surface grafting and surface composition [56].

For artificial substrates and microfluidic chip, due to size effect and large specific surface area, surface properties are particularly important. Therefore, feature surface needs treatment in many cases to achieve desired purpose including (1) weakening surface non-specific effects, (2) enhancing surface non-specific effects, (3) improving surface stability [55,56]. In our laboratory, plasma and vacuum deposition are used frequently, conveniently and stably.

2.4.1 Plasma

Plasma is an electrically neutral medium of unbound positive and negative

particles, formed by the ionization of gas-like material [57]. Plasma is a performance conductor that can be captured, moved and accelerated with a cleverly designed magnetic field. The development of plasma provides further exploration of new technologies and processes for the material, energy, information, environmental, space physics, geophysics and other scientific fields [58].

The plasma treatment is capable of treating sample surface by applying sufficient energy to thin gas for plasma state. The active components are used to achieve the purpose of cleaning and modifying [57,58].

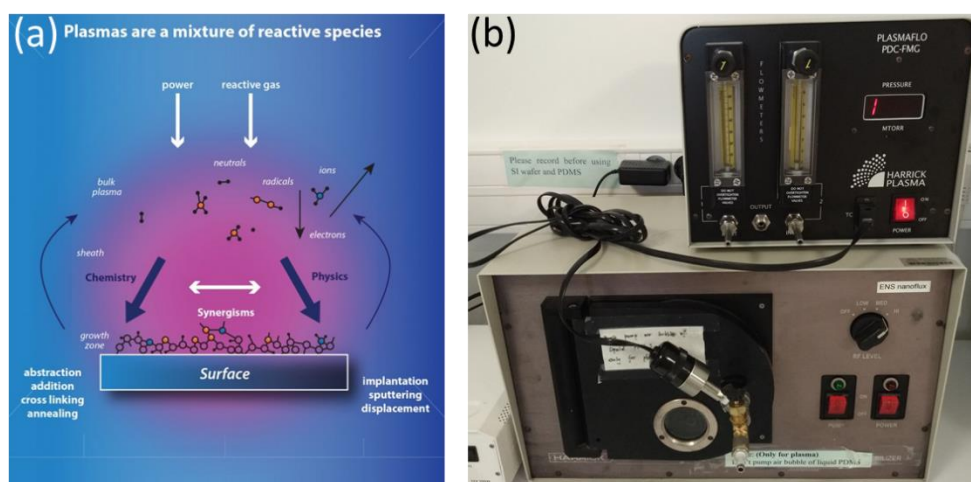


Figure 2.14 (a) Schematic diagram of plasma cleaner [59]. (b) Photo of plasma cleaner (Harrick Plasma) installed in ENS laboratory.

Plasma cleaner (schematic shown in Figure 2.14a) is a typical plasma generation device consisting of a pair of electrodes to form electric field in sealed container. When achieving the certain degree of vacuum via pump, the gas in the vacuum chamber becomes thinner and thinner (~ 300 mTorr for our lab device in Figure 2.14b), molecular spacing and molecular or ion free movement distance become longer and longer. In electric field, the molecular or ion collide to form plasma. The activity of plasma is high enough to destroy chemical bond and to cause chemical reactions.

Different plasma of supplied gas has different chemical properties, for example, oxygen plasma is with high degree of oxidation, being able to oxidize photoresist to

achieve the effect of cleaning; corrosive gas plasma is with anisotropy, being able to achieve the effect of etching. With the low temperature air plasma cleaner (Harrick Plasma), we usually process plasma treatment to polymer (PDMS, PCL, and PLGA), glass slide and photoresist sample to obtain effects as following:

(1) Bonding

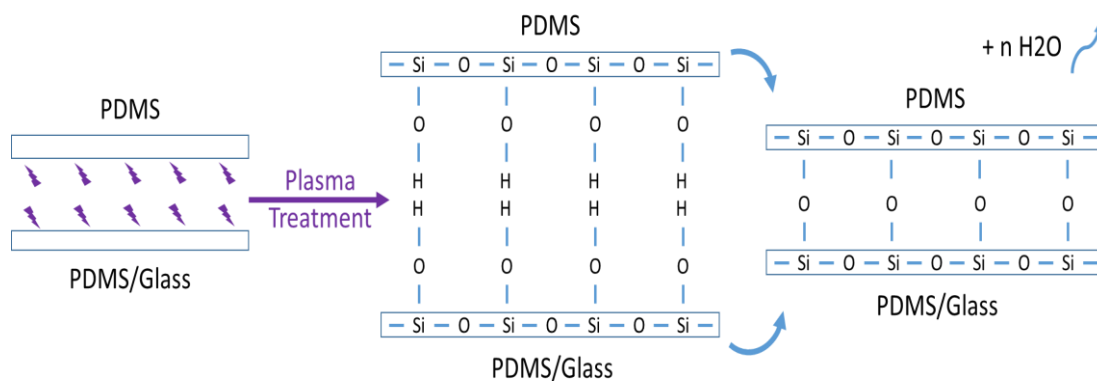


Figure 2.15 Bonding mechanism of PDMS to PDMS/glass.

PDMS bonding is widely used in the fabrication process of microfluidic chip. After peeling off from mold, cutting to appropriate size, punching through functional holes and cleaning, PDMS layer with microchannel and planar substrate (PDMS or glass) are placed in plasma cleaner. The bonding mechanism is demonstrated in Figure 2.15, plasma destroys the chemical bond of substrates, exposing the unstable SiOH- on the surface. Attaching two treated surfaces to each other, bonding surface generates significantly more stable Si-O-Si and by-product H_2O . Because plasma modifies the surface of PDMS or glass into high roughness, the treatment time should be controlled in 2 min (for ENS Lab). Bonding effect is with timeliness, after 10-15 min, the activity of treated surface becomes less, influenceable to the bonding quality and microfluidic function. After attaching and bonding, the substrates are recommended to be placed in oven for heating enhancement and stabilization for 15-30 min @ 80 °C.

(2) Hydrophilicity

For microfluidic chip, it is necessary to process microchannel to be hydrophilic

improving the fluidic wettability to the channel. For bio-engineering substrates (like cell culture), it is reasonable to increase hydrophilicity to distribute cell density during seeding and enhance the adhesion between cell and extracellular matrix (ECM). Moreover, plasma treated surface is more specified to protein (fibronectin, vitronectin) adsorption.

During plasma treatment on PDMS, the effect of hydrophilicity varies with duration, as illustrated in Figure 2.16. The most effective and powerful reacts between 0-30 s, contact angle reducing from 110° to 5°. After 1 min, the treated surface becomes rougher and rougher affecting bonding property while hydrophilicity remains in stable condition up to 1 h [60] satisfying the requirement of long-term hydrophilic experiments.

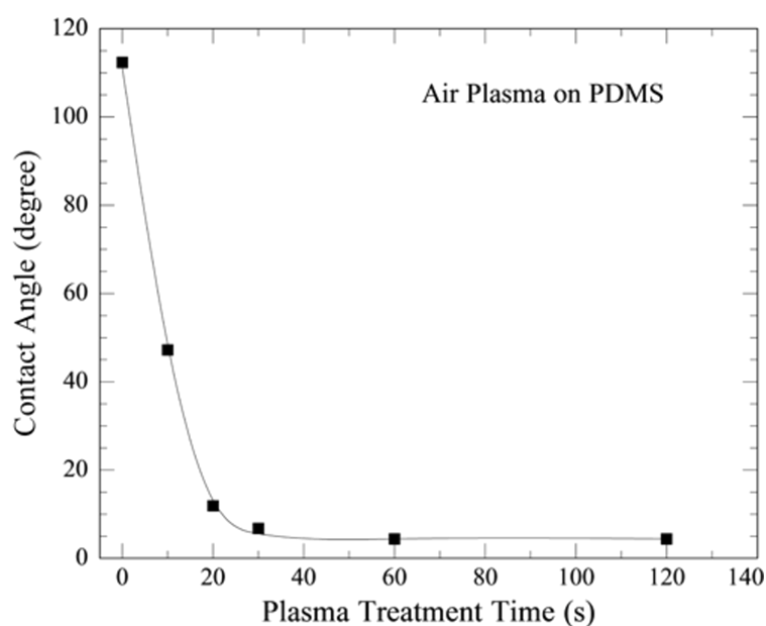


Figure 2.16 Contact angle on a blank PDMS surface as a function of air plasma treatment [60].

(3) Surface silanization

Silanization refers to the introduction of silyl group into a molecule, typically replacing active hydrogen. The treatment reduces the polarity of the compound and hydrogen bond binding in aqueous solution or gas atmosphere

Trimethylchlorosilane (TMCS) is colorless transparent liquid, soluble in benzene,

ether and perchlorethylene, volatile, flammable, toxic, and corrosive. After plasma treatment for 2 min, chemical bond is destroyed leaving OH- groups on the surface. The treated PDMS or photoresist mold is placed in a declining culture dish in which 0.5-1 ml TMCS is dropped in the bottom side waiting for volatilization and brimming the dish. For the microstructure $>10\ \mu\text{m}$, the immersion duration is 3-5 min, for $<10\ \mu\text{m}$, the duration is 30 min. The active OH- group is replaced by SiO- group with higher chemical stability and lower surface energy, which is significant to replication process [61]. The mechanism of silanization is shown in Figure 2.17.

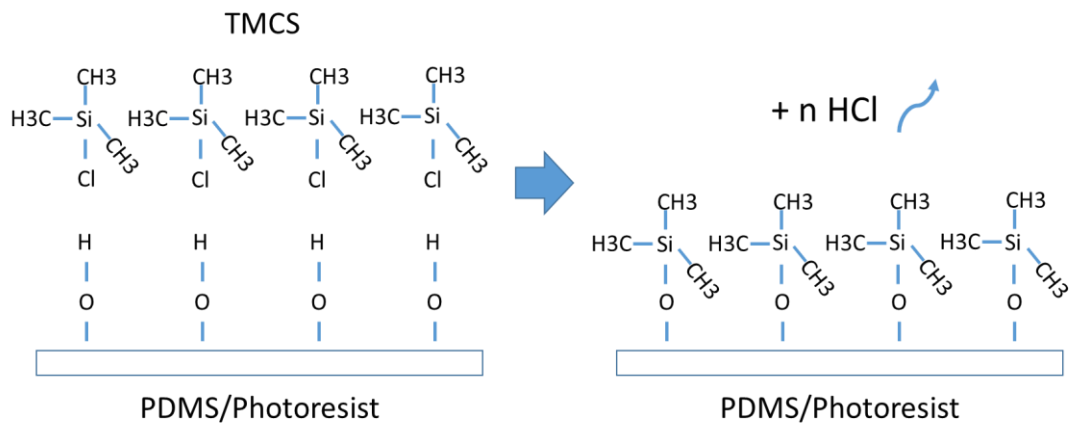


Figure 2.17 Silanization mechanism of surface treatment with TMCS.

2.4.2 Vacuum deposition

Vacuum deposition is a surface-coating technique for producing a thin film, one method of chemical vapor deposition (CVD). The technique illustrates that the solid or liquid raw material under vacuum conditions is vaporized into a gaseous atom, molecular or partially ions by specific method, for example, vacuum deposition, sputter coating, arc plasma plating, ion plating, and molecular beam epitaxy. Development to the present, the technique is applied on film deposition of metal, alloy, compound, ceramic, semiconductor and polymer [62].

We use Parylene C as polymer raw material for vacuum deposited film. The process is demonstrated in Figure 2.18. First, Parylene C dimer, in powder form, is

added to the feeding chamber and heated to 150 °C and transformed to a vapor state. Next, the dimer molecule is transported to pyrolysis furnace for heating to 690 °C in the vacuum condition of 0.5 Torr, which transform the dimer to monomer. Finally, the monomer is transformed to polymer, bonding to sample placed in the coating chamber at room temperature, and excess polymer vapor is pumped into an external liquid cold trap.

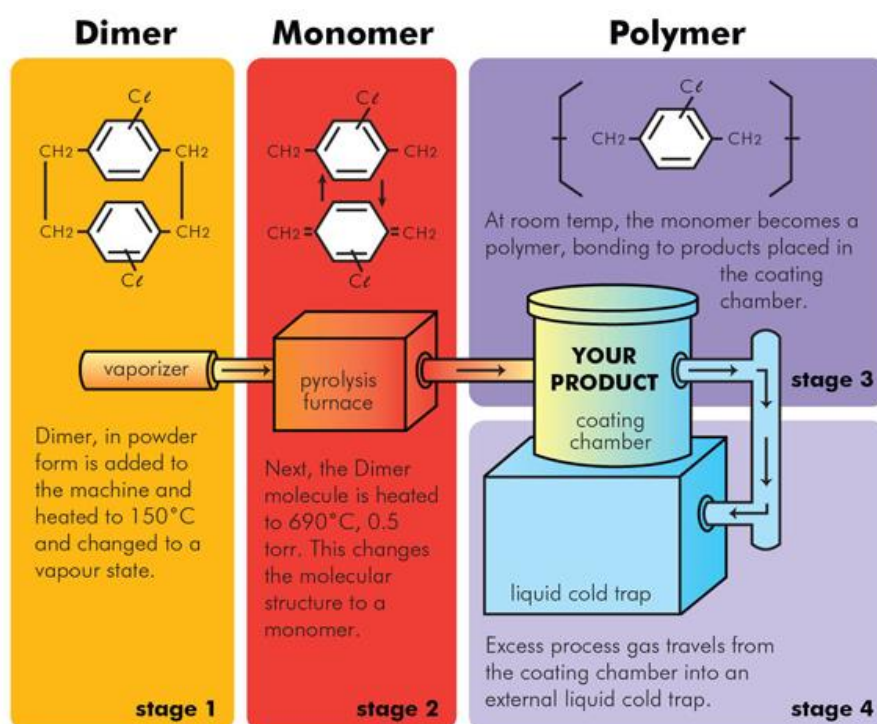


Figure 2.18 Schematic diagrams of Parylene C vacuum deposition [63].

The crystallinity of vacuum deposited film is up to 58% [64]. Parylene C film, as semi-crystalline polymer, has a particularly high resistance to small molecules, effective to anti-moisture, anti-mildew, anti-spray and protective-coating. Parylene C is deposited in the form of a dense, non-porous uniform coating film with good physical and mechanical properties, optical properties, electrical insulation, biocompatibility and corrosion resistance [65,66]. The film is not limited to the shape of the coated sample and does not affect its performance. With the equipment in ENS laboratory (shown in Figure 2.19), thin film of 1-100 μm can be easily deposited on a plurality of objects at the same time, which is particularly economical.

Particularly, vacuum deposited Parylene C film is with low surface energy of 28.64 mJ/m^2 [67], which is used in PDMS replication cast on PDMS mold as effective insulation layer [68]. This method is essential to the PDMS structure with diameter $<5 \mu\text{m}$ or aspect ratio $>5:1$.



Figure 2.19 Photo of Parylene C vacuum deposition device (PDS 2010, Specialty Coating Systems, KISCO) installed in ENS laboratory.

2.5 Electrospinning

Electrospinning technology as a classic electrohydrodynamic printing, compared to other methods, the most significant feature is the preparation of micro/nano fibers and related one-dimensional (1D) micro/nano structure in low-cost, preparation continuity, wide range of raw material, and simple process [69,70]. 1D micro/nano structures, especially micro/nano fibers, are drawing more and more attention. The electrospun structure has a long length, large specific surface area, and complex sedimentary morphology. Based on conventional process, electrospinning holds a higher application value and broader prospects on simplification, industrialization and material development, subsequently in the requirement of achieving micro/nano fibers in positioning accuracy, controllability,

stability [69].

Figure 2.20 demonstrates the basic process of electrospinning technology as: continuously dropping solution is suspended on syringe supplied via precision pump, directly below is grounded collecting device; a high-voltage power source is applied between syringe and collector. In electric field, the surface charge is aggregated and the droplet is deformed gradually (as the Taylor cone [71]). Finally, solution overcomes surface tension and other restrictions, forming charged cylindrical jet and depositing on the collector.

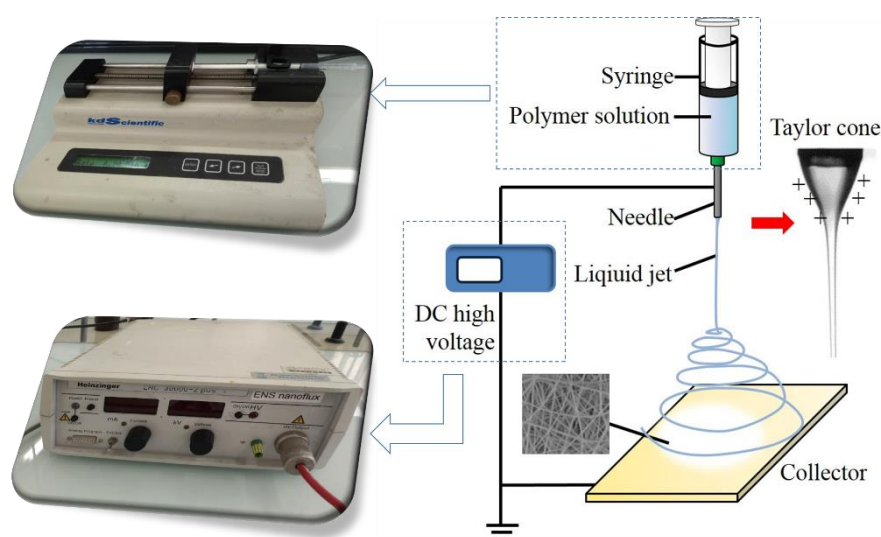


Figure 2.20 Schematic diagram of conventional electrospinning [72], and photos of devices installed in ENS laboratory, including precision syringe pump (KDS-100-CE, KDSscientific) and direct current high voltage source (LNC 30000-2pos, Heinzinger).

During electrospinning, solution is volatilized, due to change of the acceleration, fibers are gradually formed, elongated, tapered and finally deposited on the collecting device in the solid state. The morphology of final deposited fiber depends mainly on: (1) intrinsic properties of the solution, such as viscosity, concentration, elasticity, polarity, surface tension, etc. [73] (2) external conditions influenced on electric field strength, such as the distance between syringe and collector, environmental temperature and humidity, electrical conductivity etc. [74].

The improvement of electrospinning device, especially collection device, is

essential to effectively obtain fiber in arrangement. The improvement methods are mainly divided into the transformation and the motion of the collecting device.

The transformation of collection device mainly refers to the certain arrangement of grounded collector. The specific electrode arrangement results in the direction arrangement of electric field and electrostatic force, which is critical to the orderly deposition of the fibers on collector. As shown in Figure 2.21, collector consists of two parallel electrodes, with 1-mm gap, depositing aligned fiber in a certain degree. The fiber deposited on collector is precisely perpendicular to the direction of collector gap, which automatically adjusts in the direction of electrostatic force [75]. Based on the same principle, MEMS electrodes that gold-sputtered quartz substrate can control the direction of fiber deposition in time-varying order [76].

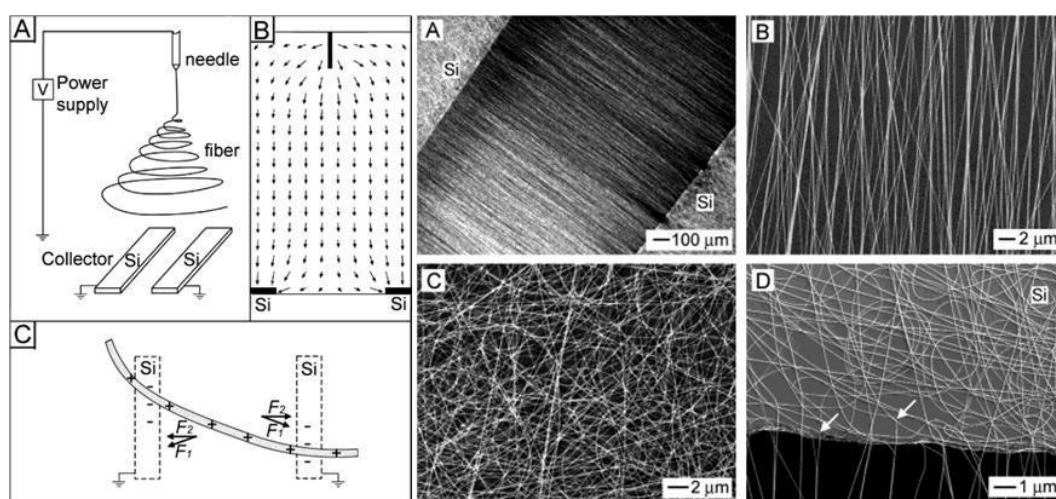


Figure 2.21 Schematic illustration of the setup for electrospinning to generate uniaxially aligned nanofibers and SEM images of uniaxially aligned nanofibers made of polyvinylpyrrolidone (PVP) [75].

The orderly layered fiber is convenient to be integrated in the plated MEMS device and micro/nano hybrid structure. In addition, the shape of the electrode, especially the appearance characteristics (such as the diameter of circular electrode, the angle of triangular electrode, etc.) affects correspondingly the shape of fiber deposition [77]. On the tip of the electrode, the fiber deposition tends to be more symmetrical, which proves the contribution of electric field influences the arrangement of fiber

deposition.

Furtherly improved the electrode from 2D plate 3D weaved wire, fiber deposits on the gap between of adjacent wire electrodes orderly and the timing-control expands the secondary structure of single fiber [78]. Combined with the concept of molds in traditional mechanics, the shape of collection device is regarded as the basis of deposited morphology, ultra-fine fibers stacks to 3D tube in centimeter scale, which is used in medical and biological tissue engineering [79]. With the similar static method, 3D micro-coil and micro-spring structure are obtained [80,81].

The difference between electrospinning and conventional spinning is that electrospinning undertakes electrostatic force as tensile force during fiber deposition, rather than by mechanical force. However, the addition of new force, especially mechanical force, can change the effects of electric field force on jet, inducing the fiber direction in design. The relative movement (translation or rotation) between syringe and collector results in the motion trajectory interacting with the motion trajectory of jet and eventually forcing fiber deposition in arrangement.

A double-helix rope-like microstructure is prepared via novel equipment that a rotating tip is connected to negative electrode and two parallel nozzles are connected to positive [82]. Two fibers ejected from the nozzles converges on the tip. The similar multi-helix structure, increasing the amount of nozzle and replacing the tip with plate extended to double helix to multiple automatically [83]. The helix structure can be applied to artificial muscle, optoelectronic devices, sensors, catalytic, textiles, filters, reinforced composites, tissue engineering, drug delivery, etc. [84].

Inducing the relative movement between collector and syringe means inducing the mechanical force generated from tensile force and viscous force, especially in consideration of polymer solution. Rotating device (such as plate [85], cage [86] and drum [87]) is introduced into electrospinning process resulting in fiber morphology with the diameter of 100-300 nm, the length of hundreds of microns, and self-assembly in parallel spacing.

Collector with rotating drum and cage, as shown in Figure 2.22, effectively

increases deposition area and uniform the contribution of electric field, compared to single turntable edge. With multi jet, the productivity of fiber increases with the increasing of nozzle amount and collector area [88]. With single jet, the position of fiber deposition can be controlled with sequential deposition effect [89]. The aligned fiber structures can be applied and integrated in electrical, optical and mechanical devices [90].

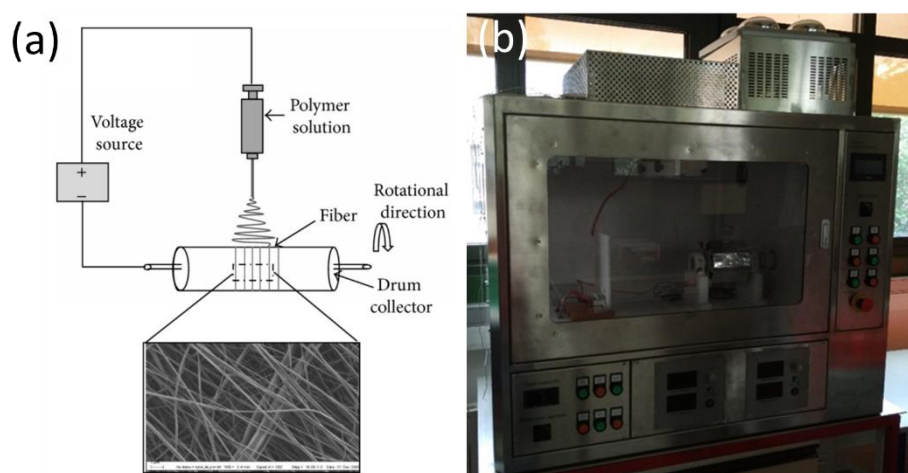


Figure 2.22 (a) Schematic diagram of rotating drum collector and deposited fiber [91]. (b) Photo of electrospinning device with rotating drum collector (TL-Pro-BM, Tongli) installed in ENS laboratory.

The final requirement of aligned even patterned fiber deposition results from the improvement of collection device. No matter what the shape, or what the motion of collector, the key factor is to ensure that the instantaneous movement of jet deposition on collector matching with the jet trajectory in electric field. Therefore, high speed is necessary in the motion of collector usually. However, Figure 2.23a illustrates a novel method to prepare aligned even patterned fiber in relatively low speed (100-200 mm/s). which is referred to near field electrospinning [92]. The basic principle of mentioned method is to shorten the distance between syringe and collector ($h < 3\text{mm}$), reducing the whipping of jet and utilizing the stably straight jet process.

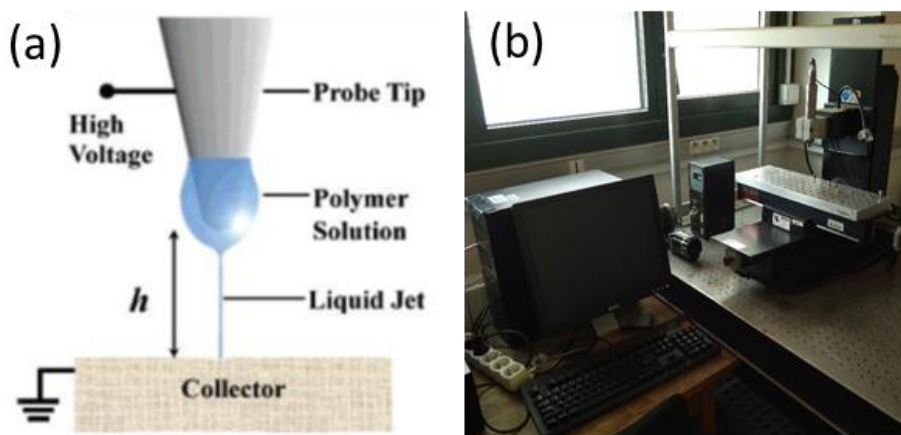


Figure 2.23 (a) Schematic diagram of near field electrospinning [92]. (b) Photo of precision motion platform (Mini-Mill/GX, Minitech Machinery) installed in ENS laboratory.

Near field electrospinning is with direct-writing feature, which is similar to the *in-situ* property of lithography but based on micro/nano fiber. First, the direct-writing characteristic is manifested in the controllability of deposition. Micro/nano fiber can be deposited on a pre-designed position, such as microchannel [93] or micropost [94]. In addition, the direct writing characteristic is embodied in the possibility of deposition pattern, especially on the centimeter-scale collector with continuous deposition of nanofibers by pattern array [95]. After fabrication of patterned nanofibers, nanogenerators based on polyvinylidene fluoride (PVDF) piezoelectric nanofibers can be achieved efficiently to convert mechanical deformation into electrical energy output within low cost [96].

Patterned fiber array is convenient and controllable with post-processing like self-assembly and MEMS techniques. Microdot array is prepared from the wetting and evaporating of ribbon-like fiber, which is based on Plateau-Rayleigh instability [97]. Nanochannel is fabricated via nanofiber etched as sacrificial layer template, in the integration of conventional MEMS processing and near field electrospinning [98].

With cell-level uniform nanofiber array, multi-deposition of continuous, complex and controllable structure realizes the application of biological scaffolds and cell culture mechanisms.

2.6 Summary

We presented micro- and nano-fabrication techniques used in this thesis. UV photolithography, pattern transfer replication (soft lithography and hot embossing), surface modification (plasma cleaner and vacuum deposition), and electrospinning. All these widely used techniques are low cost, satisfied accuracy and high throughput, which can be combined to obtain more complex surface pattern and structural fabrication with different materials. The micro- and nano-fabrication techniques retain potential for many applications in life science, and particularly in cell biology for in vitro cell culture and tissues engineering. We apply the techniques in the following chapters for studies of cell-ECM interaction.

References

1. D. Natelson, *Nanostructures and nanotechnology*. (Cambridge University Press, 2015).
2. D. Qin, Y. Xia, J. A. Rogers, R. J. Jackman, X.-M. Zhao, G. M. Whitesides, in *Microsystem technology in chemistry and life science*. (Springer, 1998), pp. 1-20.
3. S. Kang, *Micro/Nano Replication: Processes and Applications*. (John Wiley & Sons, 2012).
4. M. H. Li, P. Keller, J. Yang, P. A. Albouy, An artificial muscle with lamellar structure based on a nematic triblock copolymer. *Advanced materials* **16**, 1922-1925 (2004).
5. L. Hu, S. Dai, J. Weng, S. Xiao, Y. Sui, Y. Huang, S. Chen, F. Kong, X. Pan, L. Liang, Microstructure design of nanoporous TiO₂ photoelectrodes for dye-sensitized solar cell modules. *The Journal of Physical Chemistry B* **111**, 358-362 (2007).
6. S. Semancik, R. Cavicchi, M. Wheeler, J. Tiffany, G. Poirier, R. Walton, J. Suehle, B. Panchapakesan, D. DeVoe, Microhotplate platforms for chemical sensor research. *Sensors and Actuators B: Chemical* **77**, 579-591 (2001).
7. I. Hartl, X. Li, C. Chudoba, R. Ghanta, T. Ko, J. Fujimoto, J. Ranka, R. Windeler, Ultrahigh-resolution optical coherence tomography using continuum generation in an air-silica microstructure optical fiber. *Optics letters* **26**, 608-610 (2001).
8. J. Castillo-León, W. Svendsen, *Micro and nanofabrication using self-assembled biological nanostructures*. (William Andrew, 2014).
9. N. Xi, M. Zhang, G. Li, *Modeling and Control for Micro/Nano Devices*

and Systems. (CRC Press, 2013).

10. Z. L. Wang, Nanostructures of zinc oxide. *Materials today* **7**, 26-33 (2004).

11. S. Thomas, R. Shanks, J. Joy, *Micro-and Nanostructured Polymer Systems: From Synthesis to Applications*. (Apple Academic Press, 2015).

12. C. Yan, D. Xue, General, spontaneous ion replacement reaction for the synthesis of micro-and nanostructured metal oxides. *The Journal of Physical Chemistry B* **110**, 1581-1586 (2006).

13. V. M. Cepak, J. C. Hulteen, G. Che, K. B. Jirage, B. B. Lakshmi, E. R. Fisher, C. R. Martin, H. Yoneyama, Chemical strategies for template syntheses of composite micro-and nanostructures. *Chemistry of materials* **9**, 1065-1067 (1997).

14. D. W. Richerson, *Modern ceramic engineering: properties, processing, and use in design*. (CRC press, 2005).

15. Z. Xu, L. M. Chen, G. Yang, C. H. Huang, J. Hou, Y. Wu, G. Li, C. S. Hsu, Y. Yang, Vertical phase separation in Poly (3 - hexylthiophene): fullerene derivative blends and its advantage for inverted structure solar cells. *Advanced Functional Materials* **19**, 1227-1234 (2009).

16. G. M. Whitesides, B. Grzybowski, Self-assembly at all scales. *Science* **295**, 2418-2421 (2002).

17. Z. Fu, J. Xu, Y. Zhang, Z. Fan, Chain structure and mechanical properties of polyethylene/polypropylene/poly (ethylene - co - propylene) in - reactor alloys synthesized with a spherical Ziegler - Natta catalyst by gas - phase polymerization. *Journal of applied polymer science* **97**, 640-647 (2005).

18. J. Zhang, H. Zou, Q. Qing, Y. Yang, Q. Li, Z. Liu, X. Guo, Z. Du, Effect of chemical oxidation on the structure of single-walled carbon nanotubes. *The Journal of Physical Chemistry B* **107**, 3712-3718 (2003).

19. W. M. Moreau, *Semiconductor lithography: principles, practices, and materials*. (Springer Science & Business Media, 2012).

20. R. Infuehr, N. Pucher, C. Heller, H. Lichtenegger, R. Liska, V. Schmidt, L. Kuna, A. Haase, J. Stampfl, Functional polymers by two-photon 3D lithography. *Applied Surface Science* **254**, 836-840 (2007).

21. P. R. Gray, R. G. Meyer, *Analysis and design of analog integrated circuits*. (John Wiley & Sons, Inc., 1990).

22. W. L. Brown, T. Venkatesan, A. Wagner, Ion beam lithography. *Nuclear Instruments and Methods in Physics Research* **191**, 157-168 (1981).

23. A. Heuberger, X - ray lithography. *Journal of Vacuum Science & Technology B: Microelectronics Processing and Phenomena* **6**, 107-121 (1988).

24. R. Pease, Electron beam lithography. *Contemporary Physics* **22**, 265-290 (1981).

25. H. J. Levinson, *Lithography process control*. (SPIE Press, 1999), vol. 28.

26. C. W. Gwyn, R. Stulen, D. Sweeney, D. Attwood, Extreme ultraviolet

lithography. *Journal of Vacuum Science & Technology B: Microelectronics and Nanometer Structures Processing, Measurement, and Phenomena* **16**, 3142-3149 (1998).

27. W. Hinsberg, F. Houle, J. Hoffnagle, M. Sanchez, G. Wallraff, M. Morrison, S. Frank, Deep-ultraviolet interferometric lithography as a tool for assessment of chemically amplified photoresist performance. *Journal of Vacuum Science & Technology B: Microelectronics and Nanometer Structures Processing, Measurement, and Phenomena* **16**, 3689-3694 (1998).

28. H. J. Levinson, *Principles of lithography*. (SPIE press, 2005), vol. 146.

29. http://www.microchemicals.com/products/photoresists/az_40xt.html.

30. http://www.microchemicals.com/products/photoresists/az_9260.html.

31. <http://www.microchem.com/Prod-SU82000.htm>.

32. <http://www.microchem.com/Prod-SU83000.htm>.

33. <http://www.hamamatsu.com/jp/en/product/category/1001/3017/index.html>.

34. <https://www.suss.com/en/products-solutions/mask-aligner/mjb4>.

35. Y. Xia, G. M. Whitesides, Soft lithography. *Annual review of materials science* **28**, 153-184 (1998).

36. J. A. Rogers, R. G. Nuzzo, Recent progress in soft lithography. *Materials today* **8**, 50-56 (2005).

37. V. Chandrasekhar, *Inorganic and organometallic polymers*. (Springer, 2005).

38. C. Martos, F. Rubio, J. Rubio, J. Oteo, Surface energy of silica-TEOS-PDMS ormosils. *Journal of sol-gel science and technology* **20**, 197-210 (2001).

39. A. Esteves, J. Brokken-Zijp, J. Lavèn, H. Huinink, N. Reuvers, M. Van, G. De With, Influence of cross-linker concentration on the cross-linking of PDMS and the network structures formed. *Polymer* **50**, 3955-3966 (2009).

40. S. R. Quake, A. Scherer, From micro-to nanofabrication with soft materials. *Science* **290**, 1536-1540 (2000).

41. N. C. Lindquist, P. Nagpal, K. M. McPeak, D. J. Norris, S.-H. Oh, Engineering metallic nanostructures for plasmonics and nanophotonics. *Reports on Progress in Physics* **75**, 036501 (2012).

42. Y. Xia, E. Kim, X.-M. Zhao, J. A. Rogers, Complex optical surfaces formed by replica molding against elastomeric masters. *Science* **273**, 347 (1996).

43. R. J. Jackman, J. L. Wilbur, G. M. Whitesides, Fabrication of submicrometer features on curved substrates by microcontact printing. *Science* **269**, 664 (1995).

44. E. Kim, Y. Xia, G. M. Whitesides, Micromolding in capillaries: applications in materials science. *Journal of the American Chemical Society*

118, 5722-5731 (1996).

45. J. Kim, S.-H. Bae, H.-G. Lim, Micro transfer printing on cellulose electro-active paper. *Smart materials and structures* **15**, 889 (2006).

46. M. Worgull, *Hot embossing: theory and technology of microreplication*. (William Andrew, 2009).

47. L. Peng, Y. Deng, P. Yi, X. Lai, Micro hot embossing of thermoplastic polymers: a review. *Journal of Micromechanics and Microengineering* **24**, 013001 (2013).

48. <http://www.specac.com/products/laboratory-hydraulic-press/manual-hydraulic-press/507>.

49. H. K. Makadia, S. J. Siegel, Poly lactic-co-glycolic acid (PLGA) as biodegradable controlled drug delivery carrier. *Polymers* **3**, 1377-1397 (2011).

50. M. Dorta, O. Munguía, M. Llabres, Effects of polymerization variables on PLGA properties: molecular weight, composition and chain structure. *International Journal of Pharmaceutics* **100**, 9-14 (1993).

51. N. Samadi, A. Abbadessa, A. Di Stefano, C. Van Nostrum, T. Vermonden, S. Rahimian, E. Teunissen, M. Van Steenberghe, M. Amidi, W. Hennink, The effect of lauryl capping group on protein release and degradation of poly (d, l-lactic-co-glycolic acid) particles. *Journal of Controlled Release* **172**, 436-443 (2013).

52. <http://www.drug-dev.com/Main/Back-Issues/PLGAPEG-Block-Copolymers-for-Drug-Formulations-406.aspx>.

53. M. Labet, W. Thielemans, Synthesis of polycaprolactone: a review. *Chemical Society reviews* **38**, 3484-3504 (2009).

54. N. Hiraishi, J. Y. Yau, R. J. Loushine, S. R. Armstrong, R. N. Weller, N. M. King, D. H. Pashley, F. R. Tay, Susceptibility of a polycaprolactone-based root canal-filling material to degradation. III. turbidimetric evaluation of enzymatic hydrolysis. *Journal of endodontics* **33**, 952-956 (2007).

55. M. Gürsoy, M. Karaman, *Surface Treatments for Biological, Chemical and Physical Applications*. (John Wiley & Sons, 2016).

56. S. Ebnesajjad, C. Ebnesajjad, *Surface treatment of materials for adhesive bonding*. (William Andrew, 2013).

57. M. Thomas, K. L. Mittal, *Atmospheric Pressure Plasma Treatment of Polymers: Relevance to Adhesion*. (John Wiley & Sons, 2013).

58. N. Inagaki, *Plasma surface modification and plasma polymerization*. (CRC Press, 1996).

59. <https://plasmamatreatment.co.uk/henniker-plasma-technology/plasma-surface-technology/plasma-technology-what-is-plasma-treatment/plasma-cleaning/>.

60. H. Zheng, M. F. Rubner, P. T. Hammond, Particle assembly on patterned “plus/minus” polyelectrolyte surfaces via polymer-on-polymer stamping. *Langmuir : the ACS journal of surfaces and colloids* **18**, 4505-4510

(2002).

61. C. Priest, P. J. Gruner, E. J. Szili, S. A. Al-Bataineh, J. W. Bradley, J. Ralston, D. A. Steele, R. D. Short, Microplasma patterning of bonded microchannels using high-precision “injected” electrodes. *Lab on a chip* **11**, 541-544 (2011).
62. H. O. Pierson, *Handbook of chemical vapor deposition: principles, technology and applications*. (William Andrew, 1999).
63. <http://www.cwst.cc/parylene-coatings.html>.
64. J. M. Hsu, L. Rieth, S. Kammer, M. Orthner, F. Solzbacher, Effect of thermal and deposition processes on surface morphology, crystallinity, and adhesion of Parylene-C. *Sensors and Materials* **20**, 87-102 (2008).
65. N. B. C. Engineers, *The Complete Book on Medical Plastics*. (NIIR Project Consultancy Services, 2006).
66. C. Hassler, R. P. von Metzen, P. Ruther, T. Stieglitz, Characterization of parylene C as an encapsulation material for implanted neural prostheses. *Journal of Biomedical Materials Research Part B: Applied Biomaterials* **93**, 266-274 (2010).
67. T. Y. Chang, V. G. Yadav, S. De Leo, A. Mohedas, B. Rajalingam, C.-L. Chen, S. Selvarasah, M. R. Dokmeci, A. Khademhosseini, Cell and protein compatibility of parylene-C surfaces. *Langmuir : the ACS journal of surfaces and colloids* **23**, 11718-11725 (2007).
68. Y. S. Shin, K. Cho, S. H. Lim, S. Chung, S.-J. Park, C. Chung, D.-C. Han, J. K. Chang, PDMS-based micro PCR chip with parylene coating. *Journal of Micromechanics and Microengineering* **13**, 768 (2003).
69. J. H. Wendorff, S. Agarwal, A. Greiner, *Electrospinning: materials, processing, and applications*. (John Wiley & Sons, 2012).
70. G. Mitchell, *Electrospinning: principles, practice and possibilities*. (Royal Society of Chemistry, 2015).
71. G. Taylor, in *Proceedings of the Royal Society of London A: Mathematical, Physical and Engineering Sciences*. (The Royal Society, 1964), vol. 280, pp. 383-397.
72. <http://www.weistron.com/tech-abc/electrospinning-tech/>.
73. S. Theron, E. Zussman, A. Yarin, Experimental investigation of the governing parameters in the electrospinning of polymer solutions. *Polymer* **45**, 2017-2030 (2004).
74. J. Doshi, D. H. Reneker, Electrospinning process and applications of electrospun fibers. *Journal of electrostatics* **35**, 151-160 (1995).
75. D. Li, Y. Wang, Y. Xia, Electrospinning of polymeric and ceramic nanofibers as uniaxially aligned arrays. *Nano letters* **3**, 1167-1171 (2003).
76. D. Li, Y. Wang, Y. Xia, Electrospinning nanofibers as uniaxially aligned arrays and layer - by - layer stacked films. *Advanced materials* **16**, 361-366 (2004).
77. D. Li, G. Ouyang, J. T. McCann, Y. Xia, Collecting electrospun nanofibers with patterned electrodes. *Nano letters* **5**, 913-916 (2005).

78. D. Zhang, J. Chang, Patterning of electrospun fibers using electroconductive templates. *Advanced materials* **19**, 3664-3667 (2007).
79. D. Zhang, J. Chang, Electrospinning of three-dimensional nanofibrous tubes with controllable architectures. *Nano letters* **8**, 3283-3287 (2008).
80. G. Chang, J. Shen, Helical nanoribbons fabricated by electrospinning. *Macromolecular Materials and Engineering* **296**, 1071-1074 (2011).
81. G. Chang, G. Song, J. Yang, R. Huang, A. Kozinda, J. Shen, Morphology control of nanohelix by electrospinning. *Applied Physics Letters* **101**, 263505 (2012).
82. G. Chang, J. Shen, Fabrication of Microropes via Bi - electrospinning with a Rotating Needle Collector. *Macromolecular rapid communications* **31**, 2151-2154 (2010).
83. D. Paneva, N. Manolova, I. Rashkov, H. Penchev, M. Mihai, E. Dragan, Self-organization of fibers into yarns during electrospinning of polycation/polyanion polyelectrolyte pairs. *Digest Journal of Nanomaterials and Biostructures* **5**, 811-819 (2010).
84. B. Sun, Y. Long, H. Zhang, M. Li, J. Duvail, X. Jiang, H. Yin, Advances in three-dimensional nanofibrous macrostructures via electrospinning. *Progress in Polymer Science* **39**, 862-890 (2014).
85. A. Theron, E. Zussman, A. Yarin, Electrostatic field-assisted alignment of electrospun nanofibres. *Nanotechnology* **12**, 384 (2001).
86. L. Wannatong, A. Sirivat, P. Supaphol, Effects of solvents on electrospun polymeric fibers: preliminary study on polystyrene. *Polymer International* **53**, 1851-1859 (2004).
87. P. Katta, M. Alessandro, R. Ramsier, G. Chase, Continuous electrospinning of aligned polymer nanofibers onto a wire drum collector. *Nano letters* **4**, 2215-2218 (2004).
88. J. Kameoka, H. Craighead, Fabrication of oriented polymeric nanofibers on planar surfaces by electrospinning. *Applied Physics Letters* **83**, 371-373 (2003).
89. J. Kameoka, R. Orth, Y. Yang, D. Czaplewski, R. Mathers, G. W. Coates, H. Craighead, A scanning tip electrospinning source for deposition of oriented nanofibres. *Nanotechnology* **14**, 1124 (2003).
90. Y. Xia, P. Yang, Y. Sun, Y. Wu, B. Mayers, B. Gates, Y. Yin, F. Kim, H. Yan, One - dimensional nanostructures: synthesis, characterization, and applications. *Advanced materials* **15**, 353-389 (2003).
91. H. Junoh, J. Jaafar, M. N. A. M. Norddin, A. F. Ismail, M. H. D. Othman, M. A. Rahman, N. Yusof, W. N. W. Salleh, H. Ilbeygi, A review on the fabrication of electrospun polymer electrolyte membrane for direct methanol fuel cell. *Journal of Nanomaterials* **2015**, 4 (2015).
92. D. Sun, C. Chang, S. Li, L. Lin, Near-field electrospinning. *Nano letters* **6**, 839-842 (2006).
93. G. Zheng, W. Li, X. Wang, D. Wu, D. Sun, L. Lin, Precision deposition

of a nanofibre by near-field electrospinning. *Journal of Physics D: Applied Physics* **43**, 415501 (2010).

94. G. S. Bisht, G. Canton, A. Mirsepassi, L. Kulinsky, S. Oh, D. Dunn-Rankin, M. J. Madou, Controlled continuous patterning of polymeric nanofibers on three-dimensional substrates using low-voltage near-field electrospinning. *Nano letters* **11**, 1831-1837 (2011).

95. C. Chang, K. Limkraisiri, L. Lin, Continuous near-field electrospinning for large area deposition of orderly nanofiber patterns. *Applied Physics Letters* **93**, 123111 (2008).

96. C. Chang, V. H. Tran, J. Wang, Y.-K. Fuh, L. Lin, Direct-write piezoelectric polymeric nanogenerator with high energy conversion efficiency. *Nano letters* **10**, 726-731 (2010).

97. Y. Huang, X. Wang, Y. Duan, N. Bu, Z. Yin, Controllable self-organization of colloid microarrays based on finite length effects of electrospun ribbons. *Soft Matter* **8**, 8302-8311 (2012).

98. X. Wang, G. Zheng, L. Xu, W. Cheng, B. Xu, Y. Huang, D. Sun, Fabrication of nanochannels via near-field electrospinning. *Applied Physics A* **108**, 825-828 (2012).

Chapter 3 Cell culture on micropillar arrays of different heights

In this chapter, we describe the fabrication of micropillar arrays of different heights by replication of a mold pattern into different materials. Firstly, micro-pillars were produced by photolithography into a thin layer of SU8 resist. Then, they were replicated into polydimethylsiloxane (PDMS) by soft lithography. Afterward, the negative tone PDMS replica is used as the mold to cast again PDMS or emboss a thermoplastic polymer, i.e., poly-caprolactone (PCL). Finally, the pillar arrays are used as substrates to evaluate the surface stiffness dependency of cell culture using NIH 3T3 cells.

3.1 Introduction

Cell adhesion and cell migration are important in cell biology and biomedical studies [1,2]. For in-vitro studies, the mechanical stiffness of the substrate should be adjusted to the requested cell functions [3,4]. Ideally, the mechanical properties of the fabricated substrate should be as close as possible to that of the extracellular matrix (ECM) of the in-vivo cellular microenvironment [5,6]. Therefore, it is interesting to study cell adhesion and cell migration behaviors on artificial ECM of different stiffness. Previously, most of the investigations were performed on substrates with uniform stiffness, with or without surface patterning, which cannot be used to evaluate the cell migration behaviors [7-9]. Here, we aimed at observation of preferential cell adhesion on artificial ECM area of different stiffness. Such an observation should be necessary for clearer understanding of cell adhesion, spreading and migration. We have chosen an artificial ECM made of micropillar arrays with different heights which can be easily fabricated and used for quantitative assessment.

Micropillar arrays are now frequently used to obtain substrate of different stiffness and to determine the mechanical properties of the cells by changing the height of the pillars and measuring the deflection of the pillars [10,11]. Previous studies also demonstrated that cells are very sensitive to the stiffness of the pillars which is determined by both the material Young's module and the size/height of the

pillars. However, such a sensibility is clearly cell-type and material stiffness range dependent. The challenge was then fabricating the micropillar arrays of different height using materials of different Young's modules and demonstrating the preferential cell attachment on micropillars with more appropriate stiffness.

3.2 Micropillar arrays with different height

3.2.1 Fabrication of mold by one-step backside exposure

To achieve a better pattern resolution of the pillars, we used a backside exposure. Compared to proximity exposure and proximity exposure, the advantages of this method are simple, unnecessary for high-end equipment and high resolution ($\sim 1 \mu\text{m}$) [12]. Due to the full contact between photoresist layer and chromium (Cr) mask, the diffraction effect resulted from contact gap is avoided. The interference elimination could keep the fabricated feature in high degree of reduction, especially in sharp edge.

After Cr mask with designed pattern was obtained, we clean the mask with Isopropanol in Ultrasonic for 3 min, subsequently rinsed with Isopropanol and dried with Nitrogen. Then the mask was fully prepared for photolithography process. The fabrication flow of photolithography process is shown in Figure 3.1.

First, the planar mask was placed on the spin-coater fixed by vacuum pump. 1-2 ml of SU8-3010 photoresist was dropped on the clean surface of mask. Second, the photoresist was spread around uniformly under low spin velocity to cover the whole pattern area. Then, with the increasing of spin velocity, excess SU8 was spun out of the mask to the wall of spin-coater chamber, only $\sim 10 \mu\text{m}$ thickness remained. After soft bake for 1 min @ $65 \text{ }^\circ\text{C}$ and 3 min @ $95 \text{ }^\circ\text{C}$, the resist-coated mask was reversed, Cr pattern covering the photoresist layer, and exposed by UV lamp of power density 12.7 mJ/cm^2 for 13 s. Afterwards, the mask was reversed again and post-baked for 1 min @ $65 \text{ }^\circ\text{C}$ and 2 min @ $95 \text{ }^\circ\text{C}$. Finally, waiting for cooling down, the resist-coated mask was immersed in SU8 developer solvent for 2 min with gentle agitation and

rinsed with Isopropanol, dried with Nitrogen.

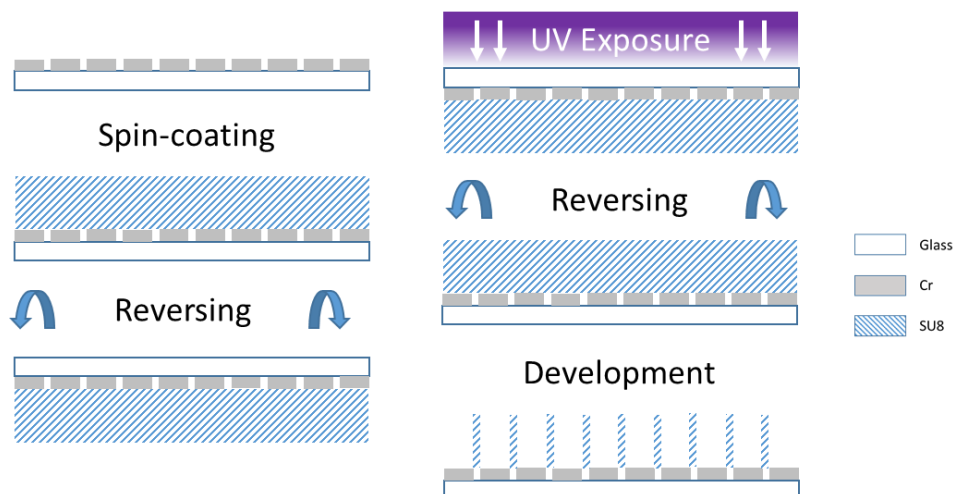


Figure 3.1 Schematic diagrams of the fabrication process of photoresist mold with one-step backside exposure.

The final photoresist mold is shown in Figure 3.2. The micropillar was fabricated with height of 10 μm , diameter 2 μm and period 5 μm . Because the dimension of pillars was fine, it was possible to peel off the micro structure during following replication. Therefore, we carried out some treatment to prove the adhesiveness between micropillars and planar Cr mask. (1) Before SU8-3010 spin-coating, we pre-spin-coated one layer of SU8-2002 ($\sim 2 \mu\text{m}$) as adhesive layer, maintaining the integrity of photoresist and increasing the contact area between photoresist and Cr mask. (2) After photolithography, we placed the final device on a hot plate for hard bake for 30 min @ 170 $^{\circ}\text{C}$, which was useful for annealing any surface cracks that may be evident after development and ensured SU8 properties stable in actual use.

For different micropillar array with different height, we chose different process parameter for different photoresist, as shown in Table 3.1.

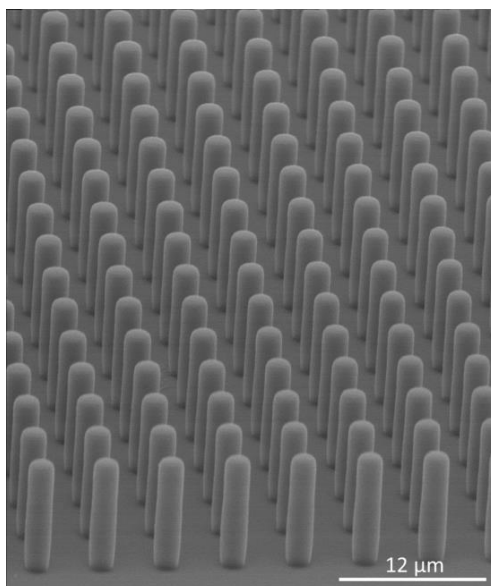


Figure 3.2 SEM image of photoresist mold with 10- μm height, 2- μm diameter and 5- μm period.

Thickness	Photoresist Type	Low Spin Velocity (Acceleration)	High Spin Velocity (Acceleration)
2 μm	SU8-2002	500 rpm (100 rpm/s)	3000 rpm (300 rpm/s)
5 μm	SU8-3005	500 rpm (100 rpm/s)	3000 rpm (300 rpm/s)
10 μm	SU8-3010	500 rpm (100 rpm/s)	3000 rpm (300 rpm/s)
Thickness	Photoresist Type	Soft Bake Duration @ 65 °C and @ 95 °C	Post Bake Duration @ 65 °C and @ 95 °C
2 μm	SU8-2002	1 min and 1 min	1 min and 2 min
5 μm	SU8-3005	1 min and 2 min	1 min and 1 min
10 μm	SU8-3010	1 min and 3 min	1 min and 2 min
Thickness	Photoresist Type	Exposure Duration	Development Duration
2 μm	SU8-2002	9 s	1 min
5 μm	SU8-3005	11 s	1.5 min
10 μm	SU8-3010	13 s	2 min

Table 3.1 Parameter summary for different height micropillar array fabricated with different type of photoresist.

3.2.2 PDMS replica of micropillar array

Since the photoresist mold was positive micropillar array, two-step replication (Figure 3.3a) was necessary to obtain final PDMS replica. First, negative replica with microholes was fabricated by casting a mixture of PDMS pre-polymer and crosslink agent at ratio of 10:1 on the photoresist mold. After PDMS casting and curing for 2 h @ 80 °C, the PDMS layer was peeled-off. Second, positive replica with micropillars was fabricated by casting PDMS mixture on the PDMS negative mold using the same casting process. The final micropillar replica with low, medium and high dimension is shown in Figure 3.3b-g.

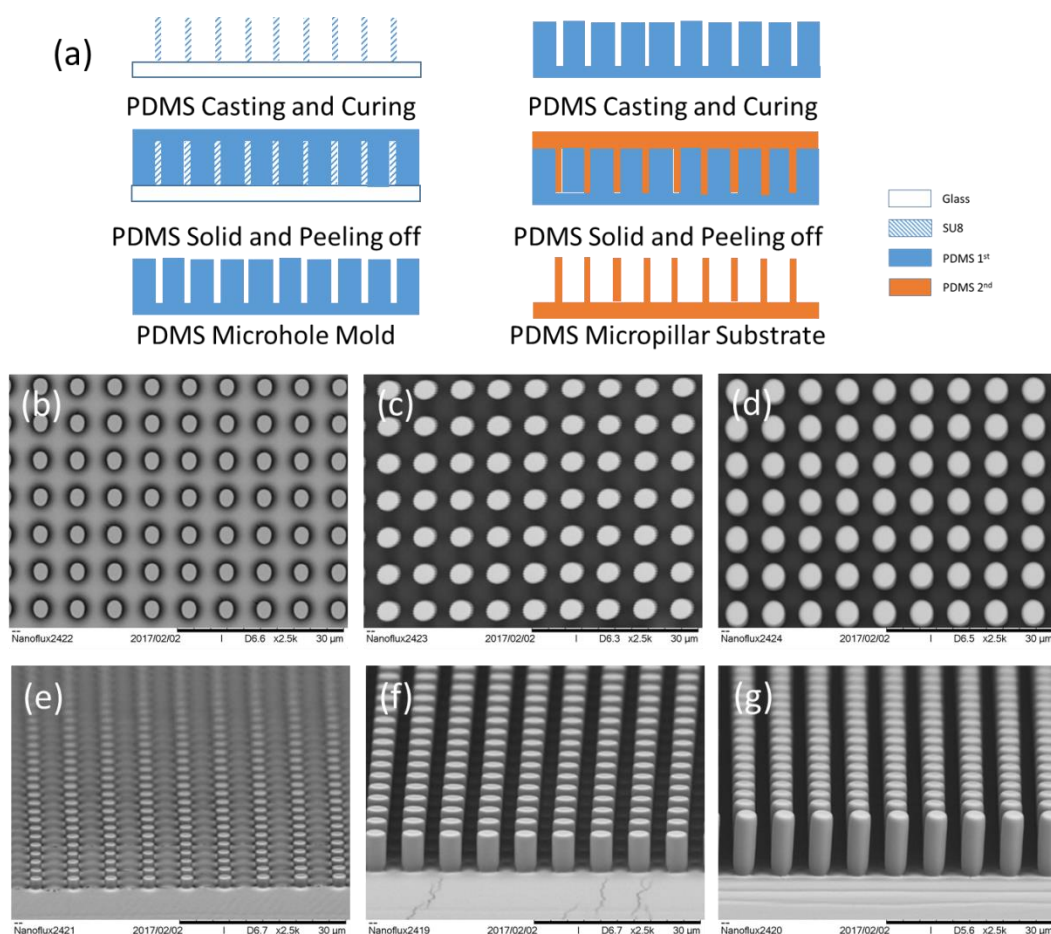


Figure 3.3 PDMS replica of micropillars, (a) schematic diagrams of the replication process with PDMS soft-lithography, SEM images of (b)(e) short micropillar replica, (c)(f) medium micropillar replica, (d)(g) high micropillar replica.

Dimension distribution of PDMS micropillar resulted from the measurement of SEM photos. As illustrated in Figure 3.4, the height of three arrays was 1.6, 6.6 and 10.7 μm respectively. The period was approximately same with 6.8 μm . The diameter of short array was 2.5 μm , compared to 4.0 μm of medium and high array. The error was mainly caused by the fabrication of Cr mask and photolithography, considering the SU8-2000 series was different from SU8-3000, and thickness of photoresist layer might result to overdose of UV exposure.

To ensure the successful replication, surface treatment was operated to the positive and negative mold for peel-off separation. (1) Before 1st casting of PDMS, the photoresist positive mold treated in oxygen plasma for 2 min and then in TMSC vapor for 30 min. (2) Before 2nd PDMS casting, 0.2- μm thick Parylene C was deposited on the PDMS negative mold via vacuum deposition system.

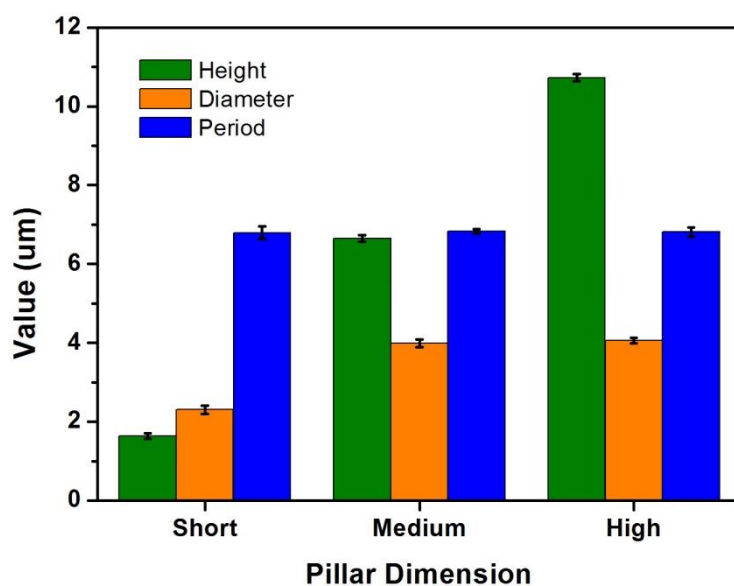


Figure 3.4 Dimension distribution of short, medium and high PDMS micropillar replica in parameter of height, diameter and period respectively.

Comparing to other fabrication processes [13-15], the present two-step technique is advantageous to achieve high quality PDMS pillar arrays, since it is relatively easy to obtain high resolution, high density and high aspect ratio SU8 pillars. It is also relatively easy to peel-off the PDMS layer from the fabricated resist pillars

and then replicate the same feature of the master due to the relative low Young's modulus of PDMS. Notably, it was convenient to use PDMS mold for 2nd replication of pillar structures with different types of polymers such as PDMS, PCL, Poly Lactic-co-Glycolic Acid (PLGA), T-Flex and Parylene C [12,16].

Flat PDMS was equivalent to the bulk material Young's modulus ~ 1 MPa [17], while PDMS micropillar substrates varied the equivalent Young's modulus with the parameter of micropillar itself. Here, the distance between pillars was significantly smaller than that of the cell initial sizes so that cells could stay on the top and spread over several pillars. To assess such effective stiffness, we might calculate the spring constant (k) of a single pillar.

$$k = \frac{3}{4} \pi E \frac{r^4}{H^3} \dots\dots\dots(3.1)$$

Where E is the Young modulus of the material, r and H are the radius and height of the pillars, respectively [18]. Then, the equivalent Young's modulus (E_e) of the surface composed of dense pillar arrays could be obtained via spring constant [19]. The equivalent Young's modulus was calculated and shown in Table 3.2.

$$E_e = \frac{9k}{4\pi r} \dots\dots\dots(3.2)$$

	r (μm)	H (μm)	E_e (KPa)
Short	1.3	1.6	905.1
Medium	2.0	6.6	47.0
High	2.0	10.7	11.0

Table 3.2 Equivalent Young's modulus of different PDMS micropillar substrates various with parameter of radius and height.

3.2.3 Cell culture on PDMS substrates

Substrate preparation

Before cell seeding, the substrates and PDMS stamps (pre-polymer:crosslinker = 30:1) were sterilized under mild cell-culture UV lamp for 30 min.

Then Fibronectin (FN) diluted in deionized water in 50 $\mu\text{g}/\text{ml}$ was dropped on soft PDMS stamps for 1 h in laminar flow hood. The excess FN solution was pipetted out of the stamps and dried in the air flow.

Afterwards, to ensure the hydrophilic behavior of substrates for cell-liquid spread and the adsorption of FN, the samples were surface-treated with plasma cleaner for 7 min.

Next, the stamps were placed on the micropillar samples gently. Ensuring the full contact between the stamps and the samples, the sample covered with the stamps were treated for 1 h in laminar flow hood at room temperature.

Finally, the stamps were carefully peeled off from the samples with micropillar standing for following cell seeding.

Cell seeding, adhesion and spread

NIH 3T3 cells were incubated (37 °C, 5% CO₂) in culture medium Dulbecco's Modified Eagle Medium (DMEM) with 10% Fetal Bovine Serum (FBS) and 1% Penicillin/Streptomycin (P/S). Before seeding, the spent medium was aspirated out and Dulbecco's Phosphate-Buffered Saline (DPBS) was added to rinse the vessel twice. Aspirating DPBS, we added Trypsin covering the vessel for 3 min in incubator (37 °C, 5% CO₂). When cells started to separate and round up, we aspirated Trypsin and add 1 ml fresh medium to remove cells from the vessel by gently squirting and pipetting the medium until the cell colonies broke up to single cell. After cell counting, centrifuging, density adjusting, cell suspension in 5×10^4 cells ml⁻¹ was added on the prepared substrates, as shown in Figure 3.5.

As shown in Figure 3.5, from + 1 h to + 12 h, the cell density of five kinds of samples approximately remained the same. During this period, the major function of

cells was adhering to the substrates and sensing environment. The adhesion appeared in + 1 h, with the enlargement of cell spread area and shape deformation. Because substrates were surface treated via plasma, compared to glass, PDMS was preferable to adsorbed FN resulting in better character for cell adhesion [20]. Cells on flat PDMS and 1.6 μm micropillars spread in fusiform from +1 h to +6, while cells on 6.8 μm and 10.7 μm micropillars contract in sphere. Even with the micropost structure, short pillars could not block the cells from elongating to bottom for more contact area. Medium pillars could support cells for 6 h. From +12 h, cells started to spread to the bottom. Cells stayed on high pillar until proliferation.

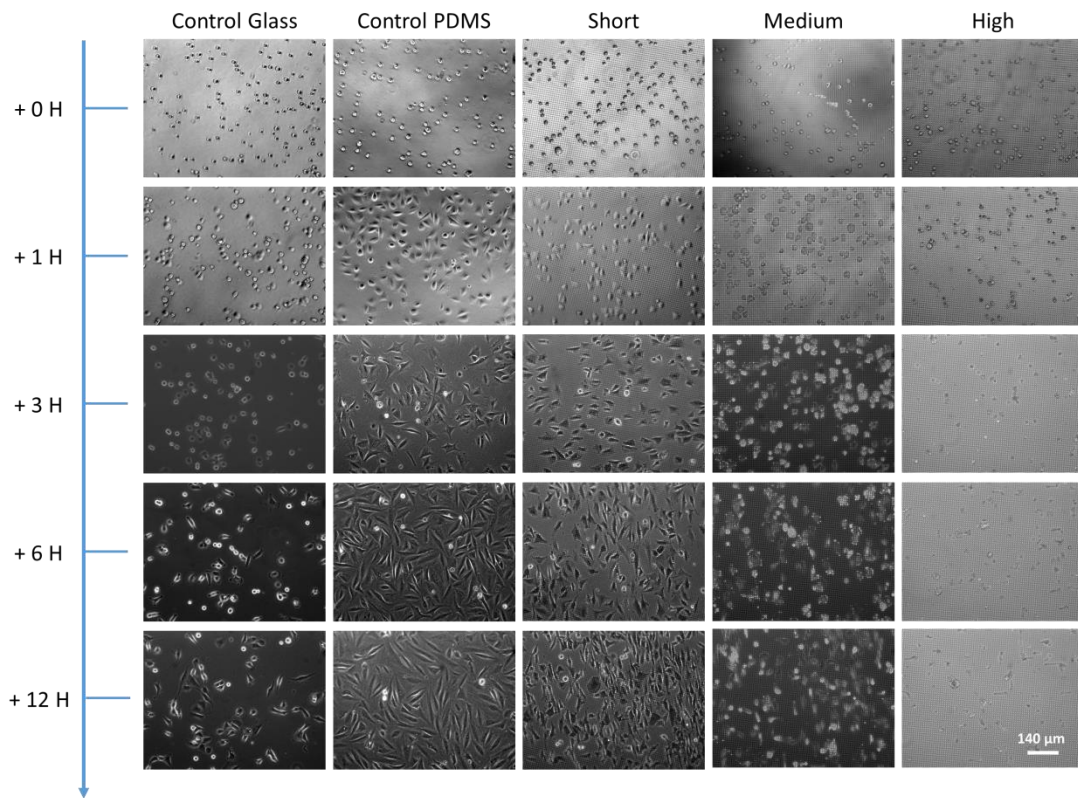


Figure 3.5 Microscope photographs of NIH-3T3 cells cultured on substrates of glass slide, flat PDMS, and PDMS micropillar array with different height.

Cell area varied with the culture duration as illustrated in Figure 3.6. On the high limit of substrates (glass slide for poor coating, high pillar for Low E_e), spread area of cells continuously increased in 0-12 h. On the other three types of substrates, cell

area increased to the certain level then adjusted to decrease. It is noteworthy that five samples could be divided to two group according to the final cell spread area, one was the flat substrates (glass and PDMS) with the area of $2000 \mu\text{m}^2$, another was the micropillar substrates (short, medium and high) with the area of 1000, 1200 and $1400 \mu\text{m}^2$, respectively, higher E_e , relatively larger spread area. Meanwhile, after 12 h incubation, cells on micropillars was with more uniform spread area (low standard deviation), compared to the flat substrates. It is observed that cells started to sense the culture substrates for following proliferation and alignment after 12 h.

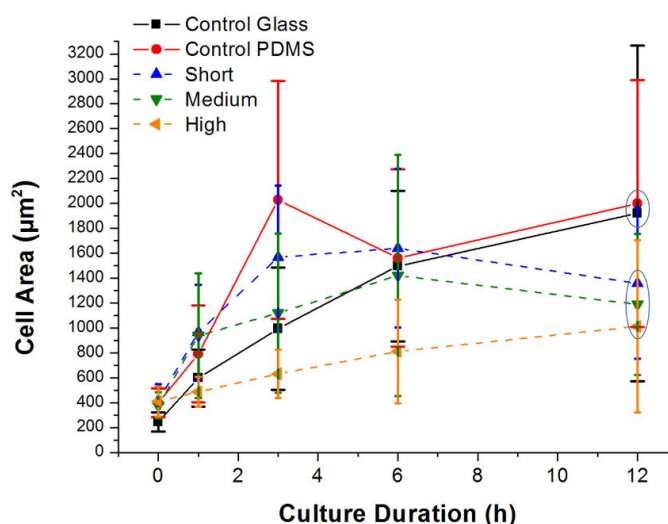


Figure 3.6 Cell area in the variation as a function of culture duration on substrates of glass slide, flat PDMS, and PDMS micropillar array with different height.

Cell proliferation and alignment

Figure 3.7 shows the typical fluorescent microscopy images of 3T3 cell cultured on substrates at Day 1 and Day 3, respectively. At Day 1, the cells were in spread shape on the flat substrates and in elongated shape on the micropillar array. With incubation time, the number of cells increased and appeared cell-cell interaction inevitably at Day 3. From the fluorescent photos, cytoskeleton was guided in the certain direction, which showed the indication at culture +12 h. On the flat substrates, cells spread randomly due to the isotropic surface. After all the space was covered up, cells arranged without guidance and laminated. On the contrary, cells on

PDMS micropillars elongated and aligned. Furthermore, large amount of cell could influence such elongation and alignment, especially on the short and medium pillar array. Even on the high pillar array, cells initially contracted at Day 1 but elongated after self-adaption and interaction. The difference of cell behaviors between spread and elongation influenced the cell proliferation and alignment in data statistics.

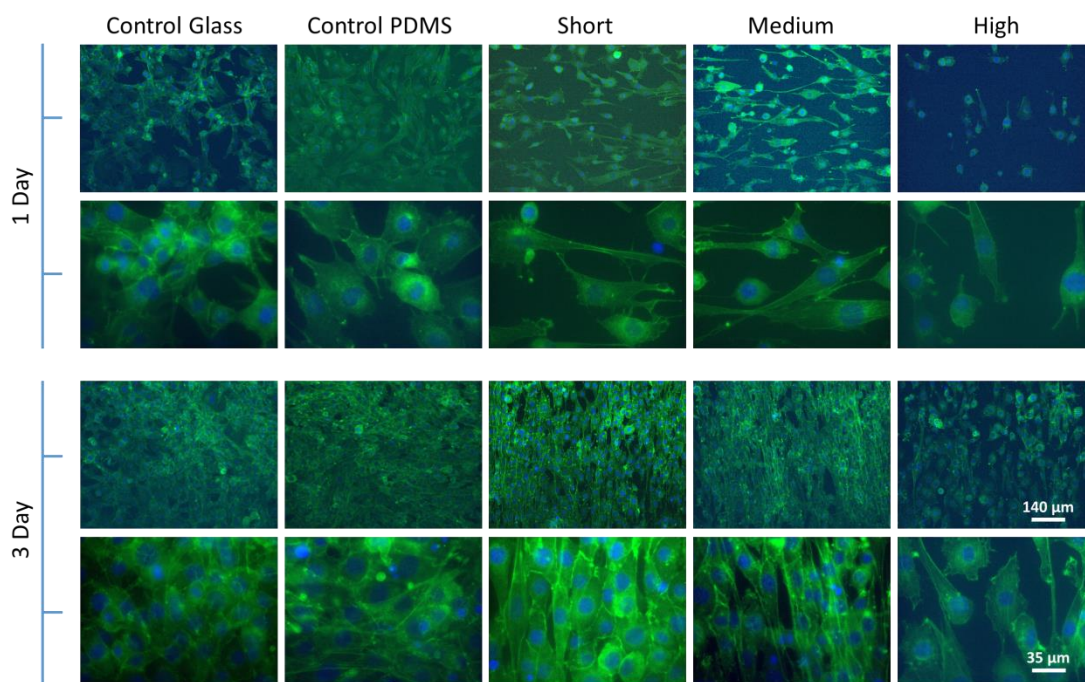


Figure 3.7 Fluorescent images of NIH-3T3 cells cultured on substrates of glass slide, flat PDMS, and PDMS micropillar array with different height. Cell nuclei (DAPI: blue) and actin cytoskeletal networks (Alexa Fluor 488 phalloidin: green).

Cell density on all substrates increased as demonstrated in Figure 3.8a. With the cell proliferation, the error of cell density distribution increased (larger standard deviation) from sample to sample. Planar substrates performed better proliferation than micropillar array, the cell density raised from 200 to 750-800 mm^{-2} . Resulting from the influence of microstructure, the cell density of 1.6 μm and 6.6 μm micropillars rose from 200 to 650 mm^{-2} , 13%-18% less than the planar substrates. Dramatical reduction of E_e with addition of height, cell density on 10.7 μm micropillars climbed from 200 to 500 mm^{-2} , 33%-37% less than planar substrates and 23% less than short and medium pillar substrates.

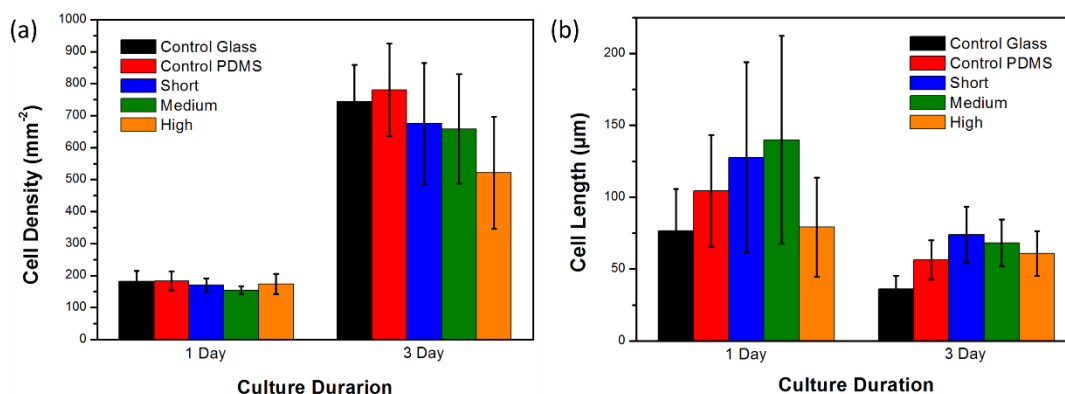


Figure 3.8 Distribution of NIH-3T3 cells (a) density and (b) length cultured on substrates of glass slide, flat PDMS, and PDMS micropillar array with different height.

On the contrary, cell length on all substrates decreased as shown in Figure 3.8b. From cell seeding to incubation 1 day, cell length on all substrates elongated with cell area increasing because there was enough space for spreading. At Day 1, the length of cells was significantly large, practically cells on the medium pillar array, the maximum length could be 250 μm and the average length could be 130 μm. Cell length on short pillar array was relatively large with average 125 μm. For flat PDMS control, cells spread large area with medium length of average 100 μm. The length of average was 75 μm on the glass slide and high pillar array, 42% shorter than the medium pillar array. After 3-day incubation, cells re-arranged and shortened, for flat glass slide, cell length dropped from 75 μm to 40 μm (47%), flat PDMS from 100 μm to 55 μm (45%), short pillar array from 125 μm to 75 μm (40%), medium pillar array from 130 μm to 70 μm (46%). Because of the short initial length, cells on high pillar array nearly did not change (from 75 μm to 65 μm). All 3-day cultured cells were with more uniform length compared to 1-day condition (smaller standard deviation).

3.2.4 PCL replica of micropillar array

Different from PDMS replication, PCL replica was fabricated by hot embossing on negative PDMS mold, as shown in Figure 3.9a. First, to obtain PCL sheet, raw materials pellet was clipped between two glass slides and placed between a pair of hot plates for 2-3 min @ 90 °C. After cooling down, PCL sheet attached on the glass

slide could be leveled off with blade and transferred on the surface of PDMS microhole mold. Then, PDMS mold covered with PCL sheet was set in hot embossing equipment, preheating for 10 min @ 90 °C. PCL sheet melted down completely, and moderated pressure was applied between two hot plates to press melted PCL fill the microholes. Finally, cooling down to room temperature in pressure condition, PCL sheet solidified with micropillar structure and was easy to be peeled off. The final micropillar replica with low, medium and high dimension is shown in Figure 3.9b-g.

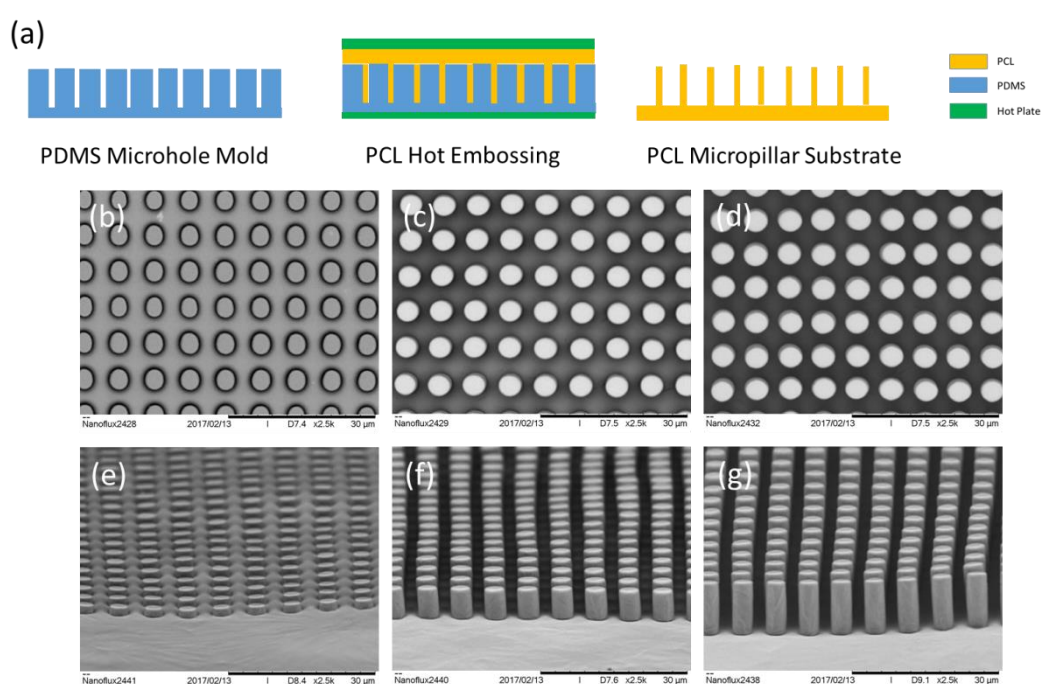


Figure 3.9 PCL replica of micropillars, (a) schematic diagrams of the replication process with PCL hot embossing, SEM images of (b)(e) short micropillar replica, (c)(f) medium micropillar replica, (d)(g) high micropillar replica.

Dimension distribution of PCL micropillar resulted from the measurement of SEM photos. As illustrated in Figure 3.10, the height of three arrays was 1.8, 6.3 and 11.2 μm respectively. The period was approximately same with 7.0 μm . The diameter of short array was 3.7 μm , compared to 4.3 μm of medium and high array. The difference between PCL pillar and PDMS pillar might be caused by the pressure applied during hot embossing. Because of the elasticity of PDMS, slight deformation of mold appeared, compared to the no-external-pressure casting.

Flat PCL was equivalent to the bulk material Young's modulus ~ 500 MPa [21], while PCL micropillar substrates varied the equivalent Young's modulus with the parameter of micropillar. To assess such effective stiffness, we could calculate k and E_e of a single pillar. The equivalent Young's modulus was calculated and shown in Table 3.3.

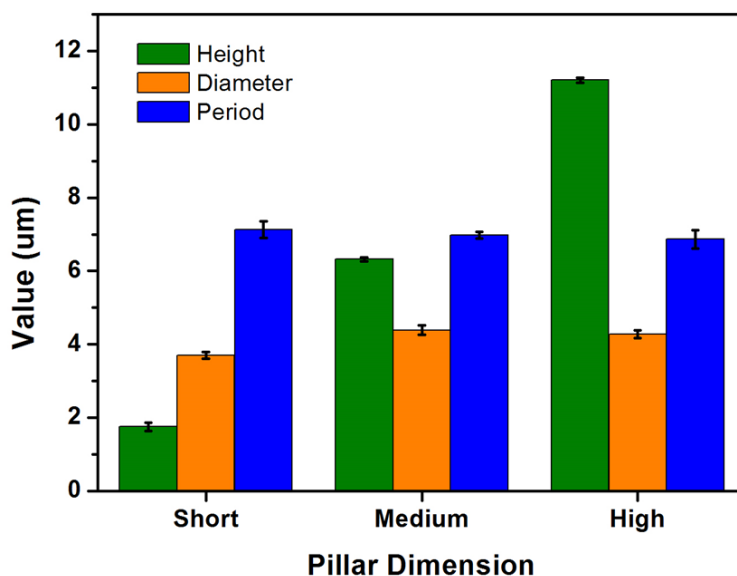


Figure 3.10 Dimension distribution of short, medium and high PCL micropillar replica in parameter of height, diameter and period respectively.

	r (μm)	H (μm)	E_e (MPa)
Short	1.9	1.8	551.3
Medium	2.2	6.3	35.9
High	2.2	11.2	6.4

Table 3.3 Equivalent Young's modulus of different PCL micropillar substrates various with parameter of radius and height.

3.2.5 Cell culture on PCL substrates

Substrate preparation

UV lamp sterilization – 30 min.

FN (50 $\mu\text{g}/\text{ml}$) coating on the soft stamps – 1 h.

Plasma surface treatment on the micropillar samples – 7 min.

The stamps on the samples – 1 h.

Cell seeding, adhesion and spreading

Cell suspension in 5×10^4 cells ml^{-1} was added on the prepared substrates, as shown in Figure 3.11 +0 h. At room temperature, the transparency and light transmission of PCL was not good even made into thin wafer, compared to PDMS. With shadow and texture occupying the whole view, it was impossible to record the cell behaviors in real time with bright filed microscope as PDMS samples. Nevertheless, it was accessible to observe round-up cells (non-adherent cells) from a light particle and determined whether cells attached to the PCL substrates. At +1 h in Figure 3.11, the number of visible particle on flat PCL and short pillar substrate was more than medium and high pillar substrates, larger contact area, easier for cell adhesion. After 3 h, cells attached to all five types of substrates. In consideration of equivalent Young's modulus in Table 3.3, PCL micropillars substrates could avoid the large structure deformation and cell contract caused by materials stiffness insufficiency.

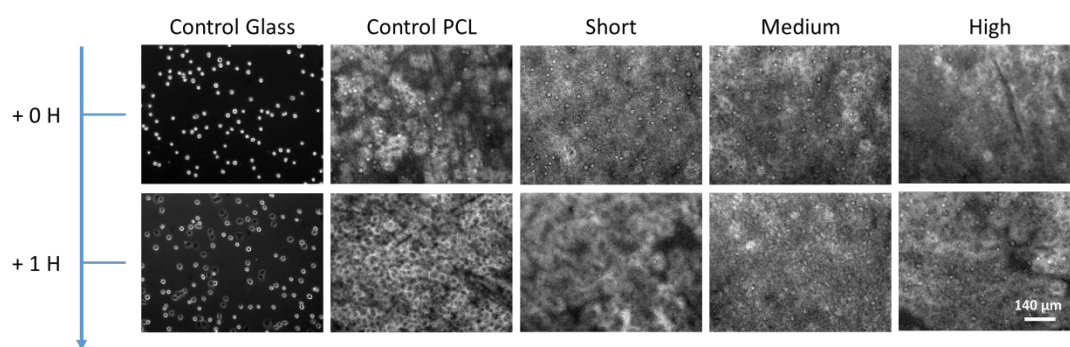


Figure 3.11 Microscope photographs of NIH-3T3 cells cultured on substrates of glass slide, flat PCL, and PCL micropillar array with different height.

Cell proliferation and alignment

Figure 3.12 shows the typical fluorescent microscopy images of fibroblast cultured on substrates at Day 1 and Day 3, respectively. Similarly, the cells were in spread shape on the flat PCL as flat PDMS and glass control. Cell morphology on PCL

wafer was comparable to PDMS wafer, with larger spread area than glass slide at Day 1. After 3-day culture, cell amount increased with unavoidable cell-cell interaction, all flat substrates (glass, PMDS and PCL) arranged without guidance and laminated disorderly. Differently, PCL micropillars with high mechanical stiffness like barriers restricted cells from spreading with rigid protruding. In comparison of the elongation of entire cytoskeletal on PDMS micropillars, action fiber formed filopodia and extreme elongation on PCL micropillars, especially on medium and high pillar array. From the fluorescent photos, cytoskeleton was guided in the certain direction. The difference of cell behaviors between spread and elongation influenced the cell proliferation and alignment in data statistics.

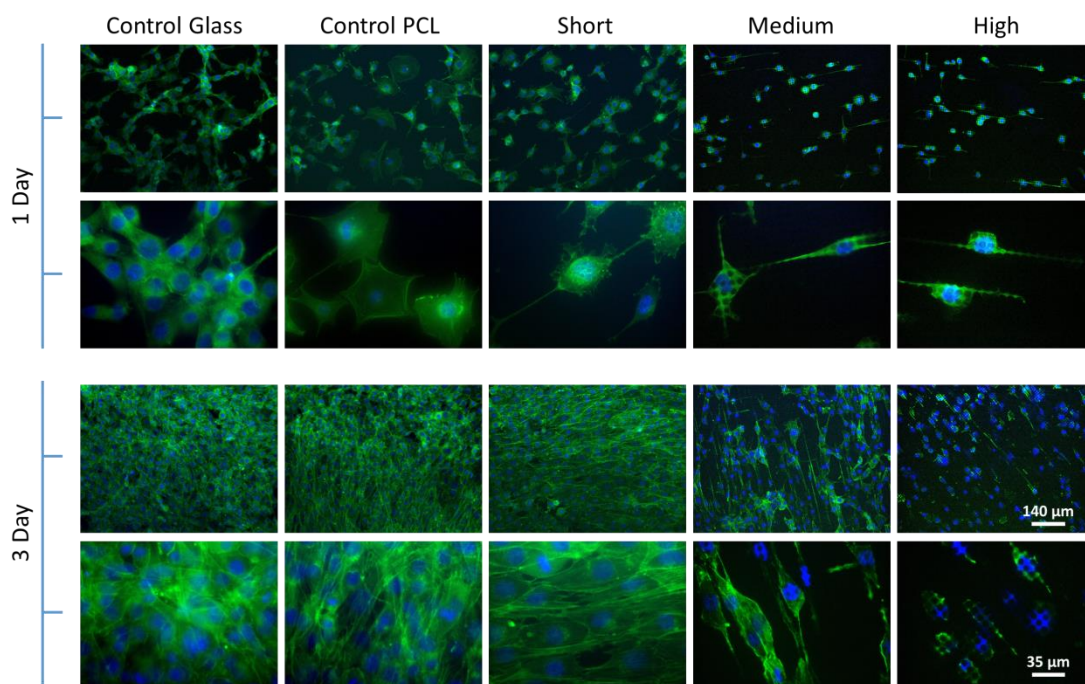


Figure 3.12 Fluorescent images of NIH-3T3 cells cultured on substrates of glass slide, flat PCL, and PCL micropillar array with different height. Cell nuclei (DAPI: blue) and actin cytoskeletal networks (Alexa Fluor 488 phalloidin: green).

Cell density on all substrates increased as demonstrated in Figure 3.13a. Cells on flat PCL were with highest proliferation rate, increasing from 200 to 950 mm^{-2} , nearly 5 times. Glass slide performed as previous result, rising from 200 to 800 mm^{-2} . Interestingly, at Day 3, cell density decreased with the increment of pillar height,

1.8- μm array with 650 mm^{-2} , 6.3- μm array with 500 mm^{-2} and 11.2- μm array with 400 mm^{-2} , only double to tribble of the initial number. With the cell proliferation, the error of cell density distribution increased (larger standard deviation) from sample to sample.

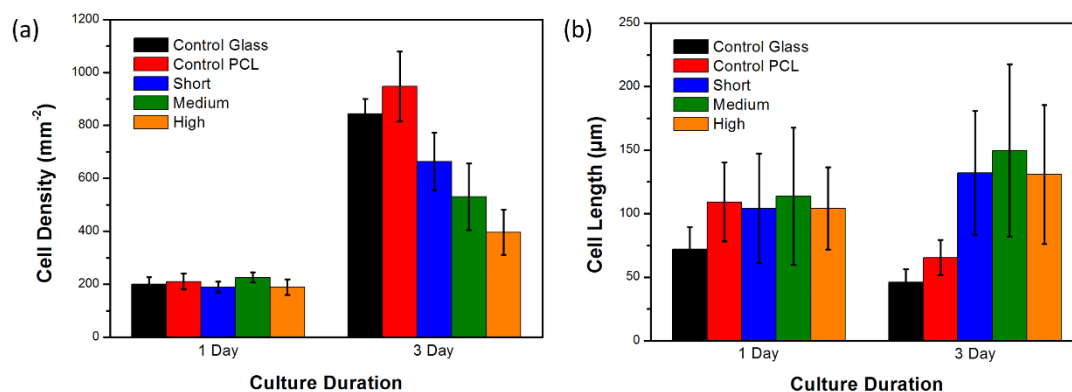


Figure 3.13 Distribution of NIH-3T3 cells (a) density and (b) length cultured on substrates of glass slide, flat PCL, and PCL micropillar array with different height.

Cell length on flat substrates decreased but increased slightly on micropillar substrates, shown in Figure 3.13b. With the increasing number of cell, insufficient space and nutrition distribution could influence cell elongation on glass slide and PCL wafer. At Day 1, the length of cells was significantly large on all PCL substrates, with average length 100-125 μm . Cells on PCL wafer spread large area with large length, while on micropillars elongated in filopodia and contract nuclei. After 3-day incubation, cells re-arranged and shortened, for flat glass slide, cell length dropped from 75 μm to 45 μm (400%), flat PCL from 110 μm to 60 μm (45%). On the contrary, cell length increased on micropillar substrates, short pillar array from 105 μm to 125 μm (19%), medium pillar array from 110 μm to 150 μm (36%) and high pillar array from 105 to 125 (19%). Especially on the medium pillar substrate, the maximum length could be 350 μm extremely. Dramatical reduction of E_e was different influence from PCL to PDMS. For soft material in KPa of PDMS, comparable to the Young's modulus of fibroblast, cells were more sensitively to the variation of pillar stiffness. For stiff material in MPa of PCL, excess materials hardness acted like fence blocking

cell growth from boarder line and deformed the cells from cytoskeletal to nuclei particularly.

3.3 Adjacent micropillar arrays with different height

3.3.1 Fabrication of mold with tow-step double-side exposure

Based on backside exposure, we added one more step of frontside exposure to fabricate designed height difference for adjacent micropillar array. Figure 3.14 shows the process flow of this novel method.

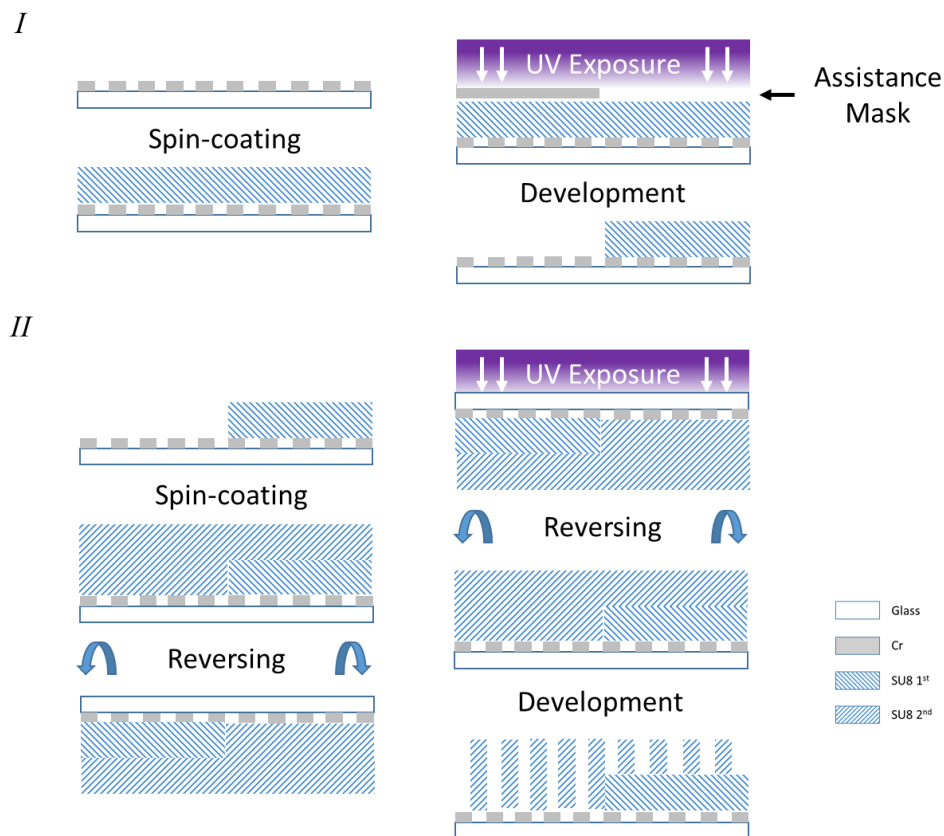


Figure 3.14 Schematic diagrams of the fabrication process of photoresist mold with tow-step double-side exposure.

First, the planar mask was placed on the spin-coater fixed by vacuum pump. 1-2 ml of SU8-3005 photoresist was dropped on the clean surface of mask. Then, the

photoresist was spread around uniformly under low spin velocity to cover the whole pattern area. With the increasing of spin velocity, excess SU8 was spun out of the mask to the wall of spin-coater chamber, only $\sim 5 \mu\text{m}$ thickness remained. After soft bake for 1 min @ $65 \text{ }^\circ\text{C}$ and 2 min @ $95 \text{ }^\circ\text{C}$, the resist-coated mask was covered by another assistance mask with pattern of blank window, and exposed by UV lamp of power density 12.7 mJ/cm^2 for 11 s. Afterwards, the mask was post-baked for 1 min @ $65 \text{ }^\circ\text{C}$ and 1 min @ $95 \text{ }^\circ\text{C}$. Waiting for cooling down, the resist-coated mask was immersed in SU8 developer solvent for 1 min with gentle agitation and rinsed with Isopropanol, dried with Nitrogen.

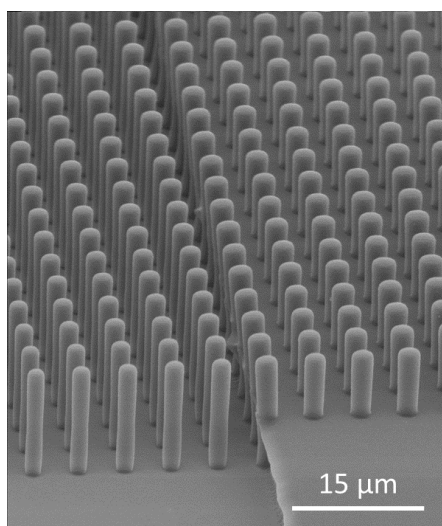


Figure 3.15 SEM image of photoresist mold with $2 \mu\text{m}$ diameter, $5 \mu\text{m}$ period and $10 \mu\text{m}$ height for higher pillar, $5 \mu\text{m}$ height for shorter pillar.

Second, same protocol as previous backside exposure, the mask with height-difference structure was placed on the spin-coater fixed by vacuum pump. 1-2 ml of SU8-3010 photoresist was dropped on the surface of mask. The photoresist was spread around uniformly under low spin velocity to cover the whole pattern area. Then, with the increasing of spin velocity, excess SU8 was spun out of the mask to the wall of spin-coater chamber, only $\sim 10 \mu\text{m}$ thickness remained. After soft bake for 1 min @ $65 \text{ }^\circ\text{C}$ and 3 min @ $95 \text{ }^\circ\text{C}$, the resist-coated mask was reversed, micro pattern covering the photoresist layer, and exposed by UV lamp 13 s. Afterwards, the

mask was reversed again and post-baked for 1 min @ 65 °C and 2 min @ 95 °C. Waiting for cooling down, the resist-coated mask was immersed in SU8 developer solvent for 2 min with gentle agitation and rinsed with Isopropanol, dried with Nitrogen.

The final photoresist mold is shown in Figure 3.15. The micropillar was fabricated with diameter 2 μm and period 5 μm . For higher micropillar, the height was 10 μm , for shorter micropillar, the height was 5 height μm . The designed height difference was achieved via novel tow-step double-side exposure method.

3.3.2 PDMS replica vs PCL replica

As mentioned previously, PDMS replica was achieved via casting and PCL replica was obtained via hot embossing. Figure 3.16 shows the final dimension of replica various from materials in SEM photos.

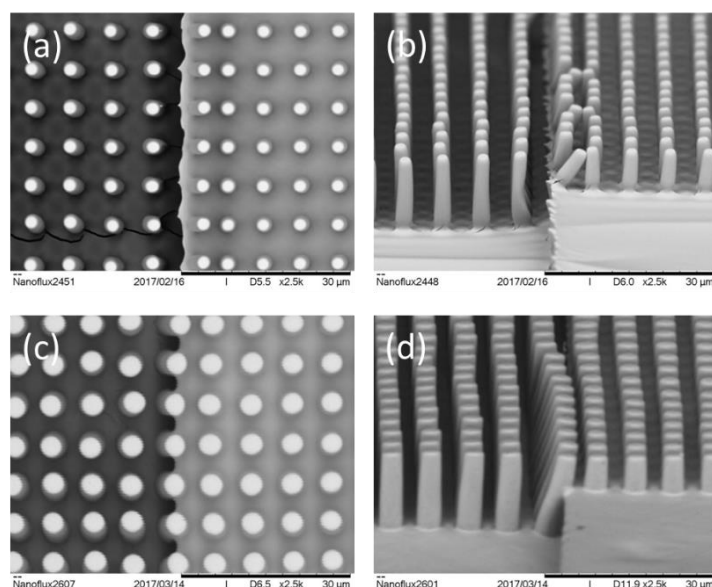


Figure 3.16 SEM images of adjacent micropillar arrays with different height micropillars in (a)(b) PDMS and (c)(d) PCL.

For PDMS replica, the height of adjacent arrays was 13.2 and 7.3 μm respectively. The period was approximately same with 6.8 and 7.1 μm . The diameter

of high array was 2.8 μm , compared to 2.5 μm of short array. For PCL replica, because dimension was deformed during pressure, the height was 13.8 and 6.3 respectively. The period was approximately same with 6.8 μm . The diameter of high array was 4.1 μm , compared to 3.8 μm of short array.

Based on Equation 3.1 and 3.2, the equivalent Young's modulus was calculated and shown in Table 3.4. The significant difference of equivalent Young's Modulus between PDMS and PCL micropillars resulted in the different standability at the height boundary. For soft PDMS, pillars were easier to collapse mutually because of the abrupt height change resulting more sensitive shape variation, as shown in Figure 3.16b. For stiff PCL, replica preserved the original shape characterization from mold, without mutual collapse or elastic recovery from oblique to erection, as shown in Figure 3.16d.

		r (μm)	H (μm)	E_e (MPa)
PDMS	H	1.4	13.2	2.2×10^{-3}
	M	1.3	7.3	9.8×10^{-3}
PCL	H	2.1	13.8	2.8
	M	1.9	6.3	22.8

Table 3.4 Equivalent Young's modulus of PDMS and PCL adjacent micropillar array various with parameter of radius and height.

Substrate preparation

Before cell seeding, the substrates were sterilized under mild cell-culture UV lamp for 30 min. Afterwards, to prove the hydrophilic of substrates for cell-liquid spread, the samples were surface-treated with plasma cleaner for 3 min. Then FN diluted in DPBS in 50 $\mu\text{g}/\text{ml}$ was dropped on the samples for 30 min at room temperature to prove cell adhesion on the micropillars. Finally, the excess FN solution was pipetted out of the samples (no need to rinse) waiting to cell seeding.

Cell proliferation and alignment

Figure 3.17 shows the typical fluorescent microscopy images of fibroblast cultured on substrates at Day 1 and Day 3, respectively. When the cells were placed on dense pillar arrays, they performed different behaviors from pillar with contacting printing coating condition. Here, the distance between pillars was significantly smaller than that of the cell sizes so that cells could stay comfortably on the top and spread over several pillars after seeding.

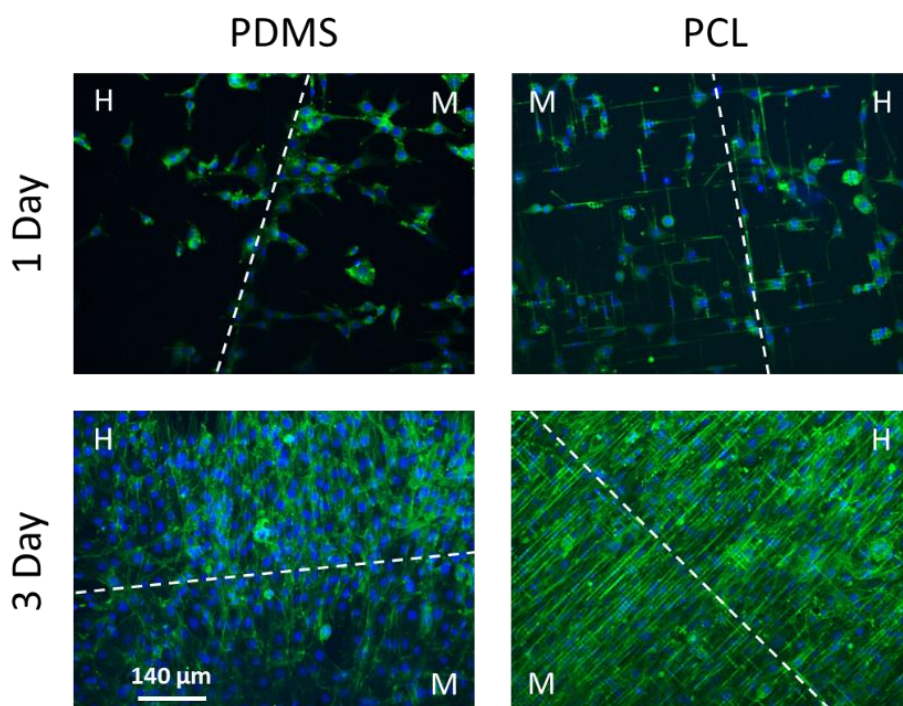


Figure 3.17 Fluorescent images of NIH-3T3 cells cultured on substrates of PDMS and PCL micropillar array (H for 13-14 μm and M for 6-7 μm) respectively. Cell nuclei (DAPI: blue) and actin cytoskeletal networks (Alexa Fluor 488 phalloidin: green).

At Day 1, the cell proliferation and alignment showed similar character from surface coating to bulk coating on PDMS pillars. On 7.3- μm array, cell spread larger area and longer filopodia compared to 13.2- μm . Since the Young's module of the PDMS pillar surface was comparable to that of migrating NIH 3T3 cells (3-12 kPa) [22], NIH 3T3 cells should be more sensitive to the variation of the stiffness of the PDMS pillars. Indeed, when cells were placed on PDMS pillars of different heights, they preferentially localized on the stiffer (smaller height) pillar areas. However, on PCL

pillars, cell performed approximately spreading area and straightly long elongation on 6.3 and 13.8 μm arrays. Coherently, much more cells were found on PCL pillars but they showed no preferential attachment since the effective Young's modules of the PCL pillars are both excessively larger than that of the cells.

At Day 3, with the adequate cell amount increasing, no obvious difference between two sides of height variation, on both PDMS and PCL substrates. The more noteworthy phenomenon was the cytoskeletal elongation and alignment in the variation of materials from PDMS to PCL, as abstractly illustrated in Figure 3.18. Cell alignment on PDMS pillars formed a holistic structure, and aligned along the direction of stiffness gradient, based on the extension. Whether it was the anisotropic gradient on a single pillar or height gradient on adjacent pillar array, the cytoskeleton of pseudopodia performed typically spreading shape, with a certain stretch arrangement in gradient direction. To the opposite, fibroblast alignment on PCL pillars formed bead-string shape. A part of the cytoskeleton wrapped around the nucleus, with stretch and deformation. The other part of the cytoskeleton spread out filamentous pseudopods, which was extremely thin and stretched along the gaps among pillars. The cells on PCL pillars were more sensitive to the stiffness anisotropy of a single pillar than the difference between adjacent arrays.

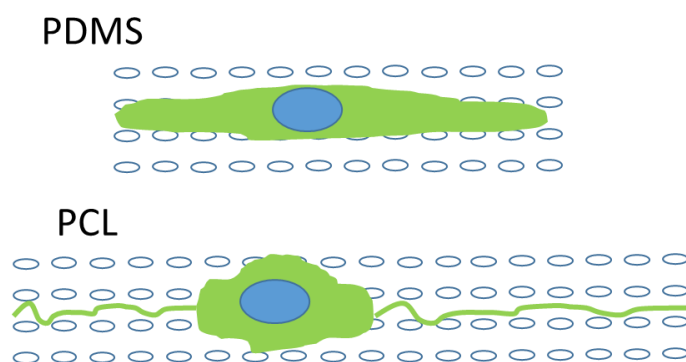


Figure 3.18 Schematic diagrams of cellular behavior in cytoskeletal elongation and alignment in the variation of materials from PDMS to PCL.

3.4 Summary

Micropillar arrays of different heights were fabricated by casting or hot embossing in PDMS and PCL, resulting culture substrates of different effective stiffness. Our results showed that NIH 3T3 cells were sensitive to the height of PDMS pillars due to their comparable Young's modules and that these cells are preferentially localized on the stiffer pillar area. However, fibroblast alignment on PCL pillars formed bead-string shape.

References

1. N. M. Alves, I. Pashkuleva, R. L. Reis, J. F. Mano, Controlling cell behavior through the design of polymer surfaces. *Small* **6**, 2208-2220 (2010).
2. T. B. Saw, S. Jain, B. Ladoux, C. T. Lim, Mechanobiology of Collective Cell Migration. *Cellular and Molecular Bioengineering* **8**, 3-13 (2015).
3. J. Li, M. Wu, J. Chu, R. Sochol, S. Patel, Engineering micropatterned surfaces to modulate the function of vascular stem cells. *Biochemical and biophysical research communications* **444**, 562-567 (2014).
4. S. Vedula, A. Ravasio, E. Anon, T. Chen, G. Peyret, M. Ashraf, B. Ladoux, Microfabricated environments to study collective cell behaviors. *Methods in cell biology* **120**, 235-252 (2013).
5. N. Annabi, A. Tamayol, J. A. Uquillas, M. Akbari, L. E. Bertassoni, C. Cha, G. Camci - Unal, M. R. Dokmeci, N. A. Peppas, A. Khademhosseini, 25th anniversary article: rational design and applications of hydrogels in regenerative medicine. *Advanced materials* **26**, 85-124 (2014).
6. J. Thiele, Y. Ma, S. Bruekers, S. Ma, W. T. Huck, 25th Anniversary article: designer hydrogels for cell cultures: a materials selection guide. *Advanced materials* **26**, 125-148 (2014).
7. Y. Ding, M. Yang, Z. Yang, R. Luo, X. Lu, N. Huang, P. Huang, Y. Leng, Cooperative control of blood compatibility and re-endothelialization by immobilized heparin and substrate topography. *Acta biomaterialia* **15**, 150-163 (2015).
8. X. Du, Y. Wang, L. Yuan, Y. Weng, G. Chen, Z. Hu, Guiding the behaviors of human umbilical vein endothelial cells with patterned silk fibroin films. *Colloids and Surfaces B: Biointerfaces* **122**, 79-84 (2014).
9. F. Mei, S. P. Fancy, Y.-A. A. Shen, J. Niu, C. Zhao, B. Presley, E. Miao, S. Lee, S. R. Mayoral, S. A. Redmond, Micropillar arrays as a high-throughput screening platform for therapeutics in multiple sclerosis. *Nature medicine* **20**, 954-960 (2014).

10. B. Ladoux, E. Anon, M. Lambert, A. Rabodzey, P. Hersen, A. Buguin, P. Silberzan, R.-M. Mege, Strength dependence of cadherin-mediated adhesions. *Biophysical journal* **98**, 534-542 (2010).
11. L. Trichet, J. Le Digabel, R. J. Hawkins, S. R. K. Vedula, M. Gupta, C. Ribault, P. Hersen, R. Voituriez, B. Ladoux, Evidence of a large-scale mechanosensing mechanism for cellular adaptation to substrate stiffness. *Proceedings of the National Academy of Sciences* **109**, 6933-6938 (2012).
12. J. Wei, J. Shi, B. Wang, Y. Tang, X. Tu, E. Roy, B. Ladoux, Y. Chen, Fabrication of adjacent micropillar arrays with different heights for cell studies. *Microelectronic Engineering* **158**, 22-25 (2016).
13. K. D. Wise, K. Najafi, Microfabrication techniques for integrated sensors and microsystems. *Science* **254**, 1335 (1991).
14. A. Hierlemann, O. Brand, C. Hagleitner, H. Baltes, Microfabrication techniques for chemical/biosensors. *Proceedings of the IEEE* **91**, 839-863 (2003).
15. K. Shah, W. Shin, R. Besser, A PDMS micro proton exchange membrane fuel cell by conventional and non-conventional microfabrication techniques. *Sensors and Actuators B: Chemical* **97**, 157-167 (2004).
16. X. Tu, J. Wei, B. Wang, Y. Tang, J. Shi, Y. Chen, Patterned parylene C for cell adhesion, spreading and alignment studies. *Microelectronic Engineering* **175**, 56-60 (2017).
17. X. Q. Brown, K. Ookawa, J. Y. Wong, Evaluation of polydimethylsiloxane scaffolds with physiologically-relevant elastic moduli: interplay of substrate mechanics and surface chemistry effects on vascular smooth muscle cell response. *Biomaterials* **26**, 3123-3129 (2005).
18. A. Saez, A. Buguin, P. Silberzan, B. Ladoux, Is the mechanical activity of epithelial cells controlled by deformations or forces? *Biophysical journal* **89**, L52-L54 (2005).
19. A. Saez, E. Anon, M. Ghibaudo, O. Du Roure, J. Di Meglio, P. Hersen, P. Silberzan, A. Buguin, B. Ladoux, Traction forces exerted by epithelial cell sheets. *Journal of Physics: Condensed Matter* **22**, 194119 (2010).
20. B. Wang, J. Shi, J. Wei, L. Wang, X. Tu, Y. Tang, Y. Chen, Fabrication of elastomer pillar arrays with height gradient for cell culture studies. *Microelectronic Engineering* **175**, 50-55 (2017).
21. K. Ragaert, I. De Baere, L. Cardon, J. Degrieck, in *6th Polymers & Mould Innovations International Conference*. (2014), pp. 339-344.
22. C. Rotsch, K. Jacobson, M. Radmacher, Dimensional and mechanical dynamics of active and stable edges in motile fibroblasts investigated by using atomic force microscopy. *Proceedings of the National Academy of Sciences* **96**, 921-926 (1999).

Chapter 4 Cell culture on nanofibers deposited on micropillar arrays

In this chapter, we present the fabrication of nanofibers on micropillar arrays for cell culture studies. PDMS micropillars are produced using the same technique as described previously. Nanofibers of poly (lactic-co-glycolic acid) (PLGA) are then deposited on the top of PDMS pillars by electrospinning. Comparing to the substrate made of PDMS pillars or PLGA nanofibers alone, such hybrid structures should gain in both biocompatibility and surface structure resemblance to the physiological extracellular matrix (EMC), where the underneath space remains highly permeable and deformable. Cell culture studies are then performed using NIH 3T3 and primary hippocampal neurons and the electrical activity of neuron cells is analyzed by calcium imaging. Our results show the advantage of the combination of nanofibers and micropillars on the formation and functionality of neuronal networks, compared to simple PDMS pillars.

4.1 Introduction

Improvement of cell culture conditions is important for biomedical research as well as advanced applications such as tissue engineering, disease modeling and cancer treatment [1-3]. Among many others, the performance of cell culture is highly dependent on the physical and biochemical properties of the culture substrate [4,5]. For example, cell adhesion and migration is guided by topographical cues [6] while cell fate decision is largely dictated by the stiffness of the substrate [7], the expression of neuronal markers and the formation of neural networks are both affected by the stiffness and the surface morphology of the culture substrates [8-10], in addition to the fine tuning of cell-material affinity by surface biomolecular coating [11,12].

In order to simultaneously modulate the stiffness and the surface morphology of the substrate, we developed a new type of substrates (shown in Figure 4.1), which consist of nanofibers on elastomer pillar arrays fabricated by electrospinning of poly-lactic-co-glycolic acid (PLGA) and casting of polydimethylsiloxane (PDMS) on a lithography patterned mold. We expected to improve the culture of primary neurons.

Previously, PDMS pillars have been repeatedly used for cell contractile force measurement [13] as well as stem cell differentiation toward neurons [14,15] due to the relatively low effective Young's modulus of the substrate. On the other hand, numerous investigations have shown that the surface morphology of electrospun nanofibers is prominent to cell culture [16] due to its resemblance to the in-vivo organization of extracellular matrix (ECM) proteins [17]. Moreover, electrospinning of both natural and synthetic polymers can be easily performed, enabling an improved bio-compatibility [18]. The present work has been motivated to take both advantages. Finally, the substrates made of nanofibers on high aspect ratio pillars provide a quasi-three-dimensional architecture with which the neurons will be supported mainly by bio-compatible nanofibers and the cell-medium exchange will be largely enhanced due to large free spaces underneath the fibers. Preliminary results of neuron culture and calcium imaging will be shown to illustrate the high potential of this approach.

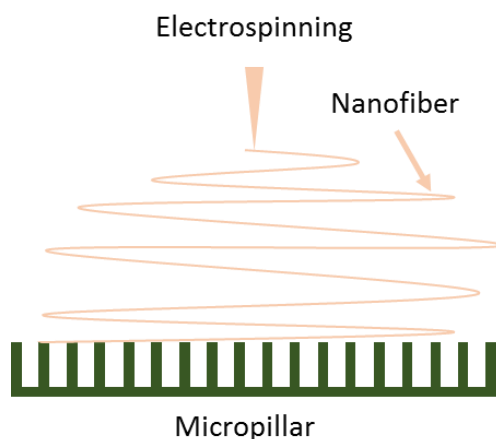


Figure 4.1 Schematic diagram of the fabrication process of electrospun nanofibers on elastomer micropillars.

4.2 Fabrication of micro/nano hybrid substrates

4.2.1 Fabrication of micropillars

Micropillar arrays used in this work were obtained by casting PDMS on a PDMS

mold with holes, whereas the PDMS mold was initially obtained PDMS casting on a photoresist mold (master) fabricated by photolithography. Firstly, micro-hole arrays were patterned on the Cr mask using a micro pattern generator (μ PG101, Heidelberg, Germany). Then, a 25- μ m-thick negative resist layer (SU8-3025) was spin-coated on the mask and back-side ultraviolet (UV) exposed. After development, pillars of 25- μ m height, 5- μ m diameter and 20- μ m spacing were obtained and used as mold features to cast a mixture of PDMS pre-polymer and crosslink agent at ratio of 10:1. Before casting, the mold was treated in oxygen plasma for 2 min and then in TMCS vapor for 30 min. After PDMS casting and curing at 80°C for 2 h, the PDMS layer was peeled-off, resulted in negative replica of the mold features. Next, 0.2- μ m thick Parylene C was deposited on the PDMS layer with a vacuum deposition system (SCS Labcoter 2, SCS Ltd, UK). Afterward, a positive-tone replica of the master was finally obtained by casting liquid PDMS on the PDMS mold using the same casting process, as shown in Figure 4.2.

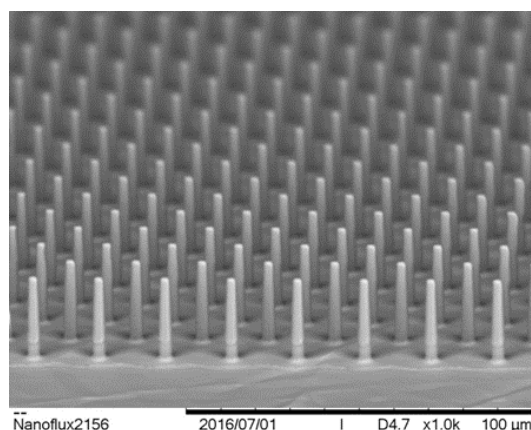


Figure 4.2 SEM image of PDMS micropillar array with 25 μ m height, 5 μ m diameter and 20 μ m period.

Comparing to other fabrication processes, the present double casting technique is advantageous to achieve high quality PDMS pillar arrays, since it is relatively easy to obtain high resolution, high density and high aspect ratio SU8 pillars. It is also relatively easy to peel-off the PDMS layer from the fabricated resist pillars and then

replicate the same feature of the master due to the relative low Young's modules of PDMS. Previously, we have shown that it was convenient to use PDMS mold for replication of pillar structures with different types of polymers such as PDMS, PCL, PLGA and T-Flex [19]. Here, the PDMS mold was coated with a thin film of Parylene C, which further facilitated the replication due to the low surface energy of Parylene C. As results, this double casting procedure allowed us producing reproducibly high density and high aspect ratio PDMS pillar arrays.

4.2.2 Fabrication of nanofibers

Solution of PLGA (Mw 76000-115000) at lactide to glycolide ratio 75:25 were prepared by dissolving PLGA in tetrahydrofuran (THF) (with higher volatility) and dimethylformamide (DMF) mixed solvent with ratio 2:3. The concentration of PLGA solution was 20 wt%. For deposition of smooth and beads-free nanofibers, ionic surfactant sodium dodecyl sulphate (SDS, Sigma, France) dissolved in ethanol was admixed into the polymer solution to a final concentration of 1 mg/ml.

The PLGA solution was kept in a 1-ml-syringe and spinneret tip that connected to the anode of a high voltage (Heinzinger, Germany) of 12 KV. The cathode was connected to the grounded aluminum wafer collector. The solution was supplied by a syringe pump (KD Scientific, USA) at a rate of 0.2 ml/h. The vertical distance between spinneret tip and the collector was 10 cm. Random PLGA nanofibers were collected for 3 min on the aluminum wafer, on which the micro pillar supporter was attached. After electrospinning, the sample was put into a vacuum chamber to volatilize the solvent overnight. As expected, we obtained a new type of culture substrate made of PLGA nanofibers on PDMS pillar arrays, as shown in Figure 4.3a.

By using freeware Image-J and SEM images of the fabricated samples, the diameter of the nanofibers could be measured (in Figure 4.3b), showing that 84.0% fibers have diameters in the range of 500-900 nm and less than 0.2% (2.5%) fibers have diameters smaller (larger) than 100 nm (1000nm).

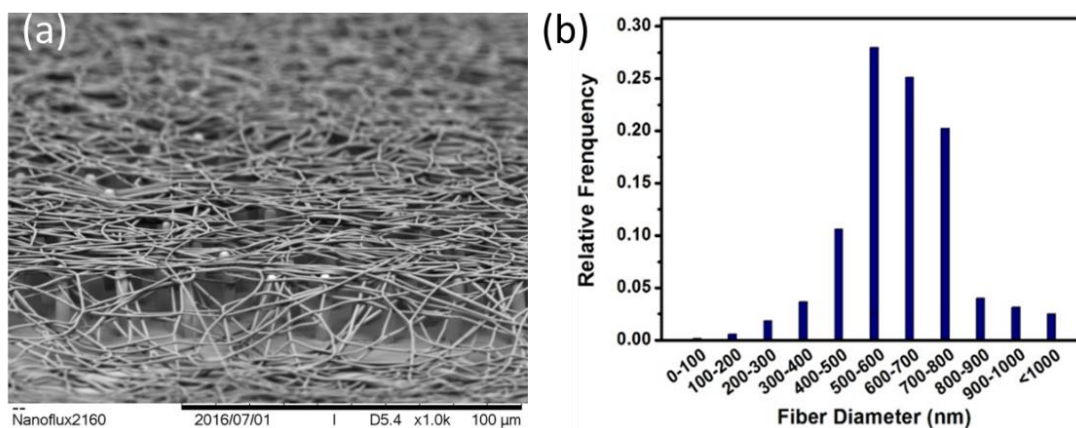


Figure 4.3 (a) SEM image of PLGA nanofibers electrospun on PDMS pillars. (b) Statistic distribution of the PLGA nanofibers.

4.3 Cell culture on hybride substrates

4.3.1 NIH 3T3 cell culture on hybride substrates

Before cell seeding, the substrates were sterilized under mild cell-culture UV lamp for 30 min. Afterwards, to prove the hydrophilic of substrates for cell-liquid spread, the samples were surface-treated with plasma cleaner for 7 min. Then FN diluted in DPBS in 50 μg/ml was dropped on the samples for 60 min at room temperature to prove cell adhesion on the micropillars. Finally, the excess FN solution was pipetted out of the samples (no need to rinse) waiting to cell seeding.

NIH 3T3 cells were incubated (37 °C, 5% CO₂) in culture medium Dulbecco's Modified Eagle Medium (DMEM) with 10% Fetal Bovine Serum (FBS) and 1% Penicillin/Streptomycin (P/S). Before seeding, the spent medium was aspirated out and Dulbecco's Phosphate-Buffered Saline (DPBS) was added to rinse the vessel twice. Aspirating DPBS, we added Trypsin covering the vessel for 3 min in incubator (37 °C, 5% CO₂). When cells started to separate and round up, we aspirated Trypsin and add 1 ml fresh medium to remove cells from the vessel by gently squirting and pipetting the medium until the cell colonies broke up to single cell. After cell counting, centrifuging, density adjusting, cell suspension in 1×10⁴ cells ml⁻¹ was added on the prepared substrates.

Different from the previously dense micropillar arrays, almost all the cells fell into the gap between the pillars due to the increased spacing, as shown in Figure 4.4 +0 day. In comparison, hybrid substrates with nanofiber extricated the cells from the limitation by the narrow space between micropillars. From +0 days to +1 day, the effect was mainly reflected in the dominant behavior of cell adhesion. Cell attached and interacted with pillars, adjusting shape and morphology. Because of the restriction, the cell area based on subsequent extension was reduced. From +2 day to +3 day, cell main behavior was proliferation. The number of cells on the hybrid substrate was larger than that on the micropillars.

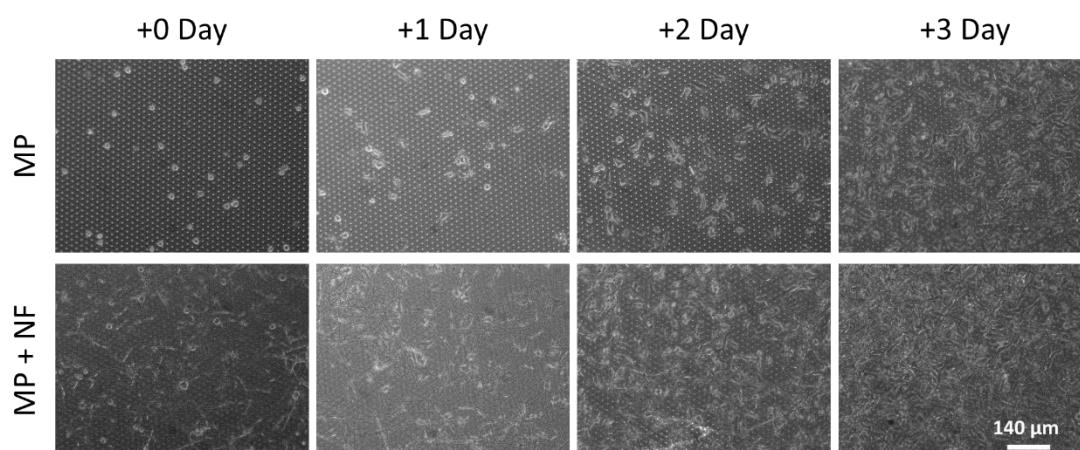


Figure 4.4 Microscope photographs of NIH-3T3 cells cultured from +0 day to +3 day on substrates of PDMS micropillars (MP) and PDMS micropillars plus PLGA nanofibers (MP + NF).

Comparing the cells on the PLGA/PDMS substrate to the PDMS micropillar array, the contour was more distinct on the micro-nano hybrid substrate. For magnification, cells on the hybrid substrate spread larger body area on the fiber and did not adhere to the PDMS flat gap area due to the support of micropillars. On contrary, the cells fell into the intentionally designed 25- μm gap and attach to the flat surface resulting restricted two-dimensional (2D) cell culture micro-environment. We expected cells contact to the culture medium both sides and as little limited contact as possible.

For detailed study, the fluorescence images (Figure 4.5) clearly shows the differences of cell amount and morphology. In terms of quantity, the cell density on

the hybrid substrate was 1.5 times more than that on the micropillar array. Through the observation of nuclei shape, cell nuclei on both substrates were elongated. On micropillars, the nucleus was in the restraint of narrow gap, and on nanofibers, the nucleus was in the constraint of ultrathin fiber. In terms of morphology, the spreading area of cell cytoskeleton on the hybrid substrate was 2 times the size of the micropillar array. Cells were not fully distributed in the limitations of the stretching on the cells between the pillars, whereas cells were entirely spread on the fibrous network formed on the microstructure. Most importantly, the fibrous structure supplied the structural cue for the cells cytoskeleton in apparently filamentous pseudopods. Certainly, we supposed that the morphological feature of filamentous network was contributed the formation of neural synapses.

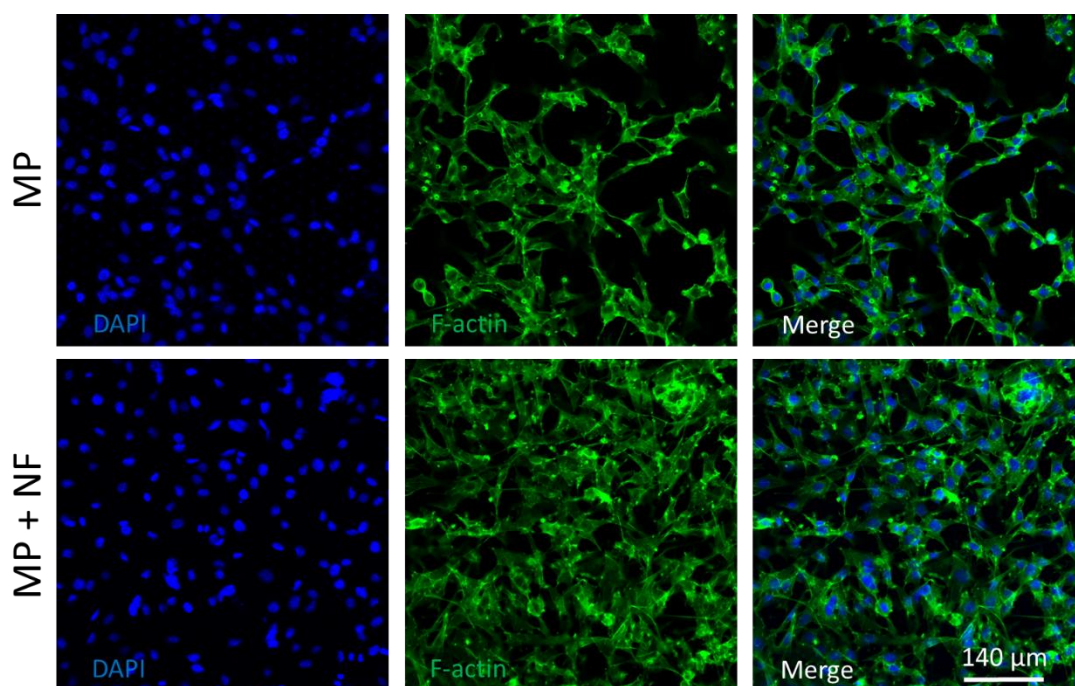


Figure 4.5 Fluorescent images of NIH-3T3 cells after 3-day incubation on substrates of PDMS micropillars (MP) and PDMS micropillars plus PLGA nanofibers (MP + NF). Cell nuclei (DAPI: blue) and actin cytoskeletal networks (Alexa Fluor 488 phalloidin: green).

4.3.2 Neuronal cell culture on hybride substrates

Cell and substrates preparation

One day before cells seeding, all the PLGA/PDMS and PDMS (control) microarrays were exposed to plasma treatment for 2 min and sterilized with UV light for 20 min. Subsequently, the substrates were left in ethanol 70% for 1 h and rinsed with sterile water. For hippocampal cells, all the samples were coated with 50 µg/ml poly-L-ornithine (Sigma-Aldrich, St. Louis, MO, USA) for overnight incubation at 37 °C. An additional coating with Matrigel (diluted 1:50 with culture medium; Corning, Tewksbury MA, USA) was performed on the substrates 20 min before cells plating.

Hippocampal neurons from Wistar rats (P2-P3) were prepared in accordance with the guidelines of the Italian Animal Welfare Act, and their use was approved by the Local Veterinary Service, the SISSA Ethics Committee board and the National Ministry of Health (Permit Number: 630-III/14) in accordance with the European Union guidelines for animal care (d.1.116/92; 86/609/C.E.). The animals were anaesthetized with CO₂ and sacrificed by decapitation, and all efforts were made to minimize suffering. After isolation of the hippocampii, cells were enzymatically dissociated and resuspended in minimum essential medium (MEM) with GlutaMAX™ supplemented with 10% dialyzed fetal bovine serum (FBS, all from Thermo Fisher Scientific, Waltham, MA, USA), 0.6% D-glucose, 15 mM Hepes, 0.1 mg/ml apo-transferrin, 30 µg/ml insulin, 0.1 µg/ml D-biotin, 1 µM vitamin B12 and 2.5 µg/ml gentamycin (all from Sigma-Aldrich). 48 hours after cells' plating, half of the medium was changed with the addition of 2 µM cytosine-β-D-arabinofuranoside (Ara-C; Sigma-Aldrich). Subsequently, half of the medium was changed twice per week. The neuronal cultures were maintained in an incubator at 37°C, 5% CO₂ and 95% relative humidity.

Immunocytochemistry and Imaging

Cells were fixed in 4% paraformaldehyde (PFA) containing 0.15% picric acid in phosphate-buffered saline (PBS), saturated with 0.1 M glycine, permeabilized with

0.1% Triton X-100, saturated with 0.5% bovine serum albumin (BSA) (all from Sigma-Aldrich) in PBS and then incubated for 1 h with primary mouse monoclonal antibodies: glial fibrillary acidic protein (GFAP, Sigma-Aldrich) and anti- β -tubulin III (TUJ1, Covance, Berkeley, CA). The secondary antibodies were goat anti-mouse Alexa Fluor[®] 594, goat anti-mouse immunoglobulin (Ig) G₁ Alexa Fluor[®] 488 and goat anti-mouse IgG_{2a} Alexa Fluor[®] 594. F-actin was marked with Alexa Fluor 488[®] phalloidin (all from Thermo Fisher Scientific) and the incubation time was 30 min. Nuclei were stained with 2 μ g/ml in PBS Hoechst 33342 (Sigma-Aldrich) for 5 min. All the incubation steps were performed at room temperature (20-22 °C). Images were acquired using a Leica DM6000 fluorescent microscope equipped with differential interference contrast (DIC) and fluorescence optics, charge-coupled device (CCD) camera and Volocity 5.4 3D imaging software (PerkinElmer, Coventry, UK). The fluorescence images were collected with a 20 \times and a 40 \times magnification (0.5 NA) objective. Image-J by W. Rasband (developed at the U.S. National Institutes of Health and available at <http://rsbweb.nih.gov/ij/>) was used for image processing.

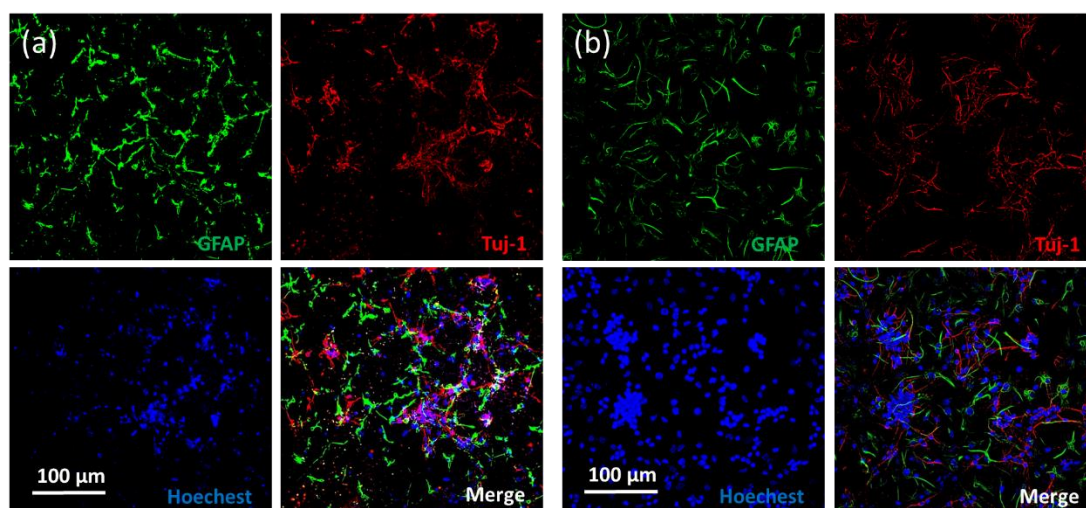


Figure 4.6 Immunofluorescence images of neurons and astrocytes on (a) PLGA/PDMS hybrid substrate and (b) glass coverslip after 48 h incubation. Astrocytes related glial fibrillary acidic protein stained by GFAP (green). Neuron-specific class III β -tubulin stained by TUJ1 (red). Cell nuclei stained by Hoechst (blue).

Primary hippocampal neurons were plated on the hybrid substrate of PLGA nanofibers on PDMS micropillars at a density of 300,000 cells/sample. Fixation and staining with the neuronal marker α -tubulin I, astrocytic marker GFAP and nuclear marker Hoechst were performed 48 hours after cell seeding. At this stage, attachment and survival of neurons (red) and astrocytes (green) on PLGA/PDMS hybrid substrate were found to be similar to that on a glass coverslip, as shown in Figure 4.6. Regardless of glial cells or neuronal cells, cytoskeleton was filamentous, retaining the intrinsic characteristics of cell composition. The difference between the two substrates was the area of cell nucleus. The area of nucleus on the 3D substrate was significantly smaller than that on the 2D glass slide. If the volume of the nucleus was approximate, it indicated that the nucleus was more elongated and dimensional on the micro-nano hybrid substrate.

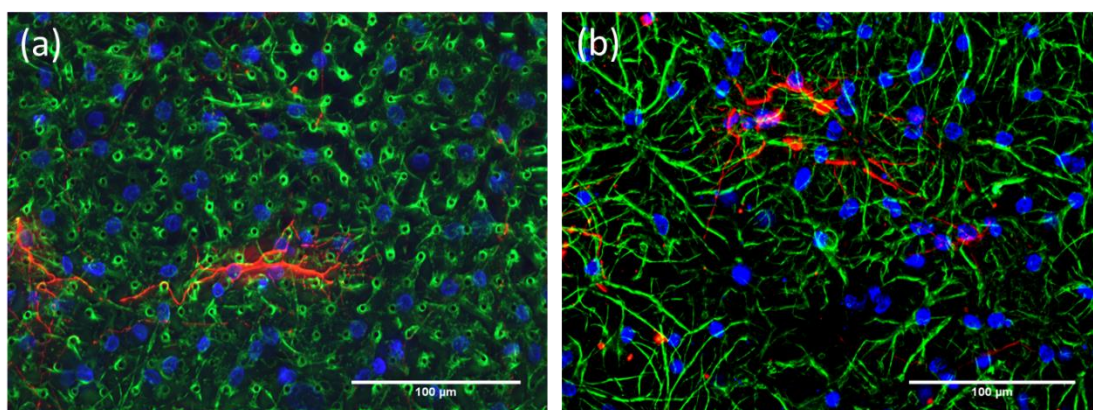


Figure 4.7 Immunofluorescence images of astrocytes on (a) PDMS micropillars and (b) PLGA/PDMS hybrid substrate after one-week incubation. Astrocytes related glial fibrillary acidic protein stained by GFAP (green). Neuron-specific class III β -tubulin stained by TUJ1 (red). Cell nuclei stained by Hoechst (blue).

However, after one week culture, the morphology of astrocytes plated on different types of substrates became significantly different. On the PDMS micropillars, glial cells were distributed in dotted array and gathered around the micropillars, in an array pattern as shown in Figure 4.7a. On the PLGA/PDMS substrate, the astrocytes showed a complex morphology with many cellular protrusions (Figure 4.7b). Glial

cells appeared longer synapses and fibrous pseudopods extended around in long distance, similar to that of in vivo systems [20]. The density of neuron cells on the two substrates neurons was approximately the same. This would suggest the importance of both surface morphology of the PLGA nanofibers and elastomeric material supporting and the PDMS pillars [21].

Calcium imaging

The cells were incubated with the non-ratiometric calcium dye Oregon Green® 488 BAPTA-1, AM, (Thermo Fisher Scientific) dissolved in anhydrous dimethyl sulfoxide (DMSO) (Sigma-Aldrich) at a concentration of 4 mM (stock solution), with the addition of Pluronic F-127 20% solution in DMSO (Thermo Fisher Scientific) for increasing the cell's permeability. The two components were dissolved at a ratio of 1:1 in Ringer's solution (145 mM NaCl, 3 mM KCl, 1.5 mM CaCl₂, 1 mM MgCl₂, 10 mM glucose and 10 mM Hepes, pH 7.4) to give a final dye concentration of 4 μM, and incubated at 37 °C for 1 hour. The cultures were then transferred to a glass-bottom Petri dish to allow visualization in a Nikon Eclipse Ti-U inverted microscope equipped with an HBO 103 W/2 mercury short arc lamp (Osram, Munich, Germany), a mirror unit (exciter filter BP 465-495 nm, dichroic 505 nm, emission filter BP 515-555) and an Electron Multiplier CCD Camera C9100-13 (Hamamatsu Photonics, Japan). The experiments were performed at room temperature for maximally 20 min/sample. Images were acquired using the NIS Element software (Nikon, Japan) with an S-Fluor 20x/0.75 NA objective at a sampling rate of 3-10 Hz. The spatial resolution was 256x256 pixels. To avoid saturation of the signals, excitation light intensity was attenuated by ND4 and ND8 neutral density filters (Nikon).

As described in our previous work [22,23], the initial video was processed with the ImageJ (U. S. National Institutes of Health, Bethesda, MA) software. Briefly, neurons were localized, and an appropriate region of interest (ROI) was selected to subtract the background. Appropriate ROIs around the cells bodies were then selected and the fluorescence intensity was measured for each ROI and expressed as a function of time $I_f(t)$. Then, the dye bleaching decay was evaluated. The Ca²⁺

transients of each cell signal were extracted in a semi-automatic manner by selecting a threshold for the smallest detectable peak that was equal three times the standard deviation of the baseline. Subsequently, the decay of $I_f(t)$ was fitted to a cubic spline interpolating $I_f(t)$ at 10 or 20 points. $I_f(t)$ was then fitted to the original optical signal to compensate for dye bleaching, and the fractional optical signal was calculated as follows: $DF/F = (I_f(t) - I_f(t_0)) / I_f(t_0)$, where $I_f(t_0)$ is the fluorescence intensity at the beginning of the recording [24,25].

The weighted mean of calcium transient amplitude was calculated for each single neuron, as well as the average Inter Event Interval, i.e. the time between two consecutive calcium transients. The correlation coefficient of the calcium transients for neuron i and neuron j (σCT_{ij}) was computed as follows [26-28]:

$$\sigma CT_{ij} = \frac{\sum n f_{in} f_{jn}}{(\sum n f_{in}^2)(\sum n f_{jn}^2)} \dots\dots\dots(4.1)$$

The total recording time, T_{tot} , was divided into N intervals (1,...,n,...,N) of a duration Δt . Thus, if f_{in} and f_{jn} are the number of calcium transients of neuron i and neuron j in the time interval Δt_n , then such that σCT_{ij} depends on Δt and varies between 0 and 1. The range of explored values of Δt was 20 s.

Once verified the neuronal attachment and survival, a functional test was performed on primary hippocampal cell cultures grown on the microarrays. The spontaneous and pharmacologically induced electrical activity of neurons was measured after two weeks of culture. At the time Domain point, the neuronal network grown in vitro represents a mature stage of development. We chose an optical recording technique that allows the simultaneous imaging of many neurons. Specifically, we measured the fluctuations in the concentration of intracellular calcium ions by use of fluorescent calcium binding dye. Calcium ions are intracellular signals that regulate a large variety of cellular functions, such as genetic expression, neurotransmitter release and neuron-to-glia communication.

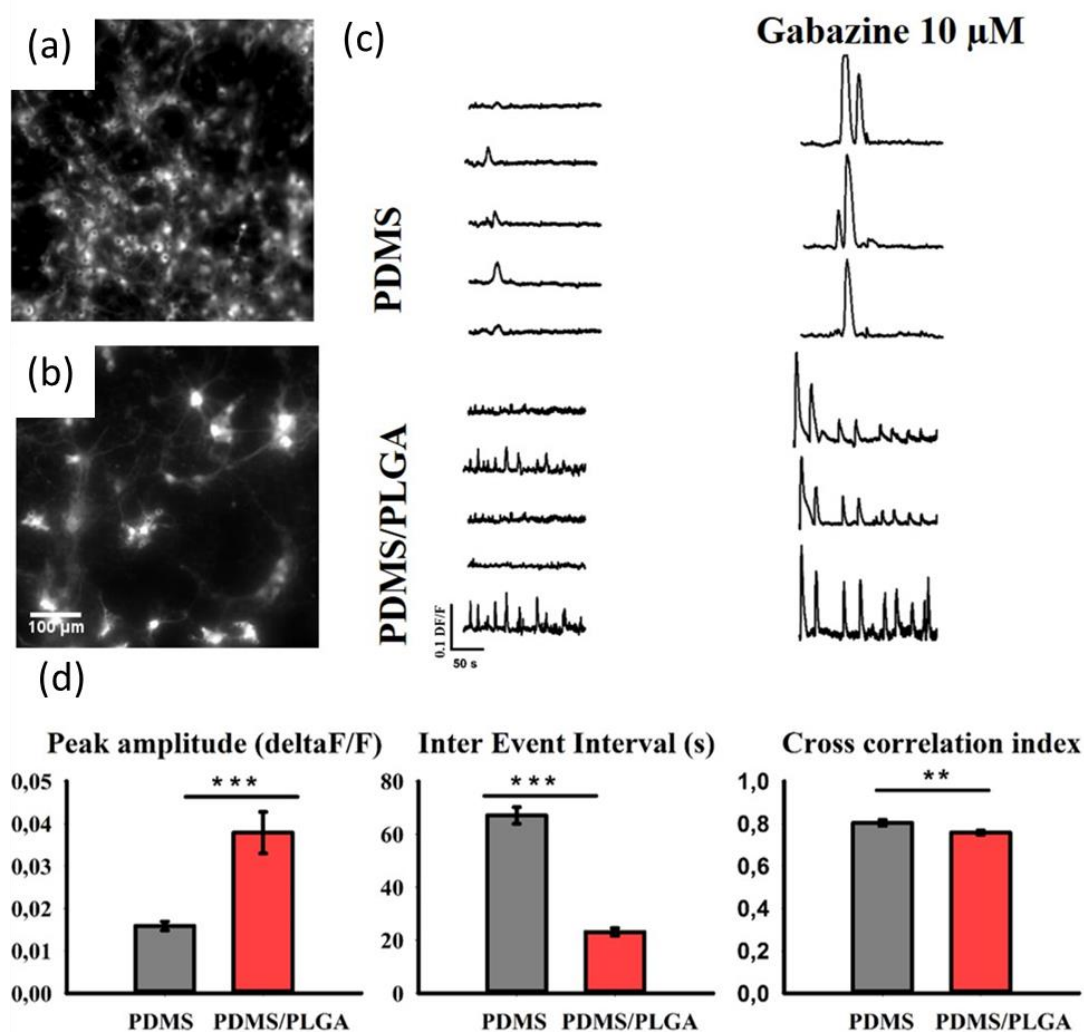


Figure 4.8 Hippocampal neurons loaded with Oregon Green[®] 488 BAPTA-1, AM after two weeks of growth on (a) PDMS and (b) PLGA/PDMS substrates. (c) Images of spontaneous and Gabazine induced calcium transients over time are also shown. (d) Average amplitude, inter event interval and cross correlation index of spontaneous calcium transients on PLGA/PDMS vs PDMS substrates (n = 12 neurons for PLGA/PDMS, n = 16 neurons for PDMS - control; **p < 0.01 ***p < 0.001 One-way ANOVA, Tukey post-hoc test).

The analysis of spontaneous calcium transients optically recorded from single cells allows comparing the functionality of the neuronal network grown on the PLGA/PDMS nanocomposite vs PDMS (control) substrates (Figure 4.8). On PDMS, we observed a few active neurons similar to the PLGA/PDMS substrates. Moreover, the calcium signals from glial cells were clearly visible on the micropillars, and

distinguishable from neuronal signals because of their slower rates of rise and decay.

The average amplitude of neuronal calcium transients was significantly increased on the nanocomposite substrate vs control while the inter event interval was decreased, meaning that the neurons grown on nanofibers have more frequent and more homogeneously distributed calcium signals over time comparing to controls. The synchronization of calcium transients over time, measured as average crosscorrelation index, was slightly increased on PDMS (control) comparing to PLGA/PDMS as shown in Figure 4.8d.

The average amplitude of neuronal calcium transients was significantly increased on the nanocomposite substrate (0.038 ± 0.004 DF/F) vs control (0.016 ± 0.001 DF/F); an elevation of intracellular calcium above a certain threshold is known to induce long-term potentiation of neuronal synapses [29]. The Inter Event Interval was instead decreased on the nanocomposite substrate vs control (23.13 ± 1.45 vs 67.07 ± 3.14 s), meaning that the neurons grown on nanofibers have more frequent and more homogeneously distributed calcium signals over time comparing to controls. The synchronization of calcium transients over time, measured as average cross correlation index between all the neuronal signals in the same field of view, was slightly increased on PDMS (0.80 ± 0.01) comparing to PLGA/PDMS (0.76 ± 0.01) as shown in Figure 4.8g. In addition, we stimulated the neuronal cultures with Gabazine $10 \mu\text{M}$ (Sigma-Aldrich), a specific GABAA receptor antagonist, and observed an increase in the amplitude and synchronization of calcium transients in both PLGA/PDMS and PDMS (control) substrates (Figure 4.8c), as expected by neuronal physiology.

4.4 Summary

We proposed a new type of culture substrates made of electrospun nanofibers on elastomeric micropillars. The advantage of such an approach relies on the ECM-like surface morphology and the low effective Young's module of the under layer as well as the high porosity of the fiber-pillar assembly. Our preliminary results

on culture of neurons and glial cells have shown improved cell morphology and electric activity compared to other types of substrates. Our further goal is to optimize the density and the stiffness of the nanofibers for improved culture of neurons as well as control stem cell differentiation toward functional neural networks.

References

1. M. Lutolf, J. Hubbell, Synthetic biomaterials as instructive extracellular microenvironments for morphogenesis in tissue engineering. *Nature biotechnology* **23**, 47-55 (2005).
2. P. Friedl, K. Wolf, Tumour-cell invasion and migration: diversity and escape mechanisms. *Nature Reviews Cancer* **3**, 362-374 (2003).
3. F. Kai, H. Laklai, V. M. Weaver, Force matters: biomechanical regulation of cell invasion and migration in disease. *Trends in cell biology* **26**, 486-497 (2016).
4. D. A. Lauffenburger, A. F. Horwitz, Cell migration: a physically integrated molecular process. *Cell* **84**, 359-369 (1996).
5. A. D. Doyle, M. L. Kutys, M. A. Conti, K. Matsumoto, R. S. Adelstein, K. M. Yamada, Micro-environmental control of cell migration—myosin IIA is required for efficient migration in fibrillar environments through control of cell adhesion dynamics. *J Cell Sci* **125**, 2244-2256 (2012).
6. D. H. Kim, C. H. Seo, K. Han, K. W. Kwon, A. Levchenko, K. Y. Suh, Guided cell migration on microtextured substrates with variable local density and anisotropy. *Advanced functional materials* **19**, 1579-1586 (2009).
7. M. Gupta, B. R. Sarangi, J. Deschamps, Y. Nematbakhsh, A. Callan-Jones, F. Margadant, R.-M. Mège, C. T. Lim, R. Voituriez, B. Ladoux, Adaptive rheology and ordering of cell cytoskeleton govern matrix rigidity sensing. *Nature communications* **6**, (2015).
8. S. Megelski, J. S. Stephens, D. B. Chase, J. F. Rabolt, Micro- and nanostructured surface morphology on electrospun polymer fibers. *Macromolecules* **35**, 8456-8466 (2002).
9. E. K. Yim, S. W. Pang, K. W. Leong, Synthetic nanostructures inducing differentiation of human mesenchymal stem cells into neuronal lineage. *Experimental cell research* **313**, 1820-1829 (2007).
10. J. Xie, W. Liu, M. R. MacEwan, Y. C. Yeh, S. Thomopoulos, Y. Xia, Nanofiber membranes with controllable microwells and structural cues and their use in forming cell microarrays and neuronal networks. *Small* **7**, 293-297 (2011).
11. S. H. Ku, J. Ryu, S. K. Hong, H. Lee, C. B. Park, General functionalization route for cell adhesion on non-wetting surfaces. *Biomaterials* **31**, 2535-2541 (2010).

12. M. A. Cole, N. H. Voelcker, H. Thissen, H. J. Griesser, Stimuli-responsive interfaces and systems for the control of protein–surface and cell–surface interactions. *Biomaterials* **30**, 1827-1850 (2009).
13. J. Fu, Y.-K. Wang, M. T. Yang, R. A. Desai, X. Yu, Z. Liu, C. S. Chen, Mechanical regulation of cell function with geometrically modulated elastomeric substrates. *Nature methods* **7**, 733-736 (2010).
14. A. Higuchi, Q.-D. Ling, Y. Chang, S.-T. Hsu, A. Umezawa, Physical cues of biomaterials guide stem cell differentiation fate. *Chemical reviews* **113**, 3297-3328 (2013).
15. Y. Sun, K. M. A. Yong, L. G. Villa-Diaz, X. Zhang, W. Chen, R. Philson, S. Weng, H. Xu, P. H. Krebsbach, J. Fu, Hippo/YAP-mediated rigidity-dependent motor neuron differentiation of human pluripotent stem cells. *Nature materials* **13**, 599-604 (2014).
16. Y. Tang, L. Liu, J. Li, L. Yu, F. P. U. Severino, L. Wang, J. Shi, X. Tu, V. Torre, Y. Chen, Effective motor neuron differentiation of hiPSCs on a patch made of crosslinked monolayer gelatin nanofibers. *Journal of Materials Chemistry B* **4**, 3305-3312 (2016).
17. M. Schindler, I. Ahmed, J. Kamal, A. Nur-E-Kamal, T. H. Grafe, H. Y. Chung, S. Meiners, A synthetic nanofibrillar matrix promotes in vivo-like organization and morphogenesis for cells in culture. *Biomaterials* **26**, 5624-5631 (2005).
18. J. Y. Lee, C. A. Bashur, A. S. Goldstein, C. E. Schmidt, Polypyrrole-coated electrospun PLGA nanofibers for neural tissue applications. *Biomaterials* **30**, 4325-4335 (2009).
19. J. Wei, J. Shi, B. Wang, Y. Tang, X. Tu, E. Roy, B. Ladoux, Y. Chen, Fabrication of adjacent micropillar arrays with different heights for cell studies. *Microelectronic Engineering* **158**, 22-25 (2016).
20. T. B. Puschmann, C. Zandén, Y. De Pablo, F. Kirchhoff, M. Pekna, J. Liu, M. Pekny, Bioactive 3D cell culture system minimizes cellular stress and maintains the in vivo - like morphological complexity of astroglial cells. *Glia* **61**, 432-440 (2013).
21. D. Landis, L. A. Weinstein, C. J. Skordeles, Serum influences the differentiation of membrane structure in cultured astrocytes. *Glia* **3**, 212-221 (1990).
22. F. P. U. Severino, J. Ban, Q. Song, M. Tang, G. Bianconi, G. Cheng, V. Torre, The role of dimensionality in neuronal network dynamics. *Scientific reports* **6**, (2016).
23. A. Mazzoni, F. D. Broccard, E. Garcia-Perez, P. Bonifazi, M. E. Ruaro, V. Torre, On the dynamics of the spontaneous activity in neuronal networks. *PloS one* **2**, e439 (2007).
24. C. Grienberger, A. Konnerth, Imaging calcium in neurons. *Neuron* **73**, 862-885 (2012).
25. D. Smetters, A. Majewska, R. Yuste, Detecting action potentials in neuronal populations with calcium imaging. *Methods* **18**, 215-221 (1999).

26. R. Kerr, V. Lev-Ram, G. Baird, P. Vincent, R. Y. Tsien, W. R. Schafer, Optical imaging of calcium transients in neurons and pharyngeal muscle of *C. elegans*. *Neuron* **26**, 583-594 (2000).
27. D. Pozzi, J. Ban, F. Iseppon, V. Torre, An improved method for growing neurons: Comparison with standard protocols. *Journal of Neuroscience Methods* **280**, 1-10 (2017).
28. J. Wei, D. Pozzi, F. P. U. Severino, V. Torre, Y. Chen, Fabrication of PLGA nanofibers on PDMS micropillars for neuron culture studies. *Microelectronic Engineering* **175**, 67-72 (2017).
29. R. A. Zalutsky, R. A. Nicoll, Comparison of two forms of long-term potentiation in single hippocampal neurons. *Science* **248**, 1619-1625 (1990).

Chapter 5 Confinement and deformation of cell nuclei in the interpillar area

In this chapter, we describe a study of the confinement and deformation of cell nuclei in the inter-pillar spaces. Micropillars made of two types of materials, i.e., elastomer PDMS and thermoplastic PCL, are used to illustrate the stiffness dependency of the confinement. Different cell lines, including cancer cells and induced pluripotent stem cells, are used to demonstrate the relevance of this study. Our results show that the nuclei of iPS cells can be more easily confined and deformed in the inter-pillar areas than that of cancer cells, due to their relative small value of Young's modules.

5.1 Introduction

Cell migration in a narrow space may cause DNA damage so that the study of the confinement and deformation of cells and cell nuclei is important for mechanistic understanding of cell migration [1], tissue engineering [2], cancer formation [3] and disease pathology [4], etc. Clearly, the structure of the extracellular matrix (ECM) is a determinant factor of such a study [5,6]. Previously sophisticated techniques such as capillary pipet [7] and AFM [8], or microfluidic chip [9] have been used to deform cells or perturb cell migration. However, these approaches merely furnish monotonous conditions which could not reveal the entire mechanisms of cell confinement and nuclei deformation and an in-vivo like ECM organization is lack for pathological modeling. Therefore, we created micropillar arrays of different stiffness and different spacing to study the cell adhesion and the nuclei confinement under various conditions.

Micropillar arrays were chosen for this study because of the possibility of simultaneous force mapping over large areas and the flexibility of modulating the substrate effective stiffness by changing, for example, the height and the materials of pillars [10-12]. The goal of this work is to observe the cell-line and stiffness dependent nucleus deformation in the confined space of micropillar arrays.

5.2 Cell confinement

Figure 5.1 shows fluorescence images of NIH3T3 cells on a flat surface (a) and SU8 pillar array of 30 μm period and 10 μm gap (b), after incubation of 48 h. Clearly, the cell density on the pillar substrate is lower than that on the flat surface, due probably to a limited rate of growth. Indeed, the cells on the flat surface also spread freely over a relatively large area whereas on the pillar substrate they may easily fall into the inter-pillar area with elongated filopodia. Interestingly, the nucleus of the cell that fell into the inter-pillar area could be significantly deformed without external force.

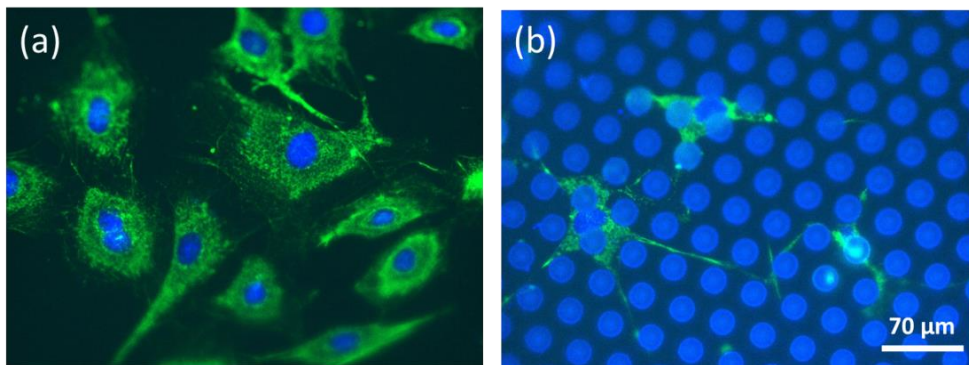


Figure 5.1 Fluorescent images of NIH-3T3 cells cultured on (a) flat silicon wafer and (b) SU8 pillar array of 30 μm period and 10 μm gap. Cell nuclei (DAPI: blue) and actin cytoskeletal networks (Alexa Fluor 488 phalloidin: green).

Depending on the stiffness of the cell and the size of the inter-pillar area, the cells explore the top and bottom surfaces of the pillar substrate. When the stiffness of the cell and the pillar density are both high, cells can stay on the top of the pillars. When the inter-pillar area is large ($>10 \mu\text{m}$), cells can easily fall into the bottom without remarkable nucleus deformation. In the intermediate range, cells could partially fall into the inter-pillar spaces, with or without strong deformation of the cell nuclei which depend on the stiffness of the nuclei. Figure 5.2 illustrates different scenarios of the cell adhesion and cell morphology changes as well as possible nuclei deformation: *i*) no deformation, *ii*) partial deformation, *iii*) complete deformation. Statistically, some cells may change their morphologies from *i*) to *ii*) and then *iii*).

Some others may stop at *i*) or *ii*) further changes. The proportion of the three nucleus states finally determined the deformation properties of the cells and the corresponding nuclear hardness properties, which highly depended on the cell type and related physical characteristics.

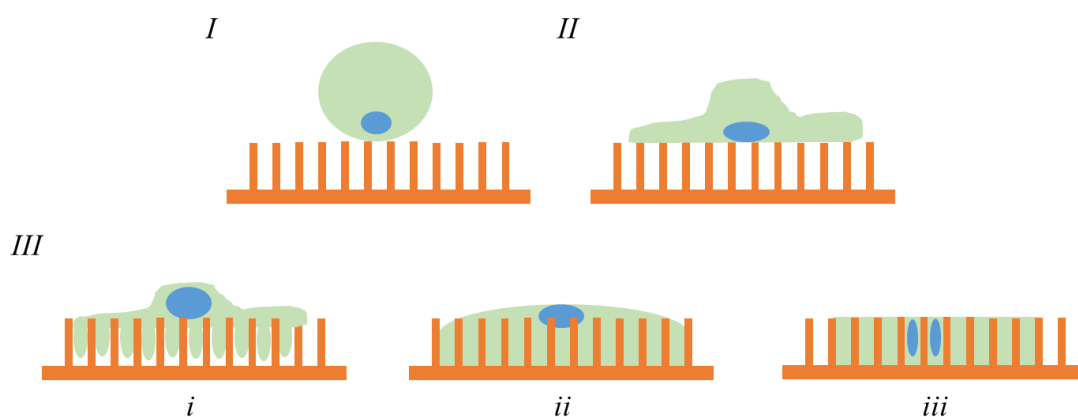


Figure 5.2 Cellular behavior upon adhesion to micropillars. *I*) Cell seeding. *II*) Cell spreading. *III*) Cell adhesion on micropillar array and three states: *i*- no deformation, *ii* - partial deformation, *iii* - complete deformation.

5.2.1 The behaviors of cancer cells

Firstly, we focus on the deformation of MCF7 and HeLa cancer cells on the micropillar substrate. PDMS micropillars of 4.0- μm diameter, 10.7- μm height and 6.8- μm period (in Figure 3.3g) and PCL micropillars of 4.3- μm diameter, 11.2- μm height and 7.0- μm period (in Figure 3.9g) have been used for test.

Before cell seeding, the substrates were sterilized under mild cell-culture UV lamp for 30 min and surface-treated with plasma cleaner for 7 min. Then, a solution of vitronectin (VN) diluted in DPBS in 5 $\mu\text{g}/\text{ml}$ was dropped on the sample surfaces. After waiting for 60 min at room temperature, the excess VN solution was pipetted out (no need to rinse).

The cancer cells were prepared with a culture medium of DMEM with 10% FBS and 1% P/S (37°C, 5% CO₂). Before seeding, the spent medium was aspirated out and DPBS was added to rinse the vessel twice. After DPBS aspiration, Trypsin was added

to cover the vessel for 3 min in incubator (37 °C, 5% CO₂). When cells started to separate and round up, we aspirated Trypsin and add 1 ml fresh medium to remove cells from the vessel by gently squirting and pipetting the medium until the cell colonies broke up to single cell. After cell counting, centrifuging, density adjusting, cell suspension in 5×10^4 cells ml⁻¹ was added on the prepared substrates.

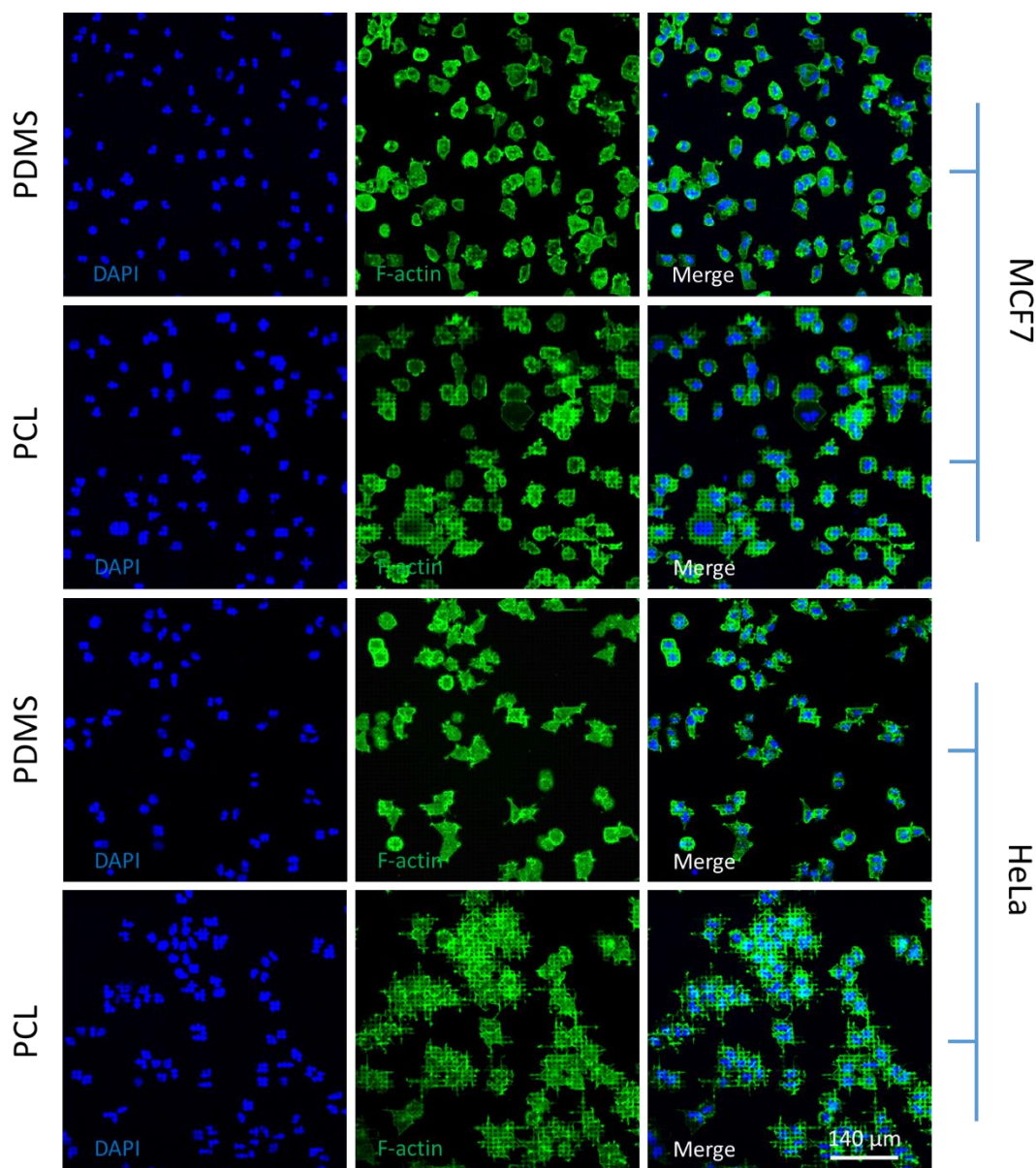


Figure 5.3 Fluorescent images of MCF7 and HeLa cells confined on the micropillar array in PDMS and PCL after 1 day incubation. Cell nuclei (DAPI: blue) and actin cytoskeletal networks (Alexa Fluor 488 phalloidin: green).

Figure 5.3 shows the behavior of cancer cells on the micropillars with adhesion

and confinement. For breast cancer cells, the deformability of nucleus on PDMS substrate was lower than that on PCL. The specific performance was that on PDMS pillars, the ratio of cell nucleus with no deformation and partial deformation was higher than that on PCL pillars. The morphology of the cytoskeleton was different from the previous fibroblasts, without alignment in the certain direction. On PDMS substrates, cells contracted obviously, while on PCL substrates, cells were divided into grid shape, rather than fibrous pseudopod.

For cervical cancer cells, the general deformability and morphology was similar to breast cancer cells, especially on PDMS substrates. The significant difference was that the cells on PCL substrate comparably appeared a relatively high proportion of cells with no deformation or partial deformation, indicating that the deformability of cervical cancer cells on rigid substrates was lower than breast cancer cells. Obviously, the cytoskeleton of HeLa cell on PCL pillars spread filamentous pseudopodia, not as long as 3T3 cells, but with higher invasion and ductility compared with MCF7 cells.

In order to further explore the deformation of cancer cells, we observed the cancer cells with amplified fluorescence image in three-view orthogonal section, as shown in Figure 5.4. From the figure, we obtained the difference between the three deformation states of cells, especially from side view. Some cells were not deformed at all, completely at the top of pillars. In the states, the spreading area of the cell without deformation was significantly larger than the cells with deformation. Some cells did not completely attach to the bottom of the micropillars, and a considerable part of a cell was at the top of micropillars. The other cells (in large proportion) were completely deformed, inserted between the columns, and the profile showing a vertical strip shape.

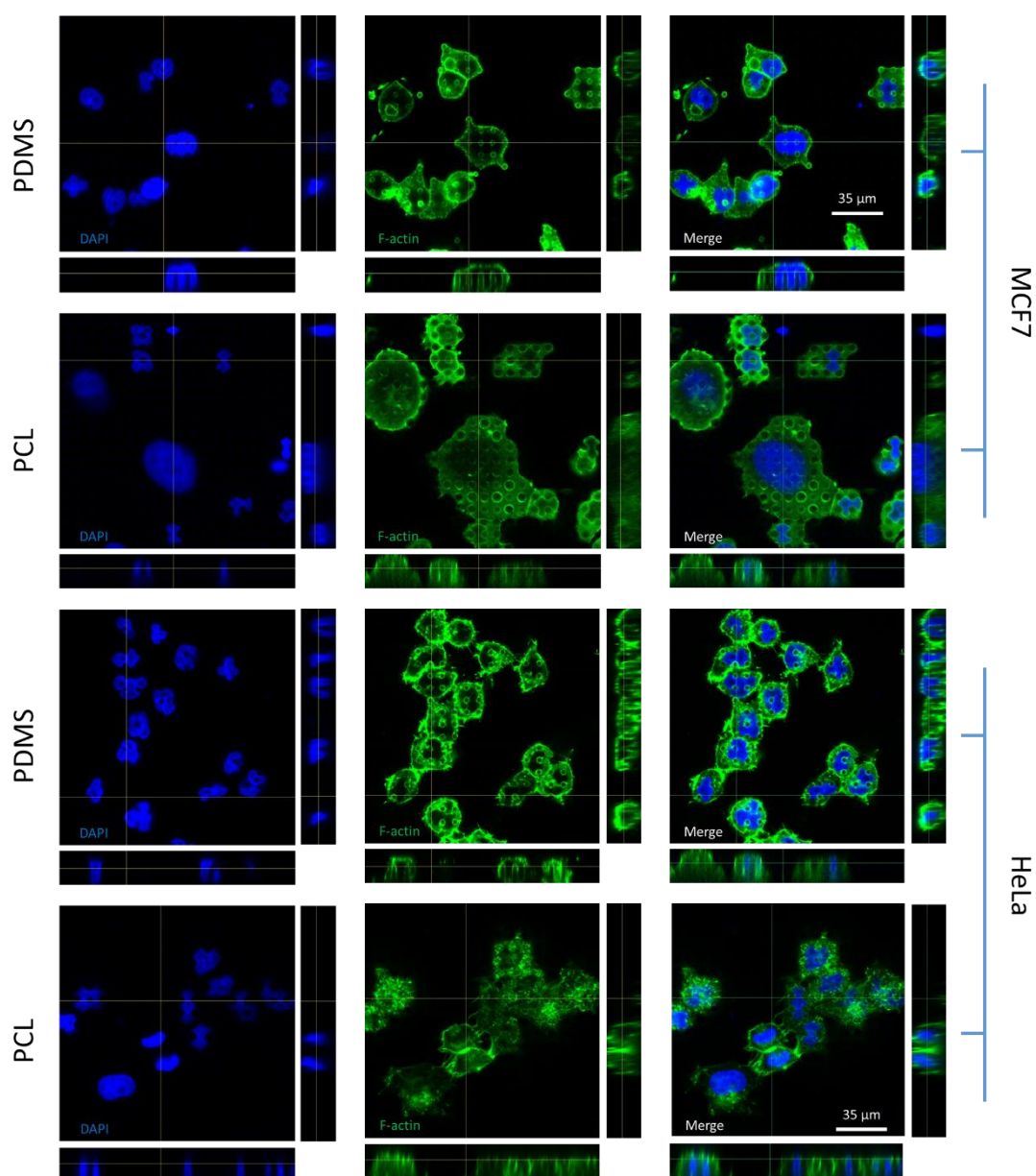


Figure 5.4 Orthogonal view fluorescent images of MCF7 and HeLa cells confined on the micropillar array in PDMS and PCL after 1 day incubation. Cell nuclei (DAPI: blue) and actin cytoskeletal networks (Alexa Fluor 488 phalloidin: green).

5.2.2 The behaviors of iPS cells

Next, we continue to study iPS cells confinement on the micropillar array with same strategies. For iPS cells, substrates in preparation as:

UV lamp – 30 min.

Plasma cleaner – 7 min.

VN in DPBS in 5 $\mu\text{g}/\text{ml}$ – 1 h.

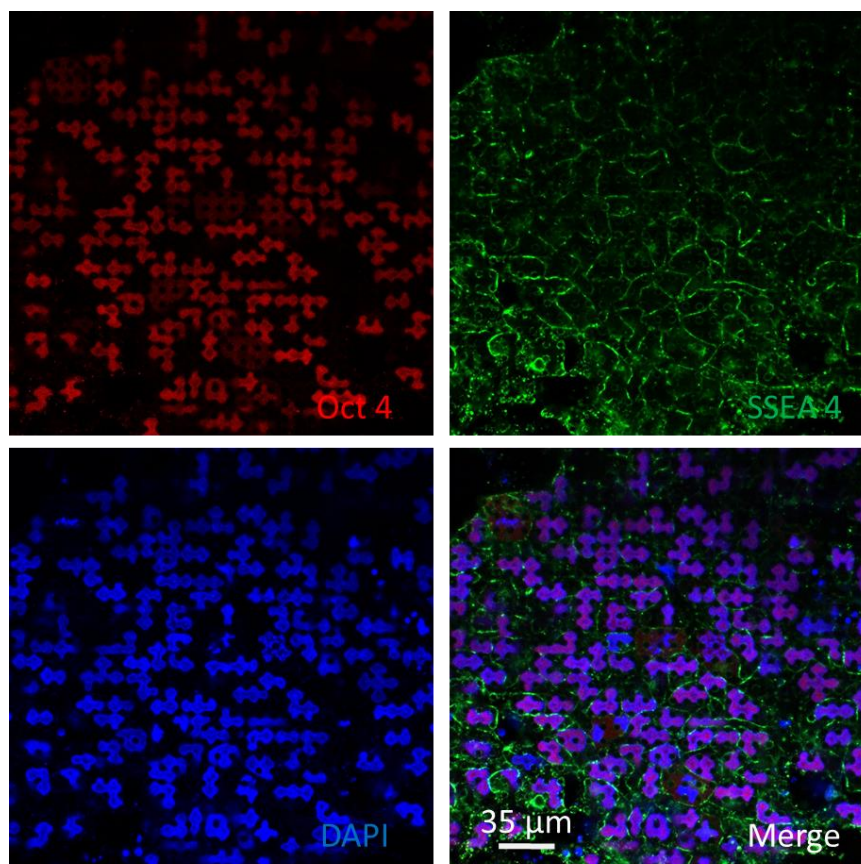


Figure 5.5 Immunocytochemistry analysis of iPS cells on PDMS micropillar array after 1-day incubation. Cell nuclei (DAPI: blue) and pluripotency of cells (Oct4: red and SSEA4: green).

iPS cells were incubated (37 °C, 5% CO₂) in culture medium Essential 8™ (E8) with 2% E8 Supplement (50×). Before seeding, the spent medium was aspirated out and DPBS was added to rinse the vessel twice. Aspirating DPBS, we added ethylenediaminetetraacetic acid (EDTA) in 0.2 mM covering the vessel for 4 min in incubator (37 °C, 5% CO₂). When cells started to separate and round up, we aspirated EDTA and add 1 ml fresh medium to remove cells from the vessel by gently squirting and pipetting the medium until the cell colonies broke up to single cell. After cell counting, centrifuging, density adjusting, cell suspension in 1.5×10^5 cells ml^{-1} in fresh medium with 0.1 % RHO/ROCK pathway inhibitor (Y-27632) were added on the prepared substrates. Because the characteristics of iPS cells were different

from 3T3 cells and cancer cells, the increment of cell density and the addition of Y-27632 were to improve cell survival. Moreover, Y-27632 could improve the adhesion of iPS cells to the artificial substrates.

Figure 5.5 shows the behavior of iPS cells on the PDMS micropillars with adhesion and confinement. Even in high-density condition, the cells appeared more significant deformation characteristics than other previous cell types. Specific performance for iPS, there was higher proportion of the cells with complete deformation. Based on experiments, there were no cells without deformation.

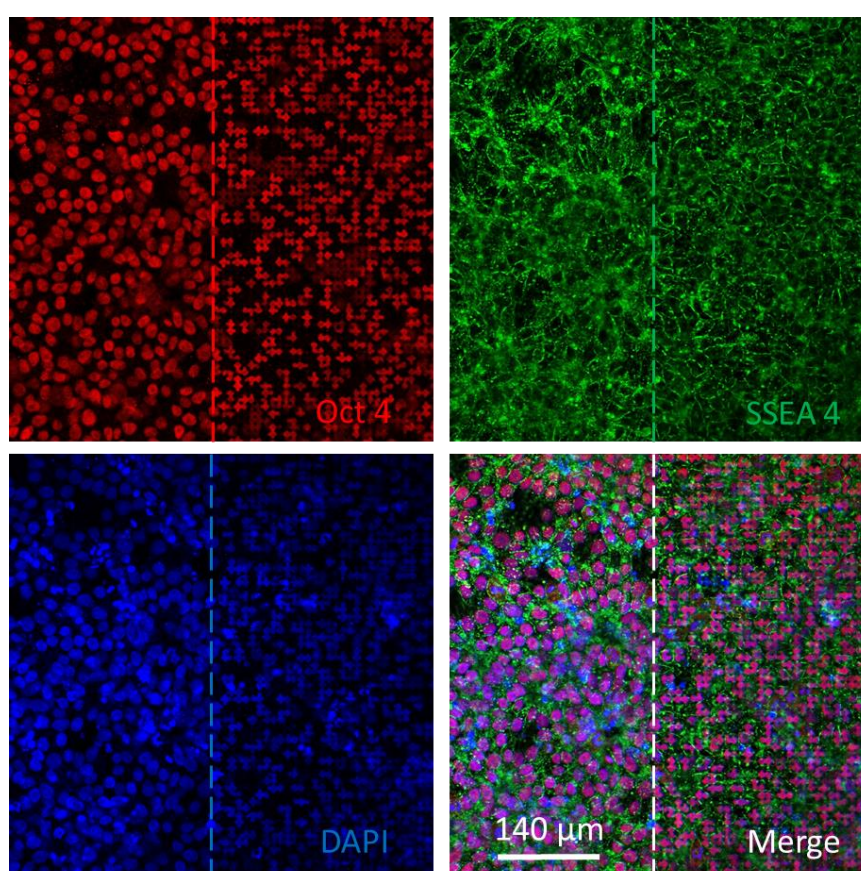


Figure 5.6 Immunocytochemistry analysis of iPS cells on PDMS micropillar area vs flat area after 1-day incubation. Cell nuclei (DAPI: blue) and pluripotency of cells (Oct4: red and SSEA4: green).

In the comparison from PDMS micropillar area to flat area, as shown in Figure 5.6, the difference in cell morphology was mainly reflected in the shape of nucleus. From the top view, the area of cell nucleus was reduced by nearly half. Further

explanation, through the morphology of nucleus, it was distinguished which areas with micropillar array, which areas without. It was helpful for identifying the substrates morphology and topography. Interestingly, in the state of deformation, the pluripotency of cells remained the same to the non-deformation, which was the critical factor for the study of iPS cells for protein and gene expression under nucleus confinement.

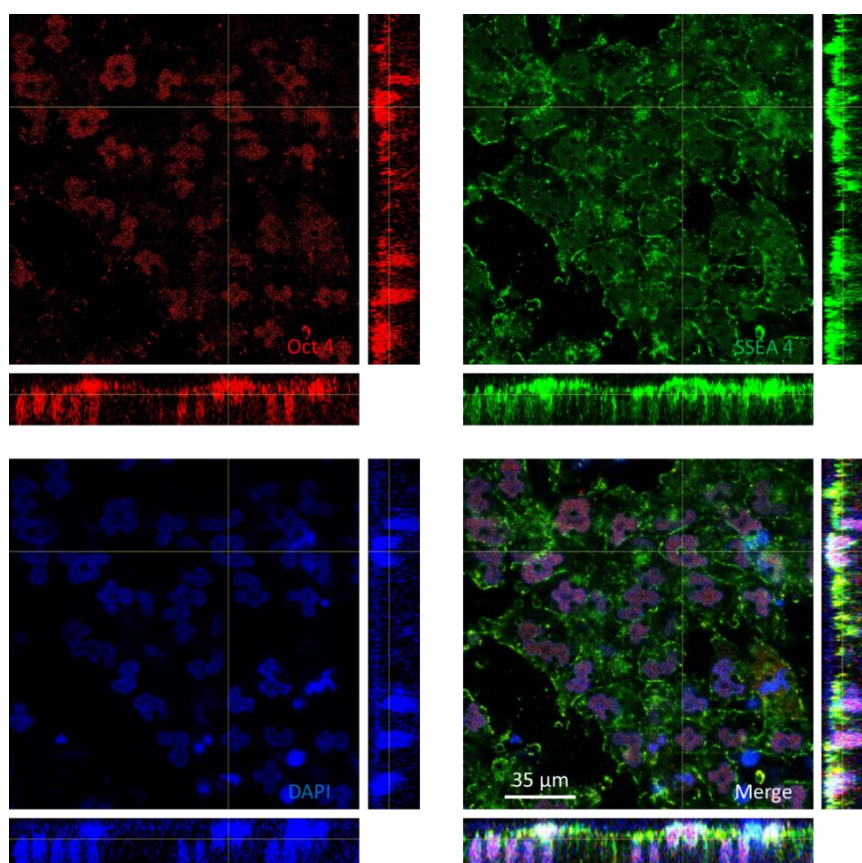


Figure 5.7 Orthogonal view immunocytochemistry analysis of iPS cells on PDMS micropillar after 1-day incubation. Cell nuclei (DAPI: blue) and pluripotency of cells (Oct4: red and SSEA4: green).

To further explore the deformation of iPS cells, we observed the cells with amplified fluorescence image in three-view orthogonal section, as shown in Figure 5.7. Similar to previous experiments with cancer cells, cells with partial deformation and complete deformation were observed after 1-day culture. For the Oct4 fluorescence expression, the pluripotency of cell nucleus fairly maintained a high

consistency of the nuclear deformation (DAPI), even in the state of complete deformation. For the SSEA fluorescent expression, the pluripotency of cell cytoplasmic components did not deform with the deformation of plastids. Most of the components located on the top surface of micropillars, in the formation of membranous. It could be concluded that the cell confinement based on micropillar array could result in a certain separation of the pluripotent component of cell nucleus and cytoplasm.

5.3 Deformability of iPS cells

Micropillar substrates made of PDMS and PCL were effective to determine the deformability of cells and cell nuclei during cell-adhesion confinement. We found that the nuclei of iPSCs can be more easily confined and deformed in the inter-pillar areas than that of cancer cells, due to their relative small value of Young's modules.

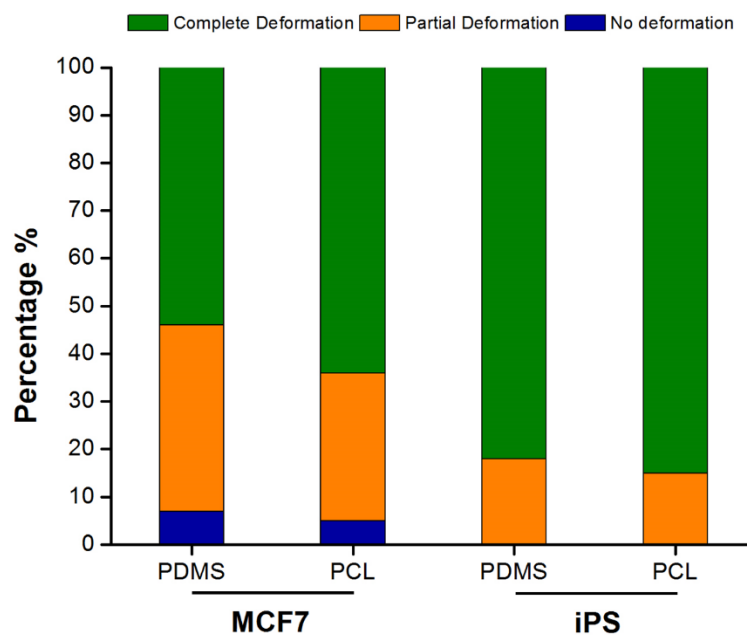


Figure 5.8 Nuclei confinement behavior of the different cell types categorized according to the three deformation states.

By comparing cell amount of in different deformation states between MCF7 and iPS cells, as demonstrated in Figure 5.8, the deformability of cell nucleus could be

obtained and the hardness of the nucleus could be deduced. MCF7 cells on PDMS & PCL micropillar array, the percentage of cell nucleus with no deformation, partial deformation, and complete deformation was 7% & 5%, 39% & 31% and 54% & 75%, respectively. For iPS cells, the proportion of cell nucleus in the three deformation states was 0% & 0%, 18% & 15% and 82% & 85%, respectively.

Figure 5.9 shows that the cell deformation varies with the height of micropillars, especially the proportion of complete deformation. On flat PDMS wafer, cell nuclei did not deform at all. When pillar height became higher, the proportion of complete deformation gradually increased.

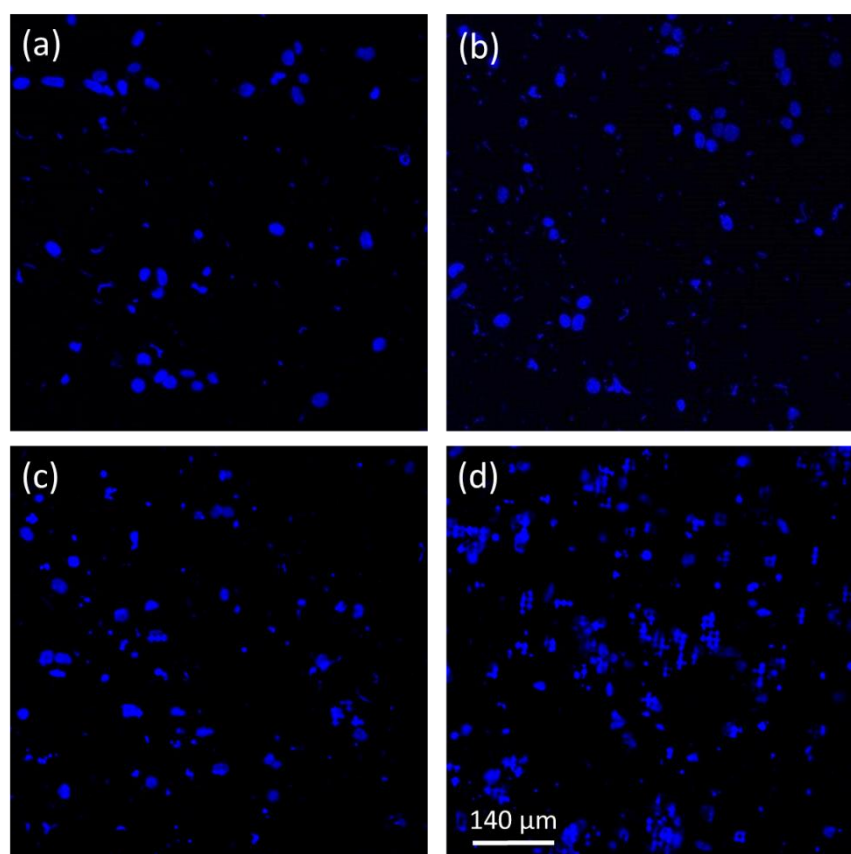


Figure 5.9 Immunocytochemistry analysis of iPS cells on (a) PDMS flat area and micropillars with (b) short, (c) medium, (d) high micropillar array after 1-day incubation. Cell nuclei (DAPI: blue).

Based on the fluorescent images on nuclei deformation on different micropillar arrays, we can account for the proportion of completely deformed cells, as illustrated

in Figure 5.10. The highest was 10-micron pillar array, as same sample as the previous experiment, the ratio of nuclear with complete deformation could reach more than 95%. For 1.6-micron micropillar array, such a small structure was not sufficient to allow the iPS cells to pass through to form complete deformation. Most of the cells could wrap 1.6-micron pillars around to form partial deformation. For 10.7-micron substrate, the cells could pass through the micropillars till the substrate bottom, resulting in nuclei complete deformation.

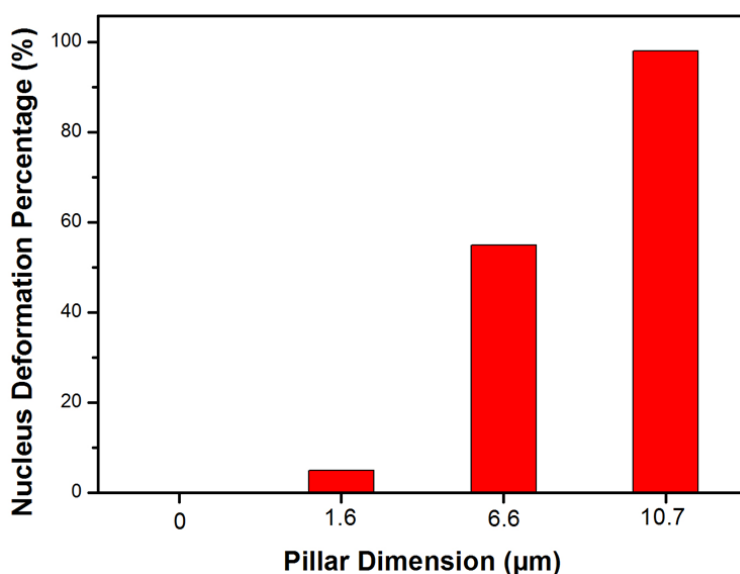


Figure 5.10 iPS cell nuclei complete deformation behavior on the flat PDMS wafer and the micropillar substrates with different height.

The deformation of cell nucleus directly resulted to the changes in cell behavior. The most obvious was the change of cell proliferation. The rate of cell proliferation on 10.7- μm micropillars was 1/2 of flat PDMS and 1.6- μm micropillar. Moreover, on all micropillar substrates, regardless of the height, iPS cells were more likely to be assembled, even with the treatment of Y-27632. Therefore, iPS cells cultured on micopillar substrates were efficient to form embryonic body.

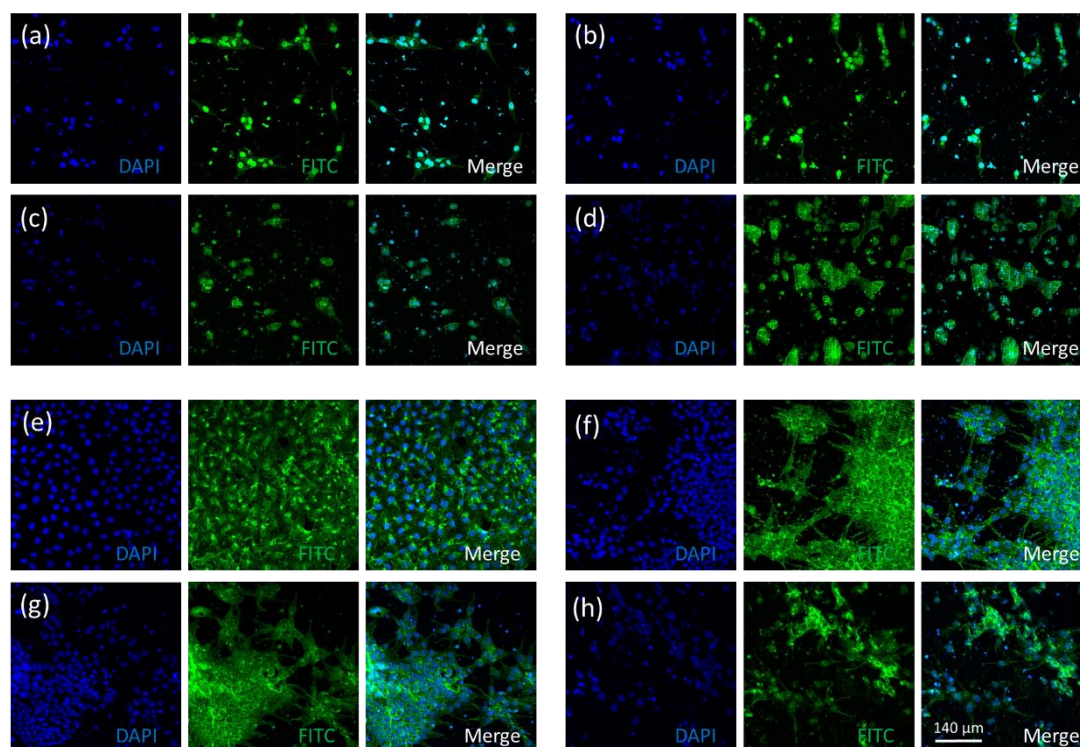


Figure 5.11 Fluorescent images of iPS cells cultured on substrates of (a)(e) flat PDMS, and PDMS (b)(f) short, (c)(g) medium, (d)(h) high micropillar array after 1-day and 3-day incubation, respectively. Cell nuclei (DAPI: blue) and actin cytoskeletal networks (Alexa Fluor 488 phalloidin: green).

5.4 Summary

The nuclei of iPS cell was with high deformability and extremely soft. The physical property, especially the stiffness, of iPS cell was highly similar to other types of stem cell. It could be inferred that the expression of Lamin A/C (in protein) and LMNA (in gene) in iPS cells was at a relatively low level and gradually increased in the process of differentiation [2,13,14].

References

1. Y.-J. Liu, M. Le Berre, F. Lautenschlaeger, P. Maiuri, A. Callan-Jones, M. Heuzé, T. Takaki, R. Voituriez, M. Piel, Confinement and low adhesion induce fast amoeboid migration of slow mesenchymal cells. *Cell* **160**, 659-672 (2015).
2. J. Swift, I. L. Ivanovska, A. Buxboim, T. Harada, P. D. P. Dingal, J.

Pinter, J. D. Pajerowski, K. R. Spinler, J.-W. Shin, M. Tewari, Nuclear lamin-A scales with tissue stiffness and enhances matrix-directed differentiation. *Science* **341**, 1240104 (2013).

3. C. T. Skau, R. S. Fischer, P. Gurel, H. R. Thiam, A. Tubbs, M. A. Baird, M. W. Davidson, M. Piel, G. M. Alushin, A. Nussenzweig, FMN2 makes perinuclear actin to protect nuclei during confined migration and promote metastasis. *Cell* **167**, 1571-1585. e1518 (2016).

4. D. G. Thomas, A. Yenepalli, C. M. Denais, A. Rape, J. R. Beach, Y.-I. Wang, W. P. Schiemann, H. Baskaran, J. Lammerding, T. T. Egelhoff, Non-muscle myosin IIB is critical for nuclear translocation during 3D invasion. *J Cell Biol*, jcb. 201502039 (2015).

5. R. J. Petrie, K. M. Yamada, Multiple mechanisms of 3D migration: the origins of plasticity. *Current opinion in cell biology* **42**, 7-12 (2016).

6. R. P. Mecham, D. E. Birk, P. D. Yurchenco, *Extracellular matrix assembly and structure*. (Academic Press, 2013).

7. J. D. Pajerowski, K. N. Dahl, F. L. Zhong, P. J. Sammak, D. E. Discher, Physical plasticity of the nucleus in stem cell differentiation. *Proceedings of the National Academy of Sciences* **104**, 15619-15624 (2007).

8. A. B. Mathur, A. M. Collinsworth, W. M. Reichert, W. E. Kraus, G. A. Truskey, Endothelial, cardiac muscle and skeletal muscle exhibit different viscous and elastic properties as determined by atomic force microscopy. *Journal of biomechanics* **34**, 1545-1553 (2001).

9. X. Cao, E. Moeendarbary, P. Isermann, P. M. Davidson, X. Wang, M. B. Chen, A. K. Burkart, J. Lammerding, R. D. Kamm, V. B. Shenoy, A Chemomechanical Model for Nuclear Morphology and Stresses during Cell Transendothelial Migration. *Biophysical journal* **111**, 1541-1552 (2016).

10. Y. Sun, K. M. A. Yong, L. G. Villa-Diaz, X. Zhang, W. Chen, R. Philson, S. Weng, H. Xu, P. H. Krebsbach, J. Fu, Hippo/YAP-mediated rigidity-dependent motor neuron differentiation of human pluripotent stem cells. *Nature materials* **13**, 599-604 (2014).

11. Y. Shao, K. Taniguchi, K. Gurdziel, R. F. Townshend, X. Xue, K. M. A. Yong, J. Sang, J. R. Spence, D. L. Gumucio, J. Fu, Self-organized amniogenesis by human pluripotent stem cells in a biomimetic implantation-like niche. *Nature materials* **16**, 419-425 (2017).

12. M. T. Yang, N. J. Sniadecki, C. S. Chen, Geometric Considerations of Micro - to Nanoscale Elastomeric Post Arrays to Study Cellular Traction Forces. *Advanced materials* **19**, 3119-3123 (2007).

13. D. E. Discher, D. J. Mooney, P. W. Zandstra, Growth factors, matrices, and forces combine and control stem cells. *Science* **324**, 1673-1677 (2009).

14. P. M. Davidson, J. Lammerding, Broken nuclei–lamins, nuclear mechanics, and disease. *Trends in cell biology* **24**, 247-256 (2014).

Chapter 6 Integration of micropillars into microfluidic devices for cell culture studies

In this chapter, we describe a method to integrate micropillar arrays into a microfluidic device for cell migration studies. PDMS pillars of 10 μm height were firstly produced on a glass slide. A thick PDMS layer with 50 μm height channels were obtained by casting and bonded to the PDMS pillar/glass slide. Afterward, NIH 3T3 cells were seeded into the channel and a concentration gradient of Fetal Bovine Serum (FBS) was generated in the channel after 2h incubation for adhesion. We observed that cells migrated to the higher FBS concentration region with a migration speed almost twice slower than that on a flat PDMS.

6.1 Introduction

Cell migration is dictated by both chemical (chemokine) and physical signals [1]. A large number of studies have been developed by using chemo-attractants, electric fields, mechanical gradients [2-4] but less has been reported on the combined use of chemical and physical cues in a dynamic fashion [5]. On one hand, microfluidic technologies are now widely used enabling delivery of reagents, nutrients, and other cell factors at high temporal resolution [6]. In particular, chemical gradients can be created in microfluidic channels allowing systematical investigation of cell migration responding the change of growth factor, hormones and chemokines [7-9]. On the other hand, a variety of patterned substrates are used to study surface morphology and material stiffness dependent cell migration. Among many others, micropillar arrays are of interest for mechano-transduction studies of cells [10]. In both cases, real-time optical microscopy can be used to measure the cell interaction induced pillar deformation and then to generate real-time force maps [11-13].

By integrating micropillars into microfluidic devices, as shown in Figure 6.1, we created a novel platform for cell migration studies. This platform allows us culturing cells and monitoring their migration behaviors under conditions of well-defined substrate stiffness and chemical gradients. The microfluidic chip fabricated via photolithography and soft lithography was composed of three parts: channel layer, pillar layer and glass support.

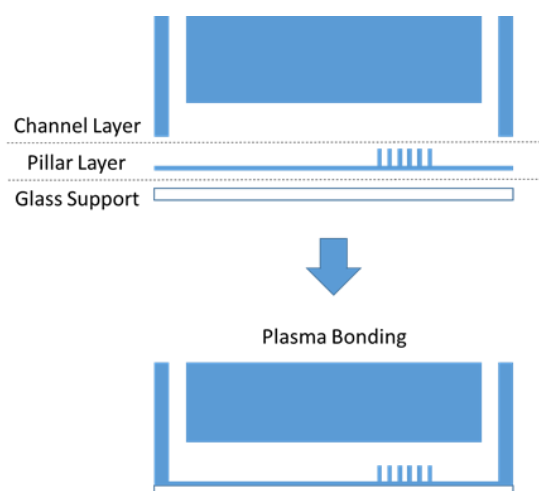


Figure 6.1 Schematic diagrams of the fabrication process of microfluidic platform.

6.2 Fabrication of Microfluidic Chip

6.2.1 Fabrication of micropillar array

Micropillar arrays used in this work were obtained by casting PDMS on a PDMS mold with holes, whereas the PDMS mold was initially obtained PDMS casting on a photoresist mold (master) fabricated by photolithography [14]. Firstly, micro-hole arrays were patterned on the Cr mask using a micro pattern generator (μ PG101, Heidelberg, Germany). Then, a 10- μ m-thick negative resist layer (SU8-3010) was spin-coated on the mask and back-side ultraviolet (UV) exposed. After development, pillars of 10- μ m height, 3- μ m diameter and 15- μ m period were obtained and used as mold features to cast a mixture of PDMS pre-polymer and crosslink agent at ratio of 10:1.

Before casting, the photoresist mold was treated in oxygen plasma for 2 min and then in TMCS vapor for 30 min. After PDMS casting and curing at 80 °C for 2 h, the PDMS layer was peeled-off, resulted in negative replica of the mold features. Next, 0.2- μ m thick Parylene C was deposited on the PDMS layer with a vacuum deposition system (SCS Labcoter 2, SCS Ltd, UK). Afterward, a positive-tone replica of the master was finally obtained by casting liquid PDMS on the PDMS mold using the same casting process. Then pillar layer was fabricated with 3- μ m-diameter, 10- μ m-high,

15- μm -period and hexagonal arrangement (as shown in Figure 6.2) on the support of a glass slide to prove rigidity of the final device.

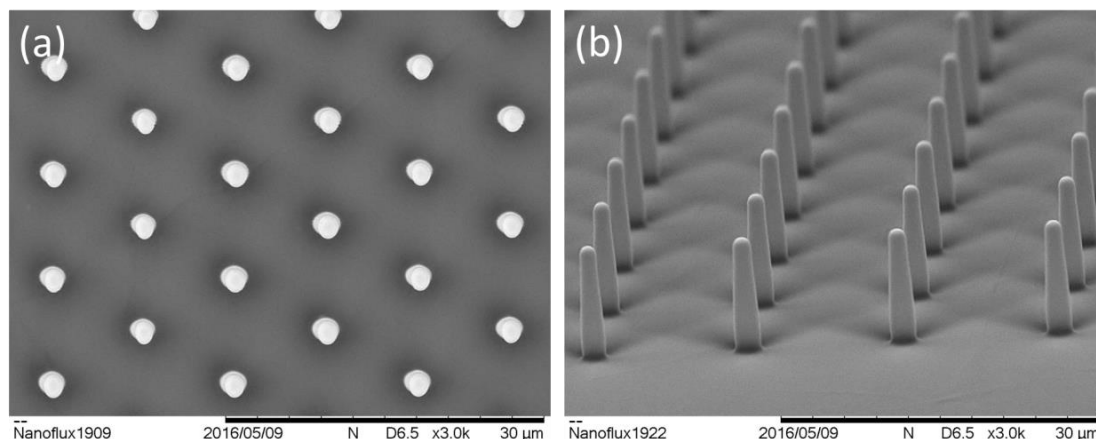


Figure 6.2 SEM images of PDMS micropillar array with 3- μm diameter, 10- μm height, 15- μm period and hexagonal arrangement.

6.2.2 Fabrication of microchannel

To control the distribution of diffusion concentration, we used a microchannel network similar to “Christmas tree”, as shown in Figure 6.3, with side-by-side laminar without turbulent mixing. Different from the fabrication process of micropillar array, the microchannel was achieved via one-step frontside photolithography and one-step soft lithography replication. First, a silicon wafer was placed on the spin-coater fixed by vacuum pump. 1-2 ml of SU8-3050 photoresist was dropped on the clean surface of the wafer. Second, the photoresist was spread around uniformly under low spin velocity to cover the whole pattern area. Then, with the increasing of spin velocity, excess SU8 was spun out of the mask to the wall of spin-coater chamber, only $\sim 50\ \mu\text{m}$ thickness remained. After soft bake for 1 min @ 65 °C and 15 min @ 95 °C, the resist-coated mask was reversed, Cr pattern covering the photoresist layer, and exposed by UV lamp for 20 s. Afterwards, the mask was reversed again and post-baked for 1 min @ 65 °C and 5 min @ 95 °C. Waiting for cooling down, the resist-coated mask was immersed in SU8 developer solvent for 10 min with gentle

agitation and rinsed with Isopropanol, dried with Nitrogen. Since the photoresist mold was positive structure, PDMS channel was fabricated by casting a mixture of PDMS pre-polymer and crosslink agent at ratio of 10:1 on the photoresist mold. After PDMS casting and curing for 2 h @ 80 °C, the PDMS layer was peeled-off. To ensure the successful replication, the photoresist positive mold was treated in oxygen plasma for 2 min and then in TMSi vapor for 30 min for peel-off separation before casting of PDMS.

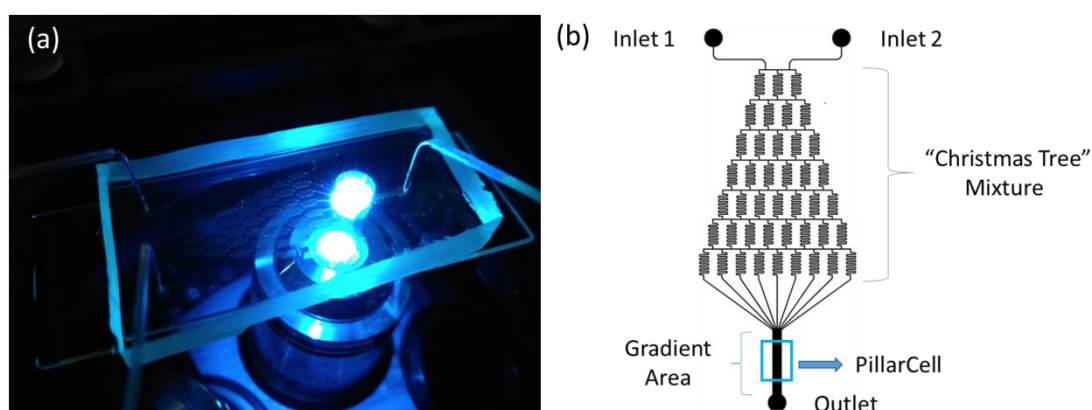


Figure 6.3 (a) The microfluidic platform under fluorescence flow experiments. (b) CAD illustration of microfluidic platform function.

Microchannel layer was achieved with 50- μm -high, 100- μm -wide branch area and 1-mm-wide gradient area. In particular, the micropillars were located only in the 1-mm-wide gradient area, as shown in Figure 6.3. After punching through holes for inputs and output in the channel layer and surface plasma treatment, the functional polydimethylsiloxane (PDMS) channel layer and pillar layer were aligned and bonded together and ready for following experiment.

6.3 Microfluidic control and gradient generation

6.3.1 Basic theory of microfluidic flow

Due to the flow in the channel networks with low Reynolds number (Re), two adjacent streams diffused on the interface along with the mixing channel and the

gradient distribution is perpendicular to the flow direction [15]. Based on Equation 5.1, low inertial/viscous value ensured that inertial force is typically inferior to viscous forces, resulting linear flow in the microfluidic channel,

$$\frac{f_i}{f_v} = \frac{\rho U_0 L_0}{\eta} \equiv \text{Re} \quad (5.1)$$

where f_i is inertial centrifugal force density, f_v is viscous force densities, L_0 is a typical length scale, U_0 is characteristic velocity scale, ρ is density, η is shear viscosity.

The dimensionless number, Péclet number (Pe), refers to the characteristics of convection/diffusion (Equation 5.2) during adjacent linear flow, the higher value the flow speed, the high value of Pe, the lower degree of diffusion [15],

$$\frac{Z}{w} \sim \frac{U_0 w}{D} \equiv \text{Pe} \quad (5.2)$$

where Z is the downstream distance scale, w is the width of the channel, D is the diffusivity.

6.3.2 Gradient generation

Fluorescein Sodium (Sigma-Aldrich, France) with concentration of 0.1 mmol/l was injected in Inlet A while Buffer (deionized water) in Inlet B. Figure 6.4 (a)-(c) shows the fluorescence gradient distribution various with supplied flow speed (1 ml/h, 0.1 ml/h, 0.01 ml/h) in the region of 1-mm-width channel.

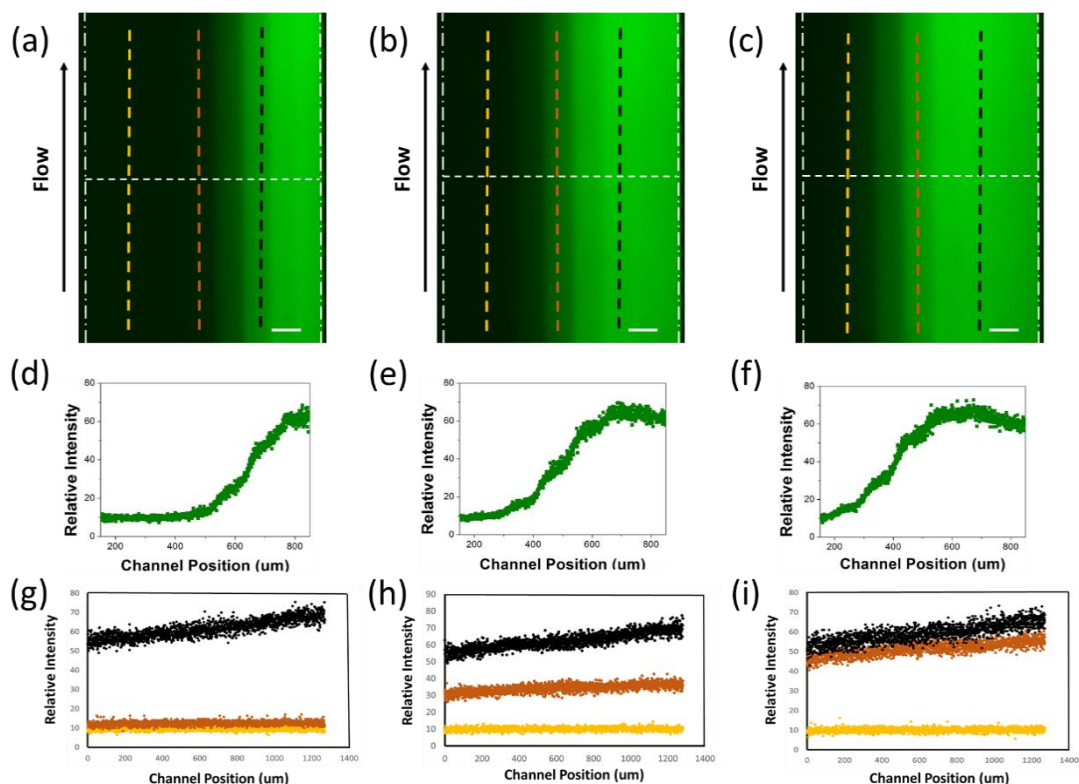


Figure 6.4 Gradients of fluorescein Sodium observed at the gradient 1mm-width area with supplied flow rates of (a) 1 ml/h, (b) 0.1ml/h and (c) 0.01 ml/h, respectively. Scale bar is 100 μm . Fluorescence intensity profile perpendicular (white dashed line) and parallel (colored dashed line) to the flow direction in the region of downstream with supplied flow rates of (d)(g) 1 ml/h, (e)(h) 0.1ml/h and (f)(i) 0.01 ml/h, respectively.

We generated a microchannel network with side-by-side laminar without turbulent mixing. Due to the flow in the channel networks with low Reynolds number (Re), two adjacent streams diffused on the interface along with the mixing channel and the gradient distribution was perpendicular to the flow direction. Figure 6.4 (d)-(f) and (g)-(i) show respectively intensity profiles of fluorescence concentration gradients at different flow rates (1, 0.1, 0.01 mL/h) in the area of 1-mm-wide channel. It is interesting to note that the linear areas of the concentration gradient are different with different flow rates. Concentration gradient in channel was nonlinear under high flow speed at the low concentration area. With reducing the flow speed, the nonlinear part shifts towards the high concentration area.

6.4 Cell culture in microfluidic chip

First, cells cultured in growth media (DMEM with 10% FBS, 1% penicillin/streptomycin), were trypsinized, centrifuged and re-suspended with cell density $\sim 10^7$ cell/ml. Then 50- μ L cell suspension was dropped on the outlet and entered into the gradient area integrated with micropillar arrays by the infiltration of the solution. Afterward, the whole chip was put in an incubator (37 °C, 5% CO₂) for 2 h for cell attachment. Finally, new culture media (DMEM with 10% FBS, 1% penicillin/streptomycin) were added in Inlet 1 and rinse media (DMEM with 0% FBS, 1% penicillin/streptomycin) were added in Inlet 2, both with a flow rate of 50 μ L/h for continuous cell culture.

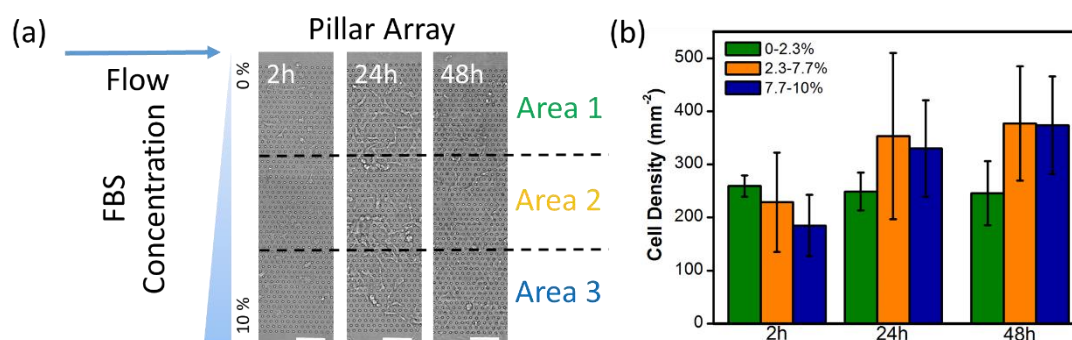


Figure 6.5 (a) Images of NIH 3T3 cell distribution and morphology after seeding 2 h static attachment and in the gradient of FBS and continuous culture for 0h, 22h and 46h respectively. Scale bar is 75 μ m. (b) Cell density various along with the culture time in three areas of 0-2.3%, 2.3-7.7% and 7.7-10% FBS.

Figure 6.5 shows the variation of NIH 3T3 cell density on micropillar areas under FBS concentration gradients versus culture time. In the areas of FBS concentration 0-2.3%, the number of cells remained constant approximately from 2 h to 48 h after seeding. Conversely, the cells amount in the region of 2.3-7.7% and 7.7-10% increased significantly after 24 h. Afterwards, the cell number continuously increased in the highest concentration area. Typically, cells on micropillars were contracted while they spread on a flat surface.

Moreover, it was noticeable that the cell migration behavior on the pillar area was different from the flat area, as shown in Figure 6.6. At the beginning, the cell migrated from flat area towards pillar area along with the direction of sensing in the speed $\sim 20 \mu\text{m}/\text{h}$. When sensing the soft micropillar, the cell shrank and slowed down in the speed $< 10 \mu\text{m}/\text{h}$. The hindering effect of pillar structure caused the decrease of cell migration speed, which might cause the uneven cell distribution.

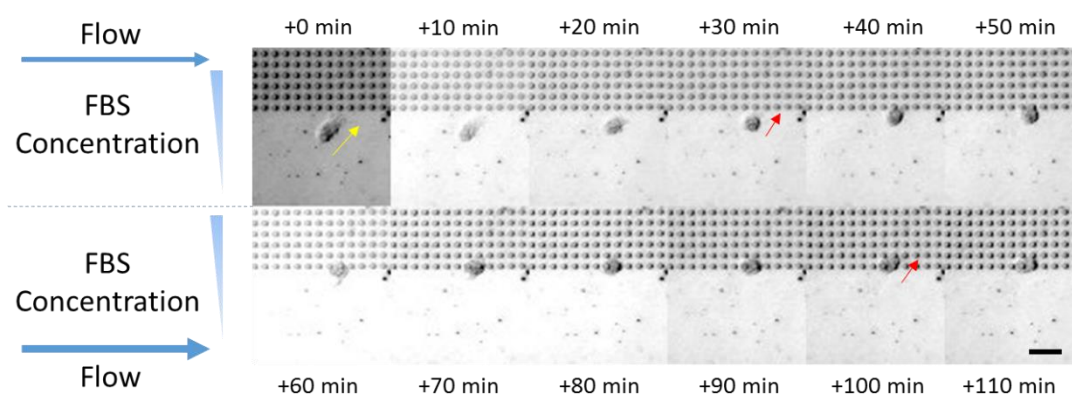


Figure 6.6 Time-lapse images of NIH 3T3 cell migration on flat area and micropillar array between 3rd and 5th hour after seeding. Scale bar is $30 \mu\text{m}$.

At low flow rate ($0.1 \text{ ml}/\text{h}$), cells were sensitive to both FBS concentration gradient and shear-force of the flow. They migrated accordingly along with the co-direction. More detailed analyses could be based on the behavior of single cell migration. Figure 6.7 shows snapshot images of the cell migration on a micropillar array, under influences of flow shear force and FBS gradient. Forces applied by cells on their environment could be evaluated by measuring the deformation of the pillar and using the pillar spring constant induced in Equation 3.1 and 3.2. In this case, $r = 1.5 \mu\text{m}$ and $H = 10 \mu\text{m}$, resulting a spring constant of $3.8 \text{ nN}/\mu\text{m}$. From time lapse microscopy images, we could track with this method the forces applied by cells over time. Taking as example as Pillar 1 at the backstream of the cell migration, its elongation at time origin ($+0.0 \text{ min}$) was $7.6 \mu\text{m}$. After outstretching, the elongation of the pillar was reduced due to a cytoskeleton re-modeling. However, a pillar bending force of $8.7\text{-}12.8 \text{ nN}$ was maintained keeping the cytoskeleton stretched.

The elongation of Pillar 2 and 3 in the front of cell migration also decreased after outstretching and re-modeling, except that the elongation of Pillar 3 slightly increased during the last stage of the time course. The elongation of Pillar 4 was reduced from 24.3 nN to 0 after cell migration since the cell had no more interaction with it. In the end, the elongation of Pillar 5 was 3.2 μm from which an interaction force of 12.5 nN could be deduced. Thus, a dynamic force mapping could be possible during cell migration on pillar arrays and more systematic investigations are expected using a designed and sophisticated cell microenvironment.

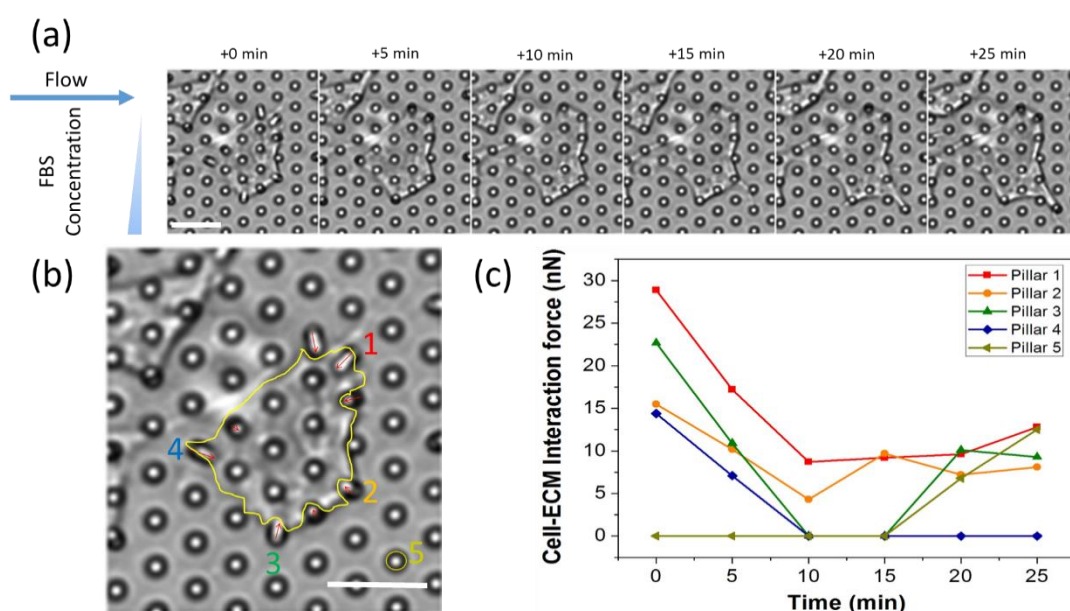


Figure 6.7 (a) Time-lapse images of cell-pillar interaction after seeding 2 hours. (b) Image of cell-pillar interaction and cell contour. Scale bar is 30 μm . (c) Cell-ECM interaction force varies along with the cell migration time.

6.5 Summary

A dynamic control platform was fabricated by integrating the micropillar array in microfluidic control (concentration gradient) chip, resulting cell studies combining of chemical microenvironment and physical factor. The results show that NIH 3T3 cells are sensitive to the concentration distribution of FBS in culture medium and migrate along with the co-direction of FBS gradient and flow. During the migration,

micropillars hinder cell movement and reduce migration speed. Due to the stiffness of micropillar, the cell-ECM interaction force can be calculated by measuring the deformation of micropillar bending during the cell migration, in the scale of nano Newton.

References

1. R. Förster, A. E. Mattis, E. Kremmer, E. Wolf, G. Brem, M. Lipp, A putative chemokine receptor, BLR1, directs B cell migration to defined lymphoid organs and specific anatomic compartments of the spleen. *Cell* **87**, 1037-1047 (1996).
2. X. Zhao, S. Jain, H. B. Larman, S. Gonzalez, D. J. Irvine, Directed cell migration via chemoattractants released from degradable microspheres. *Biomaterials* **26**, 5048-5063 (2005).
3. J. F. Feng, J. Liu, X. Z. Zhang, L. Zhang, J. Y. Jiang, J. Nolta, M. Zhao, Guided migration of neural stem cells derived from human embryonic stem cells by an electric field. *Stem cells* **30**, 349-355 (2012).
4. C.-M. Lo, H.-B. Wang, M. Dembo, Y.-I. Wang, Cell movement is guided by the rigidity of the substrate. *Biophysical journal* **79**, 144-152 (2000).
5. J. Gurdon, P.-Y. Bourillot, Morphogen gradient interpretation. *Nature* **413**, 797-803 (2001).
6. J. El-Ali, P. K. Sorger, K. F. Jensen, Cells on chips. *Nature* **442**, 403-411 (2006).
7. N. L. Jeon, H. Baskaran, S. K. Dertinger, G. M. Whitesides, L. Van De Water, M. Toner, Neutrophil chemotaxis in linear and complex gradients of interleukin-8 formed in a microfabricated device. *Nature biotechnology* **20**, 826-830 (2002).
8. M. G. Roper, J. G. Shackman, G. M. Dahlgren, R. T. Kennedy, Microfluidic chip for continuous monitoring of hormone secretion from live cells using an electrophoresis-based immunoassay. *Analytical chemistry* **75**, 4711-4717 (2003).
9. D. Irimia, S.-Y. Liu, W. G. Tharp, A. Samadani, M. Toner, M. C. Poznansky, Microfluidic system for measuring neutrophil migratory responses to fast switches of chemical gradients. *Lab on a chip* **6**, 191-198 (2006).
10. X. Du, Y. Wang, L. Yuan, Y. Weng, G. Chen, Z. Hu, Guiding the behaviors of human umbilical vein endothelial cells with patterned silk fibroin films. *Colloids and Surfaces B: Biointerfaces* **122**, 79-84 (2014).
11. L. Trichet, J. Le Digabel, R. J. Hawkins, S. R. K. Vedula, M. Gupta, C. Ribault, P. Hersen, R. Voituriez, B. Ladoux, Evidence of a large-scale mechanosensing mechanism for cellular adaptation to substrate stiffness. *Proceedings of the National Academy of Sciences* **109**, 6933-6938 (2012).

12. B. Ladoux, E. Anon, M. Lambert, A. Rabodzey, P. Hersen, A. Buguin, P. Silberzan, R.-M. Mege, Strength dependence of cadherin-mediated adhesions. *Biophysical journal* **98**, 534-542 (2010).
13. J. Fu, Y.-K. Wang, M. T. Yang, R. A. Desai, X. Yu, Z. Liu, C. S. Chen, Mechanical regulation of cell function with geometrically modulated elastomeric substrates. *Nature methods* **7**, 733-736 (2010).
14. J. Wei, J. Shi, B. Wang, Y. Tang, X. Tu, E. Roy, B. Ladoux, Y. Chen, Fabrication of adjacent micropillar arrays with different heights for cell studies. *Microelectronic Engineering* **158**, 22-25 (2016).
15. T. M. Squires, S. R. Quake, Microfluidics: Fluid physics at the nanoliter scale. *Reviews of modern physics* **77**, 977 (2005).

Chapter 7 Conclusion and perspective

The objective of this thesis is to explore micropillar arrays as substrates for cell culture studies. We fabricated micropillar arrays of different diameter, height and spacing. Dense micropillar arrays made of PDMS provide an effective stiffness of the substrate comparable to that of cells which could be used for cell adhesion and cell migration studies. The PDMS substrate with electrospun nanofibers on the pillar array offers both advantages of in-vivo like surface morphology and low stiffness, allowing culturing neurons with enhanced functionalities. PDMS pillars could also be used to observe confinement and deformation of nuclei of stem and cancer cells. Finally, PDMS pillar array has been integrated into a microfluidic device for a substrate stiffness dependent migration in a biochemical gradient.

First of all, we presented micro- and nano-fabrication techniques used in this thesis including UV photolithography, pattern transfer replication (soft lithography and hot embossing), surface modification (plasma cleaner and vacuum deposition), and electrospinning. All these widely used techniques are low cost, satisfied accuracy and high throughput, which can be combined to obtain more complex surface pattern and structural fabrication with different materials. The micro- and nano-fabrication techniques retain potential for many applications in life science, and particularly in cell biology for in vitro cell culture and tissues engineering.

Subsequently, micropillar arrays of different heights were fabricated by casting or hot embossing with different types of materials, resulting culture substrates of different stiffness, ranging from 10 KPa to 500 MPa. Our results showed that NIH 3T3 cells were sensitive to the height of PDMS pillars, due to their comparable Young's module, and the cells are preferentially localized on the stiff pillar area. Cell alignment was achieved on all micropillar substrates. However, no such effect of different morphology has been observed when cells are cultured on PCL pillars of different heights because of the excessive rigidity of the PCL pillars. Cell alignment on PDMS pillars formed a holistic structure, and on PCL pillars spread in bead-string shape. Our results suggest that micropillar substrates can be used as quasi three dimensional (3D) extracellular matrix (ECM) due to the versatility and the flexibility

offered by changing the parameters of micropillars. It can also be used for modeling of wound healing on the guidance of physical cue of stiffness. Wound healing requires the establishment of a model of movement and interforce of cells crawling mechanisms at the gap. In this case, the interaction between micropillars and cells can be clearly demonstrated, in order to modeling epithelial gap closure. Recent in vitro and in vivo experiments have shown that physical constraints, such as local tissue curvature are crucial to the regulation of gap closure mechanisms. Cell adhesions on micropillars have been implicated in the transmission of intercellular, as well as of cell-ECM, making them important in the mechanical regulation of multi cellular wound healing. Dynamically redistributed at the wound edge, cell behaviors restricted on micropillars could be mediated by contractile forces, depending on the mechanical properties of the surrounding environment. Therefore, the stiffness of the substrate, moderated by the parameters of micropillars, may affect epithelial wound healing. Different from conventional flat surface, micropillar array can guide the direction of cell spreading and migration during wounding healing, which provides a new research method to achieve improved healing process in mechanics guiding combing biology and physic cues.

Additionally, we propose a novel substrate made of electrospun nanofibers on elastomeric micropillars for the connection between micropillars and the formation of neural networks. Our results show that neurons and glial cells grow on this composed substrate with improved functionality compared to substrates of simple micropillars, due to the nanopatterned surface (PLGA nanofibers) and the underneath substrate stiffness (PDMS pillars). In deeper meaning, we applied micropillar substrates (PDMS and PCL) effectively to identify the deformability during cell-adhesion confinement. Especially for induced pluripotent stem (iPS) cells, the nuclei were inserted into the gaps between micropillars in high proportion. By comparing cell amount of in different deformation states between MCF7 and iPS cells, the nuclei of iPS cell was with high deformability and extremely soft. The physical property, especially the stiffness, of iPS cell was highly similar to other types of stem

cell. It could be inferred that the expression of Lamin A/C (in protein) and LMNA (in gene) in iPS cells was at a relatively low level and gradually increased in the process of differentiation. Stem cells, especially iPS cells cultured on micropillars are interesting in future research. For multi cells in embryonic body (EB), different height of determines the different stiffness of the substrate, thus achieving the regulation of EB morphology. In addition, on the micropillar array, appropriate stencil like PDMS patch can be helpful to control the size of EB. Due to the flexibility of micropillars, it will be a promising tool for tissue engineering and regeneration medicines. It can be very simple to replace PDMS to other biodegradable materials, such as PLGA and PCL which are biodegraded in vivo. After in vitro specific differentiation of iPSCs (neuron or cardiomyocyte), the whole cell patch can be very flexible for in vivo transplantations and therapy. For signal iPS cell, we identify a unique technique to deformation cellular nucleus which is the key aspect to gene expression and signaling adjustment during cell proliferation and differentiation. Plenty of pathology or biological model can be evolved on this basis, for example, preferentially differentiate in the stress concentration under cell confinement and the efficiency of differentiation affected by the holes defective in tissue. Novel in-vitro models are efficient biomaterial system to tissue-engineering through self-organized development of iPS cells in a bioengineered niche mimicking.

Finally, we demonstrated a microfluidic platform for cell culture and migration studies. This platform integrated micropillar arrays for the control of substrate stiffness and morphology, whereas chemical gradients would be easily generated in the channels. Thus, we successfully combined physical and chemical cues, allowing us to determine cell-pillar interaction forces during cell migration. Based on the platform, different organizational models differentiated on different micropillar arrays can be integrated into microfluidic chip to form organ on a chip or body on a chip. As a physiological model to carry out drug research and development, it can be used for drug assays which minimize the animal models with more accurately simulate human cell morphology, proliferation, differentiation and migration.

Therefore, standard chip, with simple fabrication and high versatility, is necessary to provide dynamic medium control platform that enables the spatial and temporal control of the medium surrounding of micro-organisms cultured on micropillar substrates. The standard organ on a chip consists a stable growth environment over hours of experiments, with or without convective stress and flux on the bio organisms. The novel micropillar substrates as well as nanofiber patch are hybrid components expected to reduce the statistical dispersion of cell behavior and enhance the capability to study fine deviations due to the mimicking in vivo microenvironment.

In conclusion, we presented micropillar arrays (substrates and chips) as a powerful tool for the vital field of medical, scientific and industrial relevant cell culture applications. These novel approaches close to nature environmental conditions will strongly reduce highly artificial cell behavior due to interaction of cells with hard and flat substrates as found in conventional cell culture dish. By development of mimic micro/nano structure for cell culture and morphological control, break-through in the process efficiency and cellular understanding is expected for applications such as wound healing, stem cell differentiation and organ on a chip.

Appendix A Summary in French

A.1 Introduction et méthodes

La biologie cellulaire, le criblage de médicaments et l'ingénierie tissulaire reposent largement sur l'utilisation de méthodes in-vitro comme la culture de cellules de différents types et de différentes origines, laquelle a une grande importance. Alors que la culture conventionnelle utilise des boîtes de pétri, des flacons et des plaques de multi-puits plastiques, des approches les plus récentes existent, basées sur des substrats et des dispositifs micro-fabriqués, afin de reproduire les microenvironnements cellulaires in-vivo, avec pour but d'améliorer la performance de la culture et de mieux contrôler les comportements cellulaires tels que l'adhésion, la migration, la différenciation, la prolifération, ou encore l'apoptose des cellules. En effet, dans une culture classique, les cellules adhèrent souvent sur une surface plane, sur un substrat de rigidité significativement différente de celle des cellules. En revanche, les substrats micro-fabriqués peuvent avoir une morphologie de surface ressemblant à celle des matrices extracellulaire (ECM) dans un tissu. En outre, une surface texturée facilite la diffusion des nutriments et des métabolites sous la zone d'adhésion des cellules.

Un grand nombre de substrats micro-fabriqués ont été utilisés pour étudier l'effet du substrat sur la performance de culture cellulaire. La plupart de ces études ont été consacrées à l'influence des motifs topographiques et relativement peu se sont attardées sur la dépendance à la rigidité du substrat. Cela peut probablement s'expliquer par le fait que la plus part de ces études ont été faites avec des cellules relativement peu sensibles à la rigidité de substrat, et que les cellules ont des modules Young beaucoup plus faibles que la plupart de matériaux de culture utilisés d'habitude. Des avancées plus récentes de la biologie cellulaire s'intéressent plus particulièrement à la performance des cultures de cellules souches et de cellules tumorales sont plus exigeantes au niveau de leur microenvironnement cellulaire. Par conséquent, l'importance de mener des études sur la dépendance à la rigidité du substrat cellulaire devient considérable.

Les gels possèdent souvent des modules Young comparables à celui des cellules mais ils sont trop mous pour être manipulés et il est relativement difficile de réguler leur rigidité et leur morphologie de surface. Par contre, les réseaux de micro-piliers peuvent aussi avoir une surface de rigidité effective faible et il est relativement facile d'obtenir une valeur de rigidité connue.

En règle générale, la taille d'une cellule est de l'ordre de 10 à 20 μm , de sorte que, lorsque la cellule est cultivée sur un réseau dense de micropiliers de diamètre de l'ordre de 1 μm , son comportement sera sensible à la rigidité effective du substrat qui est déterminée par le module de Young de matériau et le rapport d'aspect hauteur/largeur des piliers. En plus, un réseau de micropiliers peut servir comme une matrice extracellulaire artificielle pour le guidage de l'adhésion, la migration, la prolifération et la différenciation cellulaire. Enfin, les substrats constitués d'un réseau de micropiliers peuvent être facilement réalisés et utilisés dans différentes circonstances.

La surface de micropiliers peut être facilement modifiée biochimiquement pour moduler leur affinité d'adhésion cellulaire, ce qui peut se révéler crucial pour la recherche biomédicale ainsi que pour des applications avancées telles que l'ingénierie des tissus, la génération de modèle de certaines maladies et le traitement du cancer. En outre, les nanofibres peuvent être déposées au-dessus d'un réseau de piliers, conduisant à une morphologie ressemblant à celle de la matrice extracellulaire *in vivo*. Dans les deux cas, l'échange entre les cellules et le milieu de culture sera plus efficace par rapport à la culture sur une surface plane, dû à de grands espaces libres sous la zone d'adhésion cellulaire. Bien entendu, cette augmentation de l'efficacité des échanges affecte de façon significative les fonctions cellulaires.

Pour comprendre plus clairement comment le comportement des cellules est soumis à la fois par les signaux chimiques (chimiokines) et physiques (ECM), il est intéressant d'intégrer un substrat de micropiliers dans une puce microfluidique. Typiquement, la migration cellulaire peut être étudié finement dans un dispositif

microfluidique, qui contrôle la distribution de réactifs, de nutriments, et d'autres facteurs cellulaires à haute résolution temporelle. Généralement, des gradients chimiques peuvent être créés dans un canal microfluidique permettant des analyses systématiques de la migration cellulaire en réponse à la modification d'un facteur de croissance, des hormones ou des chimiokines. L'intégration de micropiliers dans une puce microfluidique ajoute une autre dimension pour étudier les influences à la fois biochimiques et physiques sur le comportement cellulaire.

L'objectif de ce travail est d'explorer les micropiliers pour contrôler la rigidité effective du substrat de culture. Nous avons fabriqué des réseaux de micropiliers de différentes tailles, différentes hauteurs et différents espacements dans deux types de matériaux (élastomères et thermoplastiques) pour observer l'effet de la rigidité de substrat sur l'adhésion cellulaire. Nous avons aussi déposé des nanofibres sur les micropiliers afin de créer un nouveau type de substrat hybridé et nous avons intégrés les micropiliers dans un dispositif microfluidique pour observer la migration cellulaire et les activités de neurones dépendant de la rigidité du substrat.

A.2 Culture cellulaire sur un substrat de micropiliers

A.2.1 Réseaux de micropiliers à différentes hauteurs

Les techniques de photolithographie ont été utilisées pour fabriquer des réseaux micropiliers en résine de différentes hauteurs, qui ont été utilisés comme moules pour obtenir des répliques négatives de piliers en PDMS. Ces répliques ont été ensuite utilisées pour produire des piliers en PDMS ou PCL. Tout d'abord, une réplique de tonalité négative des réseaux de piliers a été produite par un moulage de réticulation de PDMS sur le moule en résine photorsensible. Deuxièmement, des micropiliers en PDMS ont été fabriqués par un moulage par réticulation en utilisant la réplique de tonalité négative comme moule. Alternativement, les micropiliers en PCL ont été produits par un moulage thermique en utilisant la réplique à tonalité négative de PDMS comme moule. La Figure A.1 montre les images de microscopie

électronique à balayage des micropiliers en PDMS et en PCL obtenus, confirmant la faisabilité de méthodes de fabrication.

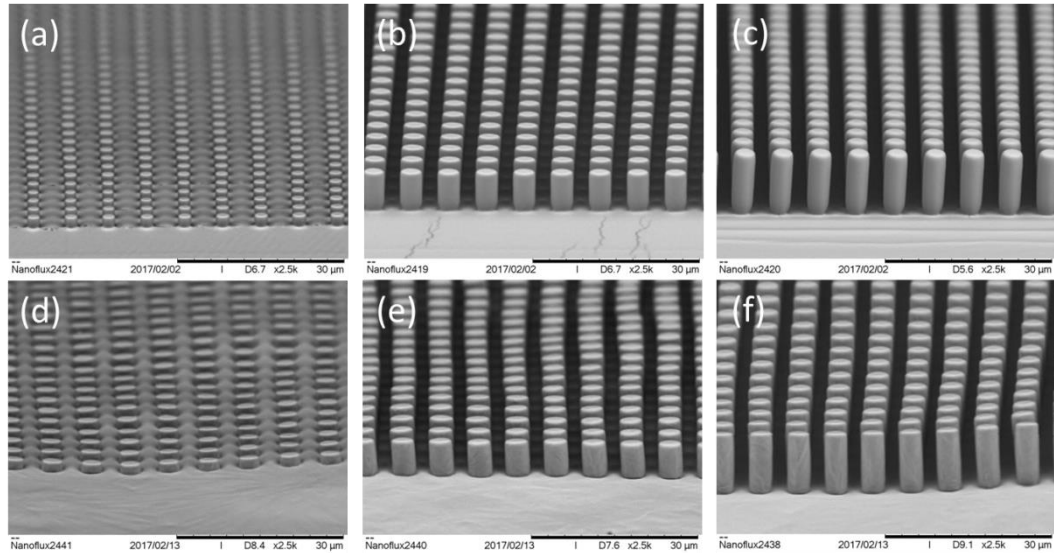


Figure A.1 Images SEM des micropiliers en PDMS (a-c) et en PCL (d-f), réalisés par la méthode de moulage par réticulation et de moulage thermique, respectivement.

A partir de ces images SEM, les hauteurs (H) et les diamètres (D) des piliers de PDMS (PCL) ont été mesurés, soit 1.6 (1.8), 6.6 (6.3) et 10.7 (11.2) μm et 2.5 (3.7), 4.0 (4.3), 4.0 (4.3) μm , pour un espacement de 6.8 (7.0) μm , respectivement. Ici, la différence de diamètre était probablement due à l'utilisation de différents types de résines qui ont des épaisseurs différentes. En effet, les piliers de petite hauteur ont été obtenus avec une résine de type SU8-2000 alors que d'autres ont été produits avec une résine de type SU8-3000, qui ont des réponses différentes à la lumière UV avec le même motif de masque. Les différences de hauteur entre les piliers PDMS et PCL pourraient être dues à la différence de procédé entre le moulage par réticulation et le moulage thermique. En fait, le moulage thermique avec un moule élastique tel que PDMS peut provoquer une déformation importante du moule à cause de l'application d'une pression relativement forte. Alors aucune pression n'a été appliquée en moulage par réticulation.

PDMS (PCL) a un module de Young d'environ 1 à 500 MPa. Dépendant

complètement de la géométrie des piliers, un substrat de piliers en PDMS ou PCL peut avoir une rigidité de surface très différente de celle du matériau massif. Pour estimer la rigidité effective du substrat de piliers, nous avons d'abord calculé le module de Young (E_e) d'un pilier pour les trois réseaux de piliers en PDMS et en PCL (Figure A.2).

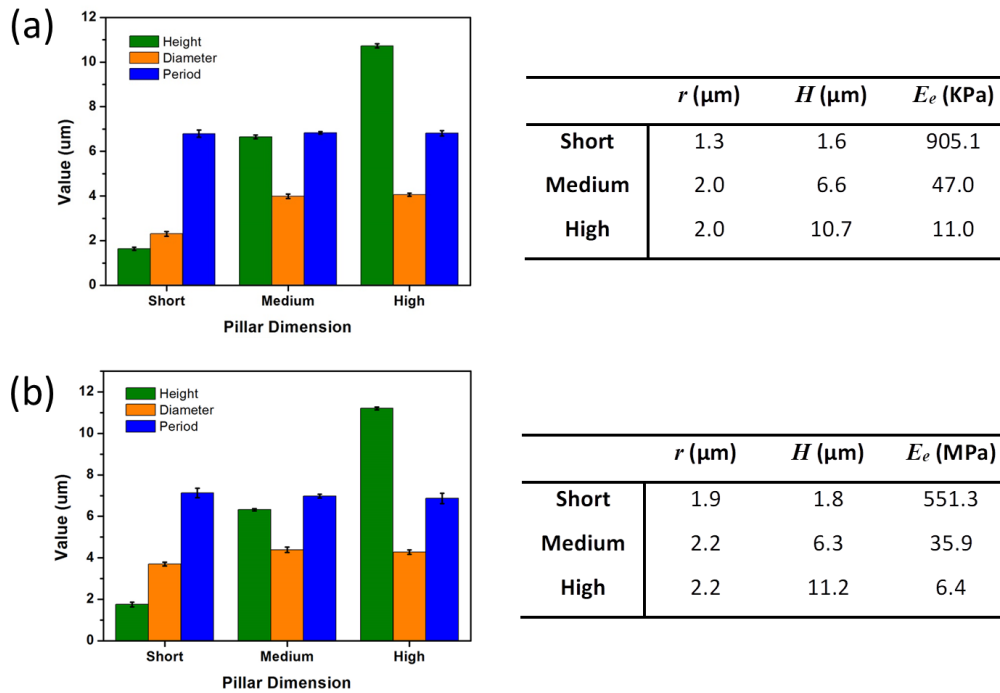


Figure A.2 Paramètres des piliers en PDMS (a) et en PCL (b) ainsi que le module de Young calculé pour chaque type de piliers.

La Figure A.3 montre les images typiques de microscopie fluorescente de cellules 3T3 cultivées sur différents types de substrats aux jours 1 et 3. Au jour 1, la morphologie cellulaire sur un substrat de PDMS est comparable à celle sur un substrat de PCL, montrant un étalement plus large que celui sur le verre. Au jour 3, les cellules s'étaient sur une surface plane au hasard. Au contraire, les cellules sur les micropiliers en PDMS et PCL sont allongées et alignées. Apparemment, les micropiliers en PCL à forte rigidité mécanique ne sont pas favorable à l'étalement de cellules. En comparaison de l'allongement de l'ensemble du cytosquelette sur les micropiliers de PDMS, la fibre d'action a formé des filopodes et un allongement

extrême sur les micropiliers de PCL, en particulier sur les rangées de pilier moyen et élevé.

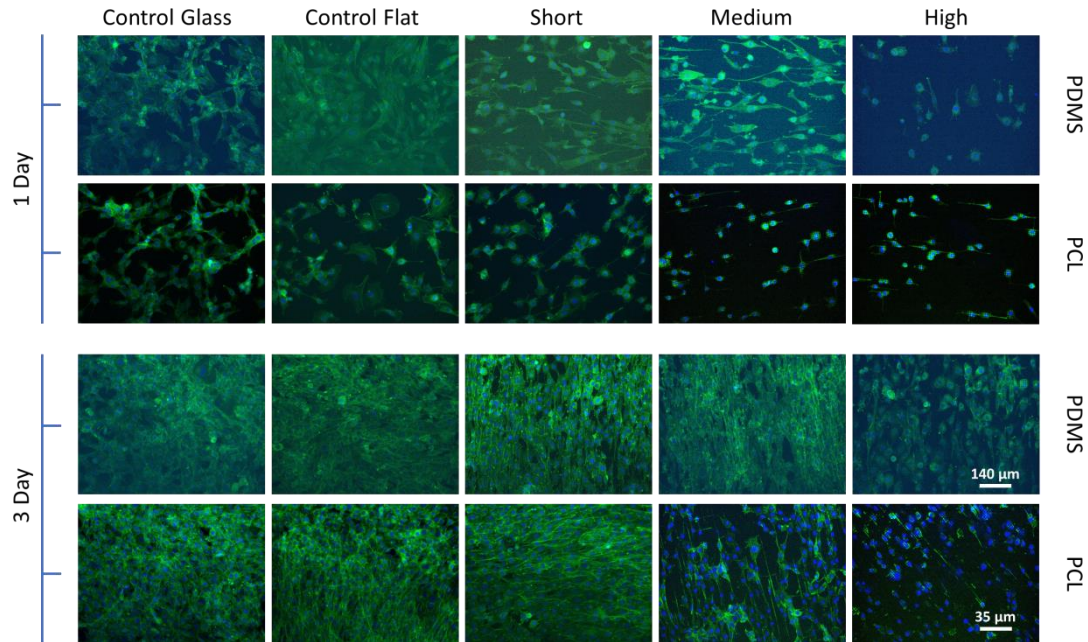


Figure A.3 Images fluorescentes de cellules NIH-3T3 cultivées sur des substrats en verre, des substrats plats, et un ensemble micropilier de PDMS et PCL court, moyen, élevé, respectivement. Réseaux de cellules nucléaires (DAPI: bleu) et d'actine cytosquelettes (Alexa Fluor 488 phalloidine: vert).

Les variations de la densité cellulaire et de la longueur de la cellule sur différents substrats sont représentées sur la Figure A.4. De toute évidence, l'augmentation de la densité cellulaire est différente selon les différents types de substrats. Nous avons observé une augmentation de la densité cellulaire de 200 mm^{-2} au jour 1 à $750\text{-}950 \text{ mm}^{-2}$ (PDMS plat), 650 mm^{-2} (piliers PDMS de hauteur $1.6 \text{ }\mu\text{m}$ et $6.6 \text{ }\mu\text{m}$) et 500 mm^{-2} (piliers PDMS de hauteur et $10.7 \text{ }\mu\text{m}$) au jour 3, respectivement. Une variation similaire peut être observée pour la densité cellulaire sur les substrats plats et micropaires PCL, c'est-à-dire que la densité cellulaire varie de 200 mm^{-2} au jour 1 à $650, 500$ et 400 mm^{-2} au jour 3 sur le rangement des piliers de hauteurs respectives : $1.8; 6.3$ et $11.2 \text{ }\mu\text{m}$.

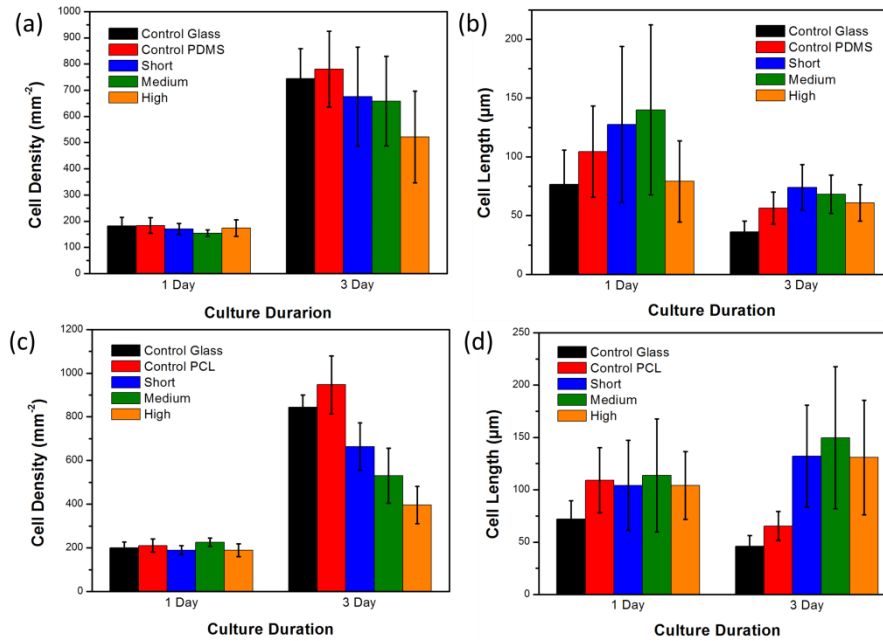


Figure A.4 Répartition de la densité et de la longueur des cellules NIH-3T3 sur des substrats en verre, des substrats plats et des matrices de micropiliers courtes, moyennes et élevées de (a) (b) PDMS et (c) (d) PCL, respectivement.

On remarque que la longueur de la cellule sur tous les substrats PDMS a diminué, mais a augmenté légèrement sur les substrats du pilier PCL. Sur les micropiliers PDMS, notamment pour les cellules sur le réseau de piliers de taille moyenne, la longueur maximale est de 250 μm et la longueur moyenne est de 130 μm. La longueur des cellules sur le réseau de piliers courts est relativement importante, avec une moyenne de 125 μm. Pour le contrôle sur PDMS plat, les cellules se propagent sur une grande surface avec une longueur moyenne de 100 μm. Après une incubation de 3 jours, les cellules se sont réarrangées et ont raccourci, allant pour un PDMS plat de 100 μm à 55 μm (45%), pour une matrice de piliers courts de 125 μm à 75 μm (40%), et pour un rang de pilier moyens de 130 μm à 70 μm (46%). En raison de leur longueur initiale courte, les cellules sur le réseau de hauts piliers n'ont presque pas changé (de 75 μm à 65 μm). Sur les substrats PCL à 1 jour, les cellules sur plaquette PCL s'étendent sur une grande surface avec une grande longueur, avec des micropiliers allongés dans des filopodes et des noyaux contractuels. Après une incubation de 3 jours, les cellules se sont réarrangées et ont

raccourci sur PCL plat de 110 μm à 60 μm (45%). Au contraire, la longueur de la cellule a augmenté sur les substrats micropillaires, sur les rangs de piliers courts de 105 μm à 125 μm (19%), sur les ranges de piliers moyens de 110 μm à 150 μm (36%) et sur le rangs de piliers élevés de 105 à 125 (19%) . Notamment sur le substrat du pilier moyen, la longueur maximale est de 350 μm . Pour un matériau rigide comme le PCL, la dureté des matériaux en excès a agi comme une clôture bloquant la croissance cellulaire de la ligne de bordure et a déformé les cellules du cytosquelette aux noyaux en particulier.

A.2.2 Micropiliers adjacents à hauteurs différentes

Comme mentionné précédemment, la réplique PDMS a été obtenue via la distribution et la réplique PCL a été obtenue par moulage à chaud. La Figure A.5 montre la dimension finale de la réplique diverse à partir de matériaux dans des images SEM. Pour la réplique PDMS (PCL), la hauteur des réseaux adjacents était respectivement 13.2 (13.8) et 7.3 (6.3) μm . L'espacement était approximativement égale à 6.8 (6.8) et à 7.1 (6.8) μm . Le diamètre de la matrice haute était de 2.8 (4.1) μm , comparativement à 2.5 (3.8) μm de matrice courte.

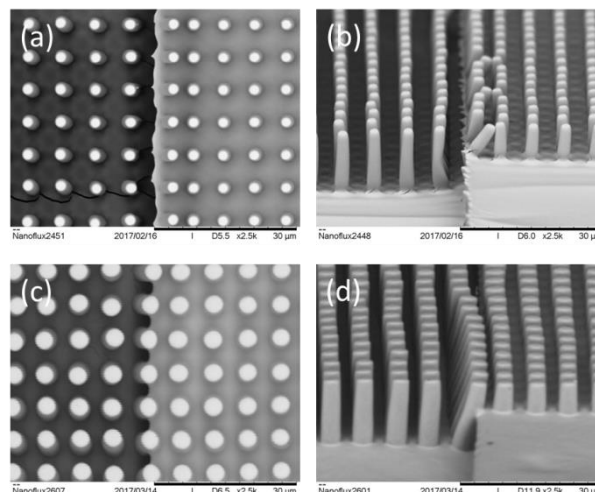


Figure A.5 Photos SEM de réseaux de micropiliers adjacents avec des hauteurs différentes en (a) (b) PDMS et (c) (d) PCL.

La Figure A.6 montre les images typiques de microscopie fluorescente de fibroblastes cultivées sur des substrats au jour 1 et au jour 3, respectivement. Lorsque les cellules ont été placées sur des matrices de pilier denses, elles ont eu des comportements différents du pilier avec une condition de revêtement d'impression en contact. Ici, la distance entre les piliers était significativement plus petite que celle de la taille des cellules, de sorte que les cellules puissent rester confortablement sur le dessus et se répartir sur plusieurs piliers après l'ensemencement.

Au jour 1, la prolifération et l'alignement cellulaire présentaient un caractère similaire à celui du revêtement de surface au revêtement massif sur les piliers PDMS. Sur un réseau de $7.3\ \mu\text{m}$, les cellules ont une plus grande surface et des filopodes plus longues que $13.2\ \mu\text{m}$. Étant donné que le module de Young de la surface du pilier du PDMS était comparable à celui des cellules migrantes NIT 3T3 (3-12 kPa), les cellules NIH 3T3 devraient être plus sensibles à la variation de la rigidité des piliers PDMS. En effet, lorsque les cellules ont été placées sur des piliers PDMS de différentes hauteurs, elles se localisaient préférentiellement sur les zones de pilier plus rigides (plus petite hauteur). Cependant, sur les piliers PCL, la cellule a eu une superficie d'étalement approximative et un allongement très long sur des réseaux de 6.3 et $13.8\ \mu\text{m}$. De manière cohérente, beaucoup plus de cellules ont été trouvées sur les piliers PCL, mais ils n'ont montré aucune attache préférentielle puisque les modules efficaces de Young des piliers PCL sont à la fois supérieurs à ceux des cellules.

Au jour 3, avec une augmentation de la quantité de cellules suffisante, aucune différence évidente entre les deux côtés de la variation de hauteur, sur les substrats PDMS et PCL n'a été observée. Le phénomène le plus remarquable a été l'allongement et l'alignement cytosquelettique selon la variation des matériaux de PDMS à PCL. L'alignement des cellules sur les piliers du PDMS forme une structure holistique qui s'aligne le long de la direction du gradient de rigidité, en fonction de l'extension. Que ce soit le gradient anisotrope sur un seul pilier ou un gradient de hauteur sur un réseau de piliers adjacents, le cytosquelette de pseudopodes a eu une

forme généralement étalée, avec un certain agencement en gradient. Au contraire, l'alignement des fibroblastes sur les piliers PCL formait une forme de cordon de perles. Une partie du cytosquelette enveloppé autour du noyau, avec étirement et déformation. L'autre partie du cytosquelette a étalé des pseudopodes filamenteux, qui étaient extrêmement mince et étirés dans les trous entre les piliers. Les cellules sur les piliers PCL étaient plus sensibles à l'anisotropie de rigidité d'un seul pilier que la différence entre les réseaux adjacents.

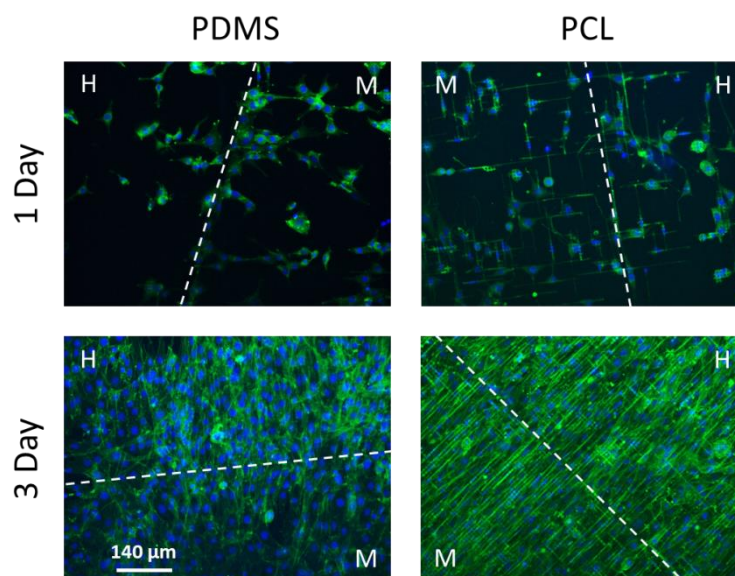


Figure A.6 Des images fluorescentes de cellules NIH-3T3 cultivées sur des substrats de PDMS et PCP micropiliers (H pour 13-14 μm et M pour 6-7 μm) respectivement. Réseaux de cellules nucléaires (DAPI: bleu) et d'actine cytosquelettes (Alexa Fluor 488 phalloïdine: vert).

A.3 Micro/Nano substrat hybride pour études de culture cellulaire

Les matrices de micropiliers utilisées dans ce travail ont été obtenues en jetant du PDMS sur un moule PDMS avec des trous, alors que le moule PDMS a été initialement obtenu à partir d'un moule en résine photosensible fabriqué par photolithographie. Tout d'abord, les réseaux de micro-trous ont été structurés sur le

masque Cr à l'aide d'un micro-patterning. Ensuite, une couche de résistance négative de 25 μm d'épaisseur (SU8-3025) a été déposée par centrifugation sur le masque et exposée aux UV du côté arrière. Après le développement, des piliers de 25 μm de hauteur, de 5 μm de diamètre et 20 μm d'espacement ont été obtenus et utilisés comme caractéristiques de moule pour jeter un mélange de prépolymère PDMS et d'agent de réticulation au rapport de 10:1. Avant la coulée, le moule a été traité dans du plasma d'oxygène pendant 2 min, puis dans de la vapeur de TMCS pendant 30 min. Après la coulée PDMS et le durcissement à 80 °C pendant 2 h, la couche de PDMS a été décollée, ce qui a entraîné une réplique négative des caractéristiques du moule. Ensuite, on a déposé du Parylene C de 0.2 μm d'épaisseur sur la couche de PDMS avec un dépôt sous vide. Par la suite, une réplique à tonalité positive du masque a finalement été obtenue en jetant du PDMS liquide sur le moule en PDMS en utilisant le même procédé de coulée, comme le montre la Figure A.7.

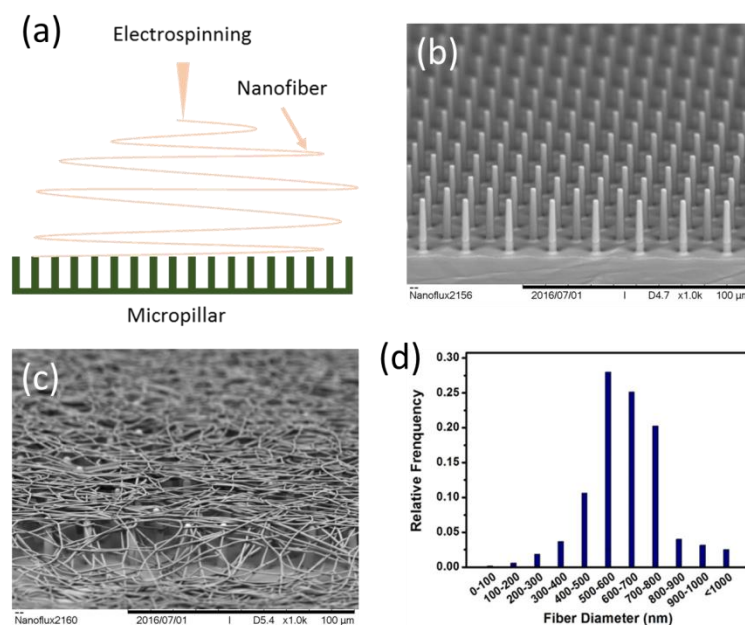


Figure A.7 (a) Diagramme schématique du processus de fabrication de nanofibres électrospun sur des micropiliers élastomères. (b) Photos SEM du réseau de micropiliers en PDMS avec 25 μm de hauteur, 5 μm de diamètre et 20 μm . (c) les nanofibres PLGA ont été déposées sur les piliers PDMS. (d) Distribution statistique des nanofibres PLGA.

Des nanofibres PLGA aléatoires ont été déposées par électrospinning sur les micropiliers. Comme prévu, nous avons obtenu un nouveau type de substrat de culture composé de nanofibres de PLGA sur les réseaux de puces PDMS, comme le montre la Figure 7c. Le diamètre des nanofibres a été mesuré, ce qui montre que 84,0% de fibres ont des diamètres dans la gamme de 500 à 900 nm et moins de 0,2% (2,5%) ont des diamètres plus petits (plus grands) que 100 nm (1000 nm).

Après une culture d'une semaine, la morphologie des astrocytes plaquées sur les différents types de substrats est devenue significativement différente. Sur les micropiliers de PDMS, les cellules gliales ont été distribuées dans la matrice en pointillés et sont réunies autour des micropiliers, dans un motif en réseau comme représenté sur la Figure A.8a. Sur le substrat PLGA / PDMS, les astrocytes ont montré une morphologie complexe avec de nombreuses saillies cellulaires (Figure A.8b). Les cellules gliales sont apparues synapses plus longues et pseudopodes fibreux étendus autour de longue distance, similaire à celle des systèmes *in vivo*. La densité des cellules neuronales sur les deux substrats neuronaux était approximativement la même. Cela suggère l'importance de la morphologie de surface des nanofibres PLGA et du support élastomère et des piliers PDMS. Une fois vérifiés l'attachement et la survie des neurones, un test fonctionnel a été effectué sur les cultures primaires de cellules de l'hippocampe cultivées sur les micropiliers. L'activité électrique spontanée et pharmacologique induite par des neurones a été mesurée au bout de deux semaines de culture. Au moment de l'analyse, nous avons choisi une technique d'enregistrement optique qui permet l'imagerie simultanée de plusieurs neurones. Plus précisément, nous avons mesuré les fluctuations de la concentration d'ions calcium intracellulaire en utilisant un colorant de liaison au calcium fluorescent. Les ions calcium sont des signaux intracellulaires qui régulent une grande variété de fonctions cellulaires, telles que l'expression génétique, la libération des neurotransmetteurs et de la communication neurone à la glie.

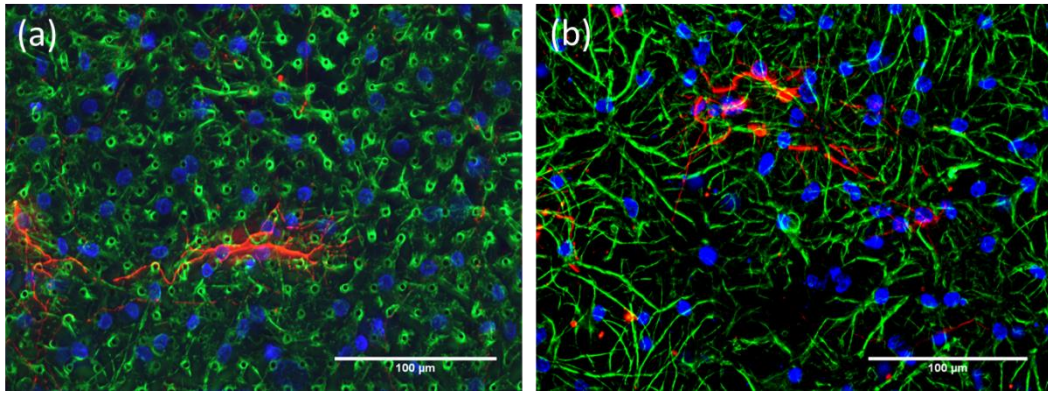


Figure A.8 Immunofluorescence des images des astrocytes sur (a) micropiliers de PDMS et (b) substrat hybride PLGA / PDMS après incubation d'une semaine. Protéine acide fibrillaire gliale apparentée aux Astrocytes teinté par GFAP (vert). Tête de β -tubuline de classe III spécifique au neurone coloré par TUJ1 (rouge). Noyaux cellulaires colorés par Hoechst (bleu).

L'analyse des courbes transitoires de calcium spontanées sont enregistrées optiquement à partir de cellules individuelles permet de comparer la fonctionnalité du réseau neuronal cultivé sur les substrats nanocomposite PLGA / PDMS vs PDMS (contrôle), comme l'illustre la Figure A.9. Sur le PDMS, nous avons observé quelques neurones actifs similaires aux supports PLGA / PDMS. En outre, les signaux de calcium provenant des cellules gliales étaient clairement visibles sur les micropiliers, et se distinguent des signaux neuronaux en raison de leur plus faible taux d'élévation et de désintégration.

L'amplitude moyenne des transitoires de calcium neuronal a été significativement augmentée sur le substrat nanocomposite par rapport au contrôle, tandis que l'intervalle entre événements a diminué, ce qui signifie que les neurones cultivés sur des nanofibres ont des signaux de calcium distribués plus fréquents et plus homogènes au fil du temps par rapport aux témoins. La synchronisation des transitoires de calcium au cours du temps, mesurée comme indice moyen de corrélation croisée, a été légèrement augmentée par rapport au PDMS (témoin) par rapport au PLGA / PDMS comme le montre la Figure A.9.

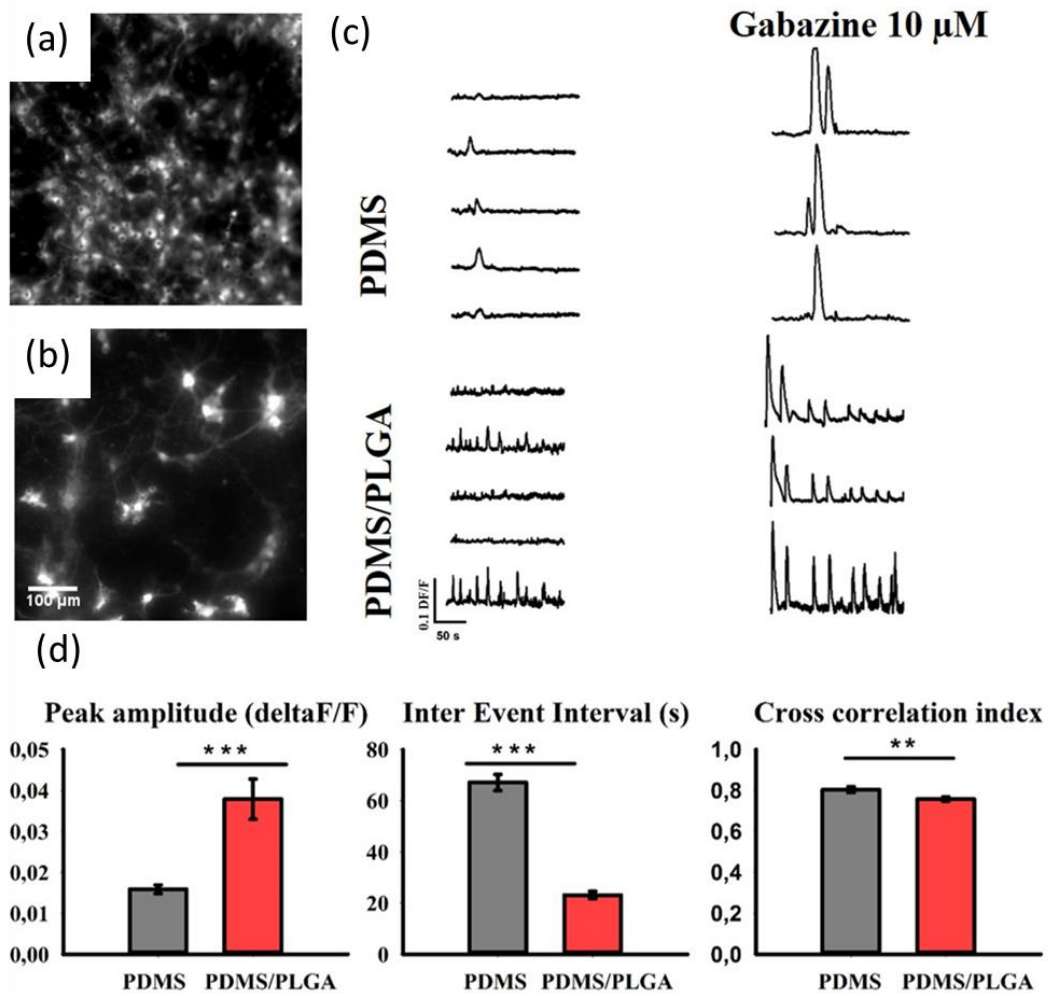


Figure A.9 Les neurones de l'hippocampe chargés avec Oregon Green® 488 BAPTA-1, AM après deux semaines de croissance sur les substrats PDMS (a) et PLGA / PDMS (b). (c) Les images des transitoires de calcium spontanés et de Gabazine au fil du temps sont également montrées. (d) L'amplitude moyenne, l'intervalle inter-événement et l'indice de corrélation croisée des transitoires de calcium spontanés sur les substrats PLGA / PDMS vs PDMS ($n = 12$ neurones pour PLGA / PDMS, $n = 16$ neurones pour PDMS - contrôle; ** pb 0,01 *** pb 0,001 One ANOVA, test post-hoc de Tukey).

L'amplitude moyenne des transitoires de calcium neuronal a été significativement augmentée sur le substrat nanocomposite (0.038 ± 0.004 DF / F) par rapport au contrôle (0.016 ± 0.001 DF / F); Une élévation du calcium intracellulaire au-dessus d'un certain seuil induit une potentialisation à long terme des synapses neuronales. L'Inter Event Interval a plutôt diminué sur le substrat des nanocomposites par rapport au contrôle (23.13 ± 1.45 vs 67.07 ± 3.14 s), ce qui

signifie que les neurones cultivés sur des nanofibres ont des signaux de calcium distribués plus fréquents et plus homogènes au fil du temps par rapport aux témoins. La synchronisation des transitoires de calcium au cours du temps, mesurée en tant qu'indice de corrélation croisé moyen entre tous les signaux neuronaux dans le même champ de vision, a été légèrement augmentée sur PDMS (0.80 ± 0.01) par rapport à PLGA / PDMS (0.76 ± 0.01), comme le montre la Figure 9. En outre, nous avons stimulé les cultures neuronales avec du Gabazine à $10 \mu\text{M}$ (Sigma-Aldrich), un antagoniste spécifique des récepteurs GABAA, et observé une augmentation de l'amplitude et de la synchronisation des transitoires de calcium dans les substrats de type PLGA / PDMS et PDMS (contrôle) (Figure A.9), comme attendu de la physiologie neuronale.

A.4 Cellules confinées sur des substrats micropiliers

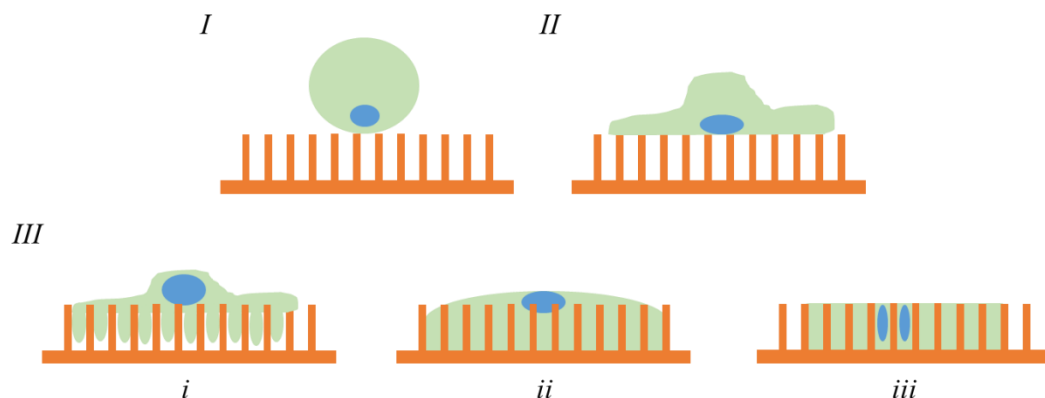


Figure A.10 Comportement cellulaire après adhésion aux micropiliers. *I* Imagerie cellulaire. *II* Épandage de cellules. *III* Adhérence cellulaire sur un réseau micropilier et trois états: *i* pas de déformation, *ii* déformation partielle, *iii* déformation complète

Dans la condition de la duplication, la morphologie cellulaire basée sur l'adhésion cellulaire changerait de manière significative, comme l'illustre la Figure A.10. Particulièrement, le noyau cellulaire s'insère entre des piliers et se déforme dans trois états: pas de déformation, déformation partielle, déformation complète. La proportion des trois états du noyau a finalement déterminé les propriétés de

déformation des cellules et les propriétés de dureté nucléaire correspondantes, qui dépendaient fortement du type de cellule et des caractéristiques physiques connexes.

Pour les cellules cancéreuses du sein, la déformabilité du noyau sur le substrat PDMS était inférieure à celle de PCL. La performance spécifique était celle des piliers PDMS, le rapport du noyau cellulaire sans déformation et déformation partielle était supérieur à celui des piliers en PCL. Sur les substrats de PDMS, les cellules se sont contractées évidemment, tandis que sur les substrats de PCL, les cellules ont été divisées en forme de grille plutôt qu'en pseudopode fibreux.

Pour les cellules cancéreuses du col de l'utérus, la déformabilité et la morphologie générales étaient similaires aux cellules cancéreuses du sein, en particulier sur les substrats de PDMS. La différence significative était que les cellules sur le substrat PCL comparaient comparativement à une proportion relativement élevée de cellules sans déformation ou déformation partielle, ce qui indique que la déformabilité des cellules cancéreuses cervicales sur des substrats rigides était inférieure aux cellules cancéreuses du sein. De toute évidence, le cytosquelette de la cellule HeLa sur les piliers PCL se propageait comme des pseudopodes filamenteux, mais avec une invasion et une ductilité plus élevées par rapport aux cellules MCF7.

Comme le montre la Figure A.11, certaines cellules n'ont pas été déformées du tout, complètement au sommet des piliers. Dans les états, la zone d'étalement de la cellule sans déformation était significativement plus grande que les cellules avec déformation. Certaines cellules ne se sont pas complètement attachées au fond des micropiliers, et une partie considérable des cellules était au sommet des micropiliers. Les autres cellules (en grande proportion) ont été complètement déformées, insérées entre les colonnes, et le profil présentant une forme de bande verticale.

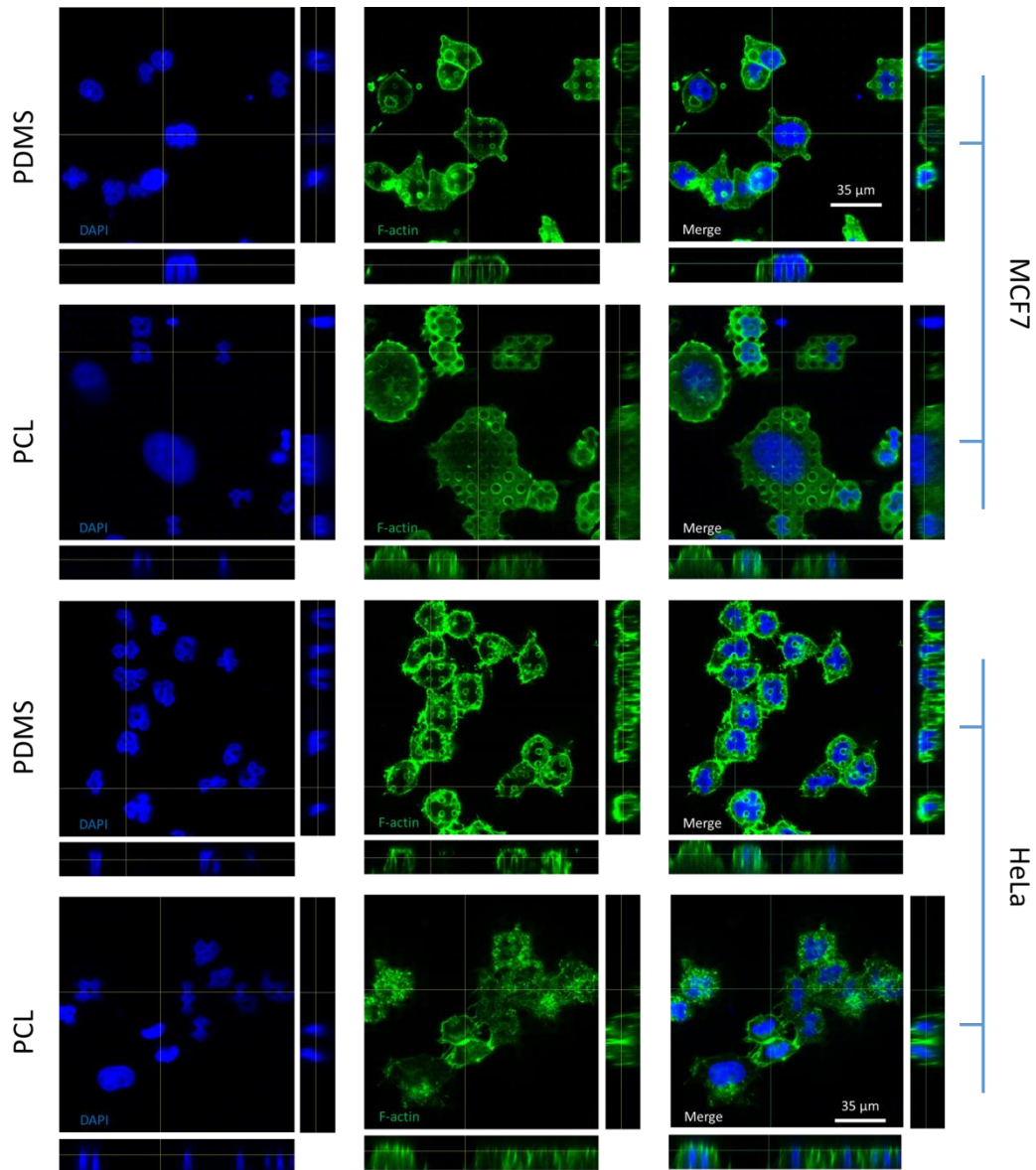


Figure A.11 Images fluorescentes vues par voie orthogonale des cellules MCF7 et HeLa confinées sur le réseau micropilier dans PDMS et PCL après 1 jour d'incubation. Réseaux de cellules nucléaires (DAPI: bleu) et d'actine cytosquelettes (Alexa Fluor 488 phalloidine: vert).

Le comportement des cellules iPS sur les micropiliers PDMS avec adhérence et confinement a ensuite été étudié. Même dans une condition de forte densité, les cellules apparaissaient comme des caractéristiques de déformation plus importantes que les autres types de cellules antérieures. Performance spécifique pour cellules iPS, une proportion plus élevée de cellules avec une déformation complète. Sur la base d'expériences, il n'y avait pas de cellules sans déformation.

Dans le cas de la zone micropilier PDMS à la surface plate, comme le montre la Figure A.12, la différence de morphologie cellulaire se reflète principalement dans la forme du noyau. Du point de vue supérieur, la zone du noyau cellulaire a été réduite de près de la moitié. De plus, à travers la morphologie du noyau, on distinguait les zones avec ou sans réseau micropilier. Il a été utile d'identifier la morphologie et la topographie des substrats. Il est intéressant de noter que, dans l'état de déformation, la pluripotence des cellules reste la même pour la non-déformation, ce qui était le facteur critique pour l'étude des cellules iPS pour l'expression des protéines et des gènes sous le confinement du noyau.

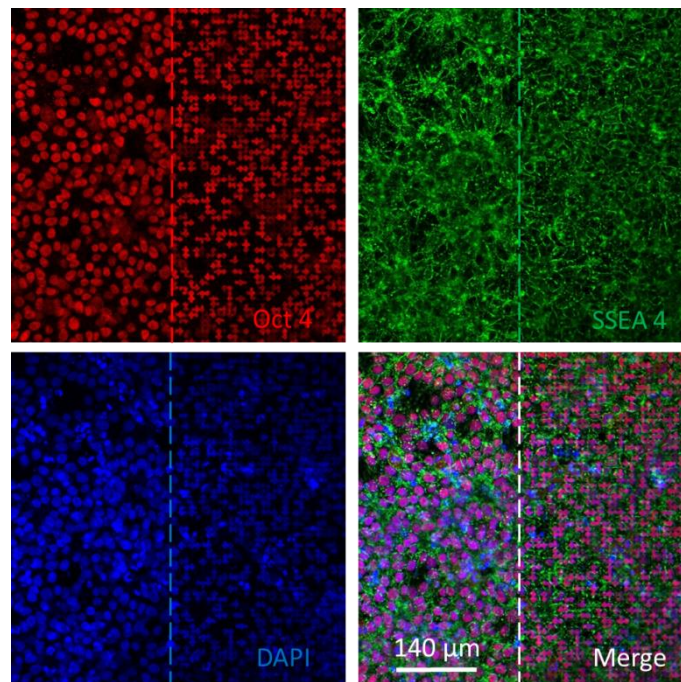


Figure A.12 Analyse immunocytochimique des cellules iPS sur la zone micropilier PDMS par rapport à la surface plate après 1 jour d'incubation. Les noyaux cellulaires (DAPI: bleu) et la pluripotence des cellules (Oct4: rouge et SSEA4: vert).

Des cellules iPS avec une déformation partielle et une déformation complète ont été observées. La pluripotence du noyau cellulaire a bien maintenu une forte consistance de la déformation nucléaire, même dans l'état de déformation complète. La pluripotence des composants cytoplasmiques cellulaires ne s'est pas déformée avec la déformation des plastides. La plupart des composants situés sur la surface

supérieure des micropiliers, dans la formation de membrane. On pourrait conclure que l'isolement cellulaire basé sur une matrice micropilier pourrait entraîner une certaine séparation du composant pluripotent du noyau cellulaire et du cytoplasme.

En comparant la quantité de cellules dans différents états de déformation entre les cellules MCF7 et iPS, comme le montre la Figure A.13, on peut obtenir la déformabilité du noyau cellulaire et on peut déduire la dureté du noyau. Les cellules MCF7 sur le réseau PDMS et PCL micropilier, le pourcentage de noyau cellulaire sans déformation, déformation partielle et déformation complète était respectivement de 7% & 5%, 39% & 31% et 54% & 75%. Pour les cellules iPS, la proportion de noyau cellulaire dans les trois états de déformation était de 0% & 0%, 18% & 15% et 82% & 85%, respectivement. Les noyaux de la cellule iPS avaient avec une forte déformabilité et extrêmement souples. Les propriétés physiques, en particulier la rigidité, de la cellule iPS était très similaire à d'autres types de cellules souches. On pourrait déduire que l'expression de Lamin A / C (en protéines) et de LMNA (dans le gène) dans les cellules iPS était à un niveau relativement bas et augmentait progressivement dans le processus de différenciation.

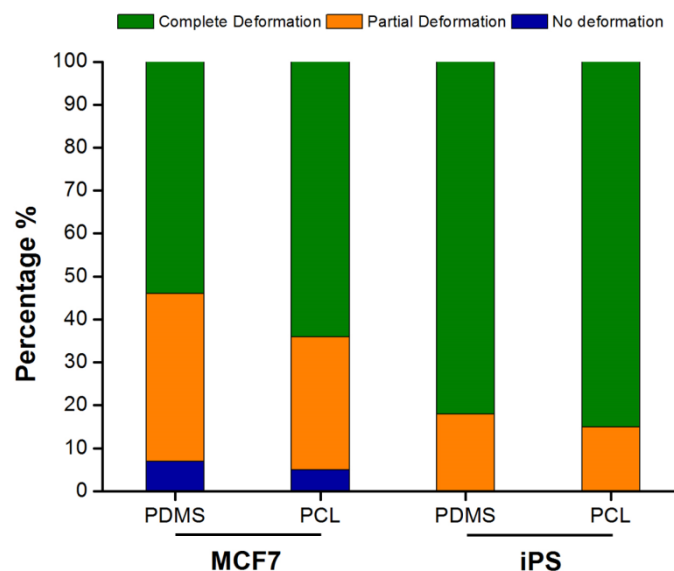


Figure A.13 Comportement de confinement des noyaux des différents types de cellules classés selon les trois états de déformation.

A.5 Intégration des micropiliers dans les dispositifs microfluidiques pour les études sur la culture cellulaire

Pour contrôler la distribution de la concentration de diffusion, nous avons utilisé un réseau de microcanaux semblable à «arbre de Noël», comme le montre la Figure A.14, avec un flux laminaire côte à côte sans mélange turbulent. Différent du processus de fabrication du réseau micropilier, le microcanal a été réalisé grâce à une photolithographie frontrière en un point et une réplcation en lithographie douce en une étape, avec une étendue de 50 μm de haut, 100 μm de largeur et une zone de gradient de 1 mm de large. Ensuite, la couche de piliers a été fabriquée avec une agencement hexagonal de 3 μm de diamètre, 10 μm de haut, 15 μm et hexagonale (comme le montre la Figure A.14cd) sur le support d'une glissière en verre pour prouver la rigidité du dispositif final. En particulier, les micropiliers étaient situés dans la zone de gradient de 1 mm de large. Après avoir poinçonné des trous pour les entrées et les sorties dans la couche de canal et le traitement au plasma de surface, la couche de canal de fonctionnelle PDMS et la couche de pilier ont été alignées et collées ensemble et prêtes pour l'expérience suivante.

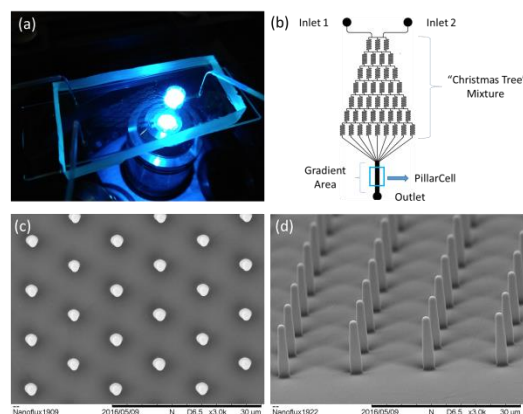


Figure A.14 (a) La plate-forme microfluidique sous des expériences de flux de fluorescence. (b) illustration CAD de la fonction de la plate-forme microfluidique. (c) (d) Images SEM du réseau PDMS micropilier avec 3 μm de diamètre, 10 μm de hauteur, période de 15 μm et agencement hexagonal.

Les milieux de culture (DMEM avec 10% de FBS, 1% de pénicilline-streptomycine) ont été ajoutés à l'entrée 1 et des milieux de rinçage (DMEM avec 0% de FBS, 1% de pénicilline -streptomycine) ont été ajoutés à l'entrée 2, tous deux avec un débit de 50 $\mu\text{L} / \text{H}$ pour la culture cellulaire en continu. La Figure A.15 montre la variation de la densité de cellules NIH 3T3 sur les zones micropiliers sous des gradients de concentration de FBS par rapport au temps de culture. Dans les zones de concentration de FBS 0-2.3%, le nombre de cellules est resté constant approximativement de 2 h à 48 h après l'ensemencement. À l'inverse, les cellules se situent dans la région de 2.3-7.7% et 7.7 à 10% ont augmenté de façon significative après 24 h. Par la suite, le nombre de cellules augmentait continuellement dans la zone de concentration la plus élevée. Typiquement, les cellules sur les micropiliers sont contractées en s'étalant sur une surface plane.

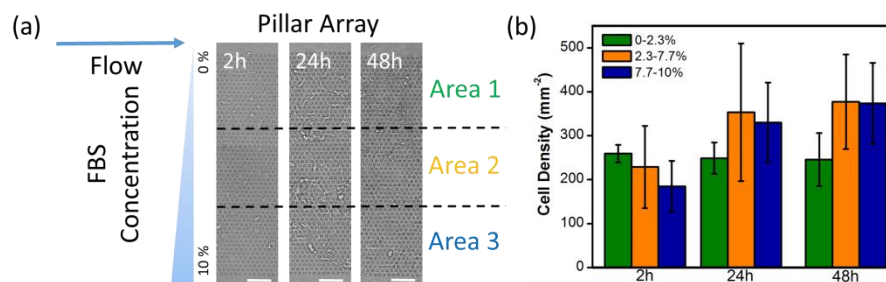


Figure A.15 (a) Images de la distribution et de la morphologie des cellules NIH 3T3 après l'ensemencement 2 h de l'attachement statique et du gradient de FBS et de la culture continue pendant respectivement 0h, 22h et 46h. La barre d'échelle est de 75 μm . (b) La densité cellulaire varie avec le temps de culture dans trois domaines de 0-2.3%, 2.3-7.7% et 7.7-10% de FBS.

À faible débit (0.1 ml / h), les cellules étaient sensibles à la fois au gradient de concentration de FBS et à la force de cisaillement du flux. Ils ont migré en conséquence avec la co-direction. Des analyses plus détaillées pourraient être basées sur le comportement de la migration de cellule unique. La Figure A.16 montre les images instantanées de la migration cellulaire sur un réseau micropilier, sous des influences de la force de cisaillement du flux et du gradient FBS. Les forces appliquées par les cellules sur leur environnement pourraient être évaluées en

mesurant la déformation du pilier Dans ce cas, $r = 1.5 \mu\text{m}$ et $H = 10 \mu\text{m}$, résultant d'une constante de ressort de $3.8 \text{ nN} / \mu\text{m}$. À partir des images de microscopie en cas de time-lapse, nous pouvons suivre avec cette méthode les forces appliquées par les cellules au fil du temps. Prenant l'exemple du Pilier 1 à l'arrière de la migration cellulaire, son allongement à l'origine de l'heure (+0.0 min) était de $7.6 \mu\text{m}$. Après avoir dépassé, l'allongement du pilier a été réduit en raison d'une nouvelle modélisation du cytosquelette. Cependant, une force de flexion du pilier de 8.7 à 12.8 nN a été maintenue en gardant le cytosquelette étiré. L'allongement du Pilier 2 et 3 à l'avant de la migration cellulaire a également diminué après l'étirement et le remaniement, sauf que l'allongement du Pilier 3 a légèrement augmenté au cours de la dernière étape du cours. L'allongement du Pilier 4 a été réduit de 24.3 nN à 0 après la migration cellulaire, car la cellule n'avait plus d'interaction avec lui. À la fin, l'allongement du Pilier 5 était de $3.2 \mu\text{m}$ dont une force d'interaction de 12.5 nN pouvait être déduite. Ainsi, une cartographie de force dynamique pourrait être possible pendant la migration cellulaire sur des réseaux de piliers et des analyses plus systématiques sont attendues en utilisant un microenvironnement cellulaire conçu et sophistiqué.

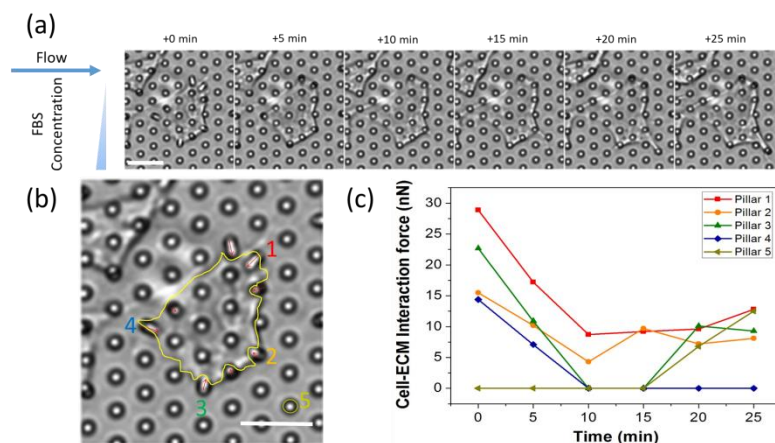


Figure A.16 (a) Images temporelles de l'interaction du pilier cellulaire après l'ensemencement de 2 heures. (b) Image de l'interaction du pilier cellulaire et du contour de la cellule. La barre d'échelle est de $30 \mu\text{m}$. (c) La force d'interaction Cell-ECM varie avec le temps de migration cellulaire.

Appendix B Quantification and simulation of microfluidic flow

B.1 Introduction

The application of computer aided design (CAD) and computer aided engineering (CAE) processing in microfluidic technology is the essential step for the standardization and industrialization of lab-on-a-chip. Especially in the early development of design and the prediction of modeling results, the processing has a high reference value for subsequent experimental as well as statistical data analysis and evaluation. CAD refers to the use of computers and related graphic devices to help accomplish design work. The start of design starts with sketch, and the sketch is automatically transitioned into entity or working drawing results via computer processing timely. CAE refers to the use of computer-aided analysis in complex engineering and product structural mechanical properties, as well as optimizing structural performance. CAE software can be used for static structural analysis, dynamic analysis; linear and nonlinear analysis as well as analysis of structure (solid), fluid, electromagnetic etc. In stage of modeling design, there is a large number of calculation, analysis and comparison to determine the optimal program. A variety of design information, such as statistics, text and graphics, can be stored in the internal or external memory of computer, convenient for search, retrieval, modification and judgment.

B.2 Simulation of diffusion based gradient generators

The microfluidic channel was draw by CAD software Solidworks finally in .STL files. The width of inlets and outlets was 500 μm , the difference was that the both ends were single channel and the center was level channel. The firs level was bypass channel with 100- μm width, and the second level was diffusion channel with 20- μm width. The area of diffusion area was $5 \times 10 \text{ mm}^2$, between the inlets and outlets. The height of the microfluidic chip was 100 μm in whole.

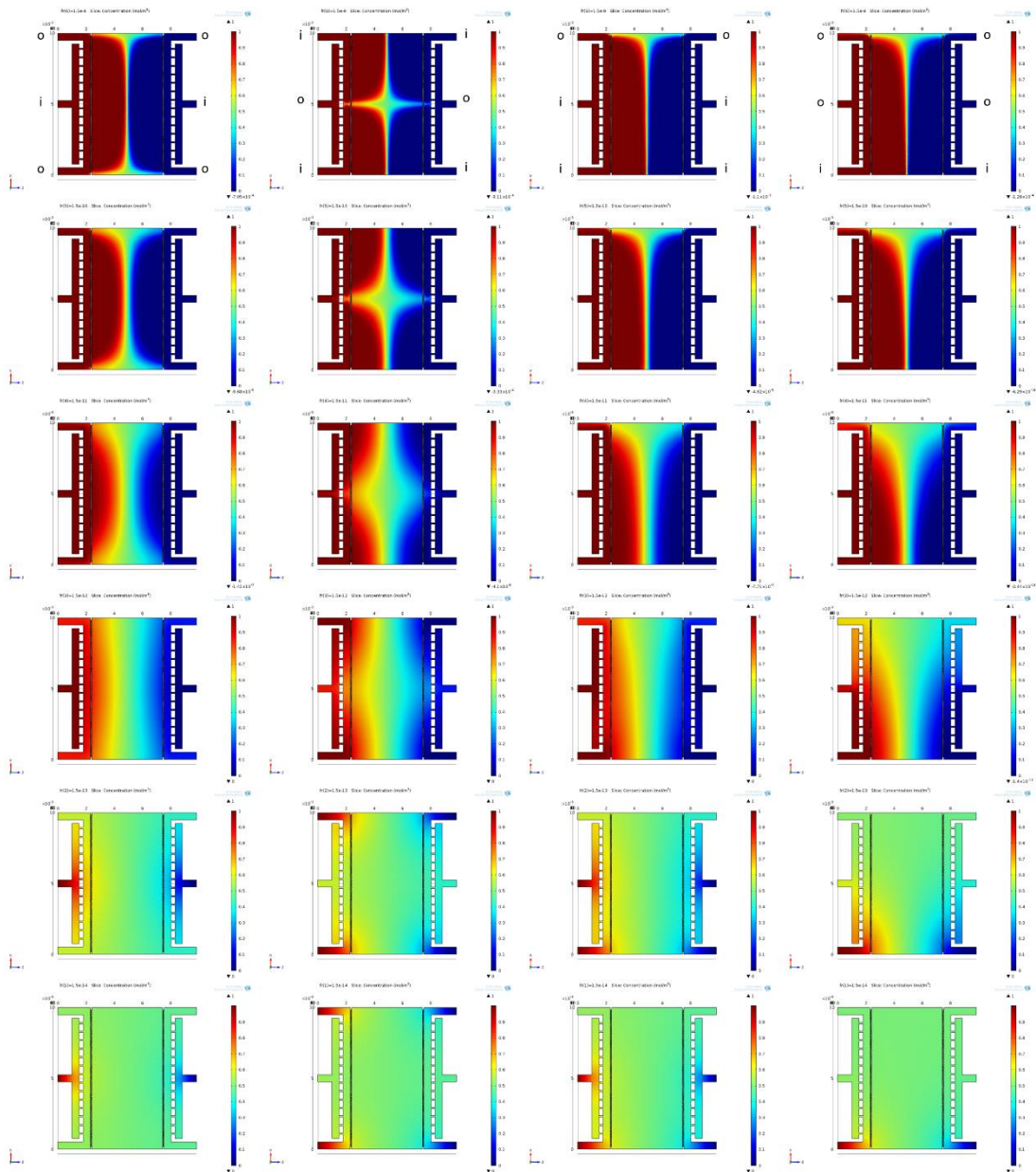


Figure B.1 Simulation of concentration characteristics in the microfluidic channel. In row, the concentration distribution varies with the arrangement of inlets and outlets, i for inlet and o for outlet. In column, the concentration distribution varies with the inlet flow rate of 1.5×10^{-9} , 1.5×10^{-10} , 1.5×10^{-11} , 1.5×10^{-12} , 1.5×10^{-13} , 1.5×10^{-14} , m^3/s , respectively.

After mold drawing, the .STL file was input into CAE software Comsol. The domain was set as Laminar Flow and Transportation of Diluted Species physics wizard and the material was set with density of $1000 \text{ Kg}/\text{m}^3$, and dynamic viscosity of $1 \times 10^{-3} \text{ Pa}\cdot\text{s}$. The initial diffusion rate was $8 \times 10^{-10} \text{ m}^2/\text{s}$ and flow concentration was $1 \text{ mol}/\text{m}^3$

at one side and 0 at the other side. By changing the position of inlets and outlets and the inlet flow rate, we can achieve the variation of concentration distribution.

Figure B.1 shows the simulation results of concentration characteristics in the microfluidic channel. First, in the condition of higher flow rate ($>1.5 \times 10^{-12} \text{ m}^3/\text{s}$), if the inlets or outlets of both sides was symmetric with same flow rate, the pattern of concentration distribution was centrosymmetric, if not, inlets or outlets was biased, the pattern was axisymmetric. Second, with decreasing the flow rate in the channels ($<1.5 \times 10^{-13} \text{ m}^3/\text{s}$), the distribution changed gradually, from distinct demarcation to blurred boundary.

Combined flow rate with concentration, as shown in Figure B.2, the concentration distribution varied with the arrangement, nevertheless the flow rate characteristics was nearly unchanged in the diffusion area (where prepared for "PillarCell" experiments subsequently). Due to the two-level channel, the flow could be isolated in the 500- μm channel with continuous diffusion supply without influence on the flow.

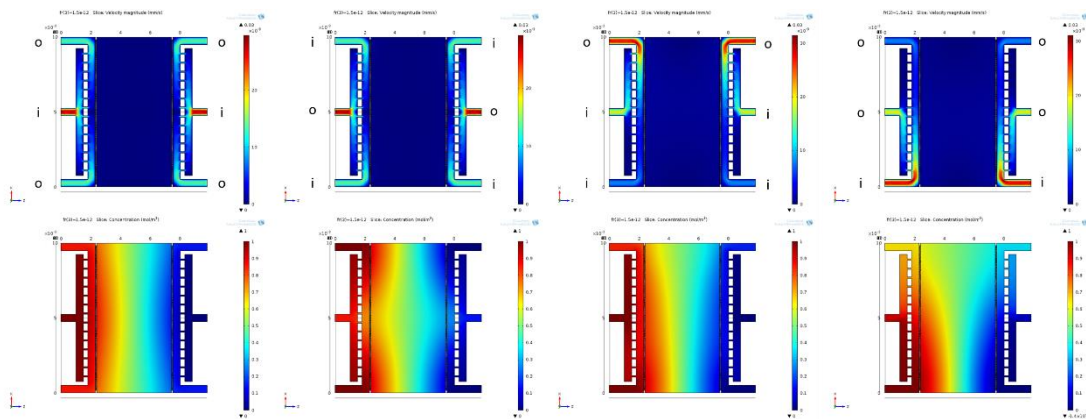


Figure B.2 Simulation of flow rate (1st row) and concentration (2nd row) characteristics in the microfluidic channel with inlet flow rate of $1.5 \times 10^{-12} \text{ m}^3/\text{s}$. The concentration distribution varies with the arrangement of inlets and outlets, i for inlet and o for outlet.

For detailed information, we selected the center line (YZ cutting slice with coordinate X 5 mm, Y 0.05 mm) as future line, as illustrated in Figure B.3. Though the

velocity distribution along the center line was tiny in various flow rates, the slight variation appeared at the flow rate of higher than $1.5 \times 10^{-10} \text{ m}^3/\text{s}$ (in the figures of first row). When the center ports were set as inlets/outlets, i.e. ports in symmetrical distribution, the first level of bypass channel influenced on reducing the flow rate near the diffusion channel. Otherwise, the asymmetric distribution lost the effect of the bypass channel. In addition, the concentration distribution was more obvious to define the importance of the inlets/outlets arrangement (in the figures of second row). Especially, when the center ports were set as outlets, the diffusion area in various flow rate conditions was kept approximately linear. With flow rate higher than $1.5 \times 10^{-12} \text{ m}^3/\text{s}$, the slopes were almost the same. The other three arrangements had linearity with different slopes, only at low flow rates (lower than $1.5 \times 10^{-12} \text{ m}^3/\text{s}$).

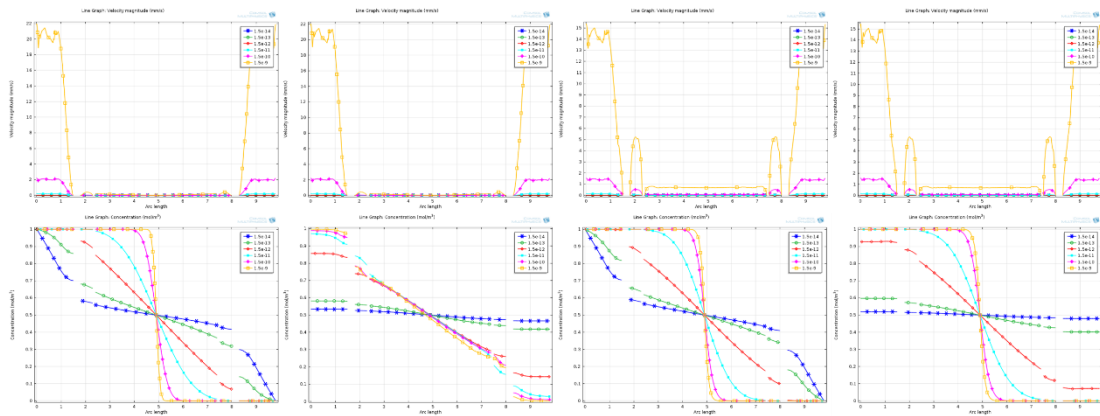


Figure B.3 Simulation of flow rate (1st row) and concentration (2nd row) characteristics in the microfluidic channel various with the inlet flow rate of 1.5×10^{-9} , 1.5×10^{-10} , 1.5×10^{-11} , 1.5×10^{-12} , 1.5×10^{-13} , 1.5×10^{-14} , m^3/s , respectively. The cutting line set on the center surface (YZ cutting slice with X 5 mm, Y 0.05 mm).

For another extreme case, when a pair of ports was blocked, the distribution of flow rate could effectively maintain unchangeable and low, similar to all ports functioning, shown in Figure B.4. While the concentration was more convincing to axisymmetric distribution, the concentration near import and inlets and outlets were significantly nonuniform. Particularly, with blocking one pair of end ports, whether the center ports were inlets or outlets was essential for final concentration

distribution.

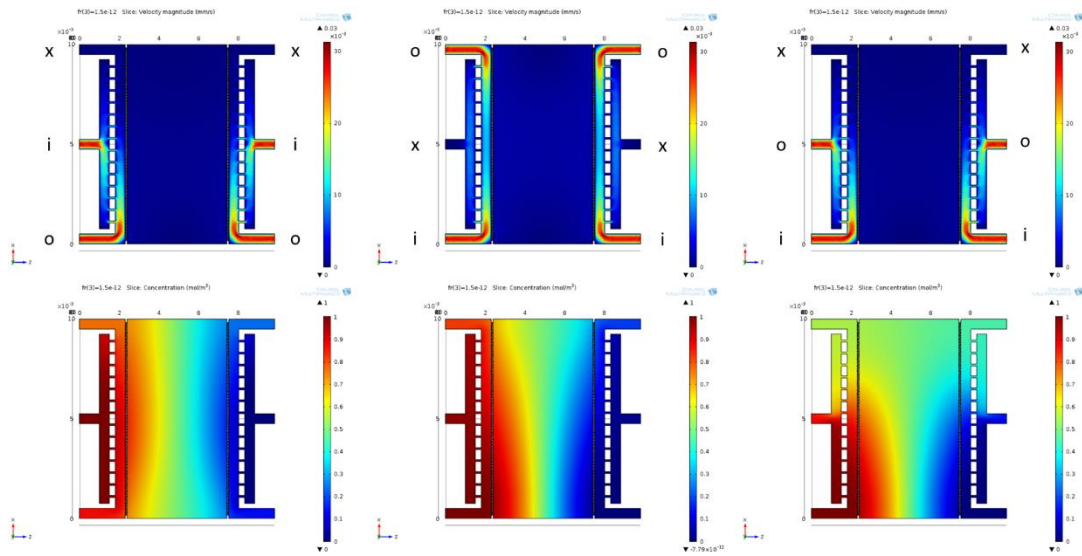


Figure B.4 Simulation of flow rate (1st row) and concentration (2nd row) characteristics in the microfluidic channel with inlet flow rate of $1.5 \times 10^{-12} \text{ m}^3/\text{s}$. The concentration distribution varies with the arrangement of inlets and outlets, i for inlet, o for outlet and x for blocked.

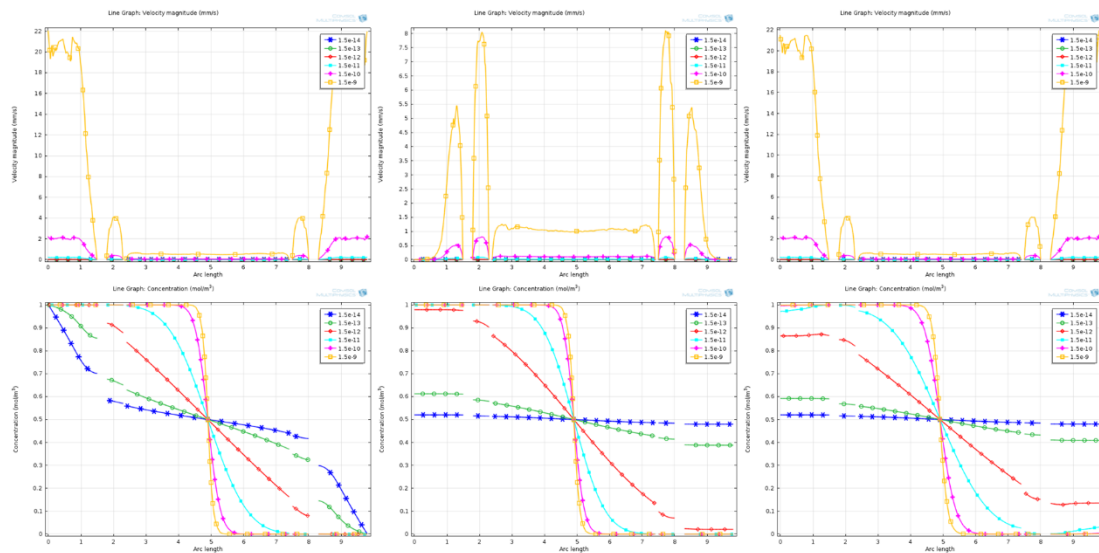


Figure B.5 Simulation of flow rate (1st row) and concentration (2nd row) characteristics in the microfluidic channel various with the inlet flow rate of 1.5×10^{-9} , 1.5×10^{-10} , 1.5×10^{-11} , 1.5×10^{-12} , 1.5×10^{-13} , $1.5 \times 10^{-14} \text{ m}^3/\text{s}$, respectively. The cutting line set on the center surface (YZ cutting slice with X 5 mm, Y 0.05 mm).

If the center ports were inlets, due to the presence of bypass channel, the concentration distribution could remain centrosymmetric, smaller difference between inlets and outlets; if the center ports were outlets, the concentration distribution was significantly biased towards the inlets end. From the line graphs of Figure B.5, in the condition of blocking a pair of ports, regardless of how to adjust the arrangement of inlets and outlets, linear feature could not be achieved when the flow rate higher than $1.5 \times 10^{-12} \text{ m}^3/\text{s}$.

B.3 Simulation of flow based gradient generators

The microfluidic channel was draw by CAD software Solidworks finally in .STL files. The width of inlets was $100 \mu\text{m}$ multiplied by 9, and the area of diffusion channel (where prepared for “PillarCell” experiments subsequently) was $1 \times 7 \text{ mm}^2$. The height of the microfluidic chip was $50 \mu\text{m}$ in whole.

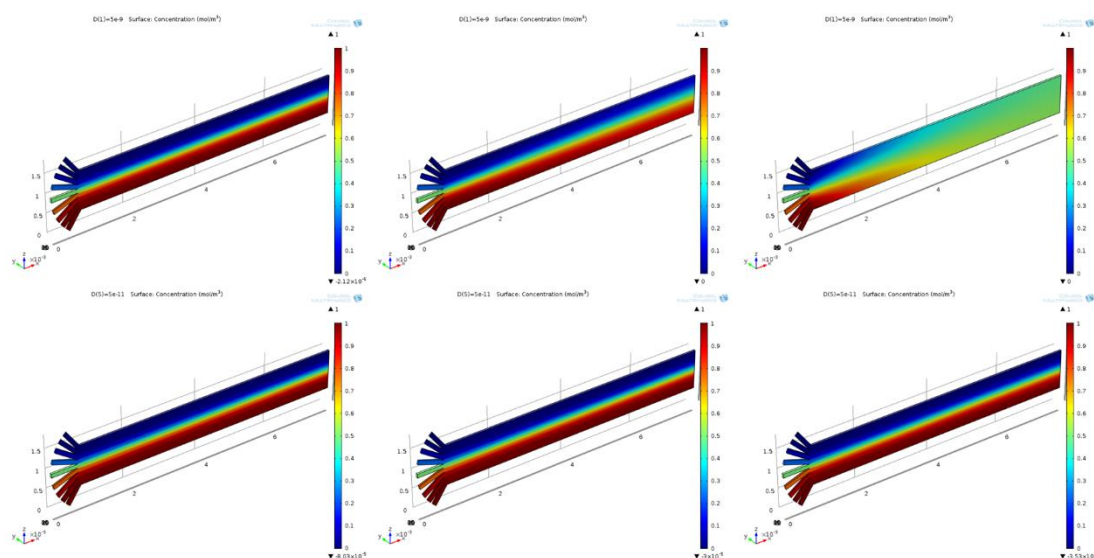


Figure B.6 Simulation of concentration characteristics in the microfluidic channel. In row, the concentration distribution varies with inlet flow rate of $1/9 \times (1, 0.1 \text{ and } 0.01) \text{ ml/h}$. In column, the concentration distribution varies with various solution diffusion constant of 5×10^{-9} and $5 \times 10^{-11} \text{ m}^2/\text{s}$, respectively.

After mold drawing, the .STL file was input into CAE software Comsol. The

domain was set as Laminar Flow and Transportation of Diluted Species physics wizard and the material was set with density of 1000 Kg/m^3 , and dynamic viscosity of $1 \times 10^{-3} \text{ Pa}\cdot\text{s}$.

Since flow motion through the whole channel from inlets to outlet, we firstly selected appropriate diffusion constant, based on which to view the influence of inlet flow rate on the generation of concentration gradient, as shown in Figure B.6.

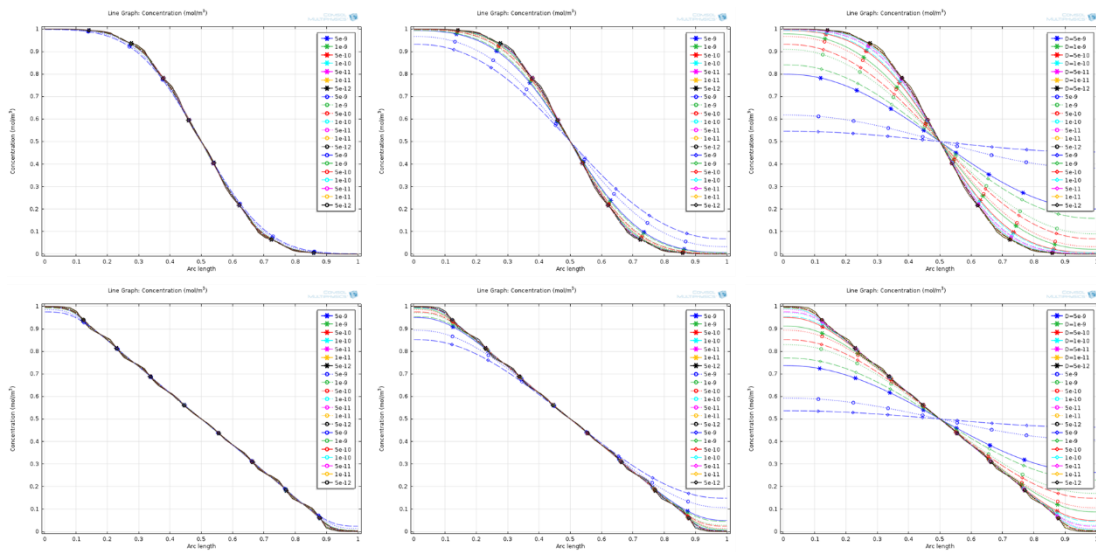


Figure B.7 Simulation of concentration characteristics in the microfluidic channel. In row, the concentration distribution varies inlet flow rate of $1/9 \times (1, 0.1 \text{ and } 0.01) \text{ ml/h}$. In column, the concentration distribution varies with various inlet flow condition of nonlinear and linear. The cutting line set on the parallel surface of YZ cutting slice with Y 0.025 mm and X 2 (solid line), 4 (dotted line) and 6 (dashed line) mm. Solution diffusion constant varies with 1×10^{-9} , 5×10^{-9} , 1×10^{-10} , 5×10^{-10} , 1×10^{-11} , 5×10^{-11} and $1 \times 10^{-12} \text{ m}^2/\text{s}$, respectively.

In various of solution diffusion constant with 1×10^{-9} , 5×10^{-9} , 1×10^{-10} , 5×10^{-10} , 1×10^{-11} , 5×10^{-11} and $1 \times 10^{-12} \text{ m}^2/\text{s}$, we compared the typical condition of 5×10^{-9} to $5 \times 10^{-11} \text{ m}^2/\text{s}$. The higher diffusion constant ($> 5 \times 10^{-9} \text{ m}^2/\text{s}$), the larger difference of concentration distribution between upstream and downstream, apparently in the condition of flow rate of 0.01 ml/h. The larger flow rate ($> 1 \text{ ml/h}$), the smaller difference of concentration distribution between upstream and downstream,

regardless of the diffusion constant, as shown in Figure B.7. Moreover, in different flow supplied condition (nonlinear and linear), reducing the flow rate lower than 0.1 ml/h resulted in linear distribution transforming to nonlinear distribution, especially with diffusion constant higher than $5 \times 10^{-10} \text{ m}^2/\text{s}$.

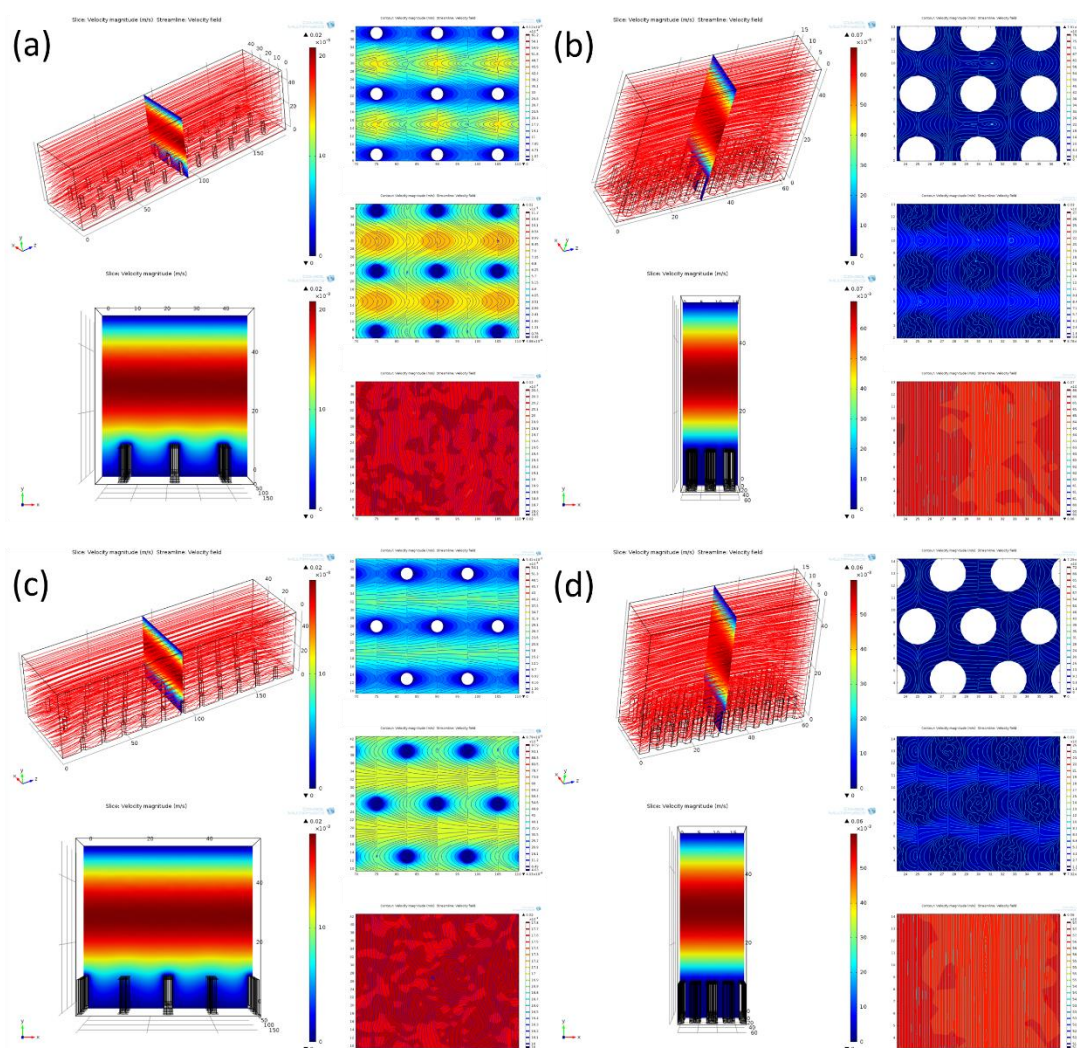


Figure B.8 Simulation of stream line and flow rate characteristics in the microfluidic channel integrated with micropillars of different array, under flow rate of 0.1 ml/h. Micropillar array with diameter of $3 \mu\text{m}$, height of $10 \mu\text{m}$ and (a) period of $15 \mu\text{m}$ and square arrangement, (b) period of $5 \mu\text{m}$ and square arrangement, (c) period of $15 \mu\text{m}$ and hexagon arrangement, (d) period of $5 \mu\text{m}$ and hexagon arrangement.

Due to the presence of flow in the concentration gradient region, it was possible to affect flow line and flow rate by introducing micropillar array. Therefore, we

simulated flow field near micropillars, as shown in Figure B.8. By adjusting the arrangement and spacing between micropillars, it was observed that the hexagonal arrangement could effectively avoid the flow rate surge and streamline vortex occurring around the micropillars. When the spacing was small (5 μm in Figure B.8d), the flow rate on the surface of micropillars was low but the flow shear force was large. When the spacing was big (15 μm in Figure B.8c), the flow rate between the micropillars varied gradually, the flow shear force could be effectively reduced.

B.4 Summary and perspective

Although the simulation results could differ from the actually experimental results, it provides us with reasonable reference and conditional selection before experimental operation. In particular, when selecting different gradient generation devices, in the subsequent considerations of integration of micropillars and cell culture in the microfluidic chips, we could make operative prediction in accordance with the simulation results, for example, the introduction of flow shear forces (which simulates blood flow effects) as well as the arrangement and parameter of micropillar array (which determines the relative position of cells).

Abbreviation list

1D	one-dimensional
2D	two-dimensional
3D	three-dimensional
AFM	atomic force microscopy
APTES	3-aminopropyl triethoxysilane
BSA	bovine serum albumin
CAD	computer aided design
CAE	computer aided engineering
CAM	computer aided manufacturing
CCD	charge-coupled device
CEA	chicken egg albumin
CNC	computer numerical control
Cr	chromium
CVD	chemical vapor deposition
DAPI	4',6-diamidino-2-phenylindole
DIC	differential interference contrast
DIW	deionized water
DMEM	Dulbecco's Modified Eagle Medium
DMSO	dimethyl sulfoxide
DMF	dimethylformamide
DNA	deoxyribonucleic acid
DPBS	Dulbecco's Phosphate-Buffered Saline
E8	Essential 8
ECM	extracellular matrix
EDTA	ethylenediaminetetraacetic acid
ENS	École normale supérieure

FBS	Fetal Bovine Serum
FDA	food and drug administration
FDM	fused deposition modeling
FN	fibronectin
GFAP	glial fibrillary acidic protein
Ig	immunoglobulin
IPA	isopropanol
iPS	induced pluripotent stem
LOM	laminated object manufacturing
μ PG	micro-pattern generator
μ TAS	micro total analysis systems
MEM	minimum essential medium
MEMS	microelectromechanical systems
MP	micropillars
NF	nanofibers
NIH	National Institutes of Health
Oct4	octamer-binding transcription factor 4
P/S	Penicillin/Streptomycin
PB	particle beam
PBS	phosphate-buffered saline
PC	polycarbonate
PCL	polycaprolactone
PDMS	polydimethylsiloxane
Pe	Péclet number
PE	polyethylene
PEG	poly ethylene glycol
PFA	paraformaldehyde
PLGA	poly lactic-co-glycolic acid
PMMA	polymethylmethacrylate

PMGI	polymethylglutarimide
PVDF	polyvinylidene fluoride
PVP	polyvinylpyrrolidone
Re	Reynolds number
RNA	ribonucleic acid
ROI	region of interest
RP	rapid prototyping
SDS	sodium dodecyl sulphate
SEM	scanning electron microscope
SLA	stereo lithography appearance
SLS	selective laser sintering
SSEA4	stage-specific embryonic antigen 4
THF	tetrahydrofuran
TMCS	trimethylchlorosilane
TUJ1	anti- β -tubulin III
US	United States
USP	US Pharmacopoeia
UV	ultraviolet
VN	vitronectin
Y-27632	RHO/ROCK pathway inhibitor

Publication list

1. **J. Wei**, D. Pozzi, F. P. U. Severino, V. Torre, Y. Chen, Fabrication of PLGA nanofibers on PDMS micropillars for neuron culture studies. *Microelectronic Engineering* 175, 67-72 (2017).
2. **J. Wei**, J. Shi, B. Wang, Y. Tang, X. Tu, E. Roy, B. Ladoux, Y. Chen, Fabrication of adjacent micropillar arrays with different heights for cell studies. *Microelectronic Engineering* 158, 22-25 (2016).
3. X. Tu, **J. Wei**, B. Wang, Y. Tang, J. Shi, Y. Chen, Patterned parylene C for cell adhesion, spreading and alignment studies. *Microelectronic Engineering* 175, 56-60 (2017).
4. B. Wang, J. Shi, **J. Wei**, L. Wang, X. Tu, Y. Tang, Y. Chen, Fabrication of elastomer pillar arrays with height gradient for cell culture studies. *Microelectronic Engineering* 175, 50-55 (2017).
5. X. Tu, L. Wang, **J. Wei**, B. Wang, Y. Tang, J. Shi, Z. Zhang, Y. Chen, 3D printed PEGDA microstructures for gelatin scaffold integration and neuron differentiation. *Microelectronic Engineering* 158, 30-34 (2016).
6. G. Zheng, L. Sun, X. Wang, **J. Wei**, L. Xu, Y. Liu, J. Zheng, J. Liu, Electrohydrodynamic direct-writing microfiber patterns under stretching. *Applied Physics A* 122, 1-9 (2016).

Résumé

Ce travail a pour but de développer des nouveaux substrats d'étude en culture cellulaire. Nous avons d'abord fabriqué des réseaux de micro-piliers en élastomère et en polymères thermoplastiques. En particulier, nous avons réalisé des réseaux de micro-piliers adjacents et de différentes hauteurs, qui dépend de la rigidité de la surface de culture. Nos résultats ont montré que les cellules étaient sensibles à la hauteur des piliers lorsque la rigidité effective du substrat était similaire à celle de la cellule et que les cellules se déplacent préférentiellement vers la partie plus rigide. Nous avons également développé une méthode pour fabriquer des nanofibres sur les piliers élastomère pour créer un substrat qui reproduit la matrice extracellulaire in vivo. Nos résultats ont montré que les neurones primaires de l'hippocampe sur un tel substrat étaient plus actifs que sur des substrats plats. En outre, nous avons analysé le confinement et la déformation des noyaux cellulaires dans les espaces inter-piliers pour les études de cellules tumorales et de cellules souches. Enfin, nous avons intégré les réseaux de micro-piliers dans un dispositif microfluidique afin de montrer que la migration cellulaire soumise à un gradient de concentration était influencée par la rigidité du substrat. En conclusion, les micropiliers ainsi fabriqués peuvent être utilisés pour réguler la rigidité d'un substrat afin d'étudier divers mécanismes en culture cellulaire.

Mots Clés

Micropiliers; Nanofibres; Microfluidique; Culture cellulaire

Abstract

This work aimed to provide new substrates for cell culture studies. We first developed a method to fabricate micropillars in both elastomer and thermoplastic polymer. In particular, we produced adjacent micropillar arrays with different heights to evaluate the surface stiffness dependent migration of cells. Our results showed that cells were sensitive to the height of the pillars when the effective stiffness of the substrate is compatible to that of the cell and that the cells were preferentially localized on the stiffer surface area. We also developed a method to fabricate nanofibers on the elastomer pillars to create in-vivo like extracellular matrix. Our results showed that primary hippocampal neurons on such a substrate were more active than on flat substrates. Furthermore, we analyzed the confinement and deformation of cell nuclei in the inter-pillar areas for both cancer and stem cell studies. Finally, we integrated the micro-pillar arrays into a microfluidic device and showed that the cell migration under concentration gradient was influenced by the substrate stiffness. Altogether, the fabricated pillar arrays can be used to regulate the stiffness of the substrate for cell culture studies.

Keywords

Micropillars; Nanofibers; Microfluidics; Cell culture